UNIVERSITÀ DI TRENTO

Department of Physics

Doctoral School in Physics

MODE MATCHING SENSING IN FREQUENCY DEPENDENT SQUEEZING SOURCE FOR ADVANCED VIRGO PLUS

Supervisor:
Prof. Antonio Perreca

Candidate:
MSc. Andrea Grimaldi

2022

Eine Entdeckung ist weder groß noch klein; es kommt darauf an, was sie für uns bedeutet.
L. Wittgenstein 1930

Una scoperta non è né grande né piccola; ciò che conta è il significato che ha per noi.

AKWNOLGEMENT

I want to thank my supervisor, Antonio Perreca, for the trust he granted me during my research journey. Without it, I would not have been able to do all the experiences that led me to the end of this journey. I am glad I shared my PhD studies with Michele Valentini, it was always nice to share different points of view, and I am indebted for all his support on Finesse. I want to thank Giovanni Prodi for teaching me the research work's administration aspects.

I am deeply thankful to Jean-Pierre Zendri. He was a trustful guide in the wonderland of Virgo Collaboration. I would have lost myself without his guide. I am indebted to Marco Vardaro for the training he gave me during the commissioning of Advance Virgo Plus. I treasured the expertise and knowledge that he shared with me.

I want to thank the commissioning team of the Virgo Quantum Noise Reduction system: Romain Bonnand for helping me design in Optocad; Fiodor Sorrentino and Valeria Sequino for supervising my (small) contribution to the Squeezed Vacuum Source; Eleonora Capocasa for teaching me the cleanest way to align a Homodyne detector; Yuefan Guo, Eleonora Polini, and Barbara Garaventa for the time spent together during the commissioning work.

I am grateful to Padova Virgo Group for providing the resources and infrastructure necessary for this research and the time spent together. I want to thank Livia Conti for sharing her view of the research world. I have always appreciated her being straightforward; she helped me see things from a new perspective. I am glad for all the discussions I had with Giacomo Ciani; sometimes too long but always stimulating. I was and still am very happy to meet Gabriella Chiarini and Luis Diego Bonavena; they brought fresh air to the team.

I am thankful to Matteo Tacca, who put his trust in me and invited me to work on the commissioning of Advanced Virgo plus. To Martina De Laurentis for the knowledge she shared during the commissioning.

In conclusion, I am deeply indebted to my family and friends for their love, encouragement, and unwavering support throughout my studies. Finally, I would like to thank my love for remembering the true meaning of a weekend.

PREFACE

Since the first detection of a Gravitational Wave, the LIGO-Virgo Collaboration has worked to improve the sensitivity of their detectors. This continuous effort paid off in the last scientific run, in which the collaboration detected an average of one gravitational wave per week and collected 74 candidates in less than one year.

This result was also possible due to the Frequency Independent Squeezing (FIS) implementation, which improved the Virgo detection range for the coalescence between two Binary Neutron Start (BNS) of 5-8%. However, this incredible result was dramatically limited by different technical issues, among which the most dangerous was the mismatch between the squeezed vacuum beam and the resonance mode of the cavities.

The mismatch can be modelled as a simple optical loss in the first approximation. If the beam shape of squeezed vacuum does not match the resonance mode, part of its amplitude is lost and replaced with the incoherent vacuum. However, this modelisation is valid only in simple setups, e.g. if we study the effect inside a single resonance cavity or the transmission of a mode cleaner. In the case of a more complicated system, such as a gravitational wave interferometer, the squeezed vacuum amplitude rejected by the mismatch still travels inside the optical setup. This component accumulates an extra defined by the characteristics of the mismatch, and it can recouple into the main beam reducing the effect of the quantum noise reduction technique[1]. This issue will become more critical in the implementation of the Frequency Dependent Squeezing. This technique is an upgrade of the Frequency Independent Squeezing one. The new setup will increase the complexity of the squeezed beam path.

The characterisation of this degradation mechanism requires a dedicated wavefront sensing technique. In fact, the simpler approach based on studying the resonance peak of the cavity is not enough. This method can only estimate the total amount of the optical loss generated by the mismatch, but it cannot characterise the phase shift generated by the decoupling. Without this information is impossible to estimate how the mismatched squeezed vacuum is recoupled into the main beam, and this limits the possibility to foreseen the degradation of the Quantum Noise Reduction technique.

For this reason, the Padova-Trento Group studied different techniques for characterising Mode Matching. In particular, we proposed implementing the Mode Converter technique developed by Syracuse University[2]. This technique can fully characterise the mismatch of a spherical beam, and it can be the first approach to monitoring the mismatch. However, this method is not enough for the Frequency Dependent Squeezer source since it cannot detect the mismatch generated by the astigmatism of the incoming beam.

In fact, the Frequency Dependent Squeezer Source case uses off-axis reflective telescopes to reduce the power losses generated by transmissive optics. This setup used curved mirrors that induce small astigmatic aberrations as a function of the beam incident angle. These aberrations are present by design, and the standard Mode Converter

Technique will not detect them. To overcome this issue, I proposed an upgrade of the Mode Converter technique, which can extend the detection to this kind of aberration.

The Quantum Noise Reduction system is currently implementing the standard Mode Converter Technique, while the astigmatic wavefront sensing is foreseen for the next detector upgrades and is still under review.

The manuscript is divided into seven chapters:

Chapter 1 I briefly introduce the reader to the gravitational wave detector with a specific focus on quantum noise. Here, We discuss the main ideas of the Quantum Noise Reduction system and why it is necessary to have real-time detection of the Mode Matching.

Chapter 2 This chapter contains all the theoretical frameworks at the foundation of the Mode Matching sensing. I start with an introduction to the resonant cavities and their transverse mode. After that, I formalise the mode matching in the case of a Simple Astigmatic Gaussian Beam and extend the standard representation proposed by Anderson[3].

Chapter 3 This chapter is dedicated to the Astigmatic Mode Matching Sensing technique. Here, I will present the detection setup required for the measurement of the mismatch, and I will discuss its experimental limits.

Chapter 4 The Mode Matching Technique was validated using a dedicated tabletop experiment built from the ground up. In this chapter, we report the full characterisation of each component.

Chapter 5 This chapter reports validating the Mode Matching Sensing technique. I first describe the experimental protocol and then discuss the measurement and the validation of the method.

Chapter 6 In this chapter, I presented the general setup of the Frequency Dependent Squeezing source and the design of the wavefront sensors dedicated to the squeezed vacuum beam. The installation of the Mode Converter Technique in the Quantum Noise Reduction System is still ongoing.

Chapter 7 We conclude the thesis with a summary of the main results and a description of the next steps of these experiments.

CONTENTS

Akwnolgement v

Preface vii

I Gravitational Wave Detection 1
- I.1 Advanced Virgo Plus 2
- I.2 Quantum Noise 6
- I.3 Quantum Noise Reduction 11

II Optical Resonators and Mode Matching 19
- II.1 Optical Resonator 20
- II.2 Mismatch of a Simple Astigmatic Gaussian Beam 34

III Astigmatic Mode mismatch Sensing 45
- III.1 Theoretical Model 45
- III.2 Experimental Limits 57

IV Experimental test of the Mode Matching Sensing 65
- IV.1 Optical Setup 66
- IV.2 Electronic Setup 104

V Validation Measurement of the Mode Matching Sensing 115
- V.1 Validation of the Mode Converter Technique 116
- V.2 Validation of Astigmatic Mismatching Sensing 119

VI Mode Matching Sensing in Quantum Noise Reduction System 125
- VI.1 Frequency Dependent Squeezing 125
- VI.2 General Design of the Frequency Dependent Squeezer 126

VII Summary and Outlook 133
- VII.1 Summary 133
- VII.2 Outlook 134

A Experimental Technique 137
- I.1 Beam Shape measurement 137
- I.2 Astigmatic Mode Matching Telescope 137

B Simulation 141
- II.1 Kat File Optical Setup 141
- II.2 Two lens telescope control 145

II.3 Two lens telescope control with Driving Matrix 146

Bibliography 150

I GRAVITATIONAL WAVE DETECTION

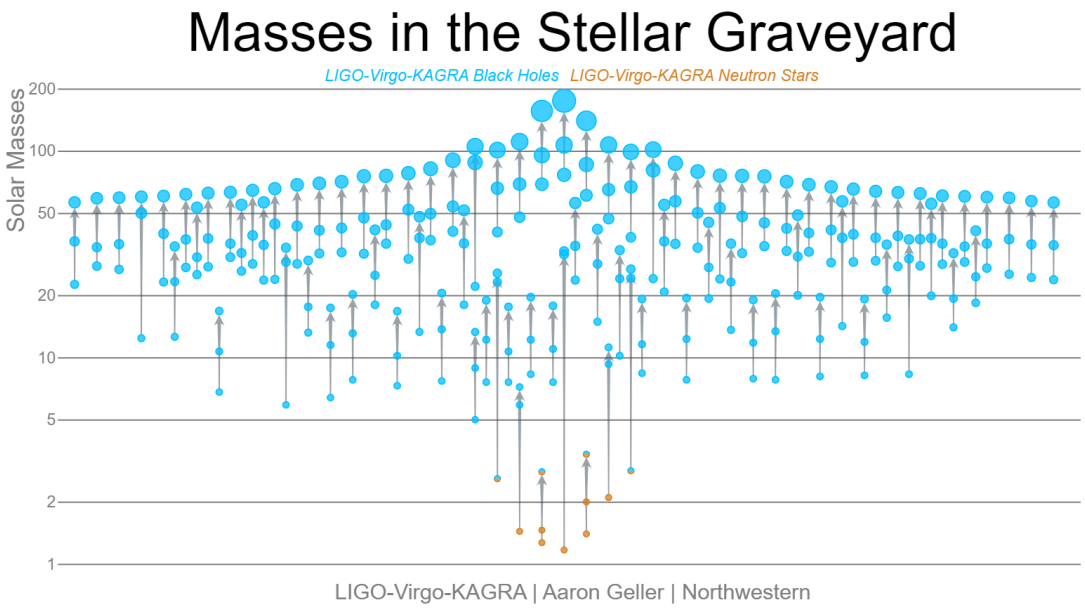

FIGURE I.1: Stellar Graveyard. Graphic representation of the source of the gravitational wave signal detected by the LIGO-Virgo Collaboration. The Black holes are represented in blue, while the Neutron stars are in orange. This version contains all events through the end of O3 with p_astro[1] > 0.5. Credit: LIGO-Virgo, Aaron Geller, Northwestern University.

During the last scientific run, the LIGO-Virgo Collaboration detected 79 candidates of Gravitational Wave events: 44 in the first six months[2], and 35 in the second five months[3]. These numbers correspond to a detection rate of more than one event per week and define a new era for the gravitational wave community.

This milestone was the result of different activities performed between the second and the third observing runs. From August 2017 until April 2019, different aspects of the detectors were improved: LIGO-Hanford and LIGO-Livingston improved the quality of their mirrors, while Virgo upgraded the suspension system of the external input bench and of the interferometer mirrors. On top of these specific upgrades, all the detectors increased the input power and implemented the Frequency Independent Squeezing technique[6].

With the conclusion of the third scientific run in March 2022, the detector of the

[1] p_astro is the probability of astrophysical origin assuming a compact binary coalescence source.
[2] Between 1 April 2019 15:00 UTC and 1 October 2019 15:00 UTC[4].
[3] Between 1 November 2019 15:00 UTC and 27 March 2020 17:00 UTC[5].

LIGO-Virgo collaboration started the installation and commissioning of a new package of upgrades. These activities are still ongoing at the time of writing, but we expect a dramatic increase in the detector performance. In particular, the Virgo interferometer is going to: increase the input optical power up to 40 W, install the Signal Recycling Mirror, and implement the Frequency Dependent Squeezing technique[7]. Similar improvements are foreseen for the LIGO interferometers[8].

The implementation of these upgrades is based on a multitude of Research and Development projects. The new hardware and the new experimental techniques are first tested in the various laboratories of the Collaboration before they are installed in the detectors.

In particular, the Frequency Dependent Squeezing was first validated on a tabletop experiment[9][10] and after in a full-scale experiment at TAMA, in Japan[11] and at LIGO[12], in U.S.A. . The information obtained from these two experiments, together with the expertise obtained during the installation of Frequency Independent Squeezing, made it possible to identify different technical issues which limit the efficiency of the technique. This upgrade is strongly limited by power losses that have to be identified and compensated everywhere possible. The work presented in this thesis is focused on one specific loss mechanism called Mode Mismatch.

This chapter will be a small introduction to the scientific context. In the first part, I will briefly introduce gravitational wave detectors and the fundamental noise generated by the quantum nature of light. Inside this background, I will present how the Frequency Dependent Squeezing technique improves the detector sensitivity and how the optical losses limit the method.

I.1. Advanced Virgo Plus

In order to understand how a gravitational wave detector works, we first need to introduce what a gravitational wave is. The formal derivation of this phenomenon arises from studying the linearised equation of the gravitational field. This analysis is beyond the scope of this thesis; however, we can use the results described in [13] to define some properties of the gravitational wave. First, the gravitational wave is the space-time metric's deformation, which changes the distance between objects. Second, the gravitational wave is transverse, so this deformation takes place orthogonal to the wave propagation. Third, the deformation is oriented along two orthogonal axes, and it is intrinsically differential, meaning that if one axis is stretched, the other one is compressed. Fourth, the gravitational waves have two polarization, rotated by 45° one with respect to the other.

The effect of a gravitational wave can be pictured by considering a set of free-falling masses arranged as in Figure I.2 and assuming a gravitational wave that crosses perpendicular to the page with polarisation oriented as $+$. The deformation of the space-time changes the distance between the masses, and the diameter along the two axes $\hat{x}$ and $\hat{y}$ will evolve as

$$\begin{aligned} L_x(t) &= L\left(1+\frac{1}{2}h(t)\right) \\ L_y(t) &= L\left(1-\frac{1}{2}h(t)\right) \end{aligned} \tag{I.1}$$

where $h(t)$ is the amplitude of the gravitational wave and L is the circle diameter at

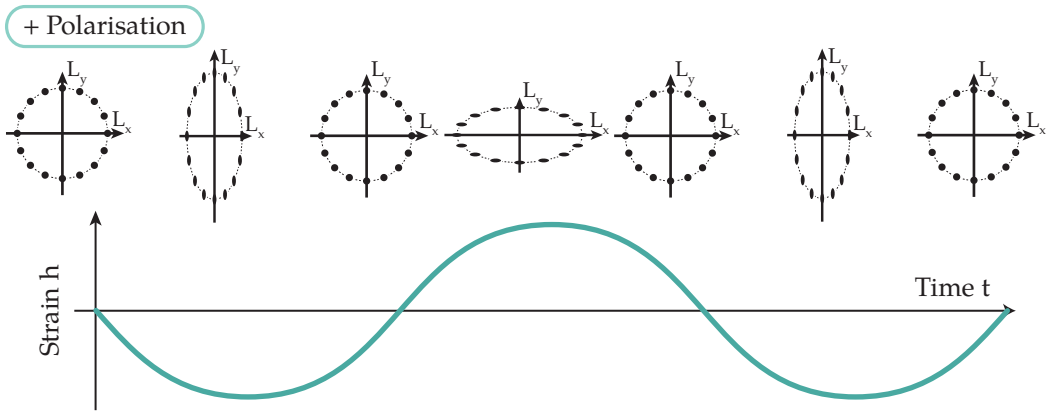

FIGURE I.2: Time Evolution of a gravitational wave. The effect of a gravitational wave is the deformation of the space-time metric.

time $t = 0$.

The differential nature of the deformation is at the foundation of the last generation of gravitational wave detectors. This pattern matches the structure of a Michelson interferometer, an optical setup designed to convert the difference between the two orthogonal paths into an optical signal. Using Figure I.3 as a reference, we have an incoming beam E_{in} that is divided by a beam splitter into two fields:

$$E_1 = E_{\text{in}}\frac{i}{\sqrt{2}} \quad \text{and} \quad E_2 = E_{\text{in}}\frac{1}{\sqrt{2}} \tag{I.2}$$

where E_1 is reflected and sent to the y Arm and E_2 is transmitted and sent to the x Arm. They respectively travel for a distance L_y and L_x and their amplitude collects a phase shift of

$$E_3 = E_1 e^{ikL_y} \quad \text{and} \quad E_4 = E_2 e^{ikL_x} \tag{I.3}$$

where k is the wave vector $k = 2\pi/\lambda$ and λ is the beam wavelength. After that, they are reflected by the two end mirrors,

$$E_5 = E_3 i \quad \text{and} \quad E_6 = E_4 i \tag{I.4}$$

and they travel back to the beam splitter, collecting a phase shift proportional to the arm lengths, L_y and L_x again:

$$E_7 = E_5 e^{ikL_y} \quad \text{and} \quad E_8 = E_6 e^{ikL_x} \tag{I.5}$$

These two are divided by the beam splitter:

$$\begin{aligned} E_9 &= \frac{E_7}{\sqrt{2}} \quad \text{and} \quad E_{11} = i\frac{E_7}{\sqrt{2}} \\ E_{10} &= \frac{E_8}{\sqrt{2}} \quad \text{and} \quad E_{12} = i\frac{E_8}{\sqrt{2}} \end{aligned} \tag{I.6}$$

and the final four beams superimpose at the two outputs of the interferometer. At the symmetric port(left), we have:

$$E_{sym} = E_{11} + E_{10} = \frac{-1}{2}\left(e^{i2kL_x} + e^{ik2L_y}\right) E_{\text{in}} \tag{I.7}$$

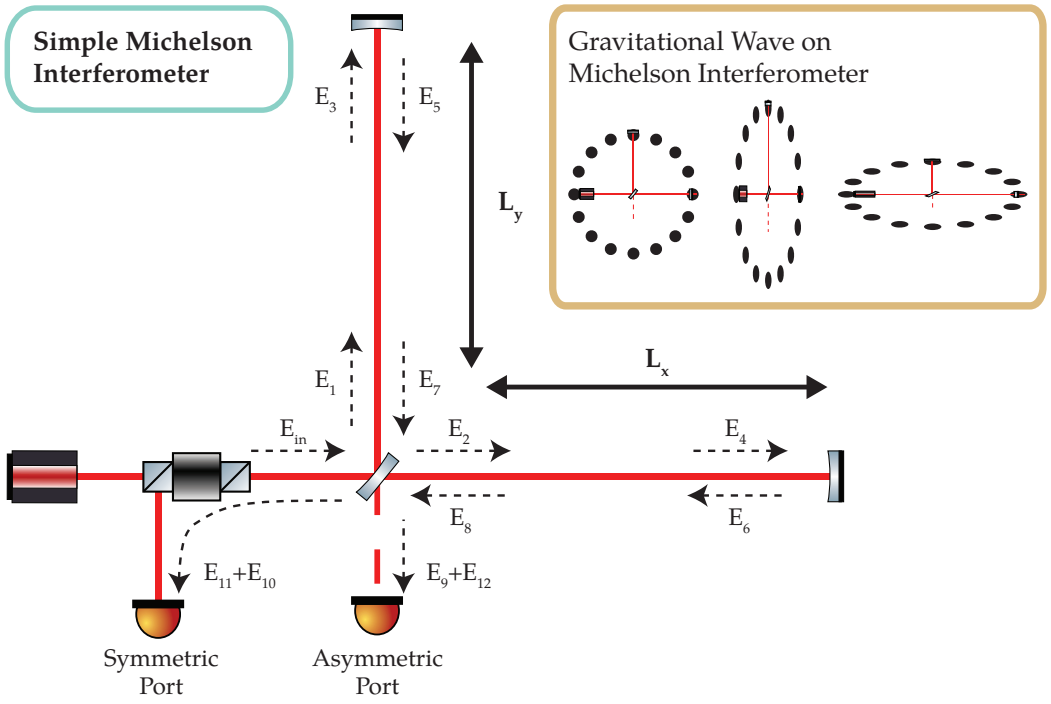

FIGURE I.3: Optical Scheme of a Michelson interferometer. If the gravitational wave polarisation is perfectly aligned with the interferometer arms, the space-time deformation induces a differential variation of the arm lengths detected at the output.

while at the anti-symmetric port(bottom):

$$E_{asy} = E_9 + E_{12} = \frac{i}{2}\left(e^{i2kL_x} - e^{ik2L_y}\right) E_{\text{in}} \tag{I.8}$$

The amplitude of the gravitational wave, $h(t)$, is encoded in the difference between the phases accumulated along the two arms. This information is most clearly represented using

$$L = \frac{L_x + L_y}{2} \quad \text{and} \quad \delta L = \frac{L_x - L_y}{2} \tag{I.9}$$

which divide the common arms length, L, from the differential one δL. The first parameter represents the interferometer size, while the second contains the signal of interest. By combining E.q. I.1 with Eq. I.9, we can see that the effect of a gravitational wave changes the differential length:

$$\delta L(t) = \frac{L_x(t) - L_y(t)}{2} = \frac{\left(L_x + \frac{1}{2}L_x h(t)\right) - \left(L_y(t) - \frac{1}{2}L_y h(t)\right)}{2} = \delta L + \frac{1}{2}h(t)L \tag{I.10}$$

while it leaves the common length unperturbed:

$$L(t) = \frac{L_x(t) + L_y(t)}{2} = \frac{\left(L_x + \frac{1}{2}L_x h(t)\right) + \left(L_y(t) - \frac{1}{2}L_y h(t)\right)}{2} = L \tag{I.11}$$

In this way, we can rewrite the beam amplitude at the asymmetric output of the

interferometer as:

$$E_{asy} = \frac{1}{2} E_{in} \left(e^{ik2(L+\delta L(t))} + e^{ik2(L-\delta L(t))} \right) = \frac{1}{2} E_{in} e^{ik2L} \left(e^{+ik\,2\delta L(t)} + e^{-ik\,2\delta L(t)} \right) = E_{in} e^{ik2L} \cos(k\,2\delta L + kh(t)L) \quad \text{(I.12)}$$

where we highlighted the dependency on the gravitational wave amplitude, $h(t)$.

The output beam is recorded with a photodiode which generates a signal proportional to the optical power:

$$P_{asy} = |E_{asy}|^2 = |E_{in}|^2 \cos^2(k2\delta L + kh(t)L) \quad \text{(I.13)}$$

and assuming that the displacement produced by the gravitational wave is smaller compared to the laser wavelength, $h(t)L/\lambda \ll 1$, we can approximate the output power as

$$P_{asy} \simeq |E_{in}|^2 \left[\cos^2(k2\delta L) + \cos(k2\delta L) \sin(k2\delta L)\, kh(t)L \right] \quad \text{(I.14)}$$

that is composed of two contributions: one that depends on the detector configuration and another that contains the gravitational wave signal. The optimisation of the detector working point is formalised in the DC readout scheme[14], and it depends on multiple technical parameters. The general approach is to limit the effect of the constant signal generated by the detector configuration, and this is obtained by reducing the offset on the differential arm length, δL, at the minimum and considering only the signal

$$S(h(t)) \propto L P_{in} \frac{2\pi}{\lambda} h(t) \quad \text{(I.15)}$$

where we replaced $|E_{in}|^2$ with the input optical power, P_{in}.

From this simple model, we can see that the gravitational wave signal is proportional to the input power of the laser, P_{in}, and the length of the interferometer arms, L. These are the key parameters in amplifying the gravitational wave signal and should be maximised in every possible way. As we can see from the complete scheme reported in Figure I.4, Advance Virgo Plus is far more complicated than a simple Michelson interferometer. The arm length is increased with a trick: instead of moving the optics far away from the beam splitter, we can install two semi-reflective mirrors, called Input mirrors, at the beginning of each path. In this way, when the beams return after travelling along the arms, they are partially reflected by the new optics and forced to travel again. The beams bounce back and forward between the arm mirrors, and for each round trip, they collect the phase delay proportional to the arm length. When the beams are transmitted from the input mirrors, they will arrive at the beam splitter with a phase proportional to multiple round trips, equivalent to an effective increase of arm lengths.

We can recycle the optical power reflected back by the Michelson interferometer to boost the input power. In fact, The DC-offset configuration exploits the destructive interference to reduce the output signal, and all the optical power is reflected from the symmetric port. All this waste can be reused by installing a semi-reflective mirror between the laser source and the beam splitter. This optics, called Power Recycling Mirror, collects the reflected optical power and sends it back to the interferometer.

These two modifications and the Signal Recycling Mirror installed at the interferometer output allow for reshaping the detector frequency response and optimising the

sensitivity to the gravitational waves. This optical setup is generally called *dual-recycled Fabry-Pérot-Michelson interferometer* and is the typical layout for the second generation of gravitational wave detectors. The analytical study of all these components is beyond the purpose of this introduction, and it does not add any relevant information to the discussion on quantum Noise. More information can be found in [15].

I.2. Quantum Noise

The performance of the gravitational wave detector is normally described by the residual noise coupled to the detected signal. In a nutshell, there are a lot of different phenomena that are not gravitational waves but which generate a similar signal inside the interferometer. These processes, called noise, define the limits to a detectable signal. If the amplitude of the gravitational wave is comparable to the residual noise, it is impossible to determine if the signal is coming from a gravitational wave or another phenomenon.

The residual noise is generally described using the sensitivity curve. This plot represents the amplitude spectral density of the background noise converted in the equivalent gravitational wave amplitude, $h(t)$. An example can be found in Figure I.5, representing the best sensitivity curve of Advance Virgo obtained during the last observing run. This plot collects all the different contributions to the detector background. Each noise source was modelled to identify the coupling mechanism and project the individual contribution to the detector sensitivity.

Among the different noise sources, the quantum noise dominates the whole spectrum. This noise is an intrinsic property of the detector scheme inasmuch is generated by the quantum nature of the light. In fact, the optical beam is not a continuum, but it is composed of a flux of photons that are randomly separated. The time delay between two different photons follows an Exponential distribution, and its fluctuation affects the interferometer. The quantum noise contribution to the sensitivity curve of a simple Michelson is reported in Fig. I.6. This plot shows the two basic mechanisms that connect the quantum fluctuation to gravitational wave detectors, which are:

The Quantum Shot Noise: It couples at the interferometer output, where the uncertainties generate a signal fluctuation proportionally to the square root of the optical power. This noise is time-uncorrelated, and its amplitude spectral density does not depend on the frequency. We can express its contribution as equivalent gravitational wave amplitude[4] [15, p.294]:

$$h_{sn}(f) = \frac{1}{L}\sqrt{\frac{\hbar c\lambda}{2\pi P_{\text{arms}}}} \tag{I.16}$$

where L is the arm length, P_{arms} the optical power in the interferometer arms ($2\,P_{\text{arms}} = P_{\text{in}}$), λ is the laser wavelength, c is the speed of light, $\hbar$ is the reduced Plank constant, and f is the noise frequency.

The Quantum Radiation Pressure: It is generated by an opto-mechaniced coupling between the optical beam and the suspended mirrors. When the optical beam is reflected, each photon transfers its momentum to the mirror. The resulting

[4] This is valid only for a Michelson interferometer, the full design of a gravitational wave detector has a more complicated frequency response that manipulates the final shape of the shot noise. This correction does not change the main results discussed in this chapter.

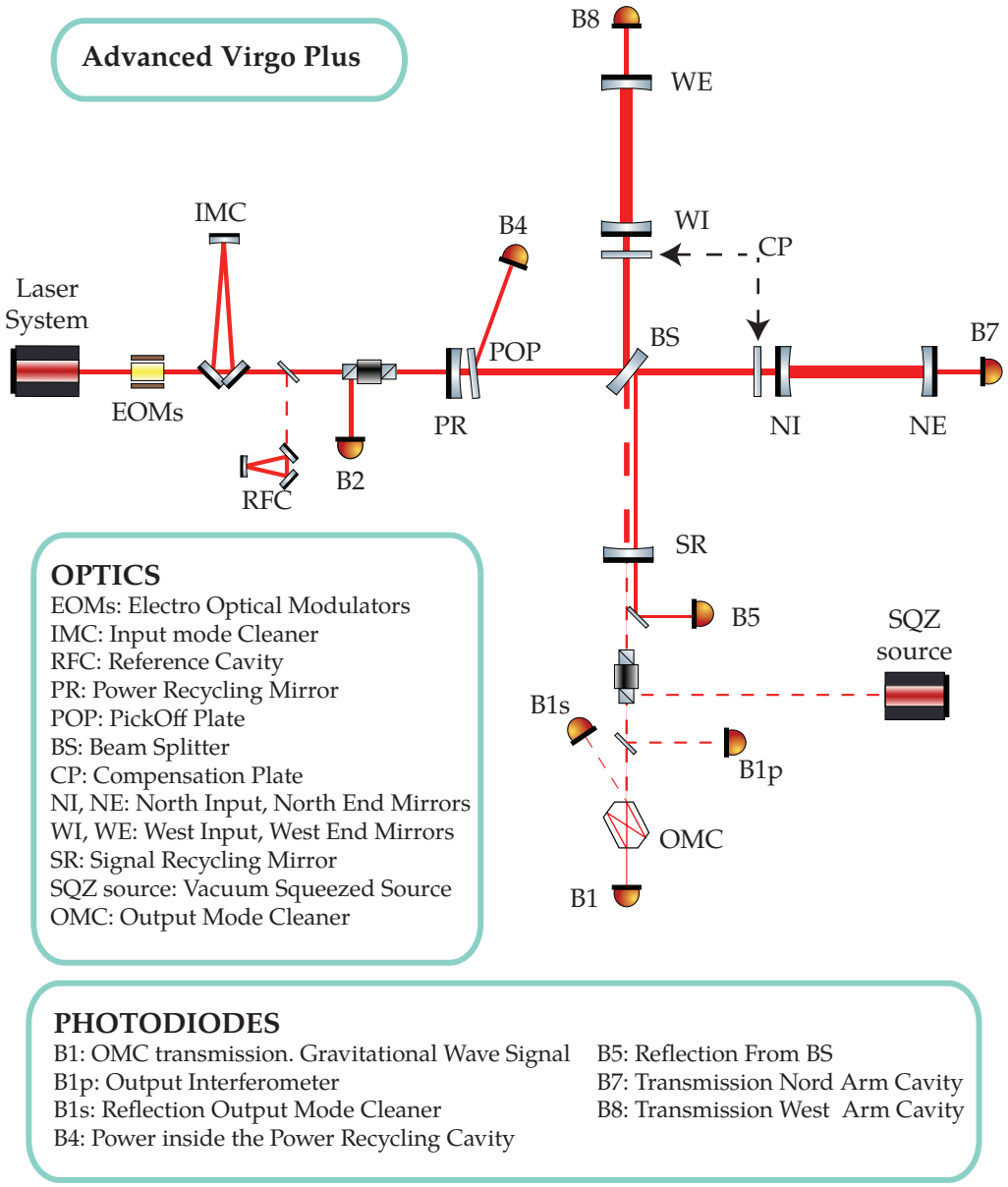

FIGURE I.4: Complete Scheme of Advanced Virgo Plus. From left to right, the beam is generated in the laser source, prepared, and sent to the main interferometer. The first mirror is the Power Recycling, which collects all the optical power reflected by the Michelson interferometer. After that, a beam splitter divides the beam and sends the new field to the two arms, North and West. The Arms are composed of Linear Cavities used to extend the effective length and amplify the gravitational wave signal. At the Asymmetric Port(bottom), there is another mirror called the Signal Recycling Mirror, which is used to modify the frequency response of the interferometer. After that, we can find the Output Mode Cleaner, an optical Cavity used to filter out the spurious component of the beam and improve the ratio between the gravitation wave signal and the background noise.

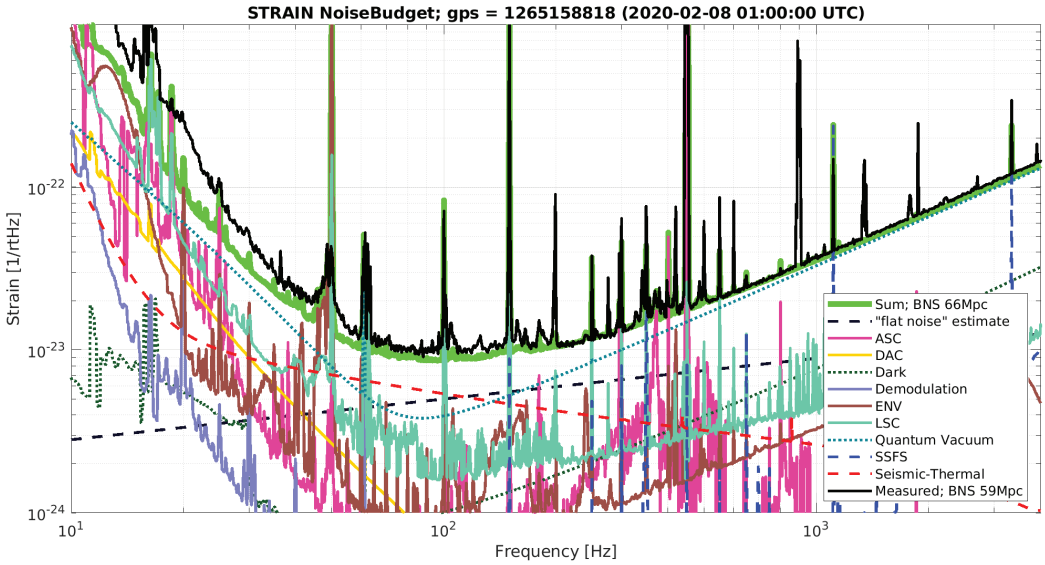

FIGURE I.5: Sensitivity curve of Advance Virgo with noise budget generated at a time of near best sensitivity of the detector (February 8th, 2020)(From [16]). Among the different noise sources, we notice how the Quantum Vacuum(dotted green line) is predominant over the spectrum. This is one of the main results of the Advance Virgo commissioning that improved the detector sensitivity up to the intrinsic limit defined by the quantum nature of the light.

pressure, called radiation pressure, is affected by the temporal inhomogeneity of photon flux and changes over time. For this reason, the mirror is randomly pushed away from its resting position and generates a false gravitational signal. This effect depends on the frequency, f, and generates an equivalent noise of

$$h_{rp}(f) = \frac{1}{\pi M f^2}\frac{1}{L}\sqrt{\frac{\hbar P_{\text{arms}}}{\pi c \lambda}} \tag{I.17}$$

where we assumed that both the end mirrors have the same mass, M, and the other parameters are equivalent to the ones used to estimate the shot noise.

These mechanisms are combined, and they form the quantum noise: the radiation pressure is responsible for the low-frequency component that falls as $1/f^2$, while the shot noise is dominant at high-frequency:

$$h_{QN}(f) = \frac{1}{L}\sqrt{\frac{\hbar c \lambda}{2\pi P} + \left(\frac{1}{\pi M f^2}\right)^2 \frac{\hbar P}{\pi c \lambda}} \tag{I.18}$$

The shot noise and the radiation pressure are a function of the optical power. We can use this parameter to control the coupling of the quantum noise to the interferometer signal. However, the power has a complementary effect on the coupling mechanism, and it is impossible to reduce the quantum noise arbitrarily. If we attenuate one noise source, we will automatically amplify the other. The minimum quantum noise can be obtained by balancing the two contributions as a function of the laser power

$$h_{sn}(P_{SQL}) = h_{rp}(P_{SQL}) \Rightarrow P_{SQL} = f^2 M c \pi \lambda \tag{I.19}$$

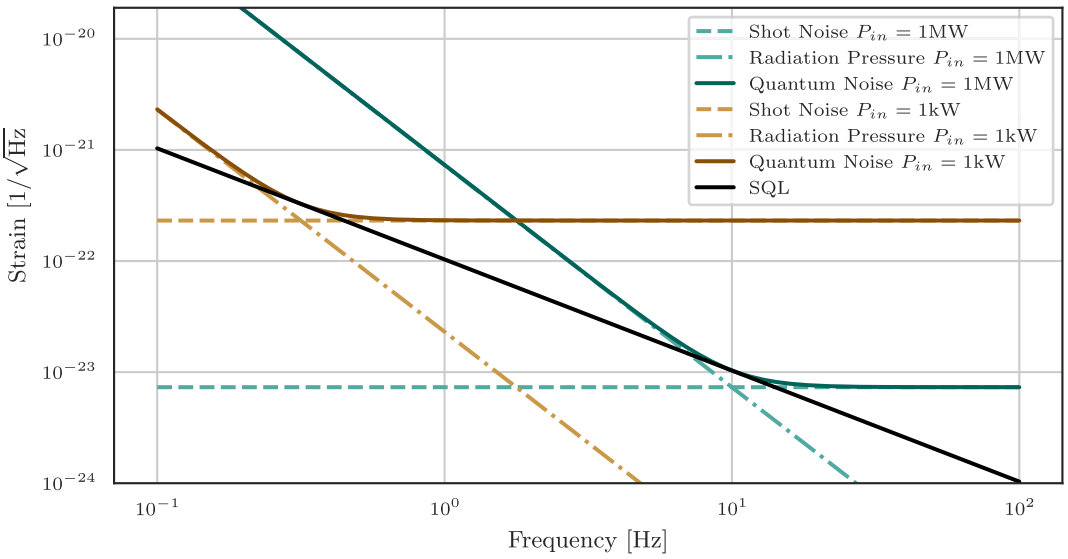

FIGURE I.6: Quantum Noise in a Michelson interferometer. The radiation pressure noise dominates at low frequency, amplified by a factor $1/f^2$. The shot noise dominates at the high frequency, where the radiation pressure noise becomes negligible. The dependency of the quantum noise from the input laser power is highlighted by the colours of the line: brown line low optical power; green high optical power. The black line represents the quantum noise limit which cannot be overcome by changing only the optical power.

but this optimisation is still frequency dependent. We identify the absolute minimum of the quantum noise

$$h_{SQL} = \sqrt{h_{sn}^2(P_{SQL}) + h_{rp}^2(P_{SQL})} = \frac{1}{L f \pi}\sqrt{\frac{\hbar}{M}} \tag{I.20}$$

that is also called Quantum Standard Limit.

I.2.1. *Source of the Quantum Noise: The Quantum Vacuum*

The debate about the origin of the quantum noise fluctuation has kept the scientific community busy for a long time, and it was resolved by Caves in their papers[17], [18]. In particular, they demonstrated that radiation pressure noises are generated by the quantum vacuum, which leaks into the interferometer from the asymmetric port. This field superimposes with the laser beam and generates the amplitude fluctuation responsible for both the radiation pressure noise inside the arms and the shot noise at the output.

The quantitative analysis of this phenomenon requires the introduction of the quantum optics theory. Without going into details, the quantisation of the light describes the optical beam as composed of multiple quanta of light, also called photons. The electric filed can be described as[19, p.16]:

$$\hat{E}(x,y,z,t) = u(x,y,z)\sqrt{\frac{\hbar\omega_0}{c\epsilon_0}}\left(\hat{X}_1(t)\cos(\omega_0 t) + \hat{X}_2(t)\sin(\omega_0 t)\right) \tag{I.21}$$

where $\omega_0 = 2\pi c/\lambda$ is the laser frequency, ϵ_0 is vacuum permittivity and $u(x,y,z)$ is the beam shape, that will be discussed in Chapter II. The operator $\hat{X}_{1,2}(t)$ are called quadrature operator, and they describe the evolution of the electric field around the principal oscillation component with frequency ω_0. In the classic limit, they correspond to the beam amplitude and phase modulation, and their fluctuation can be interpreted as field noise. These operators are bounded by the Heisenberg principle, so their uncertainties respect the following inequality:

$$\Delta X_1 \Delta X_2 > 1 \quad \text{with} \quad (\Delta X_i)^2 = \sqrt{\langle (\hat{X}_i - \langle \hat{X}_i \rangle)^2 \rangle} \tag{I.22}$$

that imposes a natural limit to the estimation of the optical beam amplitude.

In the case of high-intensity fields, it is a common practice to separate the steady state of the quadrature from their time-dependent fluctuation and write:

$$\hat{X}_i(t) = \hat{X}_i + \delta\hat{X}_i(t) \tag{I.23}$$

where the operator $\hat{X}_i$ represent the steady state,

$$\langle \hat{X}_i \rangle = \langle \hat{X}_i(t) \rangle = X_i \tag{I.24}$$

while the time dependent fluctuation are collected in $\delta X(t)$:

$$\langle \delta\hat{X}_i(t) \rangle = 0 \quad \text{and} \quad \Delta X_i = \langle (\hat{X}_i(t) - X_i)^2 \rangle = \langle (\hat{X}_i(t))^2 \rangle \tag{I.25}$$

From the analysis done in [17], the model of the Michelson interferometer should be based on the propagation of two beams, one for each input port of the beam splitter. In particular, we have a laser beam entering from the symmetric port and the quantum vacuum entering from the asymmetric port. These two beams present particular properties, and they are described by the following states of the electric field:

Coherent state The laser light used in the gravitational wave detector is described by the coherent state. In the case of a high-power field, the electric field of a coherent state can be represented by [20, p.28]:

$$\hat{E}_L = u(x,y,z) \left[\left(\sqrt{\frac{2P_{in}}{\hbar\omega_0}} + \delta X_1^L(t) \right) \cos(\omega_0 t) + \delta X_2^L(t) \sin(\omega_0 t) \right] \tag{I.26}$$

the quadrature uncertainty is equally distributed and corresponds to the minimum values defined by the uncertainty principle:

$$\Delta X_1 = \Delta X_2 = \frac{1}{2} \tag{I.27}$$

Quantum Vacuum The vacuum state is a special electric field state representing the complete absence of photons. This is the ground state and it carries an expected energy $\langle \hat{H} \rangle_0 = 1/2\hbar\omega$, called zero-point energy. In the case of vacuum, the electric field is represented only by the quadrature fluctuations:

$$\hat{E}_V = u(x,y,z) \left[\delta X_1^V \cos(\omega_0 t) + \delta X_2^V \sin(\omega_0 t) \right] \tag{I.28}$$

that are still bounded by the uncertainty principle. The zero-point energy manifest itself as fluctuation of the quadrature:

$$\Delta X_1 = \Delta X_2 = \frac{1}{2} \tag{I.29}$$

even in the absence of an average field $\langle \hat{E}_V \rangle = 0$.

We can use this formulation of the optical fields to translate the calculation presented in the previous section into the framework of quantum optics. We can follow the same steps presented in [21] and rewrite the optical power at the asymmetric port as:

$$\hat{P}_{asy}(\Omega) = 4P_{in}\left(\frac{\omega_0 \delta L}{c}\right)\left[x_s(\Omega)e^{i\Omega\tau} - e^{i\Omega 2\tau}\sqrt{\frac{\hbar}{2M\Omega^2}}\left[\sqrt{K_{Mi}}\hat{X}_1^V(\Omega) + \frac{\hat{X}_2^V(\Omega)}{\sqrt{K_{Mi}}}\right]\right] \tag{I.30}$$

where $x_s = Lh(\Omega)/2$ is the differential movement of the mirror induced by a gravitational wave, Ω is the fluctuation frequency, $2\tau = L/c$ is the travel time of a photon across the interferometer arms, δL is the difference between the two arm lengths required by the DC-offset, P_{in} is the input power, and

$$K_{Mi} = \frac{4\omega_0 P_{in}}{c^2 M\Omega^2} \tag{I.31}$$

represent the response of a simple Michelson to the quantum noise. It is important to notice that the fluctuation of the output power depends only on the vacuum quadrature to demonstrate that the quantum noise is generated only by the fluctuation of the vacuum field.

This formulation of the output power leads to the following power spectral density of the quantum noise:

$$\begin{aligned} S_{h_n h_n} &= \frac{2\hbar}{ML^2\Omega^2}\left(\overbrace{K_{Mi}}^{\text{Radiation Pressure}} + \overbrace{K_{Mi}^{-1}}^{\text{Shot Noise}}\right) \\ &= \frac{1}{L^2}\left(\frac{1}{\pi M f^2}\right)\left(\frac{\hbar P}{\pi c\lambda}\right) + \frac{1}{L^2}\left(\frac{\hbar c\lambda}{2\pi P}\right) \end{aligned} \tag{I.32}$$

where we substituted $\Omega = 2\pi f$.

I.3. Quantum Noise Reduction

In the previous section, we show that the quantum noise is intrinsically coupled with the gravitational way signal generated by a Michelson interferometer. This fundamental connection is based on two mechanisms that limit the detection sensitivity, and their effect is unavoidable due to the Heisenberg principle. In the last decades, different efforts have been made to circumvent these limitations and push the gravitational wave detectors behind the limit imposed by the quantum noise.

Among the different approaches for reducing the quantum noise, Advance Virgo and Advance LIGO have implemented the squeezing injection technique[22][23]. This approach was proposed by Caves[18] and is based on manipulating the quantum vacuum before entering the interferometer. Instead of changing the laser power to control the coupling of the vacuum field to the gravitational wave signal, the squeezing technique directly acts on the two quadrature fluctuations, $\delta\hat{X}_1$ and $\delta\hat{X}_2$. The uncertainty principle still limits this approach, and a reduction of one coupling mechanism (e.g. shoot-noise) will again correspond to the enhancement of the other (e.g. radiation pressure); it is also way more flexible in manipulating the vacuum fluctuation as a function of the frequency. This property allows the reduction of the shot noise in the high-frequency bandwidth of the spectrum and the radiation pressure noise in the low one.

I.3.1. *Squeezing Technique*

The basic principle of the squeezing technique is the manipulation of the vacuum fluctuation before entering the interferometer. This principle can be described by representing the amplitude of the electric field with the two quadrature operators, $\hat{X}_1$ and $\hat{X}_2$. Their expected values are presented by a probability distribution in the space $X_1 \times X_2$. In Figure I.7, we can find two examples: on the left, a coherent state is represented by a circular distribution with 1σ diameter of $\Delta X_1 = \Delta X_2 = 1/2$ and centred in $(\langle \hat{X}_1 \rangle, \langle \hat{X}_2 \rangle)$. In particular, the position can be defined using the polar coordinates:

$$\begin{aligned} |\alpha| &= \sqrt{\langle \hat{X}_1 \rangle^2 + \langle \hat{X}_2 \rangle^2} = \sqrt{\frac{2P}{\hbar\omega}} \\ \phi &= \mathrm{Arg}\left[\langle \hat{X}_1 \rangle + i \langle \hat{X}_2 \rangle\right] \end{aligned} \tag{I.33}$$

where $|\alpha|$ is the amplitude module and ϕ is the phase. On the right, the quantum vacuum state is represented again by a circular distribution with 1σ diameter of $\Delta X_1 = \Delta X_2 = 1/2$, but in this case, the distribution is centred at $\langle \hat{X}_1 \rangle = \langle \hat{X}_2 \rangle = 0$.

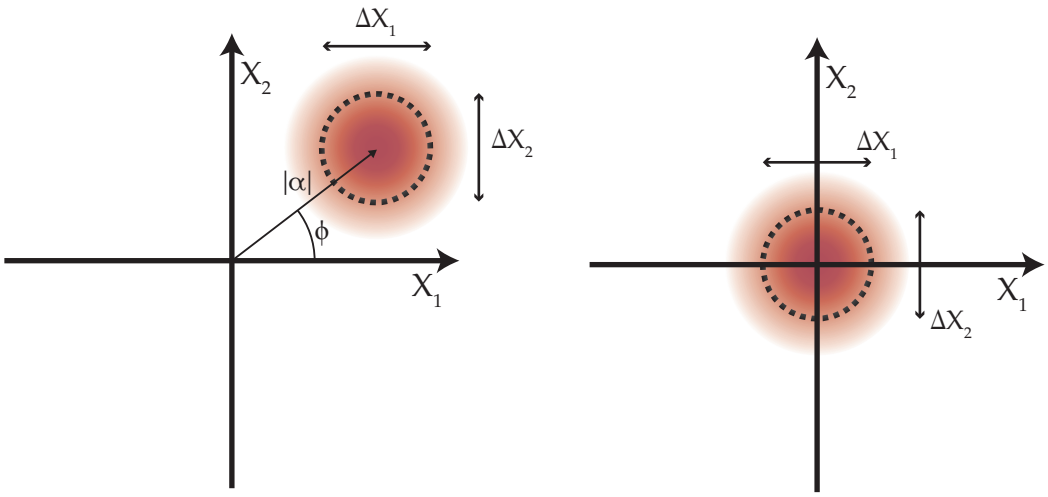

FIGURE I.7: Ball on a Stick representation of the Electric field. The multiple measurements of the Electric field can be represented as points in the phase-space defined by the two quadratures $\hat{X}_1$ and $\hat{X}_2$. On the left, it is represented as a coherent state with amplitude $|\alpha|$ and phase $|\phi|$. On the right, it represents the vacuum state.

The same circular cloud represents the fundamental uncertainty on the amplitude of the two states. The uncertainty principle limits the dimension of this ball, and it cannot be reduced at will. On the other hand, the shape is defined by the uncorrelation between the photons, and it can be changed by coupling their evolution. The most efficient way to obtain this electric field manipulation is based on Optical Parametric Amplification[24].

This method can induce a phase-sensitive amplification: the quantum vacuum is de-amplified and amplified as a function of its phase, which results in a reduction of

the fluctuation on one quadrature and the expansion of the other. In this case, the uncertainty ball becomes similar to an ellipse, with one axis stretched and the other compressed.

The result of this process is a new quantum state of the electric field called squeezed vacuum. In this case, the quadrature fluctuations are described by [21]

$$\left(\Delta X_1^{sqz}\right)^2 = \left[e^{2\xi}\sin^2(\theta) + e^{-2\xi}\cos^2(\theta)\right] \tag{I.34}$$

$$\left(\Delta X_2^{sqz}\right)^2 = \left[e^{-2\xi}\sin^2(\theta) + e^{2\xi}\cos^2(\theta)\right] \tag{I.35}$$

where, ξ represents the magnitude of the fluctuation reduction and θ the phase angle of this state. It is common practice to call squeezing the reduction of a fluctuation and anti-squeezing the amplification. The representation of this state is reported in Figure I.8(left) and it corresponds to an ellipse rotated by an angle θ and with the two axis ΔY_1 and ΔY_2:

$$\Delta Y_1 = e^{-\xi} \quad \text{and} \quad \Delta Y_2 = e^{\xi} \tag{I.36}$$

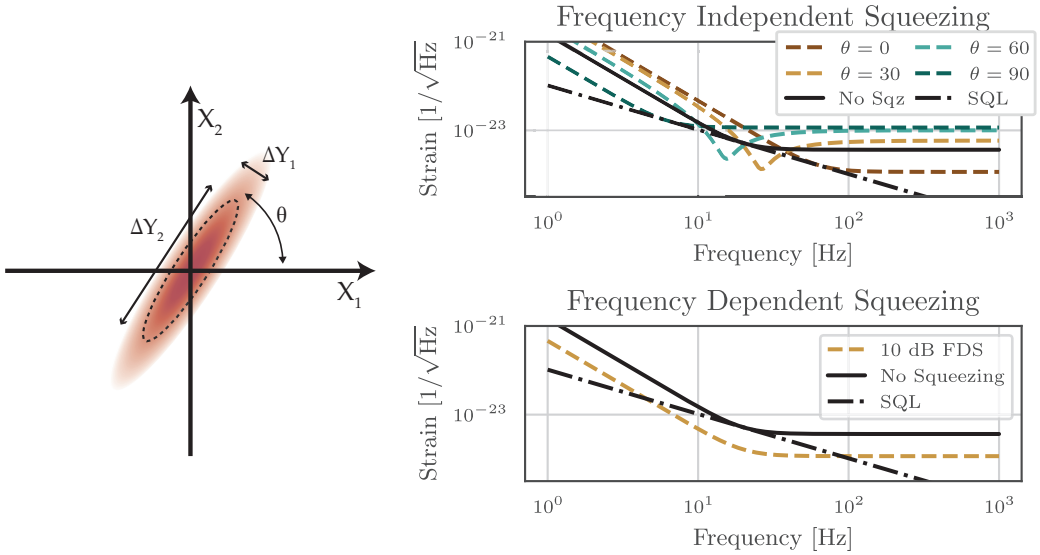

FIGURE I.8: Squeezed Vacuum. On the left, a representation of the squeezing ellipse in the $X_1 \times X_2$ space is shown. The uncertainty ball becomes an ellipse with two axes defined by the parameter ξ, and the orientation is defined by the phase θ. On the right, the effect of squeezing injection in a Michelson Interferometer is shown. Top right Frequency Independent Squeezing, Bottom Right Frequency Dependent Squeezing.

The generation of the squeezed vacuum state is the first step towards the quantum noise reduction in a gravitational wave detector. Once we prepare the vacuum field in this new state, we need to inject it into the asymmetric port of the interferometer in order to replace the quantum vacuum. The quantum noise is not randomly generated but is defined by the properties of the squeezing state, which can be controlled in order to reduce the effects on the gravitational wave detector. We can estimate the quantum noise by combining the squeezing quadrature reported in Eq. I.34 in the output power

of Eq. I.30. The power spectral density of the quantum noise becomes[21]:

$$S_{h_n h_n} = \frac{2\hbar}{ML^2\Omega^2}\left(K_{Mi} + \frac{1}{K_{Mi}}\right)\left(\cosh(2\xi) - \cos[2(\theta + \Theta(\Omega))]\sinh(2\xi)\right) \tag{I.37}$$

where

$$\Theta(\Omega) = \operatorname{arccot}(K_{Mi}) \tag{I.38}$$

In particular, the squeezing technique is divided into two different versions. The first approach, Frequency Independent Squeezing(FIS), consists of the injection of the vacuum-squeezed beam with a constant squeezing phase, $\theta = 0$, over the whole spectrum. In this case, the quantum noise of the interferometer can be written as:

$$S_{h_n h_n} = \frac{2\hbar}{ML^2\Omega^2}\left(K_{Mi}e^{-2\xi} + \frac{e^{+2\xi}}{K_{Mi}}\right) \tag{I.39}$$

where we can see that the squeezing injection acts on the radiation pressure and the shot noise in two opposite ways. The anti-squeezing will amplify the first one, and the squeezing will reduce the second one.

The second approach, called Frequency Dependent Squeezing(FDS), is based on the manipulation of the squeezing phase as a function of the frequency based on the dispersion law:

$$\theta(\Omega) = -\Theta(\Omega) \tag{I.40}$$

In this way, the squeezed vacuum adapts its phase to the requirement of the interferometer, and we can reduce the quantum noise over the whole spectrum. If we substitute Eq. I.40 in Eq. I.37, we obtain:

$$S_{h_n h_n} = \frac{2\hbar}{ML^2\Omega^2}\left(K_{Mi} + \frac{1}{K_{Mi}}\right)e^{-2\xi} \tag{I.41}$$

that indicates a reduction of the quantum noise over the whole spectrum. The effect is reported in Figure I.8, bottom right.

I.3.2. *Limitation of the Vacuum Squeezing technique*

The Squeezing techniques are strongly limited by different classical phenomena, and their effects can be separated into two main categories: the Optical Losses collected along the path of the vacuum squeezed and the Phase noise between the vacuum squeezed and the laser field of the interferometer.

Optical Losses

In the quantum optics theory, the optical losses are directly connected to an uncorrelated injection of vacuum in the optical beam. Each time a portion of the amplitude leaves the beam, a corresponding amount of quantum vacuum enters. This phenomenon can be modelled using a beam splitter, with a reflectance of $\sqrt{1-\eta}$ and a transmittance of $\sqrt{\eta}$. Following the scheme in Figure I.9, part of the beam amplitude is removed by the reflection, and the same amount of quantum vacuum is injected into the path and superimposed with the remaining beam. In the case of a squeezed beam, we can focus only on the quadrature fluctuation and estimate the output as follows:

$$\delta X_{1,2}^{out} = \sqrt{\eta}\,\delta X_{1,2}^{sqz} + \sqrt{1-\eta}\,X_{1,2}^{vac} \tag{I.42}$$

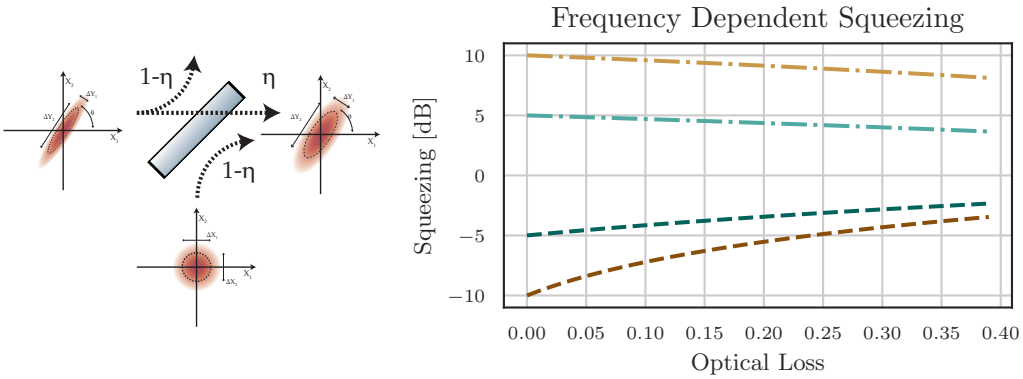

FIGURE I.9: Optical Losses. The effects of an optical loss can be modelled with a beam splitter that removes a portion $1-\eta$ of the beam amplitude and replaces it with the equivalent amount of quantum vacuum. The effect of an optical loss on the vacuum-squeezed path is represented on the left plot. We assumed a generation of 10 dB of squeezing($20\log(\xi) = 10$) for the brown lines and 5 dB for the green ones. Simple dashed lines represent the squeezing, while dashed-dotted lines represent the anti-squeezing.

This mixture between the squeezed vacuum and the uncorrelated one leads to a reduction of the effective manipulation of the Vacuum fluctuation[21]:

$$\left(\Delta X_1^{out}\right)^2 = 1 + \eta\left(e^{-2\xi} - 1\right) \tag{I.43}$$

$$\left(\Delta X_2^{out}\right)^2 = 1 + \eta\left(e^{+2\xi} - 1\right) \tag{I.44}$$

where we assumed the squeezing phase $\theta = 0$. The effective noise reduction is generally defined as the ratio between the quadrature fluctuation under measurement, ΔX_i^{out}, and the one of uncorrelated vacuum, $\Delta X_i^V = 1$:

$$r_{sqz} = 20\log\left(\frac{\Delta X_1^{out}}{\Delta X_1^V}\right) \tag{I.45}$$

$$r_{asqz} = 20\log\left(\frac{\Delta X_2^{out}}{\Delta X_2^V}\right) \tag{I.46}$$

where we can distinguish the effect of noise reduction, $r_{sqz} < 0$, represented by the squeezing and of noise amplification, $r_{asqz} > 0$, represented by the anti-squeezing. From the plots in Figure I.9, we can see how the squeezing is more affected that the anti-squeezing.

Phase Noise

The noise reduction obtained by the squeezing injection depends on the phase between the squeezed vacuum and the laser field. If this phase is not stable in time, its fluctuation will mix the effect of squeezing and anti-squeezing. In order to quantify the effect, we can write $\theta(t) = \theta_0 + \delta\theta(t)$, where we extract the phase noise fluctuation $\delta\theta(t) \ll 1$

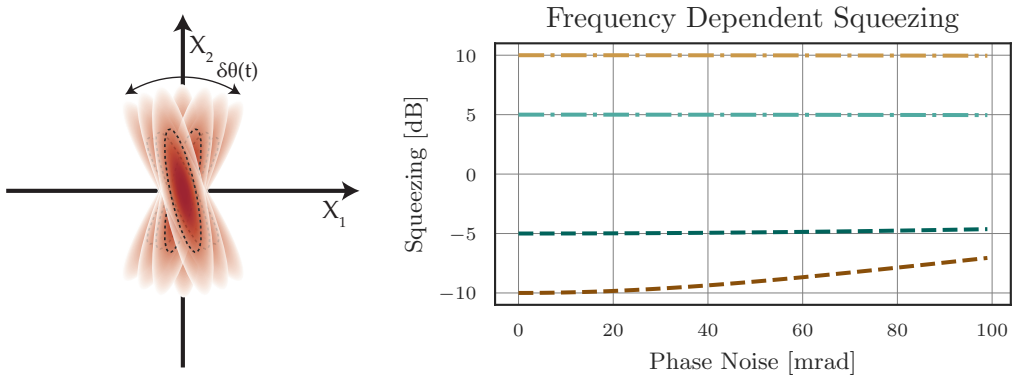

FIGURE I.10: Phase Noise. The random fluctuation of the phase of the squeezed vacuum will average the effect of squeezing and anti-squeezing, with a corresponding degradation of the effective noise reduction. The effect of phase noise on the vacuum-squeezed path is represented on the left plot. We assumed an generation of 10 dB of squeezing($20\log(\xi) = 10$) for the brown lines and 5 dB for the green ones. Simple dashed lines represent the squeezing, while dashed-dotted lines represent the anti-squeezing.

from the average value of the phase $\langle\theta\rangle = \theta_0$. In this way, we can average Eq. I.34 around $\theta_0 = 0$ and obtain:

$$\left(\Delta X_1^{out}\right)^2 = \left[e^{2\xi}\delta\theta^2(t) + e^{-2\xi}\left(1 - \delta\theta^2(t)\right)\right] \tag{I.47}$$

$$\left(\Delta X_2^{out}\right)^2 = \left[e^{-2\xi}\delta\theta^2(t) + e^{2\xi}\left(1 - \delta\theta^2(t)\right)\right] \tag{I.48}$$

$$\tag{I.49}$$

We reported the effect of the phase noise in Figure I.10, where we can see how the phase noise effect is stronger on the squeezing than on the anti-squeezing.

Mismatch and squeezing technique

Among the different sources of optical losses, the work presented in this thesis is focused on the Mismatch. This choice was based on the information collected during the last observing run in which the Virgo collaboration implemented the Frequency Independent Technique. That experience allowed us to characterise the different issues that limited the noise reduction efficiency and identified the main source of optical losses right in the Mismatch between the squeezed vacuum and the detector[22]. A precise description of the Mismatch will be introduced in Chapter II, but here we can give a general idea of the problem.

The definition of the electric field given in Eq. I.21 contains a spacial distribution factor, $u(x, y, z)$. This coefficient represents how the amplitude is distributed over space. It defines the shape of the beam, and it can be used to describe its location. Moreover, it is directly connected to the interaction between two different beams, inasmuch as only two fields that overlap can couple together, and the difference in the factors reflect this, $u(x, y, z)$. If two beams are in two different places, they will interact less than when they share the same space.

The difference in the spatial distribution of two beams is generally described as Mode Matching, and it could also affect the efficiency of the squeezing injection. If the squeezed vacuum beam does not overlap with the interferometer beam, the two fields will not be perfectly coupled. Part of the laser will interact with the quantum vacuum, and the efficiency of the quantum noise reduction will be spoiled. This effect is equivalent to an optical loss, estimated as:

$$\eta_{mm} = 1 - \frac{\left|\iint u_{las}(x,y,z)u_{sqz}(x,y,z)dxdy\right|^2}{\iint dxdy\,|u_{las}(x,y,z)|^2 \iint |u_{las}(x,y,z)|^2} \tag{I.50}$$

where $u_{las}(x,y,z)$ is the profile of the laser beam and $u_{sqz}(x,y,z)$ of the squeezed vacuum. As we will see in Chapter II, a similar phenomenon happens when a beam interacts with an optical cavity. In order to circulate inside the cavity, the beam shape has to match the geometry of the cavity. If the incoming beam does not meet this requirement, part of the amplitude *does not enter*, leading to particular optical loss.

One of the main problems in dealing with Mode Mismatch is its characterisation. For example, the analysis reported in [22] indicates that the Mismatch is not only the principal source of losses but also the one with the main uncertainty. This lack of information about mode matching is connected to different practical issues, which require the implementation of dedicated sensors that allow the characterisation of the Mismatch in real-time.

Moreover, the implementation of the Frequency Dependent Squeezing requires a specific characterisation of the mode matching. As we will see in Chapter VI, the control over the squeezing angle is obtained with a detuning cavity. If there is a mismatch between the squeezed vacuum beam and this cavity, only part of the amplitude will obtain the dispersion rule, $\theta(f) = \Theta(f)$. This incomplete manipulation will generate a degradation of the squeezed beam that is in between the phase noise and the optical loss, and it requires a full characterisation of the mismatch.

In the following chapter, we will introduce the theory required for the formalisation of the Mismatch and for the development of the sensing technique.

II OPTICAL RESONATORS AND MODE MATCHING

II.1 Optical Resonator 20
II.1.1 Longitudinal and Transversal modes 20
II.1.2 Transversal Mode of a Resonance Cavity 24
II.1.3 Resonant cavities in Ray Optics 25
II.2 Mismatch of a Simple Astigmatic Gaussian Beam 34
II.2.1 Waist Radius Perturbation 37
II.2.2 Waist Position Perturbation 38
II.2.3 Astigmatic Mismatch in the three dimensional space 40
II.2.4 Astigmatic Axis Angle 40

The main contributions presented in this thesis are the characterisation of a Mode Matching sensing technique and its upgrade for Astigmatic Aberrations. In order to discuss these results, it is mandatory to introduce beam optic theory, among which the more important is the Mode Matching itself. The first example of what we mean by Mode Matching was given in the introduction, where we described the effect of the mismatch between the squeezed vacuum beam and the interferometer beam. In that case, we focused the analysis only on the optical loss generated by the beam shape difference. As we will see later, that effect is only a part of the phenomenology of Mode Matching, and its full study requires different theoretical instruments.

In this Chapter, we will introduce the mismatch in the context of resonant cavities. This choice is based on two reasons: first, the theoretical framework of resonant cavities covers most of the topics required for the characterisation of the beam amplitude and to study its evolution; second, the techniques used for the characterisation of the mismatch are based on the interaction between a cavity and an optical beam.

In the first part, we will briefly describe what is a resonant cavity and its main properties, with a specific focus on the Transverse Resonance Mode. In the second part, we will present the Mode Mismatch between an Astigmatic beam and a cavity. In the third one, we will use this theoretical framework to present the Wavefront Sensing technique used to characterise the mismatch.

II.1. Optical Resonator

The simplest optical resonator is composed of two mirrors, with reflectance r_1 and r_2, facing each other and separated by a distance of L. When we inject laser light from the backside of a mirror, namely the input mirror, part of it is promptly reflected, and part of the light enters the cavity. The inner cavity light bounces between the two reflective surfaces until it reaches a steady state regime. If some conditions are met, the optical field interferes constructively with itself, resonating inside the cavity. This will amplify the optical power between the two mirrors. The strong field is partially leaked out in transmission, through the end mirror, and in reflection, through the input mirror. This phenomenon, called resonance, is the core of the properties of an optical cavity, and it is ruled by the mirror characteristics, the cavity geometry, and the properties of the optical beam.

We can distinguish between two distinct modes in a cavity, Longitudinal and Transversal, that describe the resonance conditions. The first modes are strictly connected to the phase accumulated along with the longitudinal propagation, and they fix the relationship between the light wavelength and the cavity length. The second kind is connected to the diffraction phenomenon that happens along the transverse plane, defining the shape of the resonant beams.

II.1.1. *Longitudinal and Transversal modes*

The Longitudinal Modes of a cavity are naturally described in the plane-wave approximation. In this approach, we can describe the optical field by the complex amplitude and ignore the transverse plane XY evolution. The amplitude evolves only along the z direction, and it is described by:

$$E(z) = a_0 e^{i\,kz}$$

where $k = 2\pi/\lambda$ is the spatial angular frequency representing the spatial periodicity, we highlight the complex amplitude in the plane-wave approximation with the small letter a_0.

The interaction between a plane wave and a resonant cavity is described by Figure II.1. In this case, we consider an incoming beam with amplitude $E(0) = a_0$ that enters an optical cavity (left) composed of two mirrors with reflectance r_i and transmittance t_i, separated by a distance, L. When this beam interacts with the input mirror, it is reflected ($a_0^r = r_1\, a_0$) and transmitted ($a_0^a = it_1\, a_0$). The transmitted component travels along the distance L between the two mirrors ($a_0^b = a_0^a e^{ikL}$) and is reflected back ($a_0^c = a_0^b\, r_2$). After travelling through the cavity again ($a_0^d = a_0^c\, e^{ikL}$), it is reflected from the first mirror ($a_1^a = r_1 a_0^d$), interacts with the original light transmitted by the input mirror, and restarts another round trip.

This process will repeat over and over, so we could describe the light after the n-th round as:

$$a_n^a = a_0^a \left(e^{i\,k2L} r_1 r_2\right)^n \tag{II.1}$$

Each time the light is reflected from the input mirror, it will superimpose with the field of the other round trip. This interference will generate a new field, called *intracavity field*:

$$a_{cav} = \sum_{n=0}^{+\infty} a_n^a = a_0^a \sum_{n=0}^{+\infty} \left(r_1 r_2\, e^{i\,k2L}\right)^n = \frac{it_1 a_0}{1 - r_1 r_2\, e^{i\,k2L}} \tag{II.2}$$

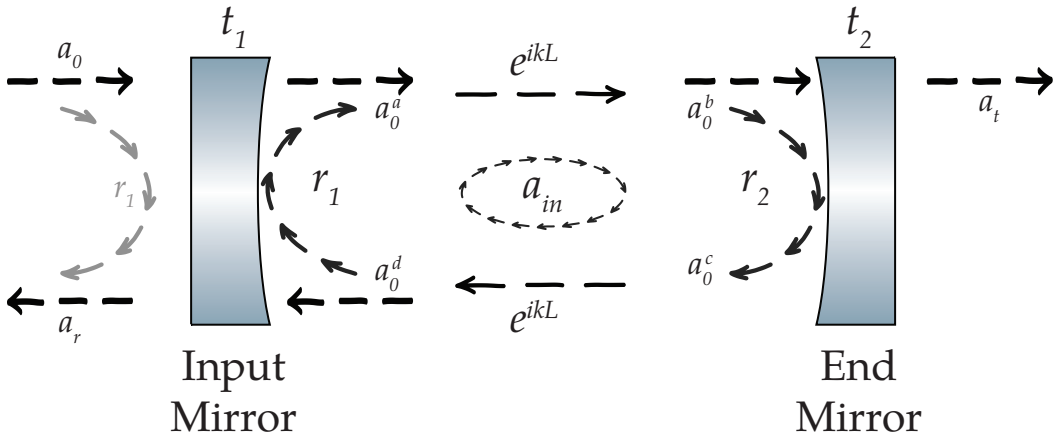

FIGURE II.1: Conceptual scheme of an optical cavity. Two mirrors, called respectively Input and End Mirrors, are separated by a distance L. The optical beam that enters the cavity circulates in a steady state round trip. The light transmitted throughout the End Mirror generates the Transmitted beam a_t, while the light transmitted throughout the Input Mirror is combined with the promptly reflected component and generates the Reflected beam a_r.

where we replaced $a_0^a = it_1\, a_0$. The a_{cav} obtained here loses the dependency from the round trip number, and it describes the steady state of the light inside the optical cavity. This field will leak throughout the mirrors, and it will produce two beams: the Transmitted beam, a_t, generated by the beam leaked by the End Mirror, and the Reflected Beam, a_r, generated by the superposition of the light transmitted by the Input Mirror and the promptly reflected component, $r_1 a_0$. Their amplitudes are given by:

$$a_t = a_0 \frac{-t_2 t_1\, e^{i\,kL}}{1 - r_1 r_2\, e^{i\,k2L}} \tag{II.3}$$

$$a_r = \frac{r_1 - (r_1^2 + t_1^2) r_2\, e^{i\,k2L}}{1 - r_1 r_2\, e^{i\,k2L}} \tag{II.4}$$

where we assume the input mirror with a loss mirrors $\rho_i = 1 - (r_1^2 + t_1^2)$. We can use Eq. II.2, Eq. II.3, and Eq. II.4 to investigate the spectral properties of the resonance cavity.

Resonance condition

We can define resonance as the condition that maximises the power inside the cavity

$$P_{cav} = |a_{cav}|^2 = \frac{T_1}{(1 - r_1 r_2)^2 + 4 r_1 r_2 \sin^2(kL)} P_0 \tag{II.5}$$

where $T_1 = t_1^2$ is the transmissitvity of the cavity and $P_0 = |a_0|^2$ is the optical power of the incoming beam. This maximum is met for $\sin^2(kL) = 0$, and it defines a specific relation between the wavelength and the cavity length:

$$kL = \arcsin(0) \Rightarrow L = l\frac{\lambda}{2} \tag{II.6}$$

where $l \in \mathbb{N}$. This relationship is generally expressed as a function of the wave frequency $f = c/\lambda$:

$$f_{\text{res}} = l\frac{c}{2L} \tag{II.7}$$

where we can identify the fundamental resonance frequency, called Free Spectral Range

$$\Delta f_{\text{fsr}} = \frac{c}{2L} \tag{II.8}$$

In general, we can identify a family of plane waves called Longitudinal Mode with a frequency multiple of Δf_{fsr}:

$$E_l = E_0 \exp[(il\,\Delta f_{\text{fsr}})t] \tag{II.9}$$

Linewidth

The resonance linewidth gives important information about the frequency response as much as it defines the "near" resonance conditions. This parameter is defined as the Full-Width Half Maximum, Δf_{FWHM}, of the internal cavity power and it indicates the boundaries of the resonance peak, $f_{1/2}^{\pm}$ as

$$f_{1/2}^{-} = f_l - \frac{1}{2}\Delta f_{\text{FWHM}} \leq f \leq f_l + \frac{1}{2}\Delta f_{\text{FWHM}} = f_{1/2}^{+} \tag{II.10}$$

where f_l is the closer Longitudinal mode to the incoming beam frequency f:

$$f_l = l\Delta f_{\text{fsr}} \quad \text{where} \quad l = \min_{l\in\mathbb{N}}(|f - l\Delta f_{\text{fsr}}|) \tag{II.11}$$

The Full-Width Half Maximum can be estimated using the intracavity power defined in Eq. II.5:

$$P_{cav} = |a_{cav}|^2 = \frac{T_1}{(1-r_1r_2)^2 + 4r_1r_2\sin^2\left(\pi\frac{f}{\Delta f_{\text{fsr}}}\right)}P_0 \tag{II.12}$$

where we highlight the frequency response $kL = \pi f/\Delta f_{\text{fsr}}$. The maximum is given for $f = n\Delta f_{\text{fsr}}$ and it is equal to

$$P_{cav}^{max} = \frac{T_1}{(1-r_1r_2)^2}P_0 \tag{II.13}$$

Using these results we can impose the Half Maximum condition as

$$\frac{T_1}{(1-r_1r_2)^2 + 4r_1r_2\sin^2\left(\pi\frac{f_{1/2}^{\pm}}{\Delta f_{\text{fsr}}}\right)}P_0 = \frac{1}{2}\frac{T_1}{(1-r_1r_2)^2}P_0 \tag{II.14}$$

and estimate the boundaries of the resonance peak:

$$f_{1/2}^{\pm} = l\Delta f_{\text{fsr}} \pm \Delta f_{\text{fsr}}\frac{1}{\pi}\arcsin\left(\sqrt{\frac{(1-r_1r_2)^2}{4r_1r_2}}\right) \tag{II.15}$$

By combining Eq. II.10 with Eq. II.15, we obtain the Full-Width Half Maximum of the resonance peak:

$$\Delta f_{FWHM} = f_{1/2}^{+} - f_{1/2}^{-} = \Delta f_{\text{fsr}}\left(\frac{1}{\pi}\arcsin\left(\frac{1-r_1r_2}{2\sqrt{r_1r_2}}\right)\right) \tag{II.16}$$

which is proportional to the Free Spectral Range. The importance of this relationship is highlighted by the definition of another parameter, the cavity Finesse:

$$\mathcal{F} = \frac{\Delta f_{\text{fsr}}}{\Delta f_{FWHM}} = \left(\arcsin\left(\frac{1 - r_1 r_2}{2\sqrt{r_1 r_2}}\right)\frac{1}{\pi}\right)^{-1} \tag{II.17}$$

which is in a one-to-one relation with the product of the reflectance of the mirrors $(r_1 r_2)$. In the case of high reflectivity mirrors, where we have that $|r_i|^2 \simeq 1$, the Finesse can be approximated as

$$\mathcal{F} \simeq \frac{\pi\sqrt{r_1 r_2}}{1 - r_1 r_2} \tag{II.18}$$

Reflectance, transmittance, and gain

The optical response of the cavity can be described by three different fields: the reflected, the transmitted, and the internal fields. From this point of view, we can reduce the cavity to a special mirror that is fully described by the reflectance, transmittance, and internal gain:

$$r_{\text{cav}} = \frac{a_r}{a_0} = \frac{r_1 - (r_1^2 + t_1^2) r_2\, e^{i\,2\pi f/f_{\text{fsr}}}}{1 - r_1 r_2\, e^{i\,2\pi f/f_{\text{fsr}}}} \tag{II.19}$$

$$t_{\text{cav}} = \frac{a_t}{a_0} = \frac{t_2 t_1\, e^{i\,2\pi f/f_{\text{fsr}}}}{1 - r_1 r_2\, e^{i\,2\pi f/f_{\text{fsr}}}} \tag{II.20}$$

$$\text{G}_{\text{cav}} = \frac{|a_{cav}|^2}{|a_0|^2} = \frac{|t_1|^2}{(1 - r_1 r_2)^2 + 4 r_1 r_2 \sin^2\left(\pi\frac{f}{f_{\text{fsr}}}\right)} \tag{II.21}$$

These parameters of the *equivalent mirror* strongly depend on the frequency of the incoming beam and we can distinguish two different regimes:

Anti-Resonance When the cavity is in anti-resonance, $f = \Delta f_{\text{fsr}}(n + 1/2)$, the power inside the cavity is at the minimum and the cavity act as a simple mirror, with

$$r_{\text{cav}} = r_1 + r_2\frac{t_1^2}{1 + r_1 r_2} \quad \text{and} \quad t_{\text{cav}} = i\frac{t_2 t_1}{1 + r_1 r_2} \tag{II.22}$$

The reflectance is given by the input mirror ones plus a small contribution of the second mirror. The transmittance is lower than the single mirrors, and there is a 90 deg phase shift.

Resonance When the cavity is in resonance, $f = \Delta f_{\text{fsr}} n$, we have the opposite situation. The external parameters are given by

$$\text{G}_{\text{cav}} = \frac{|t_1|^2}{(1 - r_1 r_2)^2} \tag{II.23}$$

$$t_{\text{cav}} = \frac{t_2 t_1}{1 - r_1 r_2} = \sqrt{\text{G}_{\text{cav}}}\, t_2 \tag{II.24}$$

$$r_{\text{cav}} = \frac{r_1 - (r_1^2 + t_1^2) r_2}{1 - r_1 r_2} \tag{II.25}$$

The cavity amplification increases the transmittance, and the phase shift disappears. On the other hand, the reflectance has a complicated behaviour: its sign change continuously as a function of $[r_1 - (r_1^2 + t_1^2)r_2]$:

$$\begin{cases} r_{\text{cav}} > 0 & \text{if} \quad r_1 > (1-\rho_1)r_2 \\ r_{\text{cav}} = 0 & \text{if} \quad r_1 = (1-\rho_1)r_2 \\ r_{\text{cav}} < 0 & \text{if} \quad r_1 < (1-\rho_1)r_2 \end{cases} \tag{II.26}$$

where $\rho_1 = 1 - (r_1^2 + t_1^2)$ is the input mirror optical loss.

II.1.2. *Transversal Mode of a Resonance Cavity*

The study of Transversal Modes requires a different approach. In this case, we need to consider the diffraction phenomenon on the transverse plane and represent the amplitude of an optical beam as

$$E(x,y,z) = U(x,y,z)e^{-ikz} \tag{II.27}$$

where we separated the beam shape $U(x,y,z)$ from the plane wave contribution. The first approach to the study of the beam amplitude across the transverse plane XY can be based on the ray optics theory. In this framework, the beam amplitude $U(x,y,z)$ is represented as a superposition of plane waves with different directions:

$$E(x,y,z) = U(x,y,z)e^{-ikz} = \sum_i E_i e^{-i\vec{k}\cdot\vec{r}} \tag{II.28}$$

where $\vec{k}$ represent the direction of component, E_i, and $\vec{r} = (x,y,z)^T$ the position where the field is evaluated. This model allows us to decompose the profile into single plane waves and focus the study on the evolution of their direction. Each sub-wave is reduced to a single ray which is defined by its origin (x,y,z) and direction (θ_x, θ_y). The evolution of this ray is defined by the interaction with diffracting objects (lens, curved mirror, ...) and it is formalised using the $\mathbb{ABCD}$ matrix formalism:

$$\begin{pmatrix} x_2 \\ y_2 \\ \theta_{x_2} \\ \theta_{y_2} \end{pmatrix} \simeq \begin{pmatrix} \mathbb{A} & \mathbb{B} \\ \mathbb{C} & \mathbb{D} \end{pmatrix} \cdot \begin{pmatrix} x_1 \\ y_1 \\ \theta_{x_1} \\ \theta_{y_1} \end{pmatrix} \tag{II.29}$$

where the ray matrix, $\mathbb{ABCD}$, is formalized by

$$\begin{pmatrix} A_x & A_{xy} & B_x & B_{xy} \\ A_{yx} & A_y & B_{yx} & B_y \\ C_x & C_{xy} & D_x & D_{xy} \\ C_{yx} & C_y & D_{yx} & D_y \end{pmatrix} \tag{II.30}$$

The estimation of the ray matrix for typical optical components is beyond the scope of this thesis. It can be found in [25].

II.1.3. *Resonant cavities in Ray Optics*

When we want to study the diffraction effect in the resonance cavity, we must consider the mirror curvature radius, R_1 and R_2. We can use the approach described in Sec. II.1.1 and apply the ray matrix theory to the beam evolution. This analysis will assume a circular symmetry of a linear cavity so that the corresponding 4×4 $\mathbb{ABCD}$ matrix can be decomposed into two identical 2×2. In this way, we can focus the calculation on one plane and extend the results at the end.

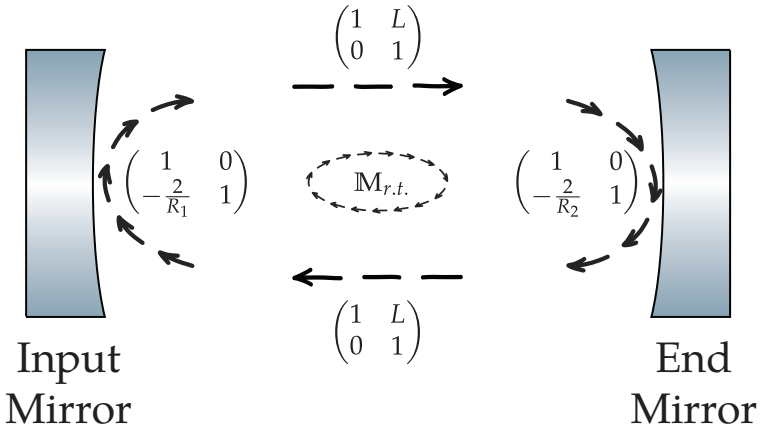

FIGURE II.2: Conceptual scheme of an optical cavity. Two mirrors, separated by a distance L, are called respectively Input and End Mirrors, and they have a radius of curvature R_1 and R_2. After each reflection, the beam is focused by the mirrors back and forward. The diffraction evolution after a round trip can be represented by an $\mathbb{ABCD}$ matrix labelled as $\mathbb{M}_{r.t.}$.

As a first approach, we can focus only on the beam inside the cavity and study the round trip made by the beam. We can use the Figure II.2 to define an $\mathbb{ABCD}$ matrix that represents the diffraction evolution after one loop:

$$\mathbb{M}_{r.t.} = \begin{pmatrix} 1 & 0 \\ -\frac{2}{R_1} & 1 \end{pmatrix} \begin{pmatrix} 1 & L \\ 0 & 1 \end{pmatrix} \begin{pmatrix} 1 & 0 \\ -\frac{2}{R_1} & 1 \end{pmatrix} \begin{pmatrix} 1 & L \\ 0 & 1 \end{pmatrix} \tag{II.31}$$

which leads to

$$\mathbb{M}_{r.t.} = \begin{pmatrix} 2g_2 - 1 & 2Lg_2 \\ \frac{2(2g_1g_2 - g_1 - g_2)}{L} & 4g_1g_2 - 1 - 2g_2 \end{pmatrix} \quad \text{with} \quad g_i = (1 - L/R_i) \tag{II.32}$$

After N round trip, the ray matrix is given by $\mathbb{M}^N_{r.t.}$ and we can estimate it using Sylvester's formula[1]

$$\mathbb{M}^N_{r.t.} = (\Lambda_2 - \Lambda_1)^{-1} \left(\mathbb{M}_{r.t.}(\Lambda_2^N - \Lambda_1^N) - i(\Lambda_2^{N-1} - \Lambda_1^{N-1}) \right) \tag{II.33}$$

where Λ_i are the eigenvalues of $\mathbb{M}$:

$$\Lambda_i = (2g_1g_2 - 1) \pm \sqrt{(2g_1g_2 - 1)^2 - 1} \tag{II.34}$$

[1] Note that this solution holds only for $\Lambda_1 \neq \Lambda_2$

Only by looking at the round trip matrix, we can classify the cavity as a function of its diffraction effects. As the longitudinal study of the cavity, the intracavity field is defined as the steady state of the cavity, so we want to analyse the diffraction evolution for $N \to +\infty$. In this case, the ray-matrix $\mathbb{M}_{r.t.}^{N}$ defines three different evolution as functions of its eigenvalues:

Marginally stable cavity $|2g_1g_2 - 1| = 1$ The eigenvalues are degenerate $\Lambda_{1,2} = 1$ and we cannot use the Sylvester's formula. Moreover, the $\mathbb{M}$ is not diagonalizable, so the stability of the steady state regime is defined by the initial ray parameters.

Unstable Cavity $|2g_1g_2 - 1| > 1$ In this case, we have $|\Lambda_1| > 1$, and the ray parameters will increase exponentially after each round trip. In particular, the ray angle will increase until the paraxial approximation does not hold anymore.

Stable cavity $|2g_1g_2 - 1| < 1$ We cannot estimate a steady state solution for the ray parameters because this case leads to complex eigenvalues. However, Sylvester's formula still gives a real matrix for $\mathbb{M}_{r.t.}^{N}$ and it is possible to show that at each round trip, the ray parameters are limited, and the beam does not diverge outside the paraxial approximation.

This thesis will work only with a stable cavity so that we can focus only on $|2g_1g_2 - 1| < 1$. However, this case does not have a steady state solution that can be described using the ray optic theory, so we need to extend the analysis of our tools. In particular, we need to consider the evolution of the amplitude profile $U(x, y, z)$ defined by the wave equation.

Paraxial Wave Equation and Beam Optics

In order to model the beam amplitude inside a cavity, it is more useful to start from the general case of the Free-space evolution. The first step will be the study of the beam shape, $U(x, y, z)$ in the paraxial approximation, which assumes that the beam amplitude $E(x, y, z)$ evolves slowly along the transverse plane. In this case, the beam shape $U(x, y, z)$ must follow the Paraxial Helmholtz Equation[25, p. 628]:

$$\left(\frac{\partial^2}{\partial x^2} + \frac{\partial^2}{\partial y^2}\right) U(x, y, z) = -i2k\frac{\partial U}{\partial z}(x, y, z) \tag{II.35}$$

The general approach used to resolve Eq.II.35 is based on the decoupling the amplitude along two planes XZ and YZ:

$$U(x, y, z) = u_x(x, z) \times u_y(y, z) \tag{II.36}$$

that allows decomposing the differential equation into:

$$\begin{cases} \left(\frac{\partial^2}{\partial x^2} + i2k\frac{\partial}{\partial z}\right) u_x(x, z) = 0 \\ \left(\frac{\partial^2}{\partial y^2} + i2k\frac{\partial}{\partial z}\right) u_y(y, z) = 0 \end{cases} \tag{II.37}$$

In this way, we can focus on the amplitude evolution along the XZ plane :

$$\left(\frac{\partial^2}{\partial x^2} - i2k\frac{\partial}{\partial z}\right) u(x, z) = 0 \tag{II.38}$$

where we drop the x subscript to highlight the generality of the solutions. Subsequently, we will extend the results to the plane YZ by replacing $x \to +y$.

The solutions of Eq. II.38 define the transverse modes of the electric field, $u_n(x,z)$, which are a complete set of functions that describes the bi-dimensional amplitude of the beam. These functions are defined as a combination of the Fundamental mode, $n = 0$:

$$u_0(x,z) = \sqrt[4]{\frac{2}{\pi w_x^2(z)}} \exp\left[\frac{-x^2}{w_x^2(z)}\right] \exp\left[\tfrac{i}{2}\Delta\psi_x - ik\frac{x^2}{2R_x(z)}\right] \tag{II.39}$$

and the Hermite-Polynomial defined by the recursive rule:

$$\mathbb{H}_n[\tau] = 2\tau\mathbb{H}_{n-1}[\tau] - 2n\mathbb{H}_{n-2}[\tau] \tag{II.40}$$

where $\tau = \sqrt{2}x/w(z)$ and $\mathbb{H}_0[\tau] = 1$. The amplitude of a general mode is described by the function:

$$u_n(x,z) = \underbrace{\frac{1}{\sqrt{2^n n!}}\mathbb{H}_n\left[\frac{\sqrt{2}x}{w_x(z)}\right]\sqrt[4]{\frac{2}{\pi w_x^2(z)}}\exp\left[\frac{-x^2}{w_x^2(z)}\right]}_{\text{Magnitude}} \overbrace{\exp\left[i\Delta\psi_x\left(\tfrac{1}{2}+n\right) - ik\frac{x^2}{2R_x(z)}\right]}^{\text{Phase}} \tag{II.41}$$

where the polynomial, $\mathbb{H}_n$, manipulates the profile along the transverse direction, x, and defines the shape of the mode as a function of the index, n.

The Fundamental mode is described by the parameters $w(z)$ and $R(z)$. The first one, $w(z)$, can be considered as the beam radius inasmuch as it defines the magnitude profile. The second one, $R(z)$ defines the phase profile of the beam, and it describes the curvature of the beam wavefront. The beam radius $w(z)$ and the beam curvature $R(z)$ are generally combined together in the complex parameter:

$$\frac{1}{q_{(x)}(z)} = \left((z - z_{x0}) + iz_{xR}\right)^{-1} := \frac{1}{R_x(z)} - \frac{i\lambda}{\pi w_x^2(z)} \tag{II.42}$$

and can be defined as function of the Rayleigh length z_R and z_0 that is the position of the minimum radius $w_0 = \min_z(w(z))$:

$$w_x(z) = w_0\sqrt{1 + \left(\tfrac{z-z_{x0}}{z_{xR}}\right)^2} \tag{II.43}$$

$$R_x(z) = (z - z_{x0})\left[1 + \left(\tfrac{z_R}{z-z_{x0}}\right)\right] \tag{II.44}$$

$$w_{x0} = \sqrt{\frac{\lambda z_{xR}}{\pi}} \quad \text{or} \quad z_{xR} = \frac{\pi w_{x0}^2}{\lambda} \tag{II.45}$$

Another essential parameter is the Gouy Phase, $\Delta\psi_x$ which represents the phase delay accumulated by the propagation of the paraxial wave with respect to the corresponding plane wave. As we will see later, this phase lag depends on the diffraction effects and, in the case of free space evolution, we can evaluate it as:

$$\Delta\psi_x = \text{Arg}[q_x(0)/q_x(z)] = \arctan\left(\tfrac{z-z_{x0}}{z_{xR}}\right) \tag{II.46}$$

The different transverse modes are distinguished by the Hermite-Polynomial, $\mathbb{H}_n$ which manipulated the beam shape. Moreover, these factors impose an important property on the modes inasmuch they induce an orthogonality rule with respect to the following product:

$$\langle u_n(x,z)|u_m(x,z)\rangle = \int_{\mathbb{R}} u_n(x,z)\overline{u_m(x,z)}dx = \delta_{n,m} \tag{II.47}$$

The functions described in Eq. II.41 represent the amplitude profile along the plane XZ and they can be extended to the YZ plane by changing x with y. These results are combined together by the Eq.II.36 and generate the three-dimensional solutions:

$$U_{nm}(x,y,z) = u_n(x,z|q_{(x)}) \times u_m(y,z|q_{(y)}) \tag{II.48}$$

The two plane components can have different complex parameters $q_{(i)}$ with $i = x,y$ for each couple of $(q_{(x)}, q_{(y)})$. They define a complete base for the solution for the Paraxial Helmholtz Equation, Eq. II.35. This property allows describing any general solution as a unique linear combination of these modes:

$$U(x,y,z) = \sum_{nm} c_{mn} u_n(x,z|q_{(x)}) u_m(y,z|q_{(y)}) \tag{II.49}$$

In the majority of the cases, we consider only the Transverse Mode defined by a unique complex factor for both the plane,$q_x = q = q_y$. These modes are called Hermite-Gauss Modes and they will be indicated in this thesis as:

$$\mathbf{HG}_{nm}(x,y,z|q) = u_n(x,z|q) \times u_m(y,z|q) \tag{II.50}$$

and they are classified as a function of their mode order, $N = n + m$. The amplitude profile of the Hermite-Gauss modes of the first two orders, $N \leq 2$ are reported in Fig. II.3.

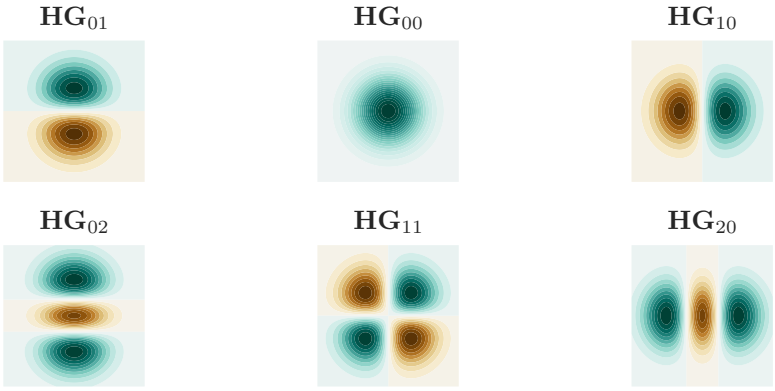

FIGURE II.3: Amplitude profile of the Hermite Gauss Modes from the Fundamental Mode, $\mathbf{HG}_{00}$ up to second order modes. The two colours indicate the amplitude sign, green positive and yellow negative.

Diffraction propagation of a Paraxial Beam

The solution of the Paraxial Helmholtz equation defined in Eq. II.41 describes the amplitude of a beam which propagates in free space. To extend this result to a general

optical system, we need to base the analysis on the "*Huygens' construction principle*" [26]. In this framework, the diffraction is described as an integral propagation

$$E(x_2, y_2|z_2) = \iint dx_1 dy_1 E(x_1, y_1|z_1) K(x_2, y_2, z_2; x_1, y_1, z_1) \tag{II.51}$$

where $E(x_1, y_1|z_1)$ is the amplitude shape at the plane $z = z_1$ and the $E(x_2, y_2|z_2)$ at $z = z_2$. These shapes are connected by the Kernel Function $K(\vec{r}_2; \vec{r}_1)$ which is defined as the propagation of an optical field at $\vec{r}_2$ generated by a point source at $\vec{r}_1$.

This approach can be applied to the solution of the Paraxial Helmholtz Equation by following the Collins' work[27]. The author was able to connect the optical ray theory with the paraxial wave equation and to define a kernel function based on the $\mathbb{ABCD}$ matrix of the optical system:

$$K(x_2, y_2, z_2; x_1, y_1, z_1) = \frac{ike^{iktildeL_0}}{2\pi(B_x B_y - B_{xy}B_{yx})} \exp\left[ik\frac{\vec{v}^T \mathbb{L} \vec{v}}{2(B_x B_y - B_{xy}B_{yx})}\right] \tag{II.52}$$

where the matrix $\mathbb{L}$ is defined by the coefficient of the $\mathbb{ABCD}$ matrix of the optical system:

$$\mathbb{L} = \begin{pmatrix} B_y A_x - B_{xy}A_{yx} & -B_y & A_{xy}B_y - B_{xy}A_y & B_{xy} \\ -B_y & D_x B_y - D_{xy}B_{yx} & B_{yx} & B_x D_{xy} - D_x B_{xy} \\ A_{xy}B_y - A_y B_{xy} & B_{yx} & B_x A_y - A_{xy}B_{yx} & -B_x \\ B_{xy} & B_x D_{xy} - D_x B_{xy} & -B_x & B_x D_y - B_{xy}D_{yx} \end{pmatrix} \tag{II.53}$$

the vector $\vec{v} = (x_1, x_2, y_1, y_2)^T$ contains the transverse coordinates, and $\tilde{L}_0$ is the optical length of the system:

$$\tilde{L}_0 = \sum_i (n_i \Delta z_i) \tag{II.54}$$

which collects all the phase shifts generate by the passing through each medium with refractive indices n_i and lengths Δz_i.,

The diffraction evolution of a general paraxial beam can be estimated by the combination of Eq. II.51 and Eq. II.52. However, the application of this method to a general paraxial beam can be simplified using the Transverse mode representation.

Propagation of Hermite-Gauss modes through an optical system

We can combine the Collins integral with the free-space solution of the Helmholtz equation and trace back the evolution of a general paraxial beam to Hermite-Gauss modes behaviour. In case we want to describe the evolution of the beam shape from the plane z_1 to z_2, we can decompose the general optical beam and represent it as a linear combination of Transverse modes:

$$E(x_1, y_1|z_1) = \sum_{mn} c_{mn} U_{mn}(x_1, y_1|z_1, q_1^{(x,y)}) \tag{II.55}$$

where $U_{mn}(x_1, y_1|z_1, q_1^{(x,y)})$ are the amplitudes of the modes defined by the beam parameters, $q_1^{(x,y)}$ at the longitudinal position $z = z_1$[2], and the c_{nm} are the linear coefficients that characterise the decomposition.

[2]When we proceed with this decomposition, the choice of the Transverse Mode base is completely free and it can use optimises in order to simplify the calculations.

Using this representation, we can exploit the linearity of the Collins Integral and divide the integral propagation as

$$E(x,y,z_2) = e^{ik\tilde{L}_0}\sum_{mn} c_{mn}\iint_{\mathbb{R}^2} K(x,y,z_2;x_1,y_1,z_1)U_{mn}(x_1,y_1,z_1;q_1^{(x,y)})dxdy \tag{II.56}$$

and focus the calculation only on the propagation of the Transverse Mode.

For the calculation used in this thesis, we can limit the resolution of the integral for an optical system that is simple astigmatic [3]. In this case, we can always define a reference system (x,y) in which the $\mathbb{ABCD}$ matrix can be decomposed in two components, one for plane XZ and another for YZ:

$$\begin{pmatrix} \mathbb{A} & \mathbb{B} \\ \mathbb{C} & \mathbb{D} \end{pmatrix} = \begin{pmatrix} A_x & 0 & B_x & 0 \\ 0 & A_y & 0 & B_y \\ C_x & 0 & D_x & 0 \\ 0 & C_y & 0 & D_y \end{pmatrix} = \begin{pmatrix} A_x & B_x \\ C_x & D_x \end{pmatrix} \times \begin{pmatrix} A_y & B_y \\ C_y & D_y \end{pmatrix} \tag{II.57}$$

In this case, the Collins Kernel can be divided into

$$K(x,y,z_2;x_1,y_1,z_1) = ike^{ik\tilde{L}_0}\, K_x(x,z_2;x_1,z_1) \times K_y(y,z_2;y_1,z_1) \tag{II.58}$$

where the single plane kernel function K_x and K_y have the same form:

$$K_\tau(\tau,z_2;\tau_1,z_1) = \frac{1}{\sqrt{2\pi}B_\tau}\exp\left[ik\frac{A_\tau\tau_1^2 - 2\tau_1\tau + D_\tau\tau^2}{2B_\tau}\right] \quad \text{where} \quad \tau = x,y \tag{II.59}$$

The decomposition done in Eq. II.55 does not have any particular requirement and we can choose the transverse modes $U_{mn}(x_1,y_1,z_1;q_1^{(x,y)})$ that are aligned with the $\mathbb{ABCD}$ matrix reference system. In this way, we can decompose the amplitude as

$$U_{mn}(x_1,y_1,z_1;q_1^{(x,y)}) = u_m(x_1,z_1;q_1^{(x)}) \times u_n(y_1,z_1;q_1^{(y)}) \tag{II.60}$$

and completely divide Eq. II.56 into two separates integrals:

$$\begin{aligned} &\iint_{\mathbb{R}} K(x,z_2;x_1,z_1)u_m(x_1,z_1;q_1^{(x)})dx \\ &\iint_{\mathbb{R}} K(y,z_2;y_1,z_1)u_n(y_1,z_1;q_1^{(y)})dy \end{aligned} \tag{II.61}$$

In particular, we will first focus the analysis on the plane XZ and extend the results to the plane YZ later. The calculations are presented in [28][4] and the final result is

$$\begin{aligned} &\int_{\mathbb{R}} K(x,z_2;x_1,z_1)u_n(x_1,z_1;q_1)dx_1 = \\ &\frac{1}{\sqrt{2^n n!}}\mathbb{H}_n\left[\frac{\sqrt{2}x}{w_2(z)}\right]\sqrt[4]{\frac{2}{\pi w_2^2(z)}}\exp\left[-\frac{ik}{2}\frac{x^2}{q_2^2}\right]\exp\left[-i\left(\tfrac{1}{2}+n\right)\mathrm{Arg}[A_xq_1+B_x]\right] = \\ &\qquad u_n(x,z_2;q_2)\exp\left[i(\tfrac{1}{2}+n)\,\mathrm{Arg}[C_xq_1+D_x]\right] \end{aligned} \tag{II.62}$$

[3] A simple astigmatic system is an optical system in which the beam evolution can be globally divided into two planar evolution. E.g. A system of cylindrical lenses with their focal axis always parallels one to each other.

[4] The starting equation used in [28] have a different definition for the Hermite-Gauss mode. The solution reported here is the evolution of a normalised Hermite-Gauss mode.

where we can see that the optical system maps a bi-dimensional transverse mode into the same one but defined by a new complex radius, q_2. In this way, the diffraction evolution is summarised by the ABCD rule:

$$q_2^{(x)} = \frac{A_x q_1^{(x)} + B_x}{C_x q_1^{(x)} + D_x} \tag{II.63}$$

Moreover, between z_1 and z_2, the beam accumulates a phase delay with respect to the plane wave evolution that can be decomposed as:

$$\begin{aligned} -\operatorname{Arg}\left[A_x q_1^{(x)} + B_x\right] &= -\operatorname{Arg}\left[\frac{A_x q_1^{(x)} + B_x}{C_x q_1^{(x)} + D_x}\right] + \operatorname{Arg}\left[C_x q_1^{(x)} + D_x\right] \\ &= \operatorname{Arg}[(q_2^{(x)}) - 1] + \operatorname{Arg}\left[C_x q_1^{(x)} + D_x\right] \end{aligned} \tag{II.64}$$

The first term is the Gouy phase for free space evolution, and it should be included in the definition of $u_n(x|z_2, q_2)$ used in Eq. II.62. The second one is the extra Gouy phase generated by the diffraction effects produced by the optical system. The evolution of the transverse mode, $u_m(y, z)$, can be obtained by replacing $x \to y$ and $n \to m$.

Estimation of the Transverse mode of a resonant Cavity

The first approach to estimating the Transverse Mode of a cavity was based on the ray optics theory, and it was unable to describe the beam evolution for a stable cavity. The hidden problem was to consider each ray separately and try to find a stable solution for each of them. This limitation is overcome by the Collins integral, which considers the beam whole amplitude, $U(x, y, z)$. In this way, it is possible to analyse the beam evolution and find a stable solution for the Transverse Mode of a cavity.

The approach used to estimate these modes is similar to the one used for the longitudinal study. We are still interested in the cavity steady state, so we need to identify a shape for the beam amplitude that does not change after $N \to \infty$ round trips. This can be formalised by imposing that the amplitude $E(x, y, z)$ at the input mirror should have the same profile after travelling inside the cavity. From the point of view of Collin's integral, this corresponds to

$$E_n(x, y, z_1) = e^{i\gamma_n} \int E_n(x_1, y_1, z_1) K_{r.t}(x, y, z_1; x_1, y_1, z_1) dx_0 \tag{II.65}$$

where $K_{r.t}$ is the kernel function defined by the round trip **ABCD** matrix, Eq.II.32, and we impose that the beam amplitude estimated after the propagation, $E_n(x, y, z_1)$ is equivalent to the original one, $E_n(x_1, y_1, z_1)$, multiplied by a phase $e^{i\gamma_n}$. This problem is equivalent to find the eigenfunctions, E_n, of the Collins integral. Once we obtain the formulation for both γ_n and $E_n(x, y, z_0)$, we can proceed with the same approach done for the plane wave approximation and estimate the internal field as superimposing of the amplitude after each round trip.

The symmetry of a linear cavity used to estimate the **ABCD** matrix in Eq.II.32 can be extended to the beam shape, $E(x, y, z)$. In this case, we can write the amplitude as:

$$E_{nm}(x, y, z) = E_n^{(x)}(x, z) \times E_m^{(y)}(y, z) \tag{II.66}$$

where we assumed that $E_n^{(x)}$ and $E_n^{(x)}$ can be different. Using the same arguments, the Collins Kernel can be factorised as

$$K(x,y,z;x_0,y_0,z_0) = e^{ik\tilde{L}_0} \underbrace{\sqrt{\frac{ik}{2\pi C_x^2}} exp\left[ik\frac{\vec{v}_x^T \mathbb{L} \vec{v}_x}{2C_x}\right]}_{K_x(x,z;x_0,z_0)} \underbrace{\sqrt{\frac{ik}{2\pi C_y^2}} exp\left[ik\frac{\vec{v}_y^T \mathbb{L} \vec{v}_y}{2C_y}\right]}_{K_y(y,z;y_0,z_0)} \tag{II.67}$$

where we keep the plane-wave phase propagation $e^{ik\tilde{L}_0}$ outside. The requirements for the steady state are now imposed on the two bi-dimensional amplitude $E_n(x,z)$ and $E_m(y,z)$

$$E_n^{(x)}(x,z_1) = e^{i\gamma_n^{(x)}} \int E_n^{(x)}(x_1,z_1) K_x(x,z_1;x_1,z_1) dx_1 \tag{II.68}$$

$$E_m^{(y)}(y,z_1) = e^{i\gamma_m^{(y)}} \int E_m^{(y)}(y_1,z_1) K_y(y,z_1;y_1,z_1) dy_1 \tag{II.69}$$

where the Kernel, K_x and k_y have the same form defined by the combination of Eq. II.52 and the $\mathbb{ABCD}$ matrix defined in in Eq. II.32.

Due to the similarity between Eq. II.68 and Eq. II.69, we can focus the calculation on the plane XZ and extend the result by replacing $x \to y$ and $n \to m$.

A similar equation, Eq. II.62, was obtained for the diffraction evolution of Hermite-Gauss modes, and it suggests these functions as a possible solution of Eq. II.68. Starting from this observation, we can impose the requirement of Eq. II.68 to the propagation of a Hermite-Guass mode:

$$u_n(x,z_1;q_2) = e^{i\gamma_n^{(x)}} \int u_n(x,z_1;q_1) K(x;x_1) dx_1 = u_n(x,z_1;q_1)\, e^{i\gamma_n^{(x)}} e^{-i\,\mathrm{Arg}[Cq+D](n+1/2)} \tag{II.70}$$

This equation is solved for the conditions

$$q_1 = q_2 \quad \text{and} \quad \gamma_n^{(x)} = \mathrm{Arg}[Cq+D](n+1/2) \tag{II.71}$$

that can be resolved using the ABCD rule

$$q_2 = q_1 = \frac{Aq_1+B}{Cq_1+D} \quad \to \quad q_1 = \frac{A-D}{2C} + \frac{1}{C}\sqrt{\left(\frac{D+A}{2}\right)^2 - 1} \tag{II.72}$$

In particular, we can use the $\mathbb{ABCD}$ matrix given in Eq ,II.32 and estimate

$$q_c = q_1 = \frac{(2g_1g_2-1)}{2g_2L} + \frac{i}{2g_2L}\sqrt{1-(2g_1g_2-1)^2} \tag{II.73}$$

The complex parameter q_c in Eq. II.73 defines a specific set of solutions of the Paraxial Wave equations which fulfil the requirements of Eq. II.68. For this reason, the planar steady state of a linear cavity can be expressed as

$$u_n(x,z) = \frac{1}{\sqrt{2^n n!}} \mathbb{H}_n\left[\frac{\sqrt{2}x}{w_c(z)}\right] \left(\frac{2}{\pi w_c^2(z)}\right)^{\frac{1}{4}} \exp\left[\frac{-ikx^2}{q_c}\right] \exp\left[-i\,\mathrm{Arg}[q_c(z)]\left(\tfrac{1}{2}+n\right)\right] \tag{II.74}$$

The second requirement in Eq. II.71 allows estimating the eigenvalue from the Gouy phase collected after a round trip:

$$\gamma_n^{(x)} = -(1/2+n)\,2\arccos(\sqrt{g_1 g_2}) \tag{II.75}$$

These results can be directly extended to the YZ plane and combined together in order to estimate the Three-dimensional modes of a cavity. Using Eq. II.66 and considering that the cylindrical symmetry imposes the same complex parameter, q_c, for both the planes, the Transverse Mode of a Linear cavity is given by the Hermite-Gauss Mode:

$$\mathbf{HG}_{nm}(x,y,z|q_c) = u_n(x,z|q_c)u_m(y,z|q_c) \tag{II.76}$$

while the round trip phase is given by:

$$\gamma_{nm} = k2L - (1+n+m)\,2\arccos(\sqrt{g_1 g_2}) \tag{II.77}$$

where we readd the plain wave phase $e^{ik\tilde{L}_0}$ that was ingored in the calculation of Eq. II.68 and Eq. II.69.

We can combine the information obtained so far with the same calculations done in Sec. II.1.1 and estimate the intracavity field. We can assume that the beam amplitude at the beginning of the first round trip is represented by a Hermite-Gauss mode with amplitude E_0 and indices n, m:

$$E_{nm}^{(0)} = E_0\mathbf{HG}_{nm}(x,y,z|q_c) \tag{II.78}$$

while the beam amplitude after a l round trip is given by the recursive relationship:

$$E_{nm}^{(l)}(x,y,z) = e^{i\gamma_{nm}}(r_1 r_2)E_{nm}^{(l-1)}(x,y,z) \tag{II.79}$$

where γ_{nm} is the round trip phase described by Eq. II.77 and $(r_1 r_2)$ is the amplitude reduction given by the reflectance of the two mirrors. This equation can be resolved as

$$E_{nm}^{(l)}(x,y,z) = \left[e^{i\gamma_{nm}}(r_1 r_2)\right]^l E_0\mathbf{HG}_{nm}(x,y,z) \tag{II.80}$$

that is similar to Eq. II.1. These electric fields will superimpose one with each another and generate the intracavity amplitude

$$E_{nm}^{in.}(x,y,z) = \sum_j^{+\infty} E^{(j)}(x,y,z) =$$
$$E_0\mathbf{HG}_{nm}(x,y,z|q_c)\sum_j^{+\infty}(r_1 r_2\exp[-ik2L - i2(1+m+n)\arccos(\sqrt{g_1 g_2})])^l \tag{II.81}$$

where we expand γ_{nm} using the definition in Eq. II.76. This result is similar to the solution obtained with Eq. II.2, but with a correction to the round trip phase:

$$E_{nm}^{(\text{in})}(x,y,z) = E_0\mathbf{HG}_{nm}(x,y,z|q_c)\frac{1}{1-r_1 r_2 e^{i\gamma_{nm}}} \tag{II.82}$$
$$\gamma_{nm} = 2k2L - 2(1+m+n)\arccos(\sqrt{g_1 g_2}) \tag{II.83}$$

In particular, the new formulation for the round trip phase modifies the resonance frequency that now depends on both the Longitudinal mode order l and the Transverse mode order $N = (m + n)$:

$$f_N = l\Delta f_{\text{fsr}} + (1 + N)\Delta f_{HOM} \quad \text{with} \quad \Delta f_{HOM} = \frac{\Delta f_{\text{fsr}}}{\pi} \arccos(\sqrt{g_1 g_2}) \tag{II.84}$$

where we defined the coefficient Δf_{HOM}, called High Order Mode separation. In order to highlight this new frequency response, we can rewrite the round trip phase, γ_{nm}, as the normalised frequency:

$$\nu(f, N) = \pi \frac{f - f_0}{\Delta f_{\text{fsr}}} = \pi \frac{f - l\Delta f_{\text{fsr}} + (1 + N)\Delta f_{\text{HOM}}}{\Delta f_{\text{fsr}}} \tag{II.85}$$

This coupling between the resonance condition and the beam shape leads to a complex diffraction phenomenon that is at the foundation of the Mode Mismatch.

II.2. Mismatch of a Simple Astigmatic Gaussian Beam

In the previous section, we saw how the resonance frequency changes as a function of the Transverse Mode order, $(n + m) = N$. This phenomenon has a considerable effect when we look at the reflectance, transmittance and internal gain of a cavity. The combination of Eq. II.84 and Eq. II.19 shows how the cavity response is now defined as a function of the mode order, N:

$$r_{\text{cav}}(f, N) = \frac{a_r}{a_0} = \frac{r_1 - (1 - \rho_1) r_2 \, e^{i\,\nu(f,N)}}{1 - r_1 r_2 \, e^{i\,\nu(f,N)}} \tag{II.86}$$

$$t_{\text{cav}}(f, N) = \frac{a_t}{a_0} = \frac{t_2 t_1 \, e^{(i\,\nu(f,N))}}{1 - r_1 r_2 \, e^{i\,\nu(f,N)}} \tag{II.87}$$

$$\nu(f, N) = \pi \frac{f - f_0}{\Delta f_{\text{fsr}}} = \pi \frac{f - l\Delta f_{\text{fsr}} + (1 + N)\Delta f_{\text{HOM}}}{\Delta f_{\text{fsr}}} \tag{II.88}$$

This dependency imposes special care when we study the interaction between an incoming beam and a cavity. In particular, we can distinguish two cases: we will talk about *Mode Matched beam* if the amplitude profile of the incoming beam corresponds to one of the Cavity Transverse Modes, and about *Mode Mismatched beam* in the other cases.

In the first case, the interaction between the beam and the cavity can be analysed in plane-wave approximation, assuming the set of parameters of the corresponding mode order. In the second case, we have to represent its amplitude using the cavity base:

$$E^{In.}(x, y) = \sum_{i,j} c_{i,j} \mathbf{HG}_{i,j}(x, y|q_c) \tag{II.89}$$

and evaluate each Transverse Mode, $\mathbf{HG}_{i,j}(x, y|q_c)$, separately. The decomposition, together with the relationship between the cavity parameters and the order of the modes, generates diffractive effects and changes the beam shape of both the reflected and transmitted beams.

The cavity reflectance, $r_{\text{cav}}(f, N)$, changes as a function of the order of the Transverse Mode, so the amplitude, $c_{i,j}$, of each mode component, $\mathbf{HG}_{i,j}(x, y|q_c)$, will be reflected with different coefficients:

$$d_{ij} = c_{i,j} r_{ij} \quad \text{where} \quad r_{ij} = r_{\text{cav}}(f, i + j) \tag{II.90}$$

The reflected beam amplitude, $E^{Ref.}$ will results in a new linear combination defined by d_{ij}:

$$\begin{array}{rccccccc} E^{In.} = & c_{00}\mathbf{U}_{0,0} & + & c_{10}\mathbf{U}_{1,0} & + & c_{01}\mathbf{U}_{0,1} & + & \cdots \\ & \downarrow r_{0,0} & & \downarrow r_{1,0} & & \downarrow r_{0,1} & & \\ E^{Ref.} = & d_{00}\mathbf{U}_{0,0} & + & d_{10}\mathbf{U}_{1,0} & + & d_{01}\mathbf{U}_{0,1} & + & \cdots \neq E^{In.} \end{array}$$

that will correspond to a different shape.

A similar effect happens to the cavity transmission: when the incoming beam is not matched with the resonance mode (e.g $\mathbf{HG}_{00}$), the optical power carried by the other components is filtered out. If we consider the analysis done in Eq. II.22 and Eq. [II.24, II.25], we can assume that only the amplitude of the resonant mode will be transmitted:

$$b_{00} = c_{00}t_{00} \quad \text{where} \quad t_{00} = \sqrt{G_{cav}}t_2 \tag{II.91}$$

while the other coefficients are suppressed by the "out of resonance" condition[5]:

$$b_{ij} = c_{ij}t_{ij} \quad \text{where} \quad t_{ij} = i\frac{t_2 t_1}{1 + r_1 r_2} \simeq 0 \tag{II.92}$$

Using these results, the effect of the Resonant Cavity can be described as a transverse mode filter suppressesing the not resonant component

$$\begin{array}{rccccccc} E^{In.} = & c_{00}\mathbf{HG}_{0,0} & + & c_{10}\mathbf{HG}_{1,0} & + & c_{01}\mathbf{U}_{0,1} & + & \cdots \\ & \downarrow t_{0,0} & & \downarrow t_{1,0} & & \downarrow t_{0,1} & & \\ E^{Tran.} = & b_{00}\mathbf{HG}_{0,0} & + & \cancel{b_{10}\mathbf{HG}_{1,0}} & + & \cancel{b_{01}\mathbf{HG}_{0,1}} & + & \cdots \end{array}$$

and transmiting only the resonant one $E^{Tran.} = d_{00}\mathbf{U}_{0,0}$.

In this thesis, we want to present a new method to measure the mismatch between a Simple Astigmatic Gaussian Beam and a Linear Cavity. The main characteristic of the Astigmatic Gaussian beam is the elliptic shape of the power profile. In the case of Simple Astigmatism, this ellipse maintains a fixed orientation during the z propagation and defines an internal reference system,$(\tilde{x}, \tilde{y})$, in which the beam amplitude can be represented with two bi-dimensional Gaussian Mode. These two modes will have different complex parameters and the normalised amplitude profile is

$$\begin{aligned} \Psi_{in} = U_{00}(q^{\tilde{x}}, q^{\tilde{y}}) &= \sqrt{\frac{2}{\pi}}\sqrt{\frac{e^{i(\Delta\psi_{\tilde{x}}(z)+\Delta\psi_{\tilde{y}}(z))}}{w_{\tilde{x}}(z)w_{\tilde{y}}(z)}}e^{\frac{ik}{2}\left(\frac{\tilde{x}^2}{q^{\tilde{x}}}+\frac{\tilde{y}^2}{q^{\tilde{y}}}\right)} \\ q^{\tilde{x}/\tilde{y}}(z) &= \left(z - z_0^{\tilde{x}/\tilde{y}}\right) + i\frac{\pi w_0^{\tilde{x}/\tilde{y}}}{\lambda} \end{aligned} \tag{II.93}$$

where U_{00} is the fundamental mode in the base defined by the complex parameters $(q^{\tilde{x}}, q^{\tilde{y}})$.

On the other hand, the resonance mode of the cavity should be described using the experimental reference system, (x, y), and the complex parameter of the cavity

[5] Here we assume that the Cavity Finesse, $\mathcal{F}$ and the High Order mode spacing Δf_{HOM} are chosen in order to have only one resonant mode at the time.

defined using Eq. II.73. The connection between the beam reference system and the experimental one is given by a rotation of an angle θ:

$$\begin{cases} \tilde{x} = x\cos(\theta) - y\sin(\theta) \\ \tilde{y} = x\sin(\theta) + y\cos(\theta) \end{cases} \tag{II.94}$$

while the beam shape of the resonant mode is defined by:

$$\begin{aligned} U_{00}(x,y,z;q_c) = \mathbf{HG}_{00}(x,y,z;q_c) = u_0(x,z;q_c)u_0(y,z;q_c) = \sqrt{\frac{2}{\pi}}\frac{1}{w_c(z)}e^{ik\frac{r^2}{2q_c}}e^{\Delta\psi(z)} \\ q_c(z) = z - \bar{z}_0 + i\frac{\pi\bar{w}_0}{\lambda} \end{aligned} \tag{II.95}$$

where $r^2 = x^2 + y^2$, q_c is the complex parameter of the cavity, and we assumed that the cavity is tuned to be resonant with the fundamental mode, $ij = 00$.

As we introduced at the beginning of this section, the interaction between a resonant cavity and a beam has to be studied using the cavity Transverse mode basis. For this reason, we need to represent the Simple Astigmatic Gaussian Beam described in Eq. II.93 using the Transverse mode of the cavity, defined by the parameter, q_c.

In order to simplify the calculation, we can exploit the circular symmetry of the linear cavity and study the mode matching using an astigmatic reference system, $(\tilde{x}, \tilde{y})$. After this first approach, we can extend the results for an arbitrary experimental reference system by using the relationship defined in Eq. II.94. In this way, we can factorise the Transverse modes into the product of two bi-dimensional profiles and study one at a time. In particular, we will present the calculation for the plane $\tilde{X}Z$ and extend the results to the three-dimensional case.

The main advantage of focusing the study on one plane at a time is that the bi-dimensional Gaussian mode is completely defined by two parameters: the beam shape using the waist dimension w_0 and the waist position z_0. This allows connecting the amplitude shape of the incoming beam to the Fundamental Resonant Mode by using the same approach presented by Anderson[3]. Both these amplitudes have the same shape defined by Eq. II.39, reported here

$$u_0(x,z,w_0,z_0) = \sqrt[4]{\frac{2}{\pi w_x^2(z)}}\exp\left[\frac{-x^2}{w_x^2(z)}\right]\exp\left[\frac{i}{2}\Delta\psi_x - ik\frac{x^2}{2R_x(z)}\right] \tag{II.96}$$

but with different beam parameters, (w_0, z_0).

In this way, the mismatch between the incoming beam and the resonance mode can be describe by the difference of the beam paramters. We will indicate the Fundamental Resonant Mode parameter with $\bar{w}_0$ and $\bar{z}_0$, while the incoming beam shape is defined as small perturbation:

$$\begin{aligned} w_0^{(\tilde{x})} &= \bar{w}_0 + \delta w_0^{(\tilde{x})} \\ z_0^{(\tilde{x})} &= \bar{z}_0 + \delta z_0^{(\tilde{x})} \end{aligned} \tag{II.97}$$

This representation is schematised in Figure II.4, where the beam shape along the XZ plane is reported: The incoming beam is indicated by the dashed line, and the resonance one by the continued lines. The two mode have differente waist radius and different waist position.

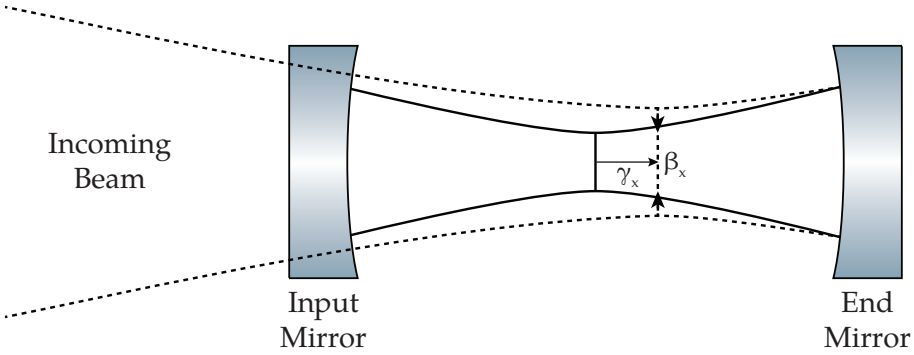

FIGURE II.4: Mismatch between the incoming beam and the cavity mode. The lines represent the evolution of $w(z)$ of the two different beam shapes: the incoming beam (dotted lines) and the cavity mode (continued line). The difference between the two beams is represented by $\gamma_{\tilde{x}} = \delta z^{(\tilde{x})}/2\bar{z}_R$ and $\beta_{\tilde{x}} = \delta w_0^{(\tilde{x})}/\bar{w}_0$ which are respectively the difference in position and dimension of the waist.

Starting from the relationship between the beam parameters described in Eq. II.97, we can represent the shape of the incoming beam as the Taylor expansion of the parameters, $w_0^{(\tilde{x})}$ and $z_0^{(\tilde{x})}$ around the values, $\bar{w}_0$ and $\bar{z}_0$

$$u_0\left(\bar{w}_0 + \delta w_0^{(\tilde{x})}, \bar{z}_0 + \delta z_0^{(\tilde{x})}\right) \simeq u_0(\bar{w}_0, \bar{z}_0) + \delta w_0^{(\tilde{x})} \left(\partial_{w_0} u_0(w_0, \bar{z}_0)|_{w_0=\bar{w}_0} + \delta z_0^{(\tilde{x})} \left(\partial_{z_0} u_0(\bar{w}_0, z_0)|_{z_0=\bar{z}_0}\right.\right. \quad \text{(II.98)}$$

In order to estimate the decomposition factor, we need to rewrite the Eq. II.98 as a function of bi-dimensional Hermite-Gauss mode with complex parameter q_c, $u_n(x, z|q_c)$. We can evaluate the derivatives in any z position, so we will choose the more comfortable one, $z = z_0$.

II.2.1. *Waist Radius Perturbation*

In order to study the effect of a waist radius perturbation, we can assume that the incoming beam and the resonance mode share the same waist position $z_0^{(\tilde{x})} = \hat{z}_0$ and estimate the Eq. II.98:

$$u_0\left(\bar{w}_0 + \delta w_0^{(\tilde{x})}, \bar{z}_0\right) \simeq u_0(\bar{w}_0, \bar{z}_0) + \delta w_0^{(\tilde{x})} \left(\partial_{w_0} u_0(w_0, \bar{z}_0)|_{\bar{w}_0}\right. . \quad \text{(II.99)}$$

Moreover, we can simplify the calculation by studying the Taylor expansion around $z = z_0^{(\tilde{x})}$ where the beam amplitude described by Eq.II.96 becomes:

$$u_0(\tilde{x}, \hat{z}_0|w_0, \bar{z}_0) = \sqrt[4]{\frac{2}{\pi}} \frac{1}{\sqrt{w_0^{(\tilde{x})}}} \exp\left(-\frac{\tilde{x}^2}{(w_0^{(\tilde{x})})^2}\right) \quad \text{(II.100)}$$

In this configuration, the derivative required in Eq. II.99 is given by

$$\begin{aligned}\left.\frac{\partial u_0(x,\hat{z}_0|w_0,\hat{z}_0)}{\partial w_0}\right|_{w_0=\bar{w}_0} &= \sqrt[4]{\frac{2}{\pi}}\left(-\frac{1}{2}\frac{1}{\sqrt{\bar{w}_0^3}}e^{-\frac{\tilde{x}^2}{\bar{w}_0^2}}+\frac{1}{\sqrt{\bar{w}_0}}\left(\frac{2\tilde{x}^2}{\bar{w}_0^3}e^{-\frac{\tilde{x}^2}{\bar{w}_0^2}}\right)\right)\\ &= \frac{1}{\bar{w}_0}\left[-\frac{1}{2}+\frac{2\tilde{x}^2}{\bar{w}_0^2}\right]\sqrt[4]{\frac{2}{\pi}}\frac{1}{\sqrt{\bar{w}_0}}e^{-\frac{\tilde{x}^2}{\bar{w}_0^2}}\end{aligned} \tag{II.101}$$

The next step is to rewrite these results as Hermite-Gauss modes. We need to factorise Eq. II.101 to the following structure:

$$u_n(\tilde{x}\hat{z}_0|\hat{z}_0,\bar{w}_0) = \left(\frac{2}{\pi}\right)^{\frac{1}{4}}\mathbb{H}_n\left(\frac{\sqrt{2}\tilde{x}}{\bar{w}_0}\right)\sqrt{\frac{1}{2^n\,n!\,\bar{w}_0}}e^{-\frac{\tilde{x}^2}{\bar{w}_0^2}} \tag{II.102}$$

by rewriting the coefficients between square brackets as Hermite polynomials. In particular, we can proceed as

$$\left(-\frac{1}{2}+\frac{2\tilde{x}^2}{\bar{w}_0^2}\right) = \frac{1}{4}\left(4\left(\frac{\sqrt{2}\tilde{x}}{\bar{w}_0}\right)^2-2\right) = \frac{1}{4}\mathbb{H}_2\left(\frac{\sqrt{2}\tilde{x}}{\bar{w}_0}\right) = \frac{1}{\sqrt{2}}\frac{1}{2\sqrt{2}}\mathbb{H}_2\left(\frac{\sqrt{2}\tilde{x}}{\bar{w}_0}\right) \tag{II.103}$$

where we highlight the normalisation factors for the Hermite-Gauss Mode of order 2, $(\sqrt{2^n n!})^{-1}$.

Using the factoring obtained in Eq. II.103, we can rewrite the derivative of Eq. II.100 as

$$\left.\frac{\partial u_0(x|w_0,\hat{z}_0)}{\partial w_0}\right|_{w_0=\bar{w}_0} = \frac{1}{\bar{w}_0}\frac{1}{\sqrt{2}}u_2(\tilde{x},z_0|\bar{w}_0) \tag{II.104}$$

and combine this results with Eq. II.99 in order to obtain:

$$u_0(\tilde{x}|\bar{w}_0+\delta w_0^{(\tilde{x})}) = u_0(\tilde{x}|\bar{w}_0)+\frac{1}{\sqrt{2}}\frac{\delta w_0^{(\tilde{x})}}{\bar{w}_0}u_2(\tilde{x}|\bar{w}_0) \tag{II.105}$$

II.2.2. *Waist Position Perturbation*

The study of the waist position, z_0, is a little bit more complicated than the previous one, inasmuch this parameter acts as reference along the $\hat{z}$ axis. This is clearer if we consider the general formulation of a fundamental Gaussian beam:

$$u_0(\tilde{x},z|\hat{w}_0,z_0) = \sqrt[4]{\frac{2}{\pi}}\frac{e^{i\frac{\Delta\psi_{\tilde{x}}(z-z_0)}{2}}}{\sqrt{w_{\tilde{x}}(z-z_0)}}e^{-\frac{ik}{2}\left(\frac{\tilde{x}^2}{q(z-z_0)}\right)} \tag{II.106}$$

where we highlight the z_0 dependency.

In this case, we cannot put $z=z_0$ and calculate the derivative as we will artificially remove z_0 from the equation. For this reason, we need an intermediate variable and to rewrite the Gaussian mode as a function of $\Delta z = z - z_0$. The perturbation of the waist position can be written as $\Delta z = 0 + \delta z_0^{(\tilde{x})}$ and the derivative as:

$$\partial_{z_0}u_0(\tilde{x}|z_0)|_{\hat{z}_0} = \left(\partial_{\Delta z}u_0(\tilde{x}|\Delta z)\cdot\partial_{z_0}\Delta z\right|_{\Delta z=0} = -\left(\partial_{\Delta z}u_0(\tilde{x}|\Delta z)\right|_{\Delta z=0} \tag{II.107}$$

We can identify three different components and estimate their independent contributions: the Gouy Phase $\Delta\psi_{\tilde{x}}$ Eq. II.46, the complex parameter q Eq. II.42, and the beam waist $w_{(\tilde{x})}$, Eq. II.44. The single contribution are given by

$$\left(\partial_{\Delta z}\Delta\psi_{\tilde{x}}(\Delta z)\right|_{\Delta z=0} = \left(\frac{1}{z_R}\frac{1}{1+\left(\frac{\Delta z}{\bar{z}_R}\right)^2}\right|_{\Delta z=0} = \frac{1}{z_R} \tag{II.108}$$

$$\left(\partial_{\Delta z}q^{-1}(\Delta z)\right|_{\Delta z=0} = \left(-\frac{1}{(\Delta z+iz_R)^2}\right|_{\Delta z=0} = \frac{1}{z_R^2} \tag{II.109}$$

$$\left(\partial_{\Delta z}\bar{w}_{\tilde{x}}(\Delta z)\right|_{\Delta z=0} = \left(\frac{\Delta z\bar{w}_0}{z_R^2\sqrt{1+\left(\frac{\Delta z}{z_R}\right)^2}}\right|_{\Delta z=0} = 0 \tag{II.110}$$

Using these results, we can rewrite the derivative of $u_0(\tilde{x}|z_0)$ as:

$$\begin{aligned}\partial_{\Delta z}u_0(\tilde{x}|\Delta z)|_{\Delta z=0} = \\ \sqrt[4]{\frac{2}{\pi}}\frac{1}{\sqrt{\bar{w}_0}}\left(\frac{+i}{2z_R}e^{i\frac{\Delta\psi_{\tilde{x}}(0)}{2}}e^{-\frac{ik}{2}\left(\frac{\tilde{x}^2}{q(0)}\right)}+e^{i\frac{\Delta\psi_{\tilde{x}}(0)}{2}}\left(\frac{-ik}{2}\frac{\tilde{x}^2}{z_R^2}\right)e^{-\frac{ik}{2}\left(\frac{\tilde{x}^2}{q(0)}\right)}\right) = \\ \left(\frac{i}{2z_R}-\frac{ik}{2}\frac{\tilde{x}^2}{z_R^2}\right)\sqrt[4]{\frac{2}{\pi}}\frac{1}{\sqrt{\bar{w}_0}}e^{i\frac{\Delta\psi_{\tilde{x}}(0)}{2}}e^{-\frac{ik}{2}\left(\frac{\tilde{x}^2}{q(0)}\right)}\end{aligned} \tag{II.111}$$

As we did in the previous section, we need to re-organise the coefficient as a second order Hermite polynomial:

$$\begin{aligned}\left(\frac{i}{2z_R}-\frac{ik}{2}\frac{\tilde{x}^2}{z_R^2}\right) = \frac{-i}{z_R}\left(\frac{-1}{2}+\frac{\tilde{x}^2}{\bar{w}_0^2}\right) = \\ \frac{-i}{8z_R}\left(-2-2+4\frac{2\tilde{x}^2}{\bar{w}_0^2}\right) = \frac{-i}{8z_R}(-2+\mathbb{H}_2\left(\frac{\tilde{x}\sqrt{2}}{\bar{w}_0}\right))\end{aligned} \tag{II.112}$$

and add the the normalisation factor of a second order Hermite-Gauss beam $(2\sqrt{2})^{-1}$:

$$\begin{aligned}\partial_{\Delta z}u_0(\tilde{x}|\Delta z)|_{\Delta z=0} = \\ 2\sqrt{2}\frac{-i}{8z_R}\frac{1}{2\sqrt{2}}\left(\mathbb{H}_2\left(\frac{\tilde{x}\sqrt{2}}{\bar{w}_0}\right)-2\right)\sqrt[4]{\frac{2}{\pi}}\frac{1}{\sqrt{\bar{w}_0}}e^{i\frac{\Delta\psi_{\tilde{x}}(0)}{2}}e^{-\frac{ik}{2}\left(\frac{\tilde{x}^2}{q(0)}\right)} = \\ \frac{1}{\sqrt{2}}\frac{-i}{2z_R}u_2(\tilde{x}|\bar{z}_0)+\frac{1}{2}\frac{i}{2z_R}u_0(\tilde{x}|\bar{z}_0)\end{aligned} \tag{II.113}$$

The final result for the waist position perturbation is given by the combination of the factoring in Eq. II.113 and Eq. II.107[6]:

$$u_0(\tilde{x}|\bar{z}_0+\delta z_0^{(\tilde{x})}) = u_0(\tilde{x}|\bar{z}_0)+\frac{i}{\sqrt{2}}\frac{\delta z_0^{(\tilde{x})}}{2z_R}u_2(\tilde{x}|\bar{z}_0)(x,y|q_c)-\left(\frac{i}{2}\frac{\delta z_0^{(\tilde{x})}}{2z_R}u_0(\tilde{x}|\bar{z}_0)\right) \tag{II.114}$$

[6]The result presented by Anderson[3] does not contain the $-2u_0$ in the perturbation of the waist position.

Combining Eq. II.98 Eq. II.105 and Eq.,II.114 we can represent the mismatch between the bi-dimensional Gaussian mode and a linear cavity as[7]

$$u_0(\tilde{x}|\bar{w}_0+\delta w_0^{(\tilde{x})},\bar{z}_0+\delta z_0^{(\tilde{x})}) = u_0(\tilde{x}|\bar{w}_0,\bar{z}_0) + \underbrace{\left(\frac{\delta w_0^{(\tilde{x})}}{\bar{w}_0}+i\frac{\delta z_0^{(\tilde{x})}}{2\bar{z}_R}\right)}_{\epsilon_{\tilde{x}}}\frac{\mathbf{u_2}(\tilde{x}|\bar{w}_0,\bar{z}_0)}{\sqrt{2}} \tag{II.115}$$

where all the information about the difference between the two modes is collected in the amplitude coefficient:

$$\epsilon_{\tilde{x}} = \left(\frac{\delta w_0^{\tilde{x}}}{\bar{w}_0}+i\frac{\delta z_0^{\tilde{x}}}{2\bar{z}_R}\right) \tag{II.116}$$

II.2.3. *Astigmatic Mismatch in the three dimensional space*

We can now extend this representation to the three dimensional incoming beam using the cavity base. We can combine Eq. II.115 with Eq. II.93:

$$\Psi_{in} = \mathbf{U}_{00}(q^{\tilde{x}},q^{\tilde{y}}) \simeq \left(u_0(\tilde{x})+\epsilon_{\tilde{x}}\frac{u_2(\tilde{x})}{\sqrt{2}}\right)\cdot\left(u_0(\tilde{y})+\epsilon_{\tilde{y}}\frac{u_2(\tilde{y})}{\sqrt{2}}\right) \tag{II.117}$$

and consider only coefficients that are linear with the perturbation. In particular, the bi-dimensional amplitude share the same complex parameter, q_c and they are combined into the Hermite-Gauss modes $\mathbf{HG}_{nm}$ using Eq. II.50:

$$\begin{aligned} u_0(\tilde{x})u_0(\tilde{y}) &= \mathbf{HG}_{00} \\ \epsilon_{\tilde{x}}u_0(\tilde{x})u_2(\tilde{y}) &= \epsilon_{\tilde{x}}\mathbf{HG}_{02} \\ \epsilon_{\tilde{y}}u_2(\tilde{x})u_0(\tilde{y}) &= \epsilon_{\tilde{y}}\mathbf{HG}_{20} \\ \epsilon_{\tilde{x}}\epsilon_{\tilde{y}}u_2(\tilde{x})u_2(\tilde{y}) &= \epsilon_{\tilde{x}}\epsilon_{\tilde{y}}\mathbf{HG}_{22} \end{aligned} \tag{II.118}$$

We can consider only the contribution that are linear with the perturbations to the $\epsilon_{\tilde{x}}$ and $\epsilon_{\tilde{y}}$ and, we can ignore $\mathbf{HG}_{22}$. In this way, Eq. II.117 is simplified to

$$\begin{aligned} \Psi_{in} \simeq \mathbf{HG}_{00}(\tilde{x},\tilde{y}|q_c) + \langle\epsilon\rangle\frac{1}{\sqrt{2}}\left(\mathbf{HG}_{20}(\tilde{x},\tilde{y}|q_c)+\mathbf{HG}_{02}(\tilde{x},\tilde{y}|q_c)\right) + \\ \delta\epsilon\frac{1}{\sqrt{2}}\left(\mathbf{HG}_{20}(\tilde{x},\tilde{y}|q_c)-\mathbf{HG}_{02}(\tilde{x},\tilde{y}|q_c)\right) \end{aligned} \tag{II.119}$$

where we have defined the common and differential mismatch as

$$\text{Common} \quad \langle\epsilon\rangle = \frac{(\epsilon_{\tilde{x}}+\epsilon_{\tilde{y}})}{2} \tag{II.120}$$

$$\text{Differential} \quad \delta\epsilon = \frac{(\epsilon_{\tilde{x}}-\epsilon_{\tilde{y}})}{2} \tag{II.121}$$

II.2.4. *Astigmatic Axis Angle*

After the formalisation of the mismatch in the astigmatic reference system, we need to extend Eq. II.119 to the experimental reference one. In this case, we need to impose a

[7] Here, we ignore the correction to the fundamental mode present in Eq. II.114.

rotation of the reference system (x, y) by applying:

$$\tilde{x} = x\cos(\theta) - y\sin(\theta) \tag{II.122}$$
$$\tilde{y} = x\sin(\theta) + y\cos(\theta) \tag{II.123}$$

to each mode in Eq. II.119. Only the modes $\mathbf{HG}_{02}$ and $\mathbf{HG}_{20}$ are not invariant by this transformation. If we look their general form defined using the rule in $\mathbf{HG}_{nm}$ with the amplitude shape define in Eq. II.41:

$$\mathbf{HG}_{20}(\tilde{x},\tilde{y}) = \sqrt{\frac{2}{\pi}}\mathbb{H}_2\left(\frac{\sqrt{2}\tilde{x}}{w(z)}\right)\sqrt{\frac{1}{2^2\,2!}}\frac{1}{w(z)}e^{-\frac{\tilde{x}^2+\tilde{y}^2}{q(z)}}e^{i3\Delta\psi(z)} \tag{II.124}$$

we can see that the only coefficient that change under rotation is the Hermite polynomial:

$$\begin{aligned}
\mathbb{H}_2\left(\tfrac{\sqrt{2}\tilde{x}}{w(z)}\right) &= 4\left(\tfrac{\sqrt{2}\tilde{x}}{w(z)}\right)^2 - 2 \\
&= 4\left(\tfrac{\sqrt{2}(x\cos(\theta)-y\sin(\theta))}{w(z)}\right)^2 - 2 \\
&= 4\left(\tfrac{\sqrt{2})}{w(z)}\right)^2 [x^2\cos^2(\theta) + y^2\sin^2(\theta) - 2xy\cos(\theta)\sin(\theta)] \\
&\quad - 2(\cos^2(\theta) + \sin^2(\theta)) \\
&= [4\left(\tfrac{\sqrt{2})}{w(z)}\right)^2 x^2 - 2]\cos^2(\theta) + [4\left(\tfrac{\sqrt{2})}{w(z)}\right)^2 y^2 - 2]\sin^2(\theta) \\
&\quad - 2\cdot 2x\left(\tfrac{\sqrt{2})}{w(z)}\right)\cos(\theta) 2y\left(\tfrac{\sqrt{2})}{w(z)}\right)\sin(\theta) \\
&= \mathbb{H}_2\left(\tfrac{\sqrt{2}x}{w(z)}\right)\cos^2(\theta) + \mathbb{H}_2\left(\tfrac{\sqrt{2}y}{w(z)}\right)\sin^2(\theta) \\
&\quad - 2\mathbb{H}_1\left(\tfrac{\sqrt{2}x}{w(z)}\right)\cos(\theta)\mathbb{H}_1\left(\tfrac{\sqrt{2}y}{w(z)}\right)\sin(\theta)
\end{aligned} \tag{II.125}$$

If we recombine this result into Eq. II.124, we obtain

$$\begin{aligned}
\mathbf{HG}_{20}(\tilde{x},\tilde{y}) = \left(\tfrac{2}{\pi}\right)^{\frac{1}{2}}\sqrt{\tfrac{1}{2^2\,2!}}\tfrac{1}{w(z)}\exp\left(-\tfrac{x^2+y^2}{q^2(z)}\right)\exp\left(-i3\Phi(z)\right)\cdot \\
\left[\mathbb{H}_2\left(\tfrac{\sqrt{2}x}{w(z)}\right)\cos^2(\theta) + \mathbb{H}_2\left(\tfrac{\sqrt{2}y}{w(z)}\right)\sin^2(\theta)\right. \\
\left. -2\mathbb{H}_1\left(\tfrac{\sqrt{2}x}{w(z)}\right)\cos(\theta)\mathbb{H}_1\left(\tfrac{\sqrt{2}y}{w(z)}\right)\sin(\theta)\right]
\end{aligned} \tag{II.126}$$

that is composed by three terms: one proportional to $\mathbb{H}_2\left(\frac{\sqrt{2}x}{w(z)}\right)$, one proportional to $\mathbb{H}_2\left(\frac{\sqrt{2}y}{w(z)}\right)$, and a third proportional to $\mathbb{H}_1\left(\frac{\sqrt{2}x}{w(z)}\right)\mathbb{H}_1\left(\frac{\sqrt{2}y}{w(z)}\right)$. The first two can be factorised into the $\mathbf{HG}_{02}(x,y)$ and $\mathbf{HG}_{20}(x,y)$:

$$\sqrt{\tfrac{2}{\pi}}\sqrt{\tfrac{1}{2^2\,2!}}\tfrac{1}{w(z)}e^{-\frac{x^2+y^2}{q(z)}}e^{3\Delta\psi(z)}\mathbb{H}_2\left(\tfrac{\sqrt{2}x}{w(z)}\right) = \mathbf{HG}_{20}(x,y) \tag{II.127}$$
$$\sqrt{\tfrac{2}{\pi}}\sqrt{\tfrac{1}{2^2\,2!}}\tfrac{1}{w(z)}e^{-\frac{x^2+y^2}{q(z)}}e^{3\Delta\psi(z)}\mathbb{H}_2\left(\tfrac{\sqrt{2}y}{w(z)}\right) = \mathbf{HG}_{02}(x,y) \tag{II.128}$$

while the last one corresponds to an Hermite-Gauss, $\mathbf{HG}_{11}(x,y)$:

$$\sqrt{\tfrac{2}{\pi}}\sqrt{\tfrac{1}{2^2\,2!}}\tfrac{1}{w(z)}e^{-\frac{x^2+y^2}{q(z)}}e^{i3\Delta\psi(z)}\mathbb{H}_1\left(\tfrac{\sqrt{2}y}{w(z)}\right)\mathbb{H}_1\left(\tfrac{\sqrt{2}x}{w(z)}\right) =$$
$$\sqrt{\tfrac{1}{2}}\left[\sqrt[4]{\tfrac{2}{\pi}}\sqrt{\tfrac{1}{2w(z)}}e^{-\frac{x^2}{q(z)}}e^{i\frac{3}{2}\Delta\psi(z)}\mathbb{H}_1\left(\tfrac{\sqrt{2}y}{w(z)}\right)\right]\cdot\left[\sqrt[4]{\tfrac{2}{\pi}}\sqrt{\tfrac{1}{2w(z)}}e^{-\frac{y^2}{q(z)}}e^{i\frac{3}{2}\Delta\psi(z)}\mathbb{H}_1\left(\tfrac{\sqrt{2}y}{w(z)}\right)\right] =$$
$$\sqrt{\frac{1}{2}}u_1(x,z|q_c)\cdot u_1(y,z|q_c) = \sqrt{\frac{1}{2}}\mathbf{HG}_{11}(x,y) \quad \text{(II.129)}$$

In conclusion, the rotation of the reference system transforms the Transverse Modes as

$$\mathbf{HG}_{20}(\tilde{x},\tilde{y}) = \mathbf{HG}_{20}(x,y)\cos^2\theta + \mathbf{HG}_{02}(x,y)\sin^2\theta - \sqrt{2}\mathbf{HG}_{11}(x,y)\cos\theta\sin\theta \quad \text{(II.130)}$$

$$\mathbf{HG}_{02}(\tilde{x},\tilde{y}) = \mathbf{HG}_{20}(x,y)\sin^2\theta + \mathbf{HG}_{02}(x,y)\cos^2\theta + \sqrt{2}\mathbf{HG}_{11}(x,y)\cos\theta\sin\theta \quad \text{(II.131)}$$

Combining all these results, we obtain the expansion of a Simple Astigmatic Gaussian beam using an arbitrary reference system for the Astigmatic axis:

$$\Psi_{in} = \mathbf{U_{00}}(x,y|q_c) + \delta\epsilon\cdot\left[\frac{\mathbf{HG}_{20}(x,y|q_c)-\mathbf{HG}_{02}(x,y|q_c)}{\sqrt{2}}\cos 2\theta - \mathbf{HG}_{11}(x,y|q_c)\sin 2\theta\right] + \langle\epsilon\rangle\cdot\frac{\mathbf{HG}_{20}(x,y|q_c)+\mathbf{HG}_{02}(x,y|q_c)}{\sqrt{2}} \quad \text{(II.132)}$$

where we can see that the change in reference system $(\tilde{x},\tilde{y}) \to (x,y)$ generates a third high order mode, $\mathbb{HG}_{11}$ which carries the information on the ellipse orientation, θ.

Connection to the standard representation

The linear combination of the Hermite-Gauss mode $\mathbf{HG}_{02}(x,y)$ and $\mathbf{HG}_{20}(x,y)$ is commonly described using a different set of solutions of the paraxial wave equation. The spherical mismatch represented by the $\langle\epsilon\rangle$, is naturally formalised using the cylindrical coordinates that lead to Laguerre-Gauss modes. These two families of Transverse mode are connected to each other by unique conversion rules[29], which leads to

$$\frac{\mathbf{HG}_{20}(x,y|q_c)+\mathbf{HG}_{02}(x,y|q_c)}{\sqrt{2}} = \mathbf{LG}_{01}(x,y|q_c) \quad \text{(II.133)}$$

where $\mathbf{LG}_{01}$ is a Laguerre Gauss mode 01:

$$\mathbf{LG}_{01}(x,y|q_c) = \sqrt{\tfrac{2}{\pi}}\frac{e^{i3\delta\psi(z)}}{w(z)}\mathbb{L}_1^0\left(\tfrac{2(x^2+y^2)}{w^2(z)}\right)\exp\left[-\tfrac{(x^2+y^2)}{w(z)} - i\tfrac{(x^2+y^2)}{2R(z)}\right] \quad \text{(II.134)}$$

that is shaped by the Laguerre Polynomial $\mathbb{L}_m^l$. This conversion can be visualised in Fig. II.5 where we can notice how the constructive interference between the two Hermite Gauss modes presents the same circular symmetry of the Laguerre-Gauss Mode.

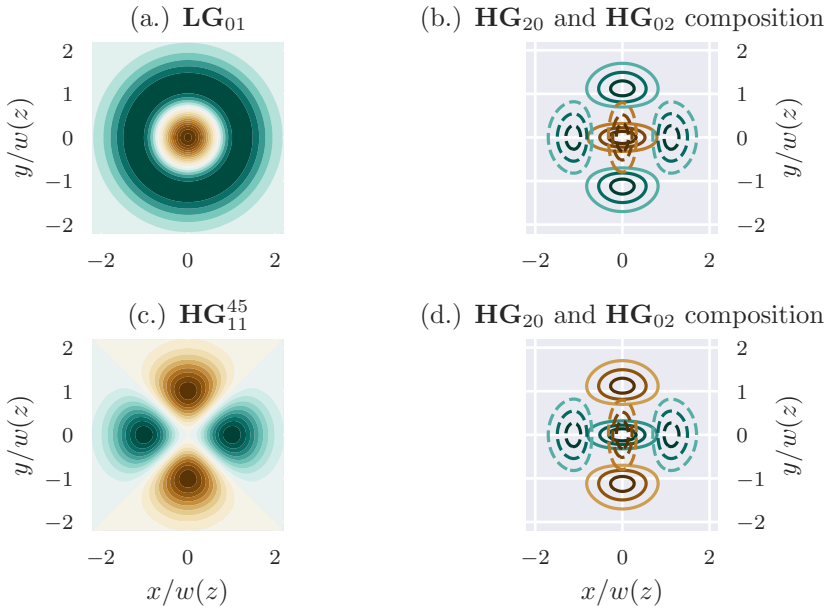

FIGURE II.5: Composition of $\mathbf{HG}_{20}$ and $\mathbf{HG}_{02}$. Left we can see the amplitude profiles of an $\mathbf{LG}_{01}$(a.) and $\mathbf{HG}^{45}_{11}$(c.). On the right, we have their decomposition into the two Hermite-Gauss modes.

On the other hand, the astigmatic mismatch, represented by $\delta\epsilon$, can be described using only the Hermite-Gauss mode 11. Following the same calculation done in Eq. II.126, we obtain:

$$\frac{\mathbf{HG}_{20}(x,y|q_c) - \mathbf{HG}_{02}(x,y|q_c)}{\sqrt{2}} = \mathbf{HG}_{11}\left(\frac{x-y}{\sqrt{2}}, \frac{x+y}{\sqrt{2}}|q_c\right) = \mathbf{HG}^{45}_{11}(x,y|q_c) \quad \text{(II.135)}$$

that is equivalent to representing the difference between the two Hermite-Gauss modes $\mathbf{HG}_{02}(x,y)$ and $\mathbf{HG}_{20}(x,y)$ as a Hermite-Gauss Mode 11 rotated by 45°, $\mathbf{HG}^{45}_{11}$. This conversion is visualised in Fig. II.5, where we can see that the two modes have a destructive interference in the centre and along the diagonals.

Using these two conversion rules, it is possible to represent the Mismatch in a more elegant way

$$\Psi_{in} = \mathbf{U_{00}}(z,x,y|q_c) + \\ \delta\epsilon \cdot \left[\mathbf{HG}^{45}_{11}(x,y|q_c)\cos 2\theta - \mathbf{HG}_{11}(x,y|q_c)\sin 2\theta\right] + \langle\epsilon\rangle \cdot \mathbf{LG}_{01} \quad \text{(II.136)}$$

This result is limited to a Simple Astigmatic Gaussian Beam in which the ellipse of constant phase and the ellipse of constant intensity are always orthogonal to each

other[30]. In particular, this expansion defines four different parameter

$$\begin{gathered}
\beta = \frac{\langle w_0 \rangle_{(\tilde{x},\tilde{y})} - \hat{w}_0}{\hat{w}_0} \quad \text{with} \quad \langle w_0 \rangle = \frac{w_0^{(\tilde{x})} + w_0^{(\tilde{y})}}{2} \\
\gamma = \frac{\langle z_0 \rangle_{(\tilde{x},\tilde{y})} - \hat{z}_0}{2\hat{z}_R} \quad \text{with} \quad \langle z_0 \rangle_{(\tilde{x},\tilde{y})} = \frac{z_0^{(\tilde{x})} + z_0^{(\tilde{y})}}{2} \\
\alpha = \frac{w_0^{(\tilde{x})} - w_0^{(\tilde{y})}}{2\hat{w}_0} \\
\eta = \frac{z_0^{(\tilde{x})} - z_0^{(\tilde{y})}}{4\hat{z}_R} \\
\langle \epsilon \rangle = \beta + i\gamma \quad \text{and} \quad \delta\epsilon = \alpha + i\eta
\end{gathered} \tag{II.137}$$

that, together with the ellipse angle θ, fully define the simple astigmatic mismatch.

III | ASTIGMATIC MODE MISMATCH SENSING

III.1 Theoretical Model 45
III.1.1 Heterodyne detection 46
III.1.2 Spherical mismatch and Mode Converter Technique 48
III.1.3 Mode Converter Robustness to Astigmatic Aberrations 53
III.1.4 Astigmatic Mismatch Error Signal 54
III.1.5 Signal Demodulation 55
III.2 Experimental Limits 57
III.2.1 Installation of Mode Converter Telescope 58
III.2.2 Partial conversion of the Hermite Gauss Mode 62
III.2.3 Unbalanced Signal Reconstruction 63

This Chapter contains the core of this thesis. Starting from the results of the previus chapter, I present a wavefront sensing technique that can characterise the mismatch between a Simple Astigmatic Gaussian Beam and a linear cavity. This method is an upgrade of the Mode Converter Telescope technique proposted by Magaña-Sandoval, Vo, Vander-Hyde, *et al.*[2] and it is based on the detection of the second order mode aplitude which carrier the mismatch information.

Here, I first present how we can extract a signal propoportional to the Astigmatic Mismatch parameter and after I will discuss some of the technical limitation of this new method.

III.1. Theoretical Model

From Eq. II.136, we know that the Astigmatic Mismatch parameters are encoded in the amplitude of the second order modes $\mathbf{LG}_{10}$, $\mathbf{HG}_{11}$, and $\mathbf{HG}^{45}_{11}$. We can measure this amplitude using a Heterodyne detection based on a special split photodiode. This approach was first demonstrated by Mueller, Shu, Adhikari, *et al.* [31] and technically improved in the Mode Conversion Technique proposed by Magaña-Sandoval, Vo, Vander-Hyde, *et al.*[2]. However, both methods were designed to detect the Laguerre-Gauss 10 mode amplitude, and they can only measure the variation of the spherical mismatch. This limitation can be overcome by a small change in the detector setup that allows characterizing two Hermite-Gauss modes, $\mathbf{HG}_{11}$ and $\mathbf{HG}^{45}_{11}$ and measuring the astigmatic mismatch parameters. This upgrade works around the Mode Conversion Technique, so we will first describe this method, and after we present our proposal.

III.1.1. *Heterodyne detection*

All the techniques mentioned before, such as the one proposed here, are based on Heterodyne detection. This method exploits the beat note generated by two fields with different frequencies to measure the product of their amplitudes. The detection scheme is divided into two parts: in the first one, we superimpose the signal field $E_s = A_s \exp(i\omega t)$ and the reference one, $E_{LO} = A_{LO} \exp(i(\omega + \Omega)t)$, generally called Local Oscillator. We measure the interference between these two beams with a photodiode and record a signal, S, proportional to the total power:

$$S \propto |E_s + E_{LO}|^2 = |A_s|^2 + |A_{LO}|^2 + \left(A_s \overline{A_{LO}} e^{-i\Omega t} + A_{LO} \overline{A_s} e^{i\Omega t}\right) \tag{III.1}$$

In the second part, we demodulate the signal generated by the photodiode by mixing it with an electronic oscillator $S_{LO} = V_{LO} e^{-i(\Omega t + \phi_0)}$:

$$\begin{aligned} S_{mix} &= \left[|A_s|^2 + |A_{LO}|^2 + \left(A_s \overline{A_{LO}} e^{-i\Omega t} + A_{LO} \overline{A_s} e^{i\Omega t}\right)\right] \cdot V_{LO} e^{-i\Omega + \phi_0} \\ &= (|A_s|^2 + |A_{LO}|^2) V_{LO} e^{-i(\Omega t + \phi_0)} + V_{LO} A_s \overline{A_{LO}} e^{-i2\Omega t + \phi_0} + V_{LO} A_{LO} \overline{A_s} e^{i\phi_0} \end{aligned} \tag{III.2}$$

and extracting the low-frequency component with a Low Pass filter:

$$S_{dem} = \cancel{(|A_s|^2 + |A_{LO}|^2) V_{LO} e^{-i(\Omega t + \phi_0)}} + \cancel{A_s \overline{A_{LO}} V_{LO} e^{-i2\Omega t + \phi_0}} + A_{LO} \overline{A_s} V_{LO} e^{i\phi_0} \tag{III.3}$$

The measured signal is given by the Real part of S_{dem}:

$$\Re[S_{dem}] = V_{LO} \left(\Re\left[A_s \overline{A_{LO}}\right] \cos(\phi_0) + \Im\left[A_s \overline{A_{LO}}\right] \sin(\phi_0)\right) \tag{III.4}$$

where the local oscillator phase ϕ_0, is generally called demodulation phase. If we assume that A_{LO} is Real, we can estimate the complex amplitude A_s by measuring the demodulated signal, S_{dem}, at ϕ =0° and ϕ = 90°.

We can implement the same scheme to characterize the amplitude of Transverse Modes reflected by the cavity. In this case, the local oscillator is generated by phase modulation of the main optical beam. This process creates two sidebands that travel together with the original beam:

$$\Psi_{in} = \hat{U}(x, y, z) \left(e^{i\omega t} + \tfrac{m}{2} e^{i(\omega + \Omega t)} - \tfrac{m}{2} e^{i(\omega - \Omega t)}\right) \tag{III.5}$$

where m and Ω are, respectively, the modulation depth and the frequency of the oscillator, while $\hat{U}(x, y, z)$ is the amplitude profile of the beam.

In order to detect the mismatch parameters, we need to force the decomposition of the beam amplitude, $\hat{U}(x, y, z)$, into the cavity Transverse Modes described in Eq. II.136. This is naturally done by the cavity reflectance that decomposes the incoming beam into the cavity mode and re-scales each component with the corresponding value defined in Eq. II.86:

$$F_N(\omega) = r_{\text{cav}}(f, N) = \frac{r_1 - (1 - \rho_1) r_2 \, e^{i\,\nu(f,N)}}{1 - r_1 r_2 \, e^{i\,\nu(\frac{\omega}{\pi},N)}}, \tag{III.6}$$

where we consider the definition of $\nu(f, N)$ given in Eq. II.85 and $\omega = 2\pi f$. In particular, the amplitude of the reflected beam is described by:

$$\begin{aligned} \Psi_{ref} =& \hat{U}_0 \left(F_0(\omega) e^{i\omega t} + F_0(\omega + \Omega) \tfrac{m}{2} e^{i(\omega + \Omega t)} - F_0(\omega - \Omega) \tfrac{m}{2} e^{i(\omega - \Omega t)}\right) + \\ & \hat{U}_2(\delta\epsilon, \langle\epsilon\rangle, \theta) \left(F_2(\omega) e^{i\omega t} + F_2(\omega + \Omega) \tfrac{m}{2} e^{i(\omega + \Omega t)} - F_2(\omega - \Omega) \tfrac{m}{2} e^{i(\omega - \Omega t)}\right) \end{aligned} \tag{III.7}$$

where $\hat{U}_0$ is the fundamental mode of the cavity, and $\hat{U}_2(\delta\epsilon, \langle\epsilon\rangle, \theta)$ collects all the second order contribution defined in Eq. II.136:

$$\hat{U}_2(\delta\epsilon, \langle\epsilon\rangle, \theta) = \delta\epsilon \cdot \left[\mathbf{HG}_{11}^{45} \cos 2\theta - \mathbf{HG}_{11} \sin 2\theta\right] + \langle\epsilon\rangle \cdot \mathbf{LG}_{10} \tag{III.8}$$

Once we have the Mode decomposition, the Heterodyne scheme requires to detect of the interference between the signal and the local oscillator. This information is contained in the power profile of the reflected beam defined by

$$\begin{aligned} P_{ref}(x,y,z) =& |\hat{U}_0(x,y,z)|^2 \left(F_0^0 + F_0^+ e^{+i\Omega t} - F_0^- e^{-i\Omega t}\right) \overline{\left(F_0^0 + F_0^+ e^{+i\Omega t} - F_0^- e^{-i\Omega t}\right)} + \\ & |\hat{U}_2(x,y,z)|^2 \left(F_2^0 + F_2^+ e^{+i\Omega t} - F_2^- e^{-i\Omega t}\right) \overline{\left(F_2^0 + F_2^+ e^{+i\Omega t} - F_2^- e^{-i\Omega t}\right)} + \\ & \left[\hat{U}_0 \overline{\hat{U}_2}(x,y,z) \left(F_0^0 + F_0^+ e^{+i\Omega t} - F_0^- e^{-i\Omega t}\right) \overline{\left(F_2^0 + F_2^+ e^{+i\Omega t} - F_2^- e^{-i\Omega t}\right)} + \text{c.c.}\right] \end{aligned} \tag{III.9}$$

where we contract the notation using:

$$F_i^0 = F_i(\omega) \quad \text{and} \quad F_i^\pm = \frac{m}{2} F_i(\omega \pm \Omega) \tag{III.10}$$

The power profile in Eq. III.9 is divided into three components, one for each line. The first line is proportional to the power of the fundamental mode, $|\hat{U}_0(x,y,z)|^2$ and corresponds to the Pound–Drever–Hall[32] signal of the Fundamental Mode; the second line is proportional to the power of the second-order modes and contains the mismatch magnitude:

$$\begin{aligned} \left|\hat{U}_2(x,y,z)\right|^2 = |\delta\epsilon|^2 \left(\left|\mathbf{HG}_{11}^{45}\right|^2 \cos^2(2\theta) + |\mathbf{HG}_{11}|^2 \sin^2(2\theta)\right) + |\langle\epsilon\rangle|^2 |\mathbf{LG}_{10}|^2 + \\ - \left[|\delta\epsilon|^2 \mathbf{HG}_{11}^{45} \overline{\mathbf{HG}}_{11} \cos(2\theta)\sin(2\theta) + \text{c.c.}\right] + \\ + \left[\delta\epsilon \overline{\langle\epsilon\rangle} \left(\mathbf{HG}_{11}^{45} \overline{\mathbf{LG}}_{10} \cos(2\theta) - \mathbf{HG}_{11} \overline{\mathbf{LG}}_{10} \sin(2\theta)\right) + \text{c.c.}\right] \end{aligned} \tag{III.11}$$

while the third line is proportional to the beats between the second-order modes and the fundamental oneand it carries the complex information of $\langle\epsilon\rangle$ and $\delta\epsilon$:

$$\hat{U}_0 \overline{\hat{U}_2} = \overline{\delta\epsilon} \cdot \left[\hat{U}_0 \overline{\mathbf{HG}}_{11}^{45} \cos 2\theta - \hat{U}_0 \overline{\mathbf{HG}}_{11} \sin 2\theta\right] + \overline{\langle\epsilon\rangle} \cdot \hat{U}_0 \overline{\mathbf{LG}}_{10} \tag{III.12}$$

All these components are summed together and we need to separate them in order to extract only the mismatched parameters. This can be done by exploiting the characteristic of the power profiles that compose Eq. III.9. In particular, we have ten different profiles:

$$|\mathbf{HG}_{00}|^2, \quad \left|\mathbf{HG}_{11}^{45}\right|^2, \quad |\mathbf{HG}_{11}|^2, \quad |\mathbf{LG}_{10}|^2 \tag{III.13}$$

$$\mathbf{HG}_{11}^{45} \overline{\mathbf{HG}}_{11}, \quad \mathbf{HG}_{11}^{45} \overline{\mathbf{LG}}_{10}, \quad \mathbf{HG}_{11} \overline{\mathbf{LG}}_{10} \tag{III.14}$$

$$\mathbf{HG}_{00} \overline{\mathbf{HG}}_{11}^{45}, \quad \mathbf{HG}_{00} \overline{\mathbf{HG}}_{11}, \quad \mathbf{HG}_{00} \overline{\mathbf{LG}}_{10} \tag{III.15}$$

among which we can distinguish three groups: in Eq. III.13 we collected the Transverse mode power profiles, in Eq. III.14 the beat-note between second-order modes, and in Eq. III.15 the beat-note between different second order and fundamental modes.

These groups can be separated using the structures of the profile amplitude. The first group is always positive, while each element of the second and third groups changes the sign as a function of the Transverse Mode polynomial, Hermite for the $\mathbf{HG}_{ij}$ and Laguerre for $\mathbf{LG}_{ij}$. These features can be exploited by using split photodiodes. These devices are composed of multiple sensors and we can optimise their shapes to match the power profile of interest. After that, we can recombine each sensor signal and discriminate the single beat-note contribution.

III.1.2. *Spherical mismatch and Mode Converter Technique*

The first step towards Astigmatic Mismatch Sensing is the Mode Converter Technique. This method was designed only for the spherical mismatch and it is not sensitive to astigmatic aberrations. In this case, we need to focus the analysis only on the transverse mode proportional to $\langle \epsilon \rangle$ in Eq. II.136, and put $\delta\epsilon = 0$:

$$\hat{U}_2^{\text{spher.}} \propto \frac{u_{02}(q_c) + u_{20}(q_c)}{\sqrt{2}} = \text{LG}_{01}(q_c) \tag{III.16}$$

This approach was tested by Mueller, Shu, Adhikari, *et al.* et all.[31], who designed a split photodiode following the shape of the $\mathbf{HG}_{00}\overline{\mathbf{LG}}_{10}$, Fig. III.1.However, this profile shape requires special care in the sensor design and it strongly limits the implementation of wavefront sensing.

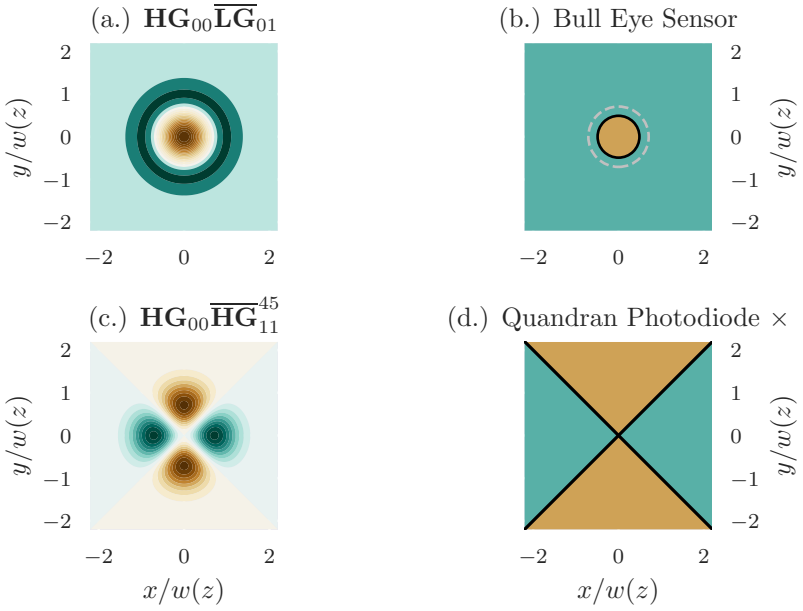

FIGURE III.1: The beat-note between a $\mathbf{LG}_{10}$ and a $\mathbf{U}_{00}$ (a) is defined by the $\mathbf{LG}_{10}$ mode. We can identify the two areas with opposite signs that suggest the sensor division (b) in two annular areas. The beat-note between a $\mathbf{HG}_{11}^{45}$ and a $\mathbf{U}_{00}$ (c) is defined by the $\mathbf{HG}_{11}^{45}$ mode. We can identify the four areas with opposite signs that suggest the sensor division (d) in four sub-sensors A_i defined in Eq. III.34.

This issue was resolved by Magaña-Sandoval, Vo, Vander-Hyde, *et al.* in their work[2]. They implemented a Mode Converter Telescope in order to manipulate the phase between $\mathbf{HG}_{02}$ and $\mathbf{HG}_{20}$ and to convert the Laguerre-Gauss into a Hermite-Gauss one

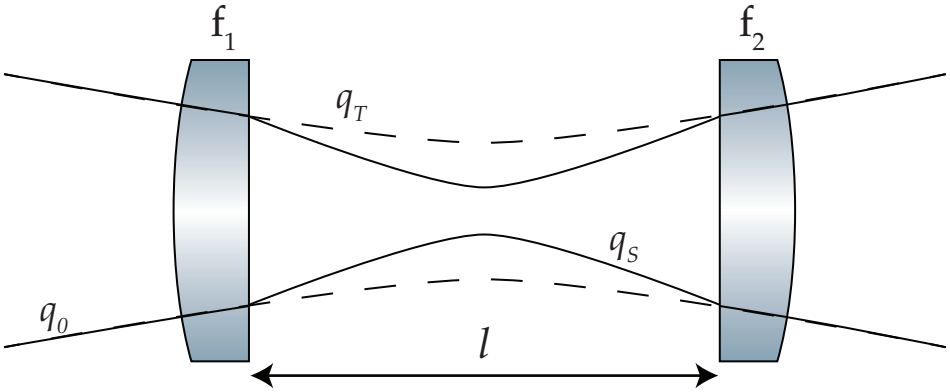

FIGURE III.2: Mode Convert Telescope. A Mode Converter Telescope is a telescope composed of two cylindrical lenses. The first one is used to change the beam shape along one plane and accelerate the Gouy phase evolution with respect to the other plane. The second lens is used to recover a circular symmetry on the beam profile. In this way, the Gouy phase stops evolving separately along the two planes. By using the difference in Gouy phase accumulated along the two planes, it is possible to convert the $\mathbf{HG}_{11}^{45}$ into a $\mathbf{LG}_{10}$.

rotated by 45°, $\mathbf{HG}_{11}^{45}$. The amplitude profile of this mode, represented in Figure III.1, shows a distribution with a perfect planar symmetry which simplifies the sensor design. This shape is easier to reproduce in the detector, and it does not have any requirement imposed by the beam shape.

Mode Converter Telescope

The conversion between the Laguerre-Gauss mode and the 45° rotated Hermite-Gauss 11, requires two steps. First, the initial beam shape has to be decomposed into two Hermite Gauss modes $\mathbf{HG}_{02}$ and $\mathbf{HG}_{20}$. Second, we need to add a phase shift of π between them. We can obtain this effect with an astigmatic telescope composed of two cylindrical lenses aligned one to the other.

The astigmatic nature of the telescope breaks the cylindrical symmetry of the optical setup and defines a specific reference system. For simplicity, we will assume that the lenses are aligned with the Sagittal plane of the optical setup. The first lens reduces the Rayleigh Range, $z_{R,s}$, along the Sagittal plane and accelerates the evolution of the Gouy phase; The second one rematches the beam shape along the Sagittal plane with the Transverse one and freezes the evolution of the phase difference.

This diffraction evolution can be represented by two separated $\mathbb{ABCD}$ matrices:

$$J_S = \begin{pmatrix} 1-\frac{l}{f_1} & l \\ \frac{l-f_1-f_2}{f_1 f_2} & 1-\frac{l}{f_2} \end{pmatrix} \quad \text{and} \quad J_T = \begin{pmatrix} 1 & l \\ 0 & 1 \end{pmatrix} \tag{III.17}$$

and its action can be formalised using the Collins's rules introduced in Eq. II.62. If we focus the analysis on the Hermite-Gauss modes $\mathbf{HG}_{02}$ and $\mathbf{HG}_{20}$, we have that:

$$\begin{aligned} \mathbf{HG}_{02}(x,y,q_0) &\rightarrow \mathbf{HG}_{02}(x,y|q_T,q_S)e^{i\Delta\psi_{0,2}} \\ \mathbf{HG}_{20}(x,y,q_0) &\rightarrow \mathbf{HG}_{20}(x,y|q_T,q_S)e^{i\Delta\psi_{2,0}} \end{aligned} \tag{III.18}$$

where the extra Gouy phase induced by the telescope is:

$$\Delta\psi_{n_T,n_S} = (n_T + \tfrac{1}{2})\psi_T + (n_S + \tfrac{1}{2})\psi_S \quad \text{with} \quad \psi_i = \text{Arg}[C_i q_0 + D_i] \tag{III.19}$$

and it depends directly on the order mode along the two planes, n_S and n_T.

This discrepancy is the core of the mode conversion, inasmuch it allows to act separately on the two modes and to change their relative phase. In particular, the telescope should satisfy two requirements: first, the difference between the Gouy phase accumulated by two modes should fulfil the conversion requirement:

$$\Delta\psi_{0,2} - \Delta\psi_{2,0} = -2\,(\psi_T - \psi_S) = \pi \tag{III.20}$$

Second, after the beam evolution after the Mode Converter, the beam should not be astigmatic, $q_T = q_S$ otherwise, the difference in Gouy Phase $\Delta\psi_{0,2} - \Delta\psi_{2,0}$ will continue to change. The first requirement given by Eq. III.20 is equivalent to impose

$$\text{Arg}\,[C_S\, q_0 + D_S] = \frac{\pi}{2} \tag{III.21}$$

while the second one is equivalent to $q_T = q_S$, and it can be estimated using the ABCD rule:

$$q_S = \frac{A_S q_0 + B_S}{C_S q_0 + D_S} = q_0 + B_T = q_T \tag{III.22}$$

The combination of Eq. III.20 and Eq. III.22 leads to

$$\begin{gathered} l = 1 + f_1 \frac{\Delta z}{z_R} \qquad f_2 = \frac{f_1 \Delta z + z_R}{f_1 + z_R} \\ \Delta z = z - z_0 \end{gathered} \tag{III.23}$$

which are the minimum requirements for the Mode Converter Telescope design. On top of these requests, we impose $f = f_1 = f_2$ to simplify the construction: the focal length becomes the only free parameter and it defines the beam shape and the lenses position

$$\begin{aligned} w_0^{(MCT)} &= \sqrt{\left(1 + \frac{1}{\sqrt{2}}\right)\frac{\lambda f}{\pi}} \\ z - z_0^{(MCT)} &= \frac{l}{2} \quad l = \sqrt{2} f \end{aligned} \tag{III.24}$$

Once the conditions for the Mode Conversion are met, the amplitude of the beam that passes across the telescope should be decomposed in the Hermite-Gauss modes aligned as the Cylindrical lens axis and with a waist of $w_0^{(MCT)}$ at the position $z_0^{(MCT)}$. In case of the Laguerre-Gauss mode, $\mathbf{LG}_{01}$, we have to consider the decomposition defined in Eq. II.133:

$$\mathbf{LG}_{01} = \frac{\mathbf{HG}_{20}(x, y|q_c) + \mathbf{HG}_{02}(x, y|q_c)}{\sqrt{2}} \tag{III.25}$$

and propagate the two modes separately

$$\begin{aligned} \mathbf{LG}_{01} = e^{i\Delta\psi_{2,0}} \frac{\mathbf{HG}_{20}(x, y|q_c) + e^{i(\Delta\psi_{0,2} - \Delta\psi_{2,0})}\mathbf{HG}_{02}(x, y|q_c)}{\sqrt{2}} = \\ e^{i\Delta\psi_{2,0}} \frac{\mathbf{HG}_{20}(x, y|q_c) - \mathbf{HG}_{02}(x, y|q_c)}{\sqrt{2}} = \mathbf{HG}_{11}^{45} e^{i\Delta\psi_{2,0}} \end{aligned} \tag{III.26}$$

Same approach should be followed fro the $\mathbf{HG}_{11}^{45}$, which is converted back to a Laguerre-Gauss mode:

$$\mathbf{HG}_{11}^{45} = e^{i\Delta\psi_{2,0}} \frac{\mathbf{HG}_{20}(x,y|q_c) - e^{i(\Delta\psi_{0,2}-\Delta\psi_{2,0})}\mathbf{HG}_{02}(x,y|q_c)}{\sqrt{2}} = e^{i\Delta\psi_{2,0}} \frac{\mathbf{HG}_{20}(x,y|q_c) + \mathbf{HG}_{02}(x,y|q_c)}{\sqrt{2}} = \mathbf{LG}_{01} e^{i\Delta\psi_{2,0}} \quad \text{(III.27)}$$

The Transverse modes with are already represented in the Hermite-Gauss base aligned with respect to the cylindrical lens axis are not decomposed by the telescope; therefore, they do not change their shape. In particular, the conversion rules for the Transverse mode of interest for this thesis are:

$$U_{00} \rightarrow U_{00} \quad \text{(III.28)}$$
$$\mathbf{HG}_{11} \rightarrow \mathbf{HG}_{11} \quad \text{(III.29)}$$
$$\mathbf{LG}_{01} \rightarrow \mathbf{HG}_{11}^{45} \quad \text{(III.30)}$$
$$\mathbf{HG}_{11}^{45} \rightarrow \mathbf{LG}_{01} \quad \text{(III.31)}$$

Spherical mismatch error signal

When the beam reflected by the cavity passes through the Mode Converter Telescope, each component is converted using Eq. [III.28, III.29,III.30, III.31]. In this case, the power profile becomes that reaches the sensors becomes:

$$\begin{aligned} P_{ref}^{conv}(x,y,z) =& |\hat{U}_0(x,y,z)|^2 \left(F_0^0 + F_0^+ e^{+i\Omega t} - F_0^- e^{-i\Omega t}\right) \overline{\left(F_0^0 + F_0^+ e^{+i\Omega t} - F_0^- e^{-i\Omega t}\right)} + \\ & |\hat{U}_2^{conv}(x,y,z)|^2 \left(F_2^0 + F_2^+ e^{+i\Omega t} - F_2^- e^{-i\Omega t}\right) \overline{\left(F_2^0 + F_2^+ e^{+i\Omega t} - F_2^- e^{-i\Omega t}\right)} + \\ & \left[\hat{U}_0 \overline{\hat{U}_2}^{conv}(x,y,z) \left(F_0^0 + F_0^+ e^{+i\Omega t} - F_0^- e^{-i\Omega t}\right) \overline{\left(F_2^0 + F_2^+ e^{+i\Omega t} - F_2^- e^{-i\Omega t}\right)} + \text{c.c.}\right] \end{aligned} \quad \text{(III.32)}$$

where the second order modes $\hat{U}_2^{conv}$ are now:

$$\hat{U}_2^{conv}(\delta\epsilon, \langle\epsilon\rangle, \theta) = \delta\epsilon \cdot \left[\mathbf{LG}_{10}\cos 2\theta - \mathbf{HG}_{11}(x',y'|q_c)\sin 2\theta\right] + \langle\epsilon\rangle \cdot \mathbf{HG}_{11}^{45} \quad \text{(III.33)}$$

As we introduced before, the Mode converter Technique is designed for Spherical Mismatch, $\langle\epsilon\rangle$, so we need to focus on the detection of the new corresponding mode, $\mathbf{HG}_{11}^{45}$. Its amplitude profile presents a planar symmetry, and we can divide its wavefront into four different areas as reported in Fig. III.1-d:

$$\begin{aligned} A_1 = \{y > |x|\}, \quad A_2 = \{x < -|y|\}, \quad \text{Orange area} \\ A_3 = \{y < -|x|\}, \quad A_4 = \{x > |y|\} \quad \text{Green area} \end{aligned} \quad \text{(III.34)}$$

with different sign of the the beat-note $\hat{U}_0\overline{\mathbf{HG}}_{10}^{45}$: in areas A_1 and A_3, it is positive, while in the other two, A_2 and A_4, it is negative. This pattern suggests the shape of the wavefront sensor: we can use four square photodiodes as in Fig. III.1 and measure the optical power of each area. After that, we will recombine the signal generated in order to extract only the mismatch signal.

Each photodiode integrates the power profile over its corresponding region, A_i, and generates a signal proportional to

$$S_i = |F_0| \int_{A_i} |\hat{U}_0(x,y,z)|^2 dxy + |F_2| \int_{A_i} |\hat{U}_2^{conv}(x,y,z)|^2 dxy + \left(F_0 \overline{F_2} \int_{A_i} \hat{U}_0 \overline{\hat{U}_2^{conv}}(x,y,z) dxy + \text{c.c.} \right) \quad \text{(III.35)}$$

where we collect the reflectance factors, F_i. In particular, we need to expand the contribution of the second-order modes and consider each profile collected in Eq.[III.13,. . . ,III.15] that corresponds to ten different integrals for each sensor.

In this section, we focused the analysis only on the spherical mismatch so that we can consider $\delta\epsilon = 0$ and study only three contributions of Eq. III.35:

$$\int_{A_i} |\hat{U}_0(x,y,z)|^2 dxy = \int_{A_i} |\mathbf{U}_{00}(x,y,z)|^2 dxy \quad \text{(III.36)}$$

$$\int_{A_i} |\hat{U}_2^{conv}(x,y,z)|^2 dxy = |\langle\epsilon\rangle|^2 \int_{A_i} |\mathbf{HG}_{11}^{45}(x,y,z)|^2 dxy \quad \text{(III.37)}$$

$$\int_{A_i} \hat{U}_0 \overline{\hat{U}_2^{conv}}(x,y,z) dxy = \overline{\langle\epsilon\rangle} \int_{A_i} \mathbf{U}_{00} \overline{\mathbf{HG}_{11}^{45}}(x,y,z) dxy \quad \text{(III.38)}$$

and simplify the calculation using the definition of A_i. In particular, we can rotate the reference system in order to align these areas with the Cartesian quadrant:

$$\begin{aligned} x \to x' &= \frac{x+y}{\sqrt{2}} \\ y \to y' &= \frac{-x+y}{\sqrt{2}} \end{aligned} \quad \text{(III.39)}$$

and we can consider the relationship among the areas of the detector:

$$\left\{ \begin{matrix} A_1 \to A_2 \\ (x',y') \to (-x',y') \end{matrix} \right\} \quad \left\{ \begin{matrix} A_1 \to A_3 \\ (x',y') \to (-x',-y') \end{matrix} \right\} \quad \left\{ \begin{matrix} A_1 \to A_4 \\ (x',y') \to (x',-y') \end{matrix} \right\} \quad \text{(III.40)}$$

The Foundamental mode $\mathbf{U}_{00}$ is completely symmetric under the transformation defined in Eq. III.40:

$$\mathbf{U}_0(\pm x', \mp y') = \mathbf{U}_0(\mp x', \pm y') = \mathbf{U}_0(x', y') \quad \text{(III.41)}$$

while $\mathbf{HG}_{11}$, is even between A_1 and A_3 and between A_2 and A_4, and odd in the other cases:

$$\begin{aligned} \mathbf{HG}_{11}^{45}(\pm x', \mp y') &= -\mathbf{HG}_{11}^{45}(x', y') \\ \mathbf{HG}_{11}^{45}(\pm x', \pm y') &= \mathbf{HG}_{11}^{45}(x', y') \end{aligned} \quad \text{(III.42)}$$

If we combine these symmetry rules, we obtain that $|\mathbf{U}_{00}|^2$ and $|\mathbf{HG}_{11}^{45}|^2$ are symmetric on each sensor areas and we can write that

$$\int_{\mathbb{R}^2} |\mathbf{U}_{00}(x,y,z)|^2 dxy = 4 \int_{A_1} |\mathbf{U}_{00}(x,y,z)|^2 dxy = 1 \quad \text{(III.43)}$$

$$\int_{\mathbb{R}^2} |\mathbf{HG}_{11}^{45}(x,y,z)|^2 \, dxy = 4 \int_{A_1} |\mathbf{HG}_{11}^{45}(x,y,z)|^2 dxy = 1 \quad \text{(III.44)}$$

The last therm, $\mathbf{U}_{00}\overline{\mathbf{HG}^{45}_{11}}(x,y,z)$ follows the symmetry of the $\mathbf{HG}^{45}_{11}$ mode, so we can reduce the calculation of the beat-note to only one integral:

$$\int_{A_1}\mathbf{U}_{00}\overline{\mathbf{HG}^{45}_{11}}(x,y,z)dxy=\int_{A_3}\mathbf{U}_{00}\overline{\mathbf{HG}^{45}_{11}}(x,y,z)dxy=-\int_{A_{2,4}}\mathbf{U}_{00}\overline{\mathbf{HG}^{45}_{11}}(x,y,z)dxy \tag{III.45}$$

that can be evaluated in the area A_1. Moreover, we can use the change of coordinate defined in Eq. III.39 to write:

$$\int_{A_1}\mathbf{HG}_{00}\overline{\mathbf{HG}}^{45}_{11}(x,y,z)dxy=\iint_0^{+\infty}\mathbf{HG}_{00}\overline{\mathbf{HG}}_{11}(x',y',z)dx'dy' \tag{III.46}$$

that leads to the following results:

$$\int_{A_1}\mathbf{HG}_{00}\overline{\mathbf{HG}}^{45}_{11}(x,y,z)dxy= \frac{1}{\pi w^2(z)}e^{-i2\Delta\psi}\iint_0^{+\infty}\mathbb{H}_1\left[\frac{\sqrt{2}x'}{w(z)}\right]\mathbb{H}_1\left[\frac{\sqrt{2}y'}{w(z)}\right]e^{-2\frac{x'^2+y'^2}{w^2(z)}}dx'dy'=\frac{e^{-i2\Delta\psi}}{2\pi} \tag{III.47}$$

where the $\Delta\psi$ is the Gouy phase at the sensor position.

We can recombine the signal S_i in order to eliminate the contribution of the power profile, Eq. III.43 and Eq. III.47, and to maximise the mode matching signal, Eq. III.47. The optical combination is given by:

$$S_{M.M}=(S_1+S_3)-(S_2+S_4) \tag{III.48}$$

that results in

$$S_{MCT}=\frac{2\overline{\langle\epsilon\rangle}}{\pi}F_0\overline{F_2}e^{-i2\Delta\psi}+\text{c.c.} \tag{III.49}$$

III.1.3. *Mode Converter Robustness to Astigmatic Aberrations*

The first step toward Astigmatic Mismatch wavefront sensing is the validation of the Mode Converter Technique. In particular, the upgrade presented here works around this technique, so we need to verify if the results of Eq. III.49 are valid even if we assume $\delta\epsilon\neq 0$.

In this case, we need to consider all the contributions in Eq. III.33 and calculate the integral of each power profile listed in Eq. [III.13, III.14, III.15]. We can reduce the calculation by exploiting the properties of the power profiles. In particular, the new modes $\mathbf{LG}_{10}$ and $\mathbf{HG}_{11}$, follows the same symmetry described in Eq. III.41:

$$\begin{aligned}\mathbf{LG}_{01}(\pm x',\mp y')&=\mathbf{LG}_{01}(\mp x',\pm y')=\mathbf{LG}_{01}(x',y')\\ \mathbf{HG}_{11}(\pm x',\mp y')&=\mathbf{HG}_{11}(\mp x',\pm y')=\mathbf{HG}_{11}(x',y')\end{aligned} \tag{III.50}$$

and this symmetry is conserved in their beat-notes: $|\mathbf{HG}_{11}|^2$, $|\mathbf{LG}_{10}|^2$, $(\mathbf{HG}_{11}\overline{\mathbf{LG}}_{10})$, $(\mathbf{U}_{00}\overline{\mathbf{HG}}_{11})$, and $(\mathbf{U}_{00}\overline{\mathbf{LG}}_{10})$. The signals generated are equivalent for each area A_i, and they are eliminated in the recombination defined in Eq. III.48.

The reaming beat-notes $(\mathbf{HG}_{11}\overline{\mathbf{HG}}^{45}_{11})$ and $(\mathbf{LG}_{10}\overline{\mathbf{HG}}^{45}_{11})$ can be evaluated combining the symmetry of the $\mathbf{HG}^{45}_{11}$, described in Eq. III.42. Even in this case, we can reduce the calculation to only one integral for $(\mathbf{HG}_{11}\overline{\mathbf{HG}}^{45}_{11})$:

$$\int_{A_1}\mathbf{HG}_{11}\overline{\mathbf{HG}^{45}_{11}}(x,y,z)dxy=\int_{A_3}\mathbf{HG}_{11}\overline{\mathbf{HG}^{45}_{11}}(x,y,z)dxy=-\int_{A_{2,4}}\mathbf{HG}_{11}\overline{\mathbf{HG}^{45}_{11}}(x,y,z)dxy \tag{III.51}$$

and an other one for $(\mathbf{LG}_{10}\overline{\mathbf{HG}}_{11}^{45})$

$$\int_{A_1} \mathbf{LG}_{10}\overline{\mathbf{HG}_{11}^{45}}(x,y,z)dxy = \int_{A_3} \mathbf{LG}_{10}\overline{\mathbf{HG}_{11}^{45}}(x,y,z)dxy = -\int_{A_{2,4}} \mathbf{LG}_{10}\overline{\mathbf{HG}_{11}^{45}}(x,y,z)dxy \tag{III.52}$$

The first integral is resolved by using the odd symmetry of $\mathbf{HG}_{11}$:

$$\mathbf{HG}_{11}\overline{\mathbf{HG}_{11}^{45}}(x,y,z) = -\mathbf{HG}_{11}\overline{\mathbf{HG}_{11}^{45}}(-x,y,z) \tag{III.53}$$

and by splitting the area A_1 as

$$B_1 = \{y > |x| \wedge x > 0\} \quad \cup \quad B_2 = \{y > |x| \wedge x < 0\} = A_1 \tag{III.54}$$

In this way, we can decompose the integral into two components that cancel each other:

$$\begin{aligned}\int_{A_1} \mathbf{HG}_{11}\overline{\mathbf{HG}_{11}^{45}}(x,y,z)dxy = \\ \int_{B_1} \mathbf{HG}_{11}\overline{\mathbf{HG}_{11}^{45}}(x,y,z)dxy + \int_{B_2} \mathbf{HG}_{11}\overline{\mathbf{HG}_{11}^{45}}(x,y,z)dxy = \\ \int_{B_1} \mathbf{HG}_{11}\overline{\mathbf{HG}_{11}^{45}}(x,y,z)dxy - \int_{B_1} \mathbf{HG}_{11}\overline{\mathbf{HG}_{11}^{45}}(x,y,z)dxy = 0\end{aligned} \tag{III.55}$$

The last integral, Eq. III.52, requires to be evaluated, and it is the only new contribution to the final signal. We can use the same parameterisation of Eq. III.38 which leads to:

$$\begin{aligned}\int_{A_1} \mathbf{LG}_{10}\overline{\mathbf{HG}_{11}^{45}}dxy &= \iint_0^{+\infty} \mathbf{LG}_{10}\overline{\mathbf{HG}_{11}}dx'dy' \\ &= \tfrac{1}{\pi w^2(z)} e^{-i2\Delta\psi} \iint_0^{+\infty} \mathbb{H}_1\left[\tfrac{\sqrt{2}x'}{w(z)}\right] \mathbb{H}_1\left[\tfrac{\sqrt{2}y'}{w(z)}\right] e^{-2\frac{x'^2+y'^2}{w^2(z)}} dx'dy' = \frac{e^{-i2\Delta\psi}}{2\pi}\end{aligned} \tag{III.56}$$

In the case of an astigmatic beam, we have the signal recorded by the Quadrant Photodiode is:

$$S_{MCT} = \frac{2\overline{\langle\epsilon\rangle}}{\pi} F_0\overline{F_2}e^{-i2\Delta\psi} + \frac{2\overline{\langle\epsilon\rangle\,\delta\epsilon\cos(2\theta)}}{\pi}|F_2|^2 e^{-i2\Delta\psi} + \text{c.c.} \tag{III.57}$$

The new coefficient generated by the beat note $\mathbf{LG}_{10}\overline{\mathbf{HG}_{11}^{45}}$ is proportional to $|F_2|$. As we will discuss later, the component proportional to this therm is ruled out if the second order modes are in anti-resonance, so it will not affect the demodulated signal.

III.1.4. *Astigmatic Mismatch Error Signal*

There is a more important result behind the robustness of the Mode Converter Technique to the Astigmatic Aberration. In fact, we demonstrated that the combination of the signals of a Quadrant Photodiode defined in Eq. III.48 is proportional only to the beat-note between a Hermite-Gauss Mode 11 oriented as the sensor axes and the Fundamental Mode. All the other contributions, except $\mathbf{LG}_{10}\mathbf{HG}_{11}^{45}$, are ruled out by the symmetry of the sensor or the signal recombination itself.

If we look at the representation of Simple Astigmatic Gaussian Beam before the mode converter:

$$\hat{U}_2 = \langle\epsilon\rangle\,\mathbf{LG}_{10} + \delta\epsilon\cos(2\theta)\mathbf{HG}_{11}^{45} - \delta\epsilon\sin(2\theta)\mathbf{HG}_{11}$$

we can see that the Astigmatic parameter, $\delta\epsilon$, is proportional to two $\mathbf{HG}_{11}$, one oriented as the experimental reference and another one rotated by 45°. This observation is all we need to design the Astigmatic Wave-front Sensing.

Using the results obtained before, we know that a Quadrant Photodiode oriented as a plus cross, $+$, will generate a signal proportional to the $\mathbf{U}_{00}\overline{\mathbf{HG}}_{11}$, $S^{+}_{M.M.}$, while a Quadrant Photodiode oriented as an x-shaped cross,$\times$, will generate a signal proportional to $\mathbf{U}_{00}\overline{\mathbf{HG}}^{45}_{11}$, $S^{\times}_{M.M.}$.

The precise formulation of these signals can be obtained from Eq. III.57 by replacing $\langle\epsilon\rangle$ with the amplitude of the corresponding mode: $\delta\epsilon\cos(2\theta)$ for $S^{\times}_{M.M.}$ and $\delta\epsilon\sin(2\theta)$ for $S^{+}_{M.M.}$. Moreover, we need to consider the cross-talk generated by the beat-note estimated in Eq. III.56. The final result is given by

$$S^{\times}_{M.M.} = \overline{\delta\epsilon}\cos(2\theta)\,\frac{2e^{i\Delta\psi(z)}}{\pi}F_0\overline{F}_2 + \frac{2\overline{\langle\epsilon\rangle\,\delta\epsilon\cos(2\theta)}}{\pi}|F_2|^2e^{-i2\Delta\psi} + \text{c.c.} \tag{III.58}$$

$$S^{+}_{M.M.} = -\overline{\delta\epsilon}\sin(2\theta)\,\frac{2e^{-i2\Delta\psi}}{\pi}F_0\overline{F}_2 + \frac{2\overline{\langle\epsilon\rangle\,\delta\epsilon\sin(2\theta)}}{\pi}|F_2|^2e^{-i2\Delta\psi} + \text{c.c.} \tag{III.59}$$

III.1.5. *Signal Demodulation*

The last setup towards the Wave-front sensing is the demodulation of the signals Eq. III.49, Eq. III.58, and Eq. III.59. In order to simplify the calculation, we can rewrite these signals as

$$S^{(i)}_{M.M.} = \frac{\overline{\hat{\epsilon}_i}}{\pi}e^{-i2\Delta\psi}F_0\overline{F}_2 + \frac{2a(\overline{\langle\epsilon\rangle\,\delta\epsilon})}{\pi}|F_2|^2e^{-i2\Delta\psi} + \text{c.c.} \tag{III.60}$$

where $i = \times, +, \text{MCT}$ with the corresponding value $\hat{\epsilon}_i = \delta\epsilon\cos(2\theta)$, $-\delta\epsilon\sin(2\theta)$ and $\langle\epsilon\rangle$, and a indicate the scaling factor of the second order modes beat note.

The demodulation of the Quadrant Photodiode signals is similar for each detector, $i = \times, +, \text{MCT}$. Moreover, the demodulation is linear, so we can demodulate the Eq.III.60 or we can demodulate the signal generated by each sector, S_j defined in Eq.III.35. In both cases, we can focus the calculation only on the components proportional to $e^{i\Omega t}$ and ignore the other factors. Moreover, this method maintains the linearity of the initial signal so that we can analyse the two components of Eq. III.60 separately.

We can start with the first one:

$$\begin{aligned}\frac{\overline{\hat{\epsilon}_i}}{\pi}e^{-i2\Delta\psi}F_0\overline{F}_2 = \frac{\overline{\hat{\epsilon}_i}}{\pi}e^{-i2\Delta\psi}\Big[&\left(F_0^0\overline{F}_2^0 + F_0^+\overline{F}_2^+ + F_0^-\overline{F}_2^-\right)\\ &+\left(F_0^0\overline{F}_2^+e^{-i\Omega t} - F_0^0\overline{F}_2^-e^{+i\Omega t} + F_0^+\overline{F}_2^0e^{+i\Omega t} - F_0^-\overline{F}_2^0e^{-i\Omega t}\right) +\\ &-\left(F_0^-\overline{F}_2^+e^{-i2\Omega t} + F_0^+\overline{F}_2^-e^{+i2\Omega t}\right) + \text{c.c.}\Big]\end{aligned} \tag{III.61}$$

where we can isolate the coefficient proportional to $e^{i\Omega t}$:

$$\begin{aligned}&\frac{\overline{\hat{\epsilon}_i}}{\pi}e^{-i2\Delta\psi}F_0\overline{F}_2(\Omega) =\\ &\qquad\frac{1}{\pi}\left[\overline{\hat{\epsilon}_i}e^{-i2\Delta\psi}\left(F_0^+\overline{F_2^0} - F_0^0\overline{F_2^-}\right) + \hat{\epsilon}_ie^{-i2\Delta\psi}\left(\overline{F_0^0}F_2^+ - \overline{F_0^-}F_2^0\right)\right]e^{+i\Omega t} + \text{c.c.}\end{aligned} \tag{III.62}$$

This technique is designed to work with a cavity in resonance, so we use Eq. II.22 and Eq. II.25 and assume that:

$$F_0^0 = \frac{r_1 - (1-\rho_1)r_2}{1 - r_1 r_2} = r_{res} \tag{III.63}$$

$$F_{0,2}^{\pm} = -\frac{m}{2}\left(r_1 + r_2\frac{t_1^2}{1 + r_1 r_2}\right) \simeq -\frac{m}{2} \tag{III.64}$$

$$F_2^0 = r_{\text{cav}} = r_1 + r_2\frac{t_1^2}{1 + r_1 r_2} \simeq 1 \tag{III.65}$$

to reduce the Ω component of Eq. III.61:

$$\frac{\overline{\hat{e}_i}}{\pi}e^{-i2\Delta\psi}F_0\overline{F}_2(\Omega) = \frac{m}{2\pi}\left[\bar{\hat{e}}e^{-i2\Delta\psi}\left(-1 + r_{res}\right) + \hat{e}e^{-i2\Delta\psi}\left(-r_{res} + 1\right)\right]e^{+i\Omega t} + \text{c.c.} = \frac{i\,m}{\pi}\Im\left[(r_{res} - 1)\bar{\hat{e}}e^{-i2\Delta\psi}\right]e^{+i\Omega t} + \text{c.c.} \tag{III.66}$$

After that, we can proceed with the second term in Eq. III.60:

$$\begin{aligned}\frac{2a(\overline{\langle\epsilon\rangle\,\delta\epsilon})}{\pi}e^{-i2\Delta\psi}|F_2|^2 = \frac{2a(\overline{\langle\epsilon\rangle\,\delta\epsilon})}{\pi}e^{-i2\Delta\psi}\left(|F_2^0|^2 + |F_2^+|^2 + |F_2^-|^2\right) \\ + \left[\left(F_2^0\overline{F}_2^+e^{-i\Omega t} - F_2^0\overline{F}_2^-e^{+i\Omega t}\right) + \text{c.c.}\right] \\ - \left(F_2^-\overline{F}_2^+e^{-i2\Omega t} + F_2^+\overline{F}_2^-e^{+i2\Omega t}\right)\end{aligned} \tag{III.67}$$

where we can use Eq. III.64 and Eq. III.65 to see that the coefficients proportional to $e^{i\Omega t}$ are ruled out in case the second order modes are out of resonance:

$$\left(F_2^0\overline{F}_2^+e^{-i\Omega t} - F_2^0\overline{F}_2^-e^{+i\Omega t}\right) = \left(-\frac{m}{2}e^{-i\Omega t} + \frac{m}{2}e^{+i\Omega t}\right) = 0 \tag{III.68}$$

In this way, we demonstrated that the component of Eq. III.60 proportional to $e^{i\Omega t}$ are only:

$$S_{M.M.}^{(i)}(\Omega) = \frac{i\,m}{\pi}\Im\left[(r_{res} - 1)\bar{\hat{e}}e^{-i2\Delta\psi}\right]e^{+i\Omega t} + \text{c.c.} \tag{III.69}$$

and the corresponding demodulated signal is:

$$V_{M.M.}^{(i)} = \frac{m}{\pi}\chi_i(r_{res} - 1)\Im\left[\bar{\hat{e}}e^{-i2\Delta\psi}\right]\sin(\phi_0) \tag{III.70}$$

where we collect the electronic conversion factors in χ_i.

As we can see, the signal generated from the Quadrant Photodiode is always proportional to the Imaginary part of the beat note between the High Order Modes and the Fundamental one. In this case, the demodulation phase ϕ_0 can be used only to maximise the detected signal:

$$V_{M.M.}^{(i)} = \frac{m}{\pi}\chi_i(r_{res} - 1)\Im\left[\bar{\hat{e}}e^{-i2\Delta\psi}\right] \tag{III.71}$$

while the decoupling of the Real and the Imaginary part of the parameter $\hat{e}_i$ can be obtained only by tuning the Gouy phase, $\Delta\phi(z)$ accumulated between the cavity and the sensor:

$$\tilde{V}_{M.M.}^{(i)}(\Delta\psi) = \frac{m}{\pi}(r_{res} - 1)\chi_i\left(\Re[\hat{e}_i]\sin(2\Delta\psi) - \Im[\hat{e}_i]\cos(2\Delta\psi)\right) \tag{III.72}$$

To obtain signals proportional to the mode matching degree of freedom, we need two different sensors for each Quadrant photodiode orientation, and they have to be separated by $2\Delta\psi(z_2) - 2\Delta\psi(z_1) = 90°$. This leads to six sensors organised as in Fig. III.3 that characterise all the astigmatic mismatch parameters listed in Table III.1.

Gouy Phase $2\Delta\psi$	MCT with QD $\times$	QD $\times$	QD $+$
$0°$	$\frac{\langle z_0\rangle_{(x,y)} - \hat{z}_0}{2\hat{z}_R}$	$\frac{z_0^{(x)} - z_0^{(y)}}{4\hat{z}_R}\cos(2\theta)$	$\frac{z_0^{(x)} - z_0^{(y)}}{4\hat{z}_R}\sin(2\theta)$
$90°$	$\frac{\langle w_0\rangle_{(x,y)} - \hat{w}_0}{\hat{w}_0}$	$\frac{w_0^{(x)} - w_0^{(y)}}{2\hat{w}_0}\cos(2\theta)$	$\frac{w_0^{(x)} - w_0^{(y)}}{2\hat{w}_0}\sin(2\theta)$

TABLE III.1: List of Quadrant Photodiode Sensor required for the characterisation of the Astigmatic Mismatch. We need six sensors divided into three couples. The first one comprises 2 Quadrant Sensors aligned as $\times$ cross, and they measure the wavefront after the Mode Converter Telescope(MCT). The second couple is again aligned as a $\times$ cross but measures before the MCT. The last one is oriented as a $+$ cross and measures before the MCT.

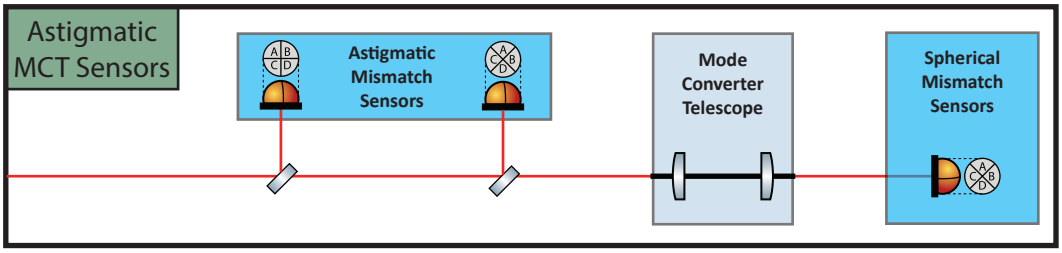

FIGURE III.3: Simplified optical scheme of Astigmatic Mode Matching Wavefront sensor. The beam reflected by the cavity is split and Analysed with three different Quadrant Photodiodes. Before the Mode Converter Telescope, two sensors are dedicated to the Astigmatic Parameters: one aligned as $\times$ cross, Eq. III.58, and one aligned as $+$ cross, Eq. III.59. After the Mode Converter Telescope, we have the other Quadrant Photodiode dedicated to the Spherical Mismatch, Eq. III.49. For each sensor in the schematic, an extra sensor must be considered for the Gouy Phase tuning.

III.2. EXPERIMENTAL LIMITS

The calculations presented in Section II.II.2 and SectionIII are based on theoretical assumptions that are not always fulfilled by the Experimental setup. In particular, we assumed that:

- The Fundamental Mode of the Cavity is perfectly matched with the Mode Converter Telescope
- The Mode Converter Telescope imposes a phase shift of $90°$ between the modes $\mathbf{HG}_{20}$ and $\mathbf{HG}_{02}$;
- The optical gains of each photodiode are equivalent;

Any deviation from these assumptions generates a technical noise in the final Mode Matching signal. From an experimental point of view, it is impossible to avoid these

issues completely, but we can estimate their action and, when it is possible, reduce their contribution to the final Mode Matching Signal.

This section will formalize the effect of deviation from each requirement listed before and describe our approach to technical noise reduction.

III.2.1. *Installation of Mode Converter Telescope*

The Mode Converter Telescope has to be installed along the path of cavity reflection, and it has to be tuned with respect to the cavity fundamental mode. When, in Eq. III.32, we applied the conversion rule to the reflected beam from the cavity, we implicitly assumed that the fundamental mode was fulfilling the requirements imposed on the shape of the converted beam. In fact, only the Laguerre-Gauss Mode $\mathbf{LG}_{01}$ with the beam parameter q_{MCT} defined in Eq. III.24:

$$q_{\mathrm{MCT}} = z_0^{\mathrm{MCT}} + \frac{i\pi}{\lambda}(w_0^{MCT})^2 \quad \text{where} \quad \begin{cases} w_0^{MCT} = \sqrt{\left(1+\frac{1}{\sqrt{2}}\right)\frac{\lambda f_{\mathrm{Cyl}}}{\pi}} \\ z0 = \frac{l}{2} \quad \text{respect to the first Cyl lens} \end{cases} \tag{III.73}$$

is perfectly converted into an Hermite-Gauss Mode $\mathbf{HG}_{11}^{45}$.

From the experimental point of view, the requirements imposed by Eq. III.24 is obtained by installing a telescope between the cavity and the Mode Converter, called *Pre-converter*. This telescope is used to couple the cavity mode q_c with the Mode Converter one q_{MCT}, and it guarantees that the Mode Converter acts on the modes of the cavity base.

Even if the requirements for the *pre-converter* are simple, the implementation hides some pitfalls. The operative procedure for the telescope installation requires tuning the lens positions with respect to an optical beam. This reference should represent the cavity fundamental mode from the cavity, which propagates from the cavity itself up to the Mode Converter. In this way, it is possible to fine-tune the mode matching and fulfill the requirement imposed by Eq. III.24.

There are two possible approaches to generating a reference for the *pre-converter*. The first method is based on the filter action of a resonant cavity. An auxiliary beam is injected from the *end mirror* and is kept in resonance with the cavity. In this way, the cavity transmittance will select only the fundamental mode, which will be leaked from the front mirror. This reference will propagate along the cavity reflection path and will represent the effective propagation of the cavity fundamental mode.

The second approach is based on the incoming beam that we want to match to the resonant cavity. In this case, we will use the reflection of the *input-mirror*. The cavity is kept out of resonance to avoid possible deformation of the beam shape, and the *pre-converter* lenses are fine-tuned on the beam shape of the incoming beam. This approach has an intrinsic limitation: the relationship between the reflected beam and the fundamental mode is based on the initial Mode Matching between the incoming beam and the cavity. For this reason, this method cannot lead to a perfect tuning of the *pre-converter* and induces intrinsic errors on the Mode Matching Sensing.

If the pre-converted is tuned on a generally reflected beam, we obtain a telescope that maps the wrong beam parameter, $\tilde{q}_c$, into the Mode Converter mode one, q_{MCT}. In this

case the $\mathbb{ABCD}$ matrix, will be defined by a new requirement:

$$q_{MCT} = \frac{\tilde{A}_\Lambda \tilde{q}_c + \tilde{B}_\Lambda}{\tilde{C}_\Lambda \tilde{q}_c + \tilde{D}_\Lambda} \tag{III.74}$$

that will generate a mismatch between the cavity fundamental mode, q_c, and the Mode Converter one.

The relationship defined in Eq. III.74 suggests using the Transverse Mode defined by $\tilde{q}$ as a basis for the evolution of the beam across the telescope. In particular, we can use the same approach described for the cavity mismatch in Eq.II.119 to represent the cavity modes defined by q_c as a perturbation of the ones defined by $\tilde{q}$. In this way, we can estimate the evolution of the reflected beam defined in Eq. III.7:

$$\begin{aligned}\Psi_{ref} =& \hat{U}_0(q_c)\left(F_0(\omega)e^{i\omega t} + F_0(\omega+\Omega)\tfrac{m}{2}e^{i(\omega+\Omega t)} - F_0(\omega-\Omega)\tfrac{m}{2}e^{i(\omega-\Omega t)}\right) + \\ & \hat{U}_2(q_c)(\delta\epsilon, \langle\epsilon\rangle, \theta)\left(F_2(\omega)e^{i\omega t} + F_2(\omega+\Omega)\tfrac{m}{2}e^{i(\omega+\Omega t)} - F_2(\omega-\Omega)\tfrac{m}{2}e^{i(\omega-\Omega t)}\right)\end{aligned} \tag{III.75}$$

where $\hat{U}_2$ is defined by Eq. II.136:

$$\hat{U}_2(\delta\epsilon, \langle\epsilon\rangle, \theta) = \delta\epsilon \cdot \left[\mathbf{HG}_{11}^{45}\cos 2\theta - \mathbf{HG}_{11}\sin 2\theta\right] + \langle\epsilon\rangle \cdot \mathbf{LG}_{10} \tag{III.76}$$

and we highlight the dependency from q_c, and the general mismatch is indicated by $\delta\epsilon$ and $\langle\epsilon\rangle$.

In order to rewrite the beam in the $\tilde{q}_c$ basis we need to study the perturbation of each transverse mode that composes Eq. III.75. We can assume that the initial mismatch between the linear cavity and the reference beam is represented by

$$\begin{aligned}\beta_0 &= \frac{\langle w_0\rangle_0 - \hat{w}_0}{\hat{w}_0} \\ \gamma_0 &= \frac{\langle z_0\rangle_0 - \hat{z}_0}{2\hat{z}_R}\end{aligned} \tag{III.77}$$

where $\langle w_0\rangle_0$ and $\langle z_0\rangle_0$ are the waist parameters that define the reference beam, and $\hat{w}_0$, $\hat{z}_0$, and $\hat{z}_R$ defines the cavity fundamental mode.

Starting from this assumption and using the results obtained in Section II.II.2, we can write the fundamental mode as:

$$U(q_c) \simeq U_0(\tilde{q}_c) + \langle\tilde{\epsilon}_0\rangle\, \mathbf{LG}_{10}(\tilde{q}_c) \tag{III.78}$$

where $\langle\tilde{\epsilon}_0\rangle = \tilde{\beta} + i\tilde{\gamma}$ is the residual mismatch defined using the incoming beam as a reference. $\tilde{\beta}$ and $\tilde{\gamma}$ are defined as:

$$\begin{aligned}\tilde{\beta} &= \frac{\hat{w}_0 - \langle w_0\rangle_0}{\langle w_0\rangle_0} \\ \tilde{\gamma} &= \frac{\hat{z}_0 - \langle z_0\rangle_0}{2\langle z_R\rangle_0}\end{aligned} \tag{III.79}$$

Similar calculations can be done for the second order mode, but they require extending the analysis done in Section. II.II.2. This study is beyond the purpose of this Thesis, but

we can make an educated guess about their Taylor expansion[1] and we can assume that the high order modes excitation is linear in $\langle\tilde{\epsilon}_0\rangle$:

$$U_i(q_c) \simeq U_i(x,\tilde{q}_c) + \langle\tilde{\epsilon}_0\rangle\, \hat{U}_n(\tilde{q}_c) \tag{III.80}$$

If we apply this perturbation to the $\hat{U}_2(q_c)$ term in Eq. III.75, we have:

$$\begin{aligned}\hat{U}_2(\tilde{q}_c)(\delta\epsilon,\langle\epsilon\rangle,\theta) = \\ \delta\epsilon\cdot\Big[\left(\mathbf{HG}_{11}^{45}(x,y|\tilde{q}_c) + \langle\tilde{\epsilon}_0\rangle\,\hat{U}_{\mathbf{HG}_{11}^{45}}(\tilde{q}_c)\right)\cos 2\theta - \\ \left(\mathbf{HG}_{11}(x,y|\tilde{q}_c) + \langle\tilde{\epsilon}_0\rangle\,\hat{U}_{\mathbf{HG}_{11}}(\tilde{q}_c)\right)\sin 2\theta\Big] + \\ \langle\epsilon\rangle\cdot\left(\mathbf{LG}_{01}(x,y|\tilde{q}_c) + \langle\tilde{\epsilon}_0\rangle\left(\hat{U}_{\mathbf{LG}_{01}}(\tilde{q}_c)\right)\right)\end{aligned} \tag{III.81}$$

where the effect of the imperfect reference is always combined with the mismatch of a general incoming beam. These two values are mainly small, and their product can be considered negligible[2]. Using these results, we can rewrite the cavity reflected beam using the $\tilde{q}_c$ basis as:

$$\Psi_{ref} = \left(\hat{U}_0(\tilde{q}_c) + \langle\tilde{\epsilon}_0\rangle\,\mathbf{LG}_{01}(\tilde{q}_c)\right)F_0 + \hat{U}_2(\tilde{q}_c)(\delta\epsilon,\langle\epsilon\rangle,\theta)F_2 \tag{III.82}$$

where we collect the Frequency contribution:

$$F_i = \left(F_i(\omega)e^{i\omega t} + F_i(\omega+\Omega)\tfrac{m}{2}e^{i(\omega+\Omega t)} - F_i(\omega-\Omega)\tfrac{m}{2}e^{i(\omega-\Omega t)}\right) \tag{III.83}$$

In this way, the beam propagation across the pre-converter telescope can be estimated using the Collins integral rules defined in Eq.III.74. In this way, the beam amplitude before the Mode Converter can be written as:

$$\begin{aligned}\Psi_{ref} = \left(\hat{U}_0(\tilde{q}_{MCT}) + \langle\tilde{\epsilon}_0\rangle\, e^{i2\,\mathrm{Arg}[\tilde{C}_\Lambda\tilde{q}_c+\tilde{D}_\Lambda]}\mathbf{LG}_{01}(\tilde{q}_{MCT})\right)F_0 + \\ \hat{U}_2\,\langle\tilde{\epsilon}_0\rangle\, e^{i2\,\mathrm{Arg}[\tilde{C}_\Lambda\tilde{q}_c+\tilde{D}_\Lambda]}(\tilde{q}_{MCT})(\delta\epsilon,\langle\epsilon\rangle,\theta)F_2\end{aligned} \tag{III.84}$$

where we consider the extra Gouy phase shift induced by the pre-converter $\Delta\phi = \mathrm{Arg}\left[\tilde{C}_\Lambda\tilde{q}_c + \tilde{D}_\Lambda\right]$.

The tuning of the pre-converter using an imperfect reference creates a new coefficient proportional to $\mathbf{LG}_{01}(q_{MCT})$. This contribution will be coupled with the Spherical Mode Matching signal. In fact, the calculation done in Section III demonstrated that a Quadrant Photodiode Sensor combined with the Mode Converter is sensitive to the $\mathbf{LG}_{01}(q_{MCT})$ amplitude. For this reason, the detector will generate a signal

$$\begin{aligned}\tilde{S}_{MCT} &= F_0\left(\overline{\langle\epsilon\rangle F_2 + \tilde{\epsilon}_0 F_0}\right)\frac{e^{-i2\Delta\psi}}{\pi} + \text{c.c} \\ &= \left(F_0\overline{F}_2\overline{\langle\epsilon\rangle} + |F_0|^2\overline{\langle\tilde{\epsilon}_0\rangle}\right)\frac{e^{-i2\Delta\psi}}{\pi} + \text{c.c} \\ &= S_{MCT} + |F_0|^2\left(\frac{e^{-i2\Delta\psi}}{\pi}\overline{\langle\tilde{\epsilon}_0\rangle} + \text{c.c}\right) \\ &= S_{MCT} + |F_0|^2\Re\left[\frac{e^{-i2\Delta\psi}}{\pi}\overline{\langle\tilde{\epsilon}_0\rangle}\right]\end{aligned} \tag{III.85}$$

[1] The effective calculation can be found in [33].

[2] Even if this assumption could be reasonable, the experimental measurements indicate a possible coupling effect generated by these terms.

composed by two terms: the spherical mode matching signal, S_{MCT}, and a systematic error proportional to $|F_0|^2$:

$$|F_0|^2 = \left| F_0^0 e^{i\omega t} + F_0^+ e^{i(\omega+\Omega t)} - F_0^- \tfrac{m}{2} e^{i(\omega-\Omega t)} \right|^2$$

The new term is exactly Eq. 3.3 of [32] that is used to derive the Pound-Drever-Hall signal. We can use the results of this paper to estimate its component proportional to $e^{i\Omega t}$. In particular, we can write

$$|F_0|^2(\Omega) = i\Im[mF_0]\, e^{-i\Omega t} + \text{c.c.} \simeq i\frac{m}{2\pi}\frac{\delta f}{\Delta f_{FWHM}} e^{-i\Omega t} + \text{c.c.} \tag{III.86}$$

where δf is the difference between the laser frequency, f_{laser} in Eq.IV.30, and the resonance one, f_0 in Eq.II.84:

$$\delta f = f_{\text{laser}} - (l\Delta f_{\text{fsr}} + \Delta f_{\text{HOM}}) \tag{III.87}$$

This term is in phase with the Spherical Mode Matching signal, S_{MCT} and it contributes to the signal demodulated from the Quadrant Photodiode Sensors:

$$\tilde{V}_{M.M.}^{MCT} = \left(\Im\left[\bar{\tilde{\epsilon}} e^{-i2\Delta\psi}\right] + \frac{1}{2}\frac{\delta f}{\Delta f_{FWHM}} \Re\left[\overline{\langle\tilde{\epsilon}_0\rangle} e^{-i2\Delta\psi}\right] \right) \frac{m\chi_i}{\pi} \sin(\phi_0) \tag{III.88}$$

In conclusion, we demonstrated that the tuning of the pre-converter based on an imperfect reference generates a cross-talk between the Spherical Mismatch error signal and the Longitudinal one. The coupling coefficient is proportional to the initial mismatch and depends on the Gouy phase of the sensor

$$\kappa = \Re\left[\overline{\langle\tilde{\epsilon}_0\rangle} e^{-i2\Delta\psi}\right] \tag{III.89}$$

We can estimate the maximum value of κ from the initial mismatch between the reference beam and the cavity. We can use the definition in Eq. III.77 and Eq. III.79, to estimate the parameters, $\tilde{\beta}$ and $\tilde{\gamma}$ as a function of the initial mismatch

$$\begin{cases} \tilde{\beta} = -\dfrac{\beta_0}{(1+\beta_0)} \\ \tilde{\gamma} = -\dfrac{\gamma_0}{(1+\beta_0)^2} \end{cases} \quad \text{and} \quad \langle\tilde{\epsilon}_0\rangle = \tilde{\beta} + i\tilde{\gamma} = -\left(\frac{\beta_0}{(1+\beta_0)} + \frac{i\gamma_0}{(1+\beta_0)^2} \right) \tag{III.90}$$

In this way, the maximum coupling can be estimated as

$$\kappa < |\langle\tilde{\epsilon}_0\rangle|^2 = \frac{1}{(1+\beta_0)^2}\sqrt{\beta_0^2(1+\beta_0)+\gamma_0^2} \lesssim |\epsilon_0| + |\epsilon_0|^2, \tag{III.91}$$

where $|\epsilon_0|^2$ is the optical loss generated by the mismatch between the reference beam and the liner cavity. This parameter can be obtained by studying the cavity transmission and using the peak amplitude, P_i, associated with the mode i:

$$|\epsilon_0|^2 = \frac{P_2}{P_0} \tag{III.92}$$

III.2.2. *Partial conversion of the Hermite Gauss Mode*

In the previous part, we discussed the effect of a mismatch between the Cavity Fundamental mode and the Mode Converter, and we estimated the effects on the Spherical Mode Matching Sensing. That approach can precisely estimate the effects of the mistuning, and it is able to quantify the crosscoupling of the external error signals. However, it requires complicated calculations that hide the effects on the converted beam.

Another approach to characterising a mistuned Mode Converter can be based on the simple model described in Section III.1.2. In particular, we can relax the requirement on the phase shift and describe the effect of the astigmatic telescope as

$$\phi = 2\,\mathrm{Arg}\left[C_S\, q_0 + D_S\right] = \pi + \delta\phi, \tag{III.93}$$

but assuming that the Transversal and Saggital modes are still matched at the output, $q_T = q_S$.

In this case, the conversion rules defined in Eq. III.31 are not valid anymore and we need to consider the evolution of each Hermite-Gauss Mode. In particular, we can focus the analysis only on $\mathbf{HG}_{11}^{45}$ and $\mathbf{LG}_{01}$ inasmuch these Modes are the only ones that are affected by the Gouy Phase detuning, $\Delta\psi_{n_T,n_S}$ defined in Eq.III.20.

The first step is to rewrite them as the overlap of the $\mathbf{HG}_{02}$ and $\mathbf{HG}_{20}$:

$$\begin{aligned}\hat{U}_2 = \langle\epsilon\rangle\,\mathbf{LG}_{01} + \delta\epsilon\cos(2\theta)\mathbf{HG}_{11}^{45} = \\ \langle\epsilon\rangle\,(\mathbf{HG}_{02} + \mathbf{HG}_{20}) + \delta\epsilon\cos(2\theta)\,(\mathbf{HG}_{02} - \mathbf{HG}_{20}) = \\ \mathbf{HG}_{02}\,(\langle\epsilon\rangle + \delta\epsilon\cos(2\theta)) + \mathbf{HG}_{20}\,(\langle\epsilon\rangle - \delta\epsilon\cos(2\theta))\,.\end{aligned} \tag{III.94}$$

The two Hermite-Gauss Modes $\mathbf{HG}_{02}$ and $\mathbf{HG}_{02}$ will gain a phase difference of $\phi = \pi + \delta\phi$

$$\begin{aligned}\hat{U}_2^{conv} = \mathbf{HG}_{02}\,(\langle\epsilon\rangle + \delta\epsilon\cos(2\theta)) + e^{i\delta\phi}\mathbf{HG}_{20}\,(\langle\epsilon\rangle - \delta\epsilon\cos(2\theta)) = \\ \left(\langle\epsilon\rangle\,\tfrac{1}{2}(1+e^{i\phi}) + \delta\epsilon\cos(2\theta)\tfrac{1}{2}(1-e^{i\phi})\right)\mathbf{LG}_{01} + \\ \left(\langle\epsilon\rangle\,\tfrac{1}{2}(1-e^{i\phi}) + \delta\epsilon\cos(2\theta)\tfrac{1}{2}(1+e^{i\phi})\right)\mathbf{HG}_{11}^{45}\end{aligned} \tag{III.95}$$

and the information on $\langle\epsilon\rangle$ and $\delta\epsilon$ will be mixed and carried by the new Hermite-Gauss Mode $\mathbf{HG}_{11}^{45}$.

Using the same calculation done in Section III, we can demonstrate that the Quadrant Photodiode Sensor after a detuned Mode Converter Telescope will generate a signal proportional to the amplitude of the $\mathbf{HG}_{11}^{45}$:

$$\begin{aligned}e^{i\phi/2}\left(\langle\epsilon\rangle\,\tfrac{1}{2}(e^{-i\phi/2} - e^{i\phi/2}) + \delta\epsilon\cos(2\theta)\tfrac{1}{2}(e^{-i\phi/2} + e^{i\phi/2})\right) = \\ e^{i\phi/2}\,(\langle\epsilon\rangle\, i\sin(-\phi/2) + \delta\epsilon\cos(2\theta)\sin(\phi/2)) = \\ \left[\langle\epsilon\rangle\cos\left(\tfrac{\delta\phi}{2}\right) + i\delta\epsilon\cos(2\theta)\sin\left(\tfrac{\delta\phi}{2}\right)\right]e^{i\delta\phi/2}.\end{aligned} \tag{III.96}$$

The signal generated by the sensor will be a mixture of two mismatch parameters, where the astigmatic contribution, $\delta\epsilon$, is rotated by a 90° phase, with respect to the spherical one, $\langle\epsilon\rangle$. This rotation connects the complementary degree of freedom. The spherical

waist dimension will couple with the astigmatic waist position and the other way round:

$$\tilde{V}^{(i)}_{M.M.}(\Delta\psi) = \frac{m}{\pi}\chi_i \left(\left(\beta \cos(\delta\tfrac{\delta\phi}{2}) + (\eta\cos(2\theta))\sin(\tfrac{\delta\phi}{2}) \right) \sin(2\Delta\psi) - \left(\gamma\cos(\delta\tfrac{\delta\phi}{2}) + (\alpha\cos(2\theta))\sin(\tfrac{\delta\phi}{2}) \right)\cos(2\Delta\psi) \right). \quad \text{(III.97)}$$

The incomplete phase shift, $\delta\phi$, can be connected to the mistuning of the *pre-converter* telescope, $\langle\tilde{\epsilon}\rangle$. The precise calculations require considering all the Transverse Mode in Eq. III.81 and comparing the final signal with Eq. III.96. These calculations are beyond this thesis goal, but we can expect that $\sin(\frac{\delta\phi}{2})$ and $\langle\tilde{\epsilon}\rangle$ are on the same order of magnitude.

III.2.3. *Unbalanced Signal Reconstruction*

The Mode Matching signal is based on the combination of the four signals, S_i, generated by the Active Area, A_i of a Quadrant Photodiode. These signal were defined in Eq.III.35 as

$$S_i = |F_0| \int_{A_i} |\hat{U}_0(x,y,z)|^2 dxdy + |F_2| \int_{A_i} |\hat{U}_2^{conv}(x,y,z)|^2 dxdy + \left(F_0\overline{F_2} \int_{A_i} \hat{U}_0\overline{\hat{U}_2^{conv}}(x,y,z)dxdy + \text{c.c.} \right)$$

and, for the sake of clarity, these signals were first recombined as

$$S_{M.M} = (S_1 + S_3) - (S_2 + S_4)$$

and after they were demodulated as

$$\tilde{V}^{(i)}_{M.M.}(2\Delta\psi) = \frac{m}{\pi}\chi_i \left(\Re[\hat{\epsilon}_i]\sin(2\Delta\psi) - \Im[\hat{\epsilon}_i]\cos(2\Delta\psi) \right)$$

However, this flow can be inverted: we can first demodulate the signals, S_i:

$$\tilde{V}_j(2\Delta\psi) = m\chi_j S_j(2\Delta\psi) \quad \text{(III.98)}$$

where χ_j is the dedicated conversion factor, and then recombine together to extract the Mismatch signal

$$\tilde{V}_{M.M.}(2\Delta\psi) = (V_1 + V_3) - (V_2 + V_4). \quad \text{(III.99)}$$

This approach is generally more flexible than the first one inasmuch as the demodulated signals are easier to manipulate and there are more methods to obtain the signal recombination of Eq. III.99[3]. Moreover, this scheme simplifies the analysis of the Mode Matching signal reconstruction.

In the real case scenario, different imperfection leads to an unbalance between the signals, S_i. The active areas of Quadrant Photodiodes can have different responsivity, or the operational circuit can diverge from the ideal operation. If we consider the demodulation-recombination, we can collect all these effects on the conversion factor, χ_j, and study the degradation of the Mode Matching Signal generated by their unbalance, $\chi_j \neq \chi_i$.

[3] e.g., we can first record the demodulated signals V_i and perform the linear operations off-line.

In the general case, the reconstructed signal presents different contributions:

$$\begin{aligned}\tilde{V}_{M.M.}(2\Delta\psi) = & m\frac{(\chi_1+\chi_3)+(\chi_2+\chi_4)}{4}(S_1(2\Delta\psi)+S_3(2\Delta\psi))-(S_2(2\Delta\psi)+S_4(2\Delta\psi))\\ & + m\frac{(\chi_1+\chi_3)-(\chi_2+\chi_4)}{4}(S_1(2\Delta\psi)+S_2(2\Delta\psi))+(S_3(2\Delta\psi)+S_1(2\Delta\psi))\\ & + m\frac{(\chi_1+\chi_4)-(\chi_2+\chi_3)}{4}(S_1(2\Delta\psi)+S_2(2\Delta\psi))-(S_3(2\Delta\psi)+S_4(2\Delta\psi))\\ & + m\frac{(\chi_1+\chi_2)-(\chi_3+\chi_4)}{4}(S_1(2\Delta\psi)+S_4(2\Delta\psi))-(S_2(2\Delta\psi)+S_3(2\Delta\psi)),\end{aligned} \tag{III.100}$$

where the first line corresponds to the Mode Matching Signal defined in Eq.III.48, the second one is the Longitudinal Error signal, and the last two are the Angular Error signals[34]. In particular, we can reorganize the conversion factor as

$$\begin{aligned}\chi_{MM} &= \frac{(\chi_1+\chi_3)+(\chi_2+\chi_4)}{4}\\ \chi_L &= \frac{(\chi_1+\chi_3)-(\chi_2+\chi_4)}{4}\\ \chi_H &= \frac{(\chi_1+\chi_4)-(\chi_2+\chi_3)}{4}\\ \chi_V &= \frac{(\chi_1+\chi_2)-(\chi_3+\chi_4)}{4}\end{aligned} \tag{III.101}$$

and rewrite the reconstructed signal as

$$\tilde{V}_{M.M.}(2\Delta\psi) = m\chi_{MM}\left(S_{M.M}(2\Delta\psi)+\frac{\chi_L}{\chi_{MM}}S_L+\frac{\chi_V}{\chi_{MM}}S_V+\frac{\chi_V}{\chi_{MM}}S_V+\right) \tag{III.102}$$

here we highlight the coupling coefficient of the Horizontal and Vertical Alignment signals, $S_{H/V}$, and of the Longitudinal one, S_L.

IV EXPERIMENTAL TEST OF THE MODE MATCHING SENSING

IV.1 Optical Setup 66
IV.1.1 Electro-Optical Modulator 66
IV.1.2 Laser Source 73
IV.1.3 Optical Cavity 79
IV.1.4 Mode Matching Telescope 83
IV.1.5 Astigmatic Mode Matching Telescope 94
IV.1.6 Wavefront Sensors 99
IV.2 Electronic Setup 104
IV.2.1 Wavefront Sensors Readout 104
IV.2.2 Longitudinal Control Loop 108

The Mode Matching Sensing Technique validation was designed around the Frequency Dependent Squeezing Source requirement. It was focused on three different properties: dynamic range, linearity of the error signals, and decoupling estimation of the mismatch parameters.

The validation was based on the direct estimation of the sensor response to the variation of mismatch parameters. This approach has the double advantage of being independent of any assumptions and characterising the three key properties with one measurement. The linearity is verified by testing the linear model directly on the data, while the decoupling is validated by studying the response to the mode matching parameter β, γ, α, and η, defined in Eq. II.137, and reported here:

$$\beta = \frac{\langle w_0 \rangle_{(\tilde{x},\tilde{y})} - \hat{w}_0}{\hat{w}_0} \quad \text{with} \quad \langle w_0 \rangle = \frac{w_0^{(\tilde{x})} + w_0^{(\tilde{y})}}{2}$$

$$\gamma = \frac{\langle z_0 \rangle_{(\tilde{x},\tilde{y})} - \hat{z}_0}{2\hat{z}_R} \quad \text{with} \quad \langle z_0 \rangle_{(\tilde{x},\tilde{y})} = \frac{z_0^{(\tilde{x})} + z_0^{(\tilde{y})}}{2}$$

$$\alpha = \frac{w_0^{(\tilde{x})} - w_0^{(\tilde{y})}}{2\hat{w}_0}$$

$$\eta = \frac{z_0^{(\tilde{x})} - z_0^{(\tilde{y})}}{4\hat{z}_R}$$

$$\langle \epsilon \rangle = \beta + i\gamma \quad \text{and} \quad \delta\epsilon = \alpha + i\eta$$

The dynamic range was compared with the requirement for optical losses. In particular, the Quantum Noise Reduction system imposed a maximum mismatch of 2 % in power for each cavity in the system[35]. This limit was inherited by the dynamic range of the Mode Matching Sensors. In fact, this sensing method will be used during the Scientific Run, and it has to monitor the evolution of mismatch when the system is

working within the requirement. For this reason, the method was characterised inside the region

$$\text{Loss} = |\epsilon|^2 = |\langle\epsilon\rangle + \delta\epsilon| = \beta^2 + \gamma^2 + \alpha^2 + \eta^2 \leq 2\,\% \tag{IV.1}$$

In order to study the detector response to the beam parameters evolution, I designed and installed an optical setup composed of a resonant linear cavity and the Mode Matching Sensing scheme described in Section III.III.1. The apparatus is described in this chapter, where I present the characterisation of the main components and I verified that the imperfection did not spoil the Mode Matching measurements.

IV.1. Optical Setup

The Optical setup is represented by the simplified layout in Fig.IV.1, while the detailed information is collected in Appendix B.II.1. The spatial constraints precluded the implementation of a complete setup for the Astigmatic Mismatch sensing technique as it was presented in Section III. The optical layout was upgraded during the experimental activity to meet the measurement requirements. These modifications changed only the Mode Matching Telescope and the configuration of the Wavefront Sensor Scheme.

In particular, we can distinguish two experimental phases: The first part was the validation of the Spherical Mode Matching sensing based on the Mode Converter technique[31]. In this case, the Mode Matching Telescope was composed only of two spherical lenses while the Wavefront Sensors setup was based on the design of the standard Mode Converter Technique, two Quadrant Photodiode Sensors after the Mode Converter Telescope (continued red line in Figure IV.1).

The second part was the validation of the Astigmatic Wavefront sensing. In this phase, I modified the Mode Matching Telescope and the Wavefront sensor setup. I installed a Cylindrical lens inside the Spherical Telescope to induce an astigmatic aberration. I used the auxiliary line (dashed line red line in Figure IV.1) to measure the beam wavefront before the Mode Converter Telescope.

Each component of the optical setup was individually characterised and optimised to improve the quality of the Mode Matching Measurement. Here, I reported a detailed description of these components and the characterisation results.

IV.1.1. *Electro-Optical Modulator*

The sidebands used by the wavefront sensing technique were generated by the periodical modulation of the beam phase. The basic idea is to induce an oscillation with frequency, Ω_{mod}, and modulation depth, m, to the beam phase, ψ:

$$\psi(t) \simeq m \sin(\Omega_{mod} t) + \psi_0 \tag{IV.2}$$

to manipulate the amplitude as

$$\Psi_{in} = \hat{U}(x,y,z) e^{i(\omega t + m \sin(\Omega_{mod} t) + \psi_0)}. \tag{IV.3}$$

In case of small modulation depths, $m < 1$, we can expand the exponential

$$\begin{aligned} \Psi_{in} &\simeq \hat{U}(x,y,z) e^{i(\omega t + \psi_0)} \left(1 + i\, m \sin(\Omega_{mod} t)\right) \\ &= \hat{U}(x,y,z) e^{i(\omega t + \psi_0)} \left(1 + \frac{m}{2} e^{i\Omega_{mod} t} - \frac{m}{2} e^{-i\Omega_{mod} t}\right) \end{aligned} \tag{IV.4}$$

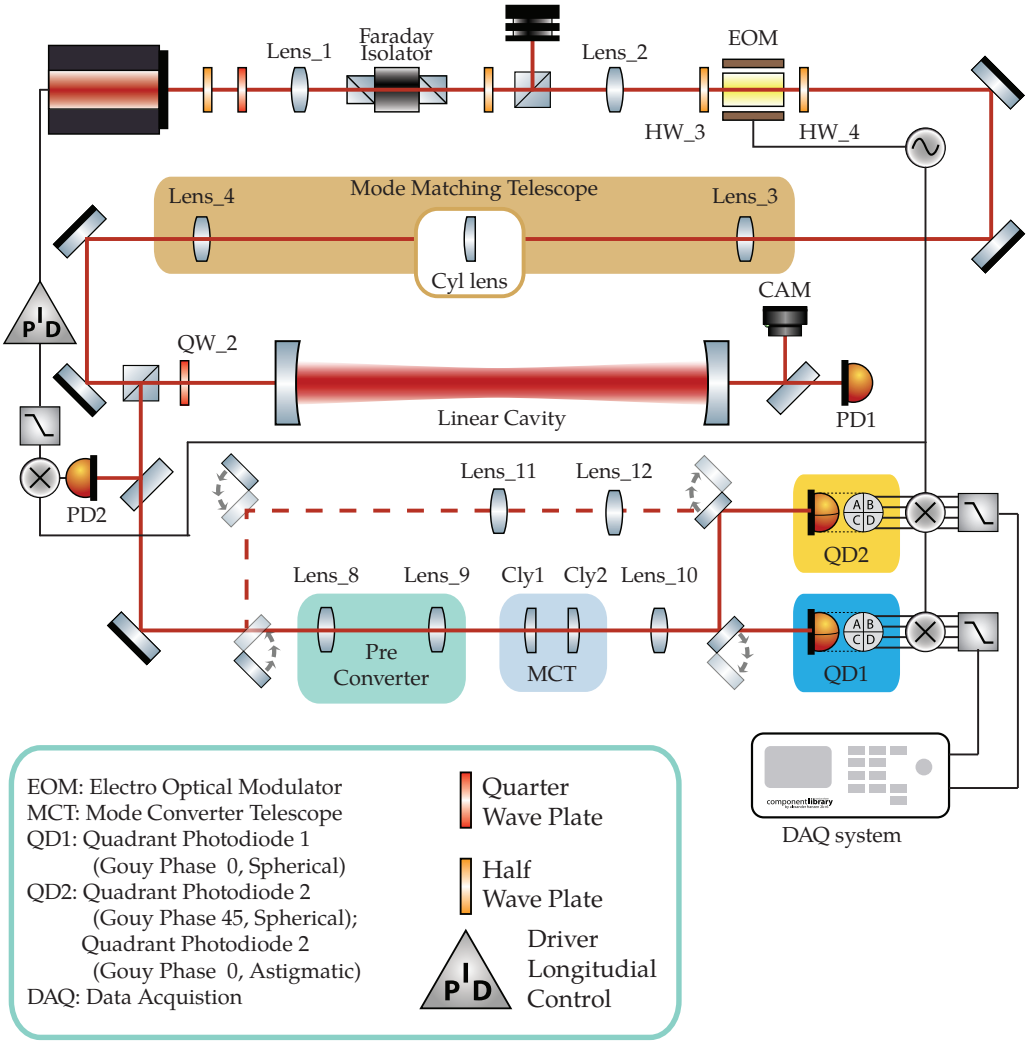

FIGURE IV.1: Experimental Optical Setup. This scheme represents the layout used for validating the Mode Converter Technique and the two upgrades required for the Astigmatic Mismatch sensing. The scheme comprises (top to bottom): the LASER source, an Electro-optical modulator, the Mode Matching Telescope(orange box), the Linear Cavity, the Mode Converter(light blue box) with the pre-converter(green box), and the wavefront sensors(blue and yellow boxes). The two upgrades for the astigmatic wavefront sensing were:(1) the installation of a cylindrical lens inside the Mode Matching Telescope(with box in the orange one), and (2) the modification of the wave front sensor setup(dashed line), required to by-pass the Mode Converter Telescope. Detailed information about the positioning and the optical elements is summarised in Appendix B.II.1.

and describe the amplitude as the sum of three different oscillating components: the original one with frequency, ω, called the carrier, and the new ones with frequency, $\omega + \Omega_{mod}$ and $\omega - \Omega_{mod}$, called sidebands.

The phase modulation was obtained with a commercial Electro-Optical Modulator. This object is based on a nonlinear crystal that can manipulate the beam phase by changing the effective optical path. When the beam passes through the crystal, it

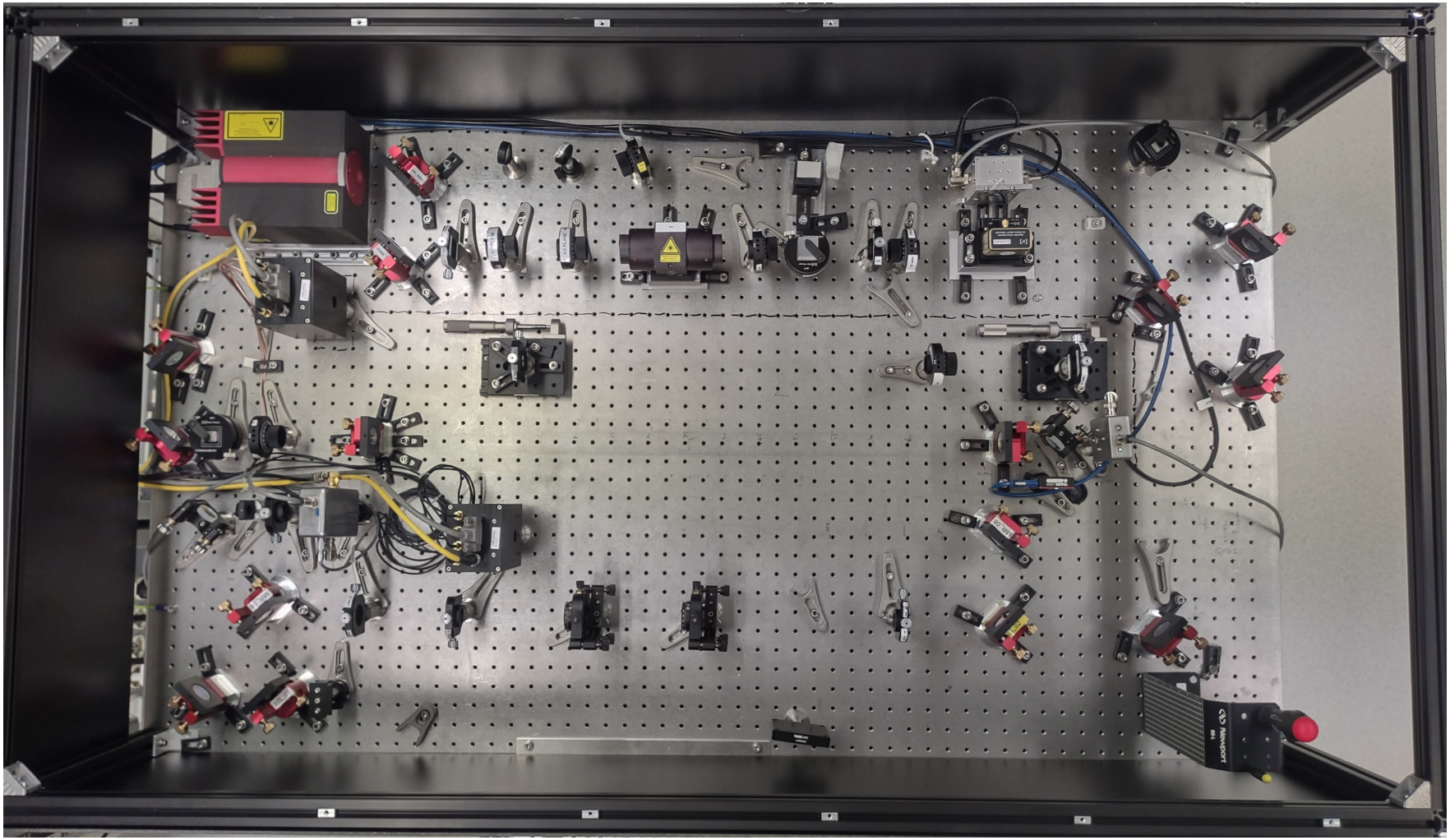

FIGURE IV.2: Experimental Setup. Picture of the optical bench used during the validation measurements. The optical path resembles the schematic in Figure IV.1.

accumulates a phase shift

$$\Delta\psi = \frac{2\pi}{\lambda} \cdot \Delta z' \tag{IV.5}$$

where $\Delta z'$ is the effective optical path defined as the product of the geometrical length of the crystal, ΔL, and the medium refractive index, n:

$$\Delta z' = \Delta L n \tag{IV.6}$$

In particular, the Electro-Optical Modulator exploits the Pockels effect to change the refractive index as a function of the electric potential applied to the crystal[36, p.837]:

$$n(V) =\simeq n_0 + \frac{1}{2} r\, n_0^3 \frac{V}{d} \tag{IV.7}$$

where n_0 is the refractive index at rest, r is the electro-optics coefficient, d is the crystal thickness, and V is the voltage difference field applied to the crystal. Combing all these equations, we can write the phase shift as:

$$\psi(V) = \psi_0 + \frac{\pi}{\lambda} \frac{r n_0^3 \Delta L}{d} \cdot V \tag{IV.8}$$

where we have the phase shift at rest, ψ_0, summed with a coefficient which is a function of the potential, V. In general, the relationship between the phase modulation and the voltage applied is collected in a single parameter called Half-wave Voltage:

$$V_\pi = \frac{d}{\Delta L} \frac{\lambda}{r n_0^3} \tag{IV.9}$$

that represents the voltage difference required to induce a phase shift of half wavelength, $\Delta\psi = \pi$.

The phase modulation described in Eq.IV.2 can be obtained by applying a periodical signal with amplitude V_0 and frequency Ω_0:

$$V(\Omega_{mod}) = V_0 \sin(\Omega_{mod} t) \tag{IV.10}$$

that induces an accumulated phase after the Electro-Optical Modulator of

$$\psi(V)\psi_0 + \pi \frac{V_0}{V_\pi} \sin(\Omega_{mod} t) \tag{IV.11}$$

The comparison between this expression and Eq.IV.2 allows to connect the amplitude of the Voltage signal, V_0, to the modulation depth, m, as:

$$m = \pi \frac{V_0}{V_\pi} \tag{IV.12}$$

The Electro-Optical Modulator used in optical setup[1] has a typical half-wave voltage of $V_\pi = 210\,\mathrm{rad\,V^{-1}}$, while the requirement for the deep modulation was $m \simeq 0.2$. Using Eq. IV.12, we can estimate an amplitude of

$$V_0 = \frac{m}{\pi} V_\pi \simeq 10\,\mathrm{V_p}(30\,\mathrm{dBm}) \tag{IV.13}$$

[1] EOM 4004, produced by New Focus™. The principal specifications are reported in Table IV.1.

Parameter	Value
Modulation Depth(mrad V^{-1}	15
V_π (V)	210
Material	$MgO:LiNbO_3$
Optical Aperture (mm)	2×2
Input Impedance (pF)	20
Max RF Power (W)	10

TABLE IV.1: Manufacture Parameters of EOM 4004 from New Focus™.

However, this value is outside the dynamic range of our Signal Generator[2] and I had to amplify the Voltage signal before injecting it into the crystal. In particular, I collaborated with the Electronic Workshop of the European Gravitational Observatory to produce an LC resonator Circuit.

LC Resonant Circuit

The passive resonant circuit is divided into three components: the effective LC circuit used to amplify the signal, a transformer used to decouple the input impedance, and a probe used to monitor the effective Voltage applied to the crystal.

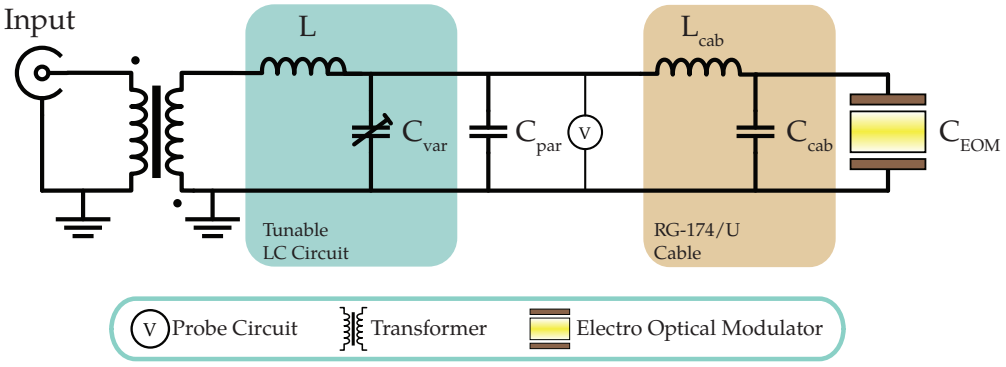

FIGURE IV.3: LC Circuit from EGO. From left to right: the input for the Voltage signal; the transformer to decouple the input Independence; the LC resonant circuit, composed by the Inductance, L and the variable Capacitor, C_{var}; the parasite Capacitor, C_{var}; and the RG-174/U cable,C_{cab} and L_{cab}; the Electro-Optical Modulator Crystal, C_{EOM}.

The effective LC circuit is based on the schematic described in Fig. IV.3, and its resonance frequency can be estimated by[38, p.52]

$$f_{LC} = \frac{1}{2\pi}\frac{1}{\sqrt{LC}}$$

In particular, we considered all the capacitance contributions:

- Variable capacitor ($C_{var} = 3\,\text{pF}$ to $28\,\text{pF}$)

[2]The experiment used a Direct Digital Synthesis produced by the Electronic Workshop of the INFN-Padova [37, p91] that can generate an electronic Local Oscillator with Frequency from 4 MHz to 500 MHz and maximum amplitude of 0.7 V_p (7 dBm)

- MgO:$LiNbO_3$ crystal of the 4004 EOM from New Focus™ ($C_{cry} = 22\,\text{pF}$)
- Cables from the LC case to the Electro-optical Modulator (6 cm of RG-174/U: $C_{cab} = 6.0(6)\,\text{pF}$ and $L_{cab} = 12(1)\,\text{pH}$)
- Other parasite components (case, connectors, ...) $C_{par} = 5.0(5)\,\text{pF}$

that correspond to a total capacitance of C_{tot} between 36 pF and 51 pF, and we produced a hand-made inductor in order to have a resonance frequency around 17 MHz. We wrapped 16 rounds of capton-silver-coated wire around a powdered iron toroid (T80-6), and we obtained an inductance of $L = 2.0(2)\,\mu\text{H}$. The theoretical value for the resonance frequency was

$$14.4(53)\,\text{MHz} \leq f_{LC} \leq 18.8(34)\,\text{MHz} \tag{IV.14}$$

that was experimentally verified by measuring the Transfer Function of the resonant circuit. Using the multi-function tool Moku:lab, we studied the resonant frequency as a function of the variable capacitor, C_{var} and we identified the maximum and minimum resonance frequency of the circuit, respectively 15 MHz to 17 MHz. Moreover, we calibrated the probe circuit with a conversion factor of 1:1733 and a voltage Gain of 27 dB on resonance.

Optimisation of the Electro-optical modulator

I optimised the Electro-Optical Modulator during the installation to compensate for two main side effects: the Residual Amplitude Modulation and the Acoustic Resonance.

Residual Amplitude Modulation

The Residual Amplitude Modulation was generated by the birefringent nature of the Pockels cell. The refractive index of the MgO:$LiNbO_3$ crystal is anisotropic, and it changes as a function of the beam polarisation. In particular, the crystal geometry defines two axes, extraordinary and ordinary, associated with two refractive indexes, $n_e^{(0)}$ and $n_o^{(0)}$, and two electro-optical coefficients r_e and r_o. When the crystal is excited with a Voltage difference, V, applied parallel to the extraordinary axis, the Pockel effect defines different evolution for the two effective refractive indexes, $n_{e,o}(V)$:

$$n_o(V) = n_o^{(0)} - \frac{1}{2} r_o (n_o^{(0)})^3 \frac{V}{d} \tag{IV.15}$$

$$n_e(V) = n_e^{(0)} - \frac{1}{2} r_e (n_e^{(0)})^3 \frac{V}{d} \tag{IV.16}$$

This anisotropy is visible when the polarisation of the incoming beam is not aligned with the crystal axes. In this case, the beam amplitude is split into two polarisation components parallel to the crystal axes, which will accumulate two different phase shifts:

$$\psi_o(V) = \psi_o^{(0)} - \frac{\pi}{\lambda} \frac{r_o (n_o^{(0)})^3 \Delta L}{d} \cdot V \tag{IV.17}$$

$$\psi_e(V) = \psi_e^{(0)} - \frac{\pi}{\lambda} \frac{r_e (n_e^{(0)})^3 \Delta L}{d} \cdot V \tag{IV.18}$$

$$\tag{IV.19}$$

The two amplitudes are recombined at the crystal end, and their phase difference $\delta\psi = \psi_e - \psi_o$ bound together the output beam polarisation and the external Voltage. The amplitude at the output can be described by [39]:

$$\Psi_{in} = \hat{U}(x,y,z)e^{i\omega t}\left(\sin(\beta)\hat{e}_{ord}e^{i\psi_o(V)} + \cos(\beta)\hat{e}_{ex}e^{i\psi_e(V)}\right) \tag{IV.20}$$

where β is the angle of the input polarisation with respect to the extraordinary axis and $\hat{e}_{ex/ord}$ represent the polarisation components parallel to the two crystal axis.

When we apply a periodical Voltage signal, $V(t) = V_0\sin(\Omega t)$, to induce the phase modulation described in Eq.IV.2, we also obtain the polarisation modulation described in Eq. IV.20. This extra effect can be converted into amplitude modulation using a polariser installed after the crystal. In that case, the output optical power is described by[39]

$$|\Psi_{in}|^2 = P_0\left(\cos^2(\beta-\gamma) + \cos^2(\beta+\gamma) + \frac{\sin(2\beta)\cos(2\gamma)}{2}\cos\left(M\sin(\Omega_{mod}t) + \Delta\psi_0\right)\right), \tag{IV.21}$$

where β is the orientation of the polarisation at the input of the Electro-Optical Modulator and γ is the orientation of the polariser installed after the crystal.

To reduce this effect, I followed the approach presented in [40], optimising the input polarisation, β, and the output polariser, γ. Using Fig. IV.1 as a reference, I added a dumper between the cavity mirrors to avoid spurious signals generated by the resonance. I measured the amplitude modulation with the fast photodiode PD2 and optimised the polarisation before and after the Electro-optical modulator by rotating HW_03 and HW_4 to minimise the spurious signal at frequency Ω_{mod}.

Piezo Mechanic Resonance of the Crystal

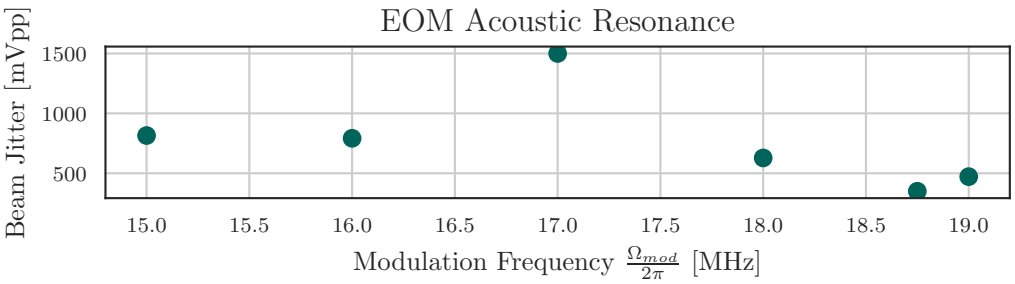

FIGURE IV.4: Modulation Frequency Tuning. I used the Quadrant Photodiode sensor to estimate the alignment jitter and optimised the modulation Frequency Ω_{mod} to minimise the crystal mechanical oscillation. The final best frequency was 18.75 MHz.

The other effect was the alignment jitter induced by the mechanical oscillation of the crystal. This effect was generated by the acoustic stress induced by the piezoelectric response to the MgO:$LiNbO_3$[41]. This phenomenon makes the crystal mechanically oscillate, generating a fluctuation in the beam alignment. When the beam is divided by the split areas of the Quadrant Photodiode Sensors, this beam jitter is converted into amplitude modulation and can spoil the Mode Matching Signal recorded by the sensors.

Even if the piezoelectric effect is small and the beam deflection is generally negligible, this phenomenon can be amplified by the crystal mechanical resonance. Unfortunately, this was the case during the first configuration of the Electro-Optical Modulator, when I chose a modulation frequency of $\Omega_{mod} = 2\pi \times 17\,\mathrm{MHz}$. To minimise this effect, I modified the optical setup described in Fig. IV.1: as before, I added a dumper between the mirrors cavity to avoid spurious signal generated by the resonance; after that, I took a pick-off of the beam before the Mode Converter, and I centred it on the Quadrant Photodiode Sensor 2. With this optical setup, I recorded the signal generated by one of the active areas and minimised the component at Ω_{mod} by changing the modulation frequency. The data are collected in Fig IV.4, where we can see how the initial choice was the worst one. The final modulation frequency was set to $\Omega_{mod} = 2\pi \times 18.75\,\mathrm{MHz}$.

IV.1.2. *Laser Source*

The Laser source used for the experiment was a Mephisto Laser produced by Coherent. The typical characteristics of this source are listed in Table IV.2. The characterisation was focused on two key parameters for the validation measurement: the shape of the output beam and the actuator on the laser frequency.

The initial beam shape defines the best Mode Matching achievable between the incoming beam and the resonant cavity. In fact, if the beam cannot be represented as a Gaussian mode, we need to assume the presence of extra Tranveserse modes in the beam shape. Moreover, the estimation of the initial beam shape was necessary for the design of the optical setup.

The characterisation of the frequency actuator is not directly connected to the validation of the Mode Matching sensing technique, but it gives an important tool for other studies. In particular, the actuation range of the frequency controller imposes some constrain on the design of the linear cavity, Section IV.1.3, and the calibration of the actuator response is necessary for the characterisation of the residual motion of the Logitundal Error Signal, Section IV.2.2.

Parameter	Value
Beam Quality M^2	< 1.1
Thermal Tuning Coefficient $((\mathrm{GHz\,K^{-1}})\,\mathrm{K\,V^{-1}})$	-3 (1)
Thermal Response Bandwidth (Hz)	1
PTZ[a] tuning Coefficient (Hz)	2.4[b]
PTZ[a] maximum input voltage (V)	± 100
PTZ[a] Response Bandwidth (kHz)	100
Spectral line $(\mathrm{kHz\,ms^{-1}})$	100
Waist location w.r.t laser Head (mm)	-105

TABLE IV.2: Manufactures parameters for the Mephisto Laser Source. Model Mephisto 500NE, SN Laser System: HDP.1235936.110-140001; SN Electronic: MEPH14010001; [a] Piezo electric Transducer; [b] Manufacturer Characterisation in 2014.

Beam Shape

The beam generated by the Mephisto laser was characterised by two different measurements of the shape: the first one was used to estimate the initial beam parameters, and

the second one was used to characterise the beam quality.

In both cases, I used the beam profiler BC106N-VIS/M produced by Thorlabs™ to measure the beam shape at different longitudinal positions, z_i. These measurements were done at the beginning of the installation, and the optical setup was composed only of the LASER and two mirrors MIR_01 and MIR_02 with low reflectivity $R < 0.02$, used to reduce the optical power from P_{laser}350 mW to less than 1 mW.

Initial Beam Parameters

In the first measurement, I used the method described in Appendix A.I.1 to characterise the beam shape at the output of the LASER head. I measured the evolution of the beam radius along the two axes of the iso-power ellipse, and I interpolated these values to obtain the beam parameter. The data are presented in Fig. IV.5, and the beam parameters are reported in Table. IV.3. These values were used to design the optical setup described in Fig. IV.1.

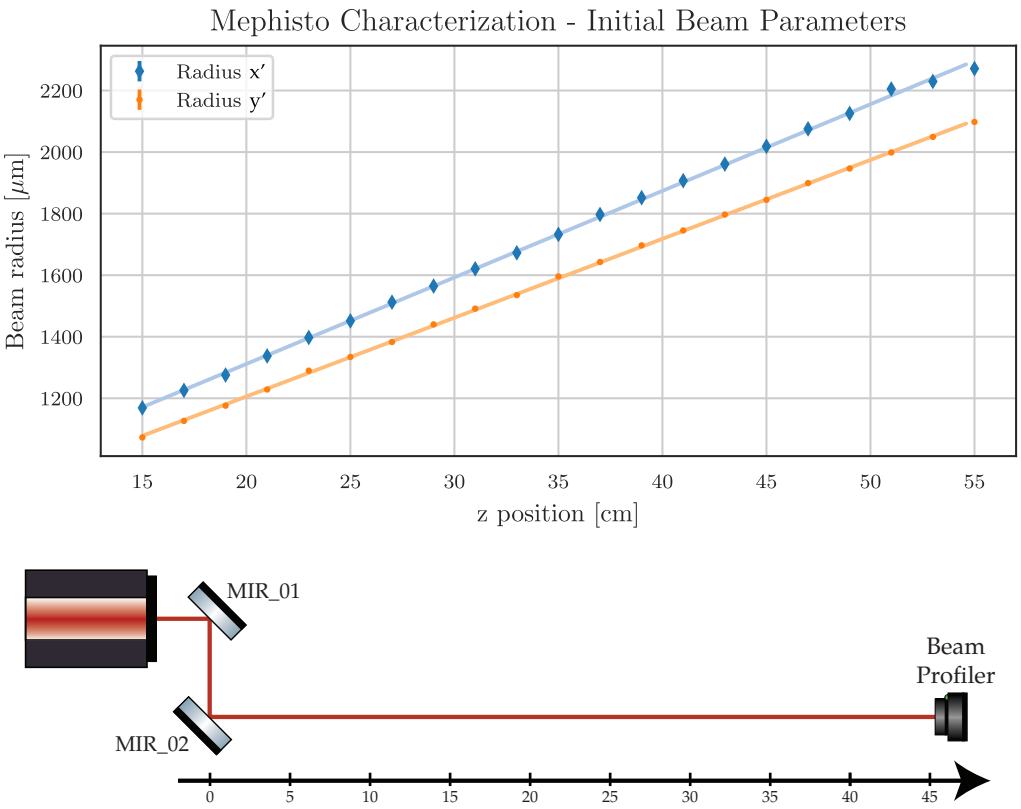

FIGURE IV.5: Mephisto Laser Beam Characterisation. The Beam was characterised using the procedure described in Appendix A.I.1. The point represents the estimation of the beam radius along the two axes of the iso-power ellipse, while the two continuous lines represent the fit used to estimate the beam parameters. The beam shape was measured using MIR_02 as $z = 0$ reference. This Mirror was installed approximately 20 cm after the laser output.

Axis	$w_0^{(i)}$ [µm]	$z_0^{(i)}$ [cm]
x'-axis	120.1(7)	−31.3(4)
y'-axis	131.7(3)	−31.6(2)

TABLE IV.3: Mephisto Laser Beam Characterisation. The Beam Parameters are estimated in the internal reference of the beam. The reference $z = 0$ was MIR_02 that was installed at 20 cm after the laser output port. The data are reported in Fig. IV.5.

Beam Quality Measurement

In the second measurement, I characterise the beam quality using the procedure defined by the ISO Standard 11146. I installed a lens L_1 with focal length $f_1 = 230(1)$ mm after MIR_02, and I measured the beam profile with the 4σ method[3]. In this case, the beam diameter is defined as :

$$2w(z) = d_\sigma(z) = 2\sqrt{2}\sqrt{\sigma_x^2 + \sigma_y^2} \tag{IV.22}$$

where σ_i^2 is the second order momentum of the power density distribution of the beam shape long the i-axis[42, p.93]:

$$\sigma_x^2 = \frac{\iint_{\mathbb{R}^2} (x - \bar{x})^2 \, P(x,y,z) dxy}{\iint_{\mathbb{R}^2} P(x,y,z) dxdy} \tag{IV.23}$$

and $\bar{x}$ is the centroid position[42, p.94]:

$$\bar{x} = \frac{\iint_{\mathbb{R}^2} x \, P(x,y,z) dxdy}{\iint_{\mathbb{R}^2} P(x,y,z) dxdy} \tag{IV.24}$$

The ISO Standard 11146 describes the beam shape using the diameter $d_\sigma(z)$ and defines its evolution on the longitudinal axis, z, as:

$$d_\sigma^2(z) = a + b \cdot z + c \cdot z^2 \tag{IV.25}$$

where the polynomial coefficients, (a, b, c), are directly connected to the beam parameters:

$$z_0 = \frac{-b}{2c} \quad \text{and} \quad w_0 = \frac{1}{4\sqrt{c}} \sqrt{4ac - b^2} \tag{IV.26}$$

Moreover, the ISO standard defines a figure of merit for the beam quality, called M^2, that can be estimated by the beam evolution in Eq. IV.25:

$$M^2 = \frac{\pi}{8\lambda} \sqrt{4ac - b^2} \tag{IV.27}$$

This parameter corresponds to the Beam propagation parameter[42, p. 605]:

$$M^2 = \frac{\lambda}{\pi} w_0 \cdot \theta_0 \tag{IV.28}$$

where λ is the wavelength, w_0 is the waist radius, and θ_0 is the beam divergence defined as

$$\theta_0 = \lim_{(z - z_0) \to \infty} \left(\frac{2\tilde{w}(z)}{z - z_0} \right) \tag{IV.29}$$

[3] This estimation is compatible with the standard definition of $w(z)$ given in Eq. II.42[42, p.94].

Using this definition, we can see that the condition $M^2 = 1$ are verified only for a perfect Gaussian Beam, while for a general beam shape, we will have $M^2 > 1$.

The measurements are reported in Fig. IV.6 and the estimated beam parameters are reported in Table IV.4. In particular, I estimated $M^2 = 1.1(4)$ that is compatible with the manufacturer specification $M^2 < 1.1$.

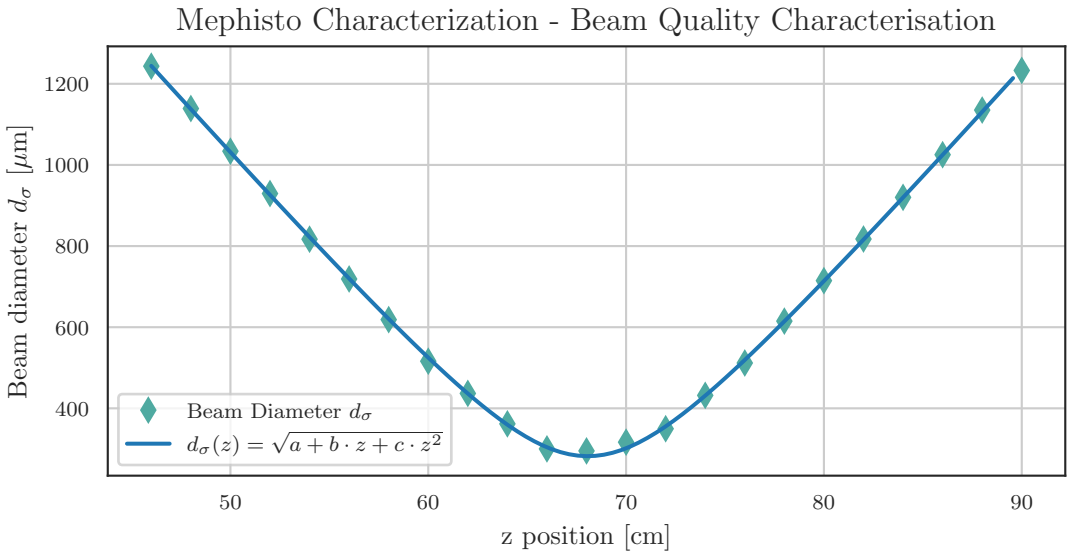

FIGURE IV.6: Mephisto Laser Beam Quality. Beam profile Measurement. The beam generated by the Mephisto Laser was focused using a lens with Effective Focal Length 230(1) mm in order to measure the beam shape around the waist position. The beam diameter was estimated using the ISO 11146 method, and the data were interpolated using Eq. IV.22. The estimated parameters are reported in Table IV.4.

Parameter	Value
$2w_0$ (µm)	282.1(7)
z_0 (cm)	68.1(2)
M^2	1.1(4)

TABLE IV.4: Mephisto Laser Beam Quality. Beam Parameter estimated using the model described in Eq. IV.22 on the data reported in Fig. IV.6.

Frequency Tuning

The frequency of the laser beam was controlled using two actuators installed on the Mephisto itself. Both these actuators change the length of the resonant cavity inside the LASER source, and their actions are always combined. The effective frequency of the laser can be described by

$$\omega = \omega_0 + \delta\omega_{slow} + \delta\omega_{fast} \tag{IV.30}$$

where ω_0 is the frequency at rest, $\delta\omega_{slow}$ is controlled by the temperature actuator and $\delta\omega_{fast}$ by the Piezo Electric Transducer. The differences between the two actuators are the response time and the dynamic range. The thermal actuator is slower with a

Bandwidth of 1 Hz, but it has a large actuation range between 6 GHz and 9 GHz. The Piezo Electric Transducer has a fast response, and bandwidth around 100 kHz, but it has a smaller actuation range of 200 MHz.

For most applications, I used the fast actuator to control the laser frequency. In particular, I used a signal generator and a High Voltage Amplifier[4], to generate a Voltage signal from 0 V to 100 V[5] that was sent to the Piezo Electric Transducer.

The conversion factor between the applied voltage and the effective frequency shift of the laser was characterised using the Linear cavity described in Section IV.1.3. I generated two sidebands using the Electro-Optical Modulator to add a fixed reference, and I used the power transmitted by the cavity to study the frequency components of the beam.

From the calculation done in Section IV.1.1, the two sidebands have the frequency

$$\omega_{\pm} = \omega \pm \Omega_{mod} \tag{IV.31}$$

where ω is the laser frequency, and Ω_{mod} is the modulation frequency. These two frequency components can be detected by measuring the power transmitted by the cavity as a function of the voltage applied to the Piezo Electric Transducer. In particular, I recorded a spectrum reported in Figure IV.7, and I identified the voltage signal required to have the two side-bands resonance with the cavity:

$$\omega_{\pm} = \omega_0 + \delta\omega_{fast}(V_{f_{\pm}}) \pm \Omega_{mod} = 2\pi\, l \Delta f_{\text{fsr}} \tag{IV.32}$$

where l is the longitudinal mode order. If frequency modulation is lower than the free spectral range, Δf_{fsr}, the two peaks will have a frequency distance of $\Delta f_{\pm} = 2\Omega_{mod}$, and we can use their peak as a frequency reference.

I interpolated the resonance peak with a Lorentzian function[6], and I estimated the voltage corresponding to the peak position, $V_{f_{\pm}}$. The calibration factor was estimated by:

$$\kappa = \frac{1}{2\pi} \frac{2\Omega_{mod}}{V_{f_+} - V_{f_-}} \tag{IV.33}$$

In general, a Piezo Electric Transducer response is not linear and changes as a function of the DC offset. For this reason, the calibration factor is trustful only around the piezo voltage used for the estimation:

$$\kappa(\langle V \rangle) = \frac{1}{2\pi} \frac{2\Omega_{mod}}{V_{f_+} - V_{f_-}} \quad \text{where} \quad \langle V \rangle = \frac{V_{f_+} + V_{f_-}}{2} \tag{IV.34}$$

In order to study this behaviour, I used the temperature control to move the frequency scan done using the Piezo Electric Transducer and estimate the $\kappa(\langle V \rangle)$ at different DC Voltage $\langle V \rangle$. The data are shown in Fig. IV.7, where we can see a linear dependency between the voltage $\langle V \rangle$ and the calibration factor. In order to marginalise this effect, I used the temperature actuation to keep the resonance mode always around $\langle V \rangle \simeq 50\,\text{V}$, and I considered the calibration factor:

$$\kappa(50\,\text{V}) = 2.55(5)\,\text{MHz}\,\text{V}^{-1} \tag{IV.35}$$

[4] SVR150/3 produced by Piezomechanik. Output range from −30 V to 150 V

[5] It is a common rule not to excite a piezoelectric transducer with a bi-polar signal.

[6] See Section IV.1.3 for details

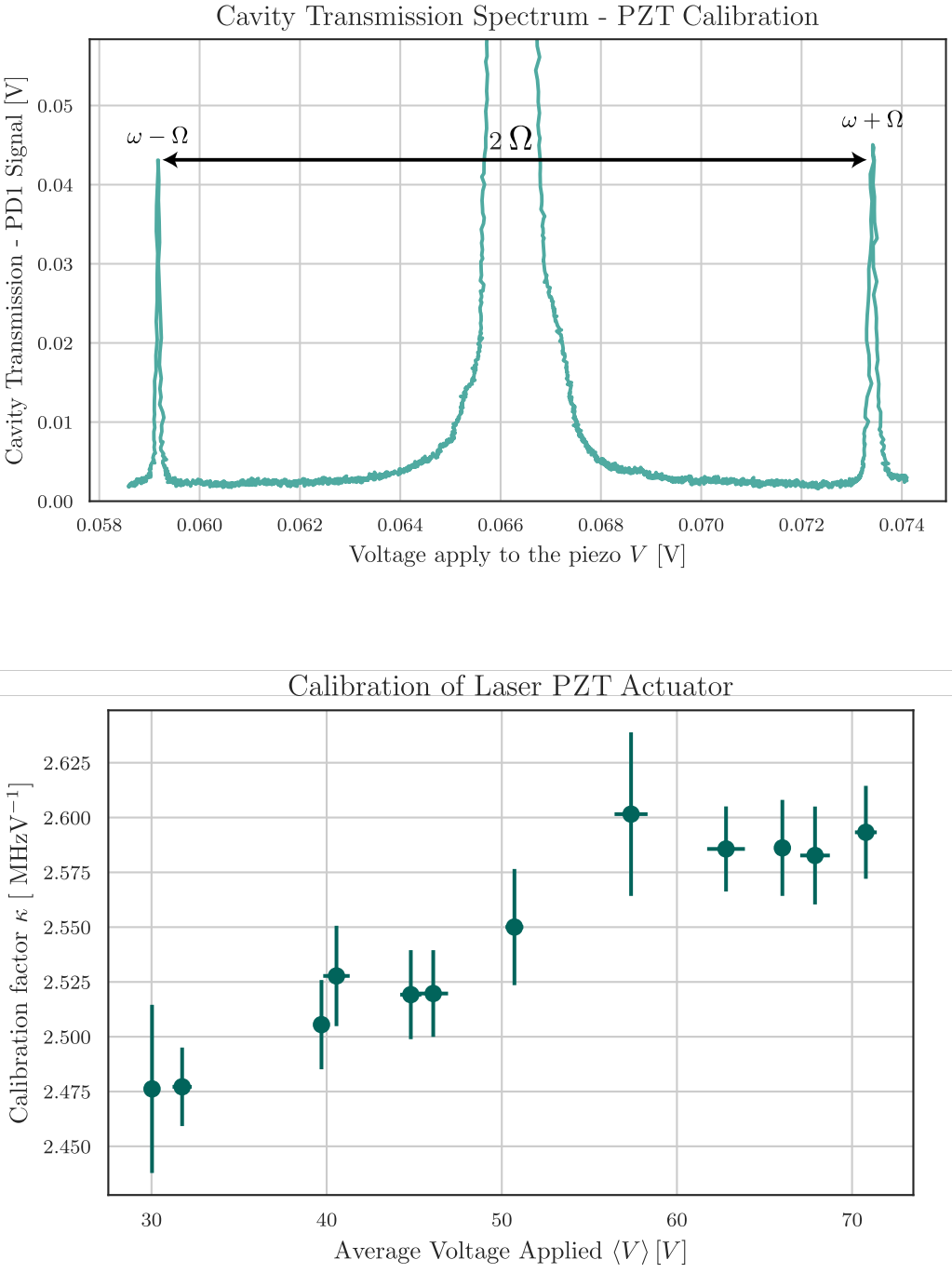

FIGURE IV.7: Cavity Spectrum near Resonance of the Fundamental Mode. (top plot) I used the cavity transmission to measure the voltage difference between the two sidebands peak. I used Eq. IV.33 to estimate the calibration factor, κ. (bottom plot) I recorded multiple spectra with different set-point for the Piezo Electric Transducer and estimated the dependency between the calibration factor and the average voltage, $\langle V \rangle$.

IV.1.3. *Optical Cavity*

Geometry Optimisation

The design of the optical cavity was based on the experimental constraints defined by the available hardware and by the requirements of the wavefront sensing technique. In particular, the hardware limitations were:

Maximum Free Spectral Range In order to characterise the cavity spectrum, I needed to scan the laser frequency over a Free Spectral Range, Δf_{fsr}. In this way, I could record the transmitted power by the cavity as a function of the laser frequency and detect all the High Order Mode Components of the incoming beam. The combination of the Mephisto Specification[7] and the HV amplifier defined a maximum dynamic range of 240 MHz. I decided to imposed a conservative requirement on the Free Spectral Range and set a maximum value of $\Delta f_{\text{fsr}} \leq 200\,\text{MHz}$. This corresponds to a minimum cavity length of $L_{cav} \geq 75\,\text{cm}$.

Cavity Stability At the time of the installation, I had only two mirrors available with Radius of Curvature, $RoC = 1.00(5)\,\text{m}$. The requirement on the cavity stability discussed in Section II.1.3 imposes $0 < (1 - L_{cav}/RoC_1)(1 - L_{cav}/RoC_2) < 1$. This corresponds to a limit to the cavity length, $L_{cav} \leq 200\,\text{cm}$.

Optical Table size The experiment was installed on a small optical bench with size 1.5 m×0.9 m. The small space limited the possible configurations for the optical layout and imposed a limit to the maximum cavity length of $L_{cav} \leq 100\,\text{cm}$.

These three aspects directly constrained the cavity length, L_{cav}, and they defined a possible range $L_{cav} \in [0.75\,\text{m}; 1.0\,\text{m}]$. On top of these requirements, the wavefront sensing theory imposed two other constraints:

Wave-front sensing The Eq. III.62 obtained in Section III assumes that all the frequency components (carrier and side-bands) of the second order modes are not resonant with the cavity. This request was necessary to neglect the beat note between the different second-order modes and to generate a signal proportional only to the mismatch parameters.

Pound-Drever-Hall Error Signal Each Transverse Mode generates an error signal for the longitudinal control. In order to reduce the coupling, the resonance frequency of the High Order Modes is kept outside the range defined by the Modulation frequency $[+f_{Mod}; -f_{Mod}]$

Following these guidelines, I optimised the cavity length to avoid the resonance of the first ten order modes and their sidebands. In particular, I estimated the distance between the resonance frequency of N-th order mode and the fundamental one using:

$$\Delta f_N = f_N - f0 = N\Delta f_{HOM} = N\frac{\Delta f_{\text{fsr}}}{\pi}\arccos(\sqrt{g_1 g_2}) \tag{IV.36}$$

where

$$g_1 * g_2 = \left(1 - \frac{L_{cav}}{RoC}\right)^2 \quad \text{and} \quad \Delta f_{\text{fsr}} = \frac{c}{2L_{cav}} \tag{IV.37}$$

[7] See Table IV.2 for more details.

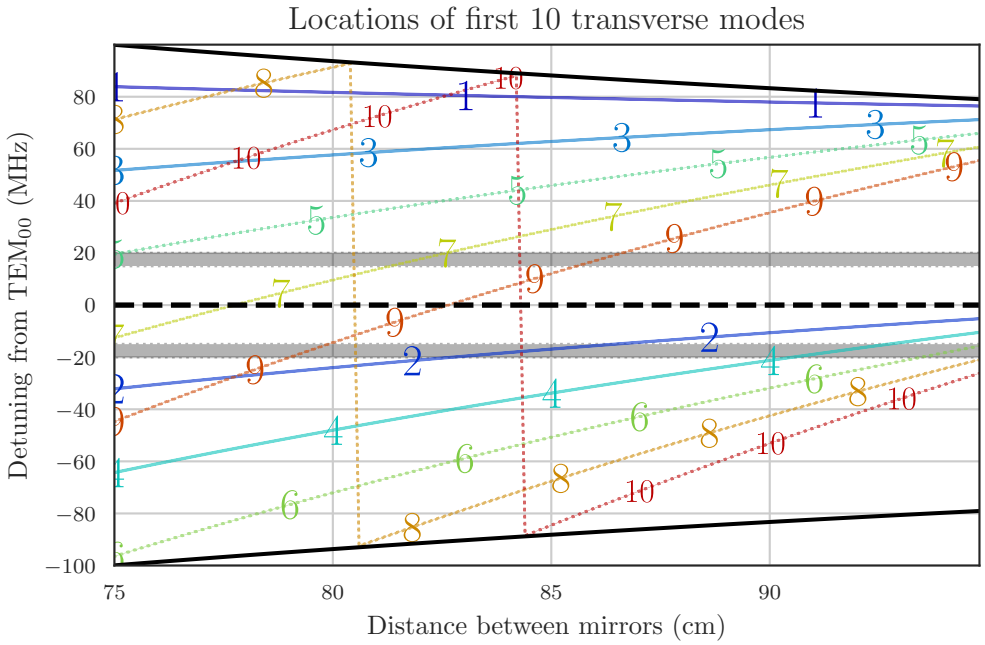

FIGURE IV.8: Optimisation of the Cavity Length, study on the High Order Mode Separation. This plot represents the resonance frequency of the first ten High Order Modes as a cavity length function. These frequencies are estimated with respect to the Fundamental Mode one, see Eq. IV.36. The zero line is highlighted with a dashed line, and the possible side-bands are indicated with two grey boxes at the centre frequency of EOM resonant Circuit, 16.6 MHz and −16.6 MHz. If a Higher Order Mode line crosses the zero(dashed line), that mode is co-resonance with the fundamental mode. If a Higher Order Mode line crosses the Modulation frequency region (grey boxes), one of its sidebands is co-resonance with the fundamental mode.

and I represented their dependency from the cavity length, L_{cav} in Fig. IV.8. I considered a region centred around the fundamental resonance frequency. Inside this area, I represented Δf_N module f_{fsr} as function of L_{cav}. Each High Order Mode frequency is labelled with its mode order, N, while the fundamental Mode is indicated with a black dashed line. Moreover, I highlighted the possible modulation frequencies using two grey boxes. This plot can be read as follow:

- If a Higher Order Mode line crosses the zero, that Mode is co-resonant with the fundamental Mode;
- If a Higher Order Mode line crosses the Modulation frequency region(two grey boxes), the side-bands of the corresponding Mode can be co-resonant with the Fundamental one[8]

From Plot in Fig. IV.8, we can see that around $L_{cav} \simeq 77.5\,\text{cm}$ and $L_{cav} \simeq 84\,\text{cm}$ the 7-th and 9-th order transverse modes are co-resonant with the fundamental one, and at $L_{cav} \simeq 82.5\,\text{cm}$ the second order modes cross the EOM modulation frequency.

[8] If the resonance frequency of the mode U_N has an offset comparable with the modulation frequency $2\pi N \Delta f_{HOM} \simeq \pm\Omega_{mod}$, the corresponding side-bands is shifted by $\mp\Omega_{mod}$ and it will be co-resonant with the Carrier of the Fundamental Mode.

I chose a cavity length of $L_{cav} = 80\,\text{cm}$ inasmuch as it is the longest cavity with the second order mode outside the sidebands region. Once I defined the cavity length, I used the equation derived in Section II.II.1 to estimate the theoretical parameters of the cavity. The values are collected in the second column of Table IV.5.

Parameter	Theoretical Value	Measured Value
L_{cav} (cm)	80	80.1(1) [b]
RoC_1 (m)	1	1.00(5) [c]
RoC_2 (m)	1	1.00(5) [c]
$\mathcal{F}$	1046	1.2(2) k [d]
Δf_{fsr} (MHz)	187	187.2(3)
Δf_{FWHM} (kHz)	180	152(34)
Δf_{HOM} (MHz)	82	82.7(4) [e]
$w_0^{(c)}$ (µm)	407	None
$z_0^{(c)}$ (cm)	40 [a]	None

TABLE IV.5: Linear Cavity Parameters. Column two reports the parameters estimated by theory. Column three reports the values experimentally estimated. [a] Reference $z = 0$ at the input mirror; [b] Estimate from the Δf_{fsr}; [c] From manufacture; [d] Estimate from the Δf_{fsr} and Δf_{FWHM}; [e] Average between two estimation describe in Eq. IV.46

Experimental Characterisation

The linear cavity was experimentally characterized using the cavity spectrum, defined as the relationship between the transmitted optical power and the laser frequency.

Resonance Line Width

The cavity Line Width was estimated by studying the resonance peak of the Fundamental Mode. From Eq. II.19, we have that the transmitted power from the cavity is given by

$$P_t(\omega) = |t_{cav}|^2 = P_0|t_1t_2|^2\frac{1}{(1-r_1r_2)^2 + 4r_1r_2\sin^2(\nu(\omega,0))} \tag{IV.38}$$

where t_i and r_i are the transmittance and reflectance of the cavity mirrors, and

$$\nu(\omega, N) = \pi\frac{\omega - f_N}{\Delta f_{\text{fsr}}} \tag{IV.39}$$

is the normalised frequency defined as the difference between the laser frequency, ω, and the cavity resonance f_N, Eq. II.84 divided by the Free spectral Range, Δf_{fsr}. The transmitted power in Eq. IV.38 can be rewritten as function of its maximum value P_{max}:

$$P_t(\omega) = \underbrace{\frac{P_0|t_1t_2|^2}{(1-r_1r_2)^2}}_{P_{\text{max}}}\frac{1}{1 + 4\frac{r_1r_2}{(1-r_1r_2)^2}\sin^2(\nu(\omega,0))} \tag{IV.40}$$

that, in case of high Finesse, can be approximated as

$$P_t(\omega) = P_{\text{max}}\frac{1}{1 + 4\left(\frac{\mathcal{F}}{\pi}\right)^2\sin^2(\nu(\omega,0))} \tag{IV.41}$$

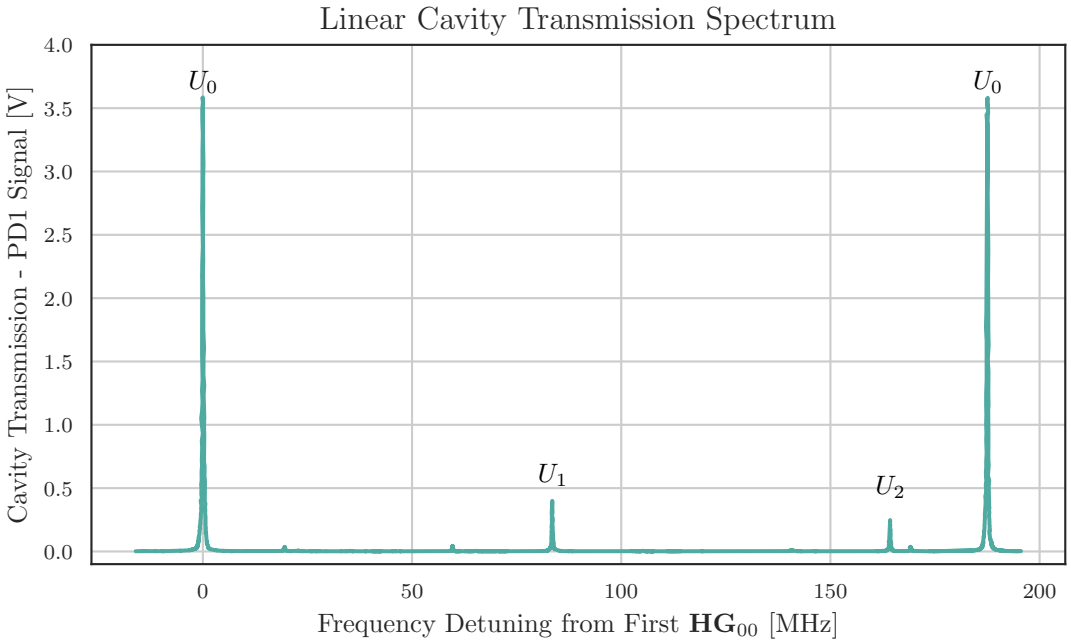

FIGURE IV.9: Calibrated Cavity Spectrum with HOM. The first two High Order Modes, U_1 and U_2, where artificially exited by misaligning and mismatching the input beam. This spectrum was used to estimate the Free Spectral Range, Δf_{fsr}, and the High Order Mode Separation, Δf_{HOM}. The frequency calibration is discussed in Section IV.1.2.

On top of this, near resonance $\nu(\omega) \simeq 0$, we can highlight the difference between the laser frequency and the resonance one

$$\omega - f_0 = \delta\omega + l\Delta f_{\text{fsr}} \tag{IV.42}$$

where $\delta\omega$ is the remainder of the division $\omega/\Delta f_{\text{fsr}}$. In this case, we can assume $\delta\omega \ll 1$ and approximate the normalised frequency as

$$\nu(\omega, N) = \pi\frac{\delta\omega}{\Delta f_{\text{fsr}}} + l\pi \quad \rightarrow \quad \sin^2(\nu(f,0)) \simeq \left(\pi\tfrac{\delta\omega}{\Delta f_{\text{fsr}}}\right)^2$$

that allows expanding the power peak as

$$P_t(\delta\omega) \simeq P_{\text{max}}\frac{1}{1+\left(2\mathcal{F}\frac{\delta\omega}{\Delta f_{\text{fsr}}}\right)^2} = \frac{P_{max}}{1+\left(2\frac{\delta f}{\Delta f_{FWHM}}\right)^2} \tag{IV.43}$$

where in the last passage, we use the definition of Finesse given in Eq. II.17, $\mathcal{F} = \Delta f_{\text{fsr}}/\Delta f_{FWHM}$.

I used this model to study the cavity spectrum represented in Fig. IV.9. These measurements were obtained using the calibration factor estimated in Section IV.1.2 to study the transmitted power as a function of the laser frequency. In particular, I collected multiple spectra of the cavity, and for each one, I fitted the resonance peak using the Lorentzian function:

$$\mathbf{L}(x) = \frac{I_{max}}{1+\left(2\frac{f-f_0}{\Delta f_{FWHM}}\right)^2} \tag{IV.44}$$

The line widths, Δf_{FWHM}, of the fundamental Mode were averaged in order to obtain the following estimation:

$$\Delta f_{\mathrm{FWHM}} = 152(34)\,\mathrm{kHz} \tag{IV.45}$$

.

Free Spectral Range and High Order Mode Separation

The Free Spectral Range and High Order Separation were estimated by studying the distance among the resonance peaks of the Transverse Modes of different orders. I misaligned and mismatched the cavity to excite the first and second order mode components, and I measured the spectrum reported in Fig. IV.9. During the measurement, I verified the correspondence between the resonance peaks and the mode order by recording the transmitted beam shape with the infrared camera, CAM in Fig IV.1. I used the first occurrence of the Fundamental Mode as zero reference and estimated the relative frequency shift using the interpolation of the Lorentzian function. I used these data to estimate the experimental values in Table IV.5. The distance between the two peaks of the fundamental Mode, U_0, is the Free Spectral Range, Δf_{fsr}; the distances between the first fundamental Mode and the High Order Modes give the High Order Mode Separation, Δf_{HOM}:

$$\begin{aligned} f_1 - f_0 &= \Delta f^{(1)}_{\mathrm{HOM}} = 83.5(3)\,\mathrm{MHz} \\ f_2 - f_0 &= 2\Delta f^{(2)}_{\mathrm{HOM}} = 163.9(3)\,\mathrm{MHz} \end{aligned} \tag{IV.46}$$

where f_1 is the resonance frequency of the first High Order Mode and f_2 of the second one.

IV.1.4. *Mode Matching Telescope*

The validation of the Wave-front sensor technique was focused on three different aspects: the ability to discriminate the mismatch parameters, the linearity of the error signals and the dynamic range of the sensor. These goals impose specific requirements on the manipulation of the incoming beam shape. In particular, we need to independently control each mismatch degree defined in Eq. II.137, and this actuation should scan a large region of the parameters space.

These requirements are directly imposed on the Mode Matching telescope that should be able to separately control the mismatch parameters of the incoming beam, defined in Eq. II.137. The experimental activities were divided into two separate steps: First, I validated the Spherical mode matching sensing based on the Mode Converter; after that, I upgraded the optical setup to validate the Astigmatic mode matching sensing.

Spherical Mode Matching Telescope

The first step was the design of a Spherical Mode Matching telescope able to separately actuate on the mode matching parameters, β and γ, defined in Eq. II.137, and explore a large region of their phase space. The telescope is represented in the Orange box in Figure IV.1, and it was composed of two lenses with Effective Focal Length[9] $f_3 =$

[9] The Effective Focal Length was estimated using the substrate geometry and the refractive index of the material.

226 mm and $f_4 = 282$ mm mounted on two linear translation stages.[10] The telescope was controlled by changing the lenses positions, L_3 and L_4, with two veneer screws.

The analytical relationship between the position of the lenses and the beam parameters inside the cavity can be estimated with the $\mathbb{ABCD}$ rule defined in Eq. II.63. In particular, I considered the beam shape before the telescope, w_0^b and z_0^b, and I propagated these values by taking into account the complete diffraction system: Lens_3, Lens_4 and the input mirror of the cavity, IM_cav. The effective $\mathbb{ABCD}$ is defined by:

$$\mathbb{ABCD}(L_3, L_4) = \begin{pmatrix} 1 & 0 \\ -\frac{1}{f_{mir}} & 1 \end{pmatrix} \begin{pmatrix} 1 & \Delta L_{after} \\ 0 & 1 \end{pmatrix} \begin{pmatrix} 1 & 0 \\ -\frac{1}{f_4} & 1 \end{pmatrix} \begin{pmatrix} 1 & \Delta L_{mid} \\ 0 & 1 \end{pmatrix} \begin{pmatrix} 1 & 0 \\ -\frac{1}{f_3} & 1 \end{pmatrix} \begin{pmatrix} 1 & L_3 \\ 0 & 1 \end{pmatrix} \tag{IV.47}$$

where L_3 is the position of Lens_3 with respect to the beam waist position, z_0^b; $L_{mid} = L_4 - L_3$ is the distance between the two lenses; $L_{after} = L_{mir} - L_4$ is the distance between Lens_4 and the input mirror, and f_{mir} is the effective focal length of the input mirror:

$$f_{mir} = -\frac{1 - n_1}{\mathrm{RoC}_1} \simeq 450(20)\,\mathrm{mm} \tag{IV.48}$$

estimated by the Mirror Radius of Curvature $\mathrm{RoC} = 1.00(5)$ m and the refractive index $n_1 = 1.45$ of the substrate.

Using this $\mathbb{ABCD}$ matrix and knowing the beam parameters before the telescope (z_0^b, w_0^b), we can estimate the analytical relationship between the lens positions (L_3, L_4) and the shape of the beam injected inside the cavity, $z_0^{(cav)}(L_3, L_4)$ and $w_0^{(cav)}(L_3, L_4)$. Combining these values with the beam parameters of the resonance mode, $\hat{z}_0$ and $\hat{w}_0$, estimated using Eq. II.73, we can estimate the normalised mismatch parameters:

$$\gamma(L_3, L_4) = \frac{z_0(L_3, L_4) - \hat{z}_0}{2z_R} \tag{IV.49}$$

$$\beta(L_3, L_4) = \frac{w_0(L_3, L_4) - \hat{w}_0}{2w_0} \tag{IV.50}$$

$$\epsilon = \sqrt{\beta^2(L_3, L_4) + \gamma^2(L_3, L_4)} \tag{IV.51}$$

as a function of the telescope configuration, (L_3, L_4). However, this relationship is not trivial, and it hides important information. For this reason, I decided to linearise this model:

$$\begin{pmatrix} \gamma \\ \beta \end{pmatrix} \simeq \begin{pmatrix} \gamma_0 \\ \beta_0 \end{pmatrix} + \begin{pmatrix} \partial_{L_3}\gamma & \partial_{L_4}\gamma \\ \partial_{L_3}\beta & \partial_{L_4}\beta \end{pmatrix}_{(L_3^0, L_4^0)} \cdot \begin{pmatrix} \delta L_3 \\ \delta L_4 \end{pmatrix} \tag{IV.52}$$

where δL_3 and δL_4 are the lenses movement with respect to the initial position (L_3^0, L_4^0). In this way, all the relevant information about the telescope actuation is contained in the Jacobian matrix:

$$\Gamma = \begin{pmatrix} \partial_{L_3}\gamma & \partial_{L_4}\gamma \\ \partial_{L_3}\beta & \partial_{L_4}\beta \end{pmatrix} \tag{IV.53}$$

generally called Driving Matrix.

[10] The choice of the focal length was imposed by the table dimension and by the availability of lenses at the time of installation.

The main advantage of this approximation is the invertibility of the linear relationship between lens movements $(\delta L_3, \delta L_4)$ and mode matching parameters, (γ, β). By inverting this matrix, we can estimate the required movements in order to have a specific combination of γ and β:

$$\begin{pmatrix} \delta L_3 \\ \delta L_4 \end{pmatrix} = \Gamma^{-1} \begin{pmatrix} \delta\gamma \\ \delta\beta \end{pmatrix} \tag{IV.54}$$

and we can separately control the beam parameters by defining two sets of lens positions, one that induces a change on γ but keeps β constant and another one that does the opposite:

$$\begin{pmatrix} \delta L_3^{\gamma} \\ \delta L_4^{\gamma} \end{pmatrix} = \Gamma_1^{-1}\delta\gamma \quad \text{and} \quad \begin{pmatrix} \delta L_3^{\beta} \\ \delta L_4^{\beta} \end{pmatrix} = \Gamma_2^{-1}\delta\beta \tag{IV.55}$$

where Γ_i^{-1} is the (i) column of the matrix Γ^{-1}, ΔL_j^{γ} and ΔL_j^{β} are the variation of lens j positions to induce a variation of $\Delta\gamma$ and $\Delta\beta$, separately.

The estimation of this linearised model was obtained in two different way. First, I used the tool FINESSE [43] to simulate the function Eq. IV.49 and Eq. IV.50, and I numerically estimated the linearized model of the telescope, defined in Eq. IV.53. Second, I experimentally characterised the telescope action setup by measuring the beam shape between the cavity mirrors as a function of L_3 and L_4.

Simulation of the Spherical Telescope actuation

Using the software FINESSE [43], I simulated the optical setup described in Fig. IV.1. I design the *kat file*[11] reported in Appendix B.II.1 and I implemented a code to control the telescope by changing the positions of the lenses, δL_i, reported in Appendix B.II.2.

In this way, I estimated Eq. [IV.49, IV.50, IV.51] over the telescope range[12]. The results, reported in Fig. IV.10, give an overview of the telescope actuation. In particular, we can see that the telescope action is not linear over the whole range and the linearization described in Eq. IV.52 can be generally applied. For this reason, I focused the analysis in the identification of a region of the space $(L_3 \times L_4)$ in which the linearized model is trustable.

In order to define the limit of the linearized model, I estimated the Jacobian using the gradient function of the numpy package[44]:

$$\vec{\nabla}\gamma[L_3, L_4] = \begin{pmatrix} \partial_{L_3}\gamma \\ \partial_{L_4}\gamma \end{pmatrix}^T \quad \text{and} \quad \vec{\nabla}\beta[L_3, L_4] = \begin{pmatrix} \partial_{L_3}\beta \\ \partial_{L_4}\beta \end{pmatrix}^T \tag{IV.56}$$

that can be use to estimate the Driving matrix as:

$$\Gamma = \begin{pmatrix} \vec{\nabla}\gamma[L_3, L_4] \\ \vec{\nabla}\beta[L_3, L_4] \end{pmatrix} \tag{IV.57}$$

This matrix has been calculated for each point $(\delta L_3^{(i)}, \delta L_4^{(j)})$ obtained by the simulation and the results are reported in Figure IV.11. In particular, the vectors, $\vec{\nabla}\gamma[L_3, L_4]$ and

[11] A kat file is a file which contains all the relevant information of the layout of the optical setup. It defines the properties of the optics and their reciprocal distances.

[12] I simulated the first version of the setup in which the lenses where mounted on two linear stages with dynamic range of 50 mm.

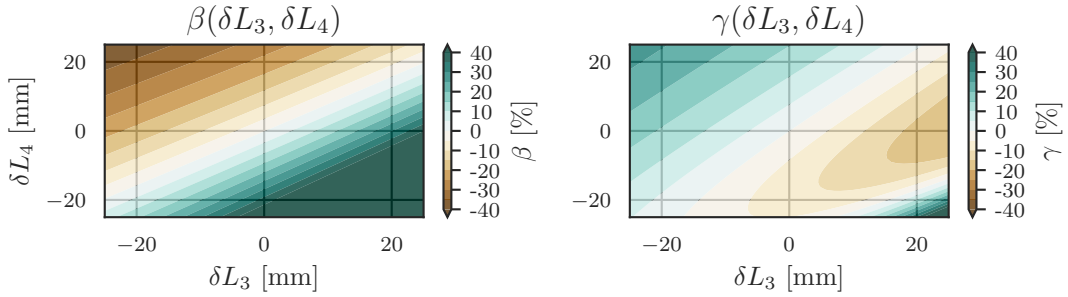

FIGURE IV.10: Simulation of the Mode Matching telescope. The two plots represent the telescope actuation on the mismatch parameters β(right) and γ(left) for each configuration of the lenses, $(\delta L_3, \delta L_4)$

.

$\vec{\nabla}\beta[L_3, L_4]$ are represented with their orientation angles, Θ_γ and Θ_β:

$$\Theta_\gamma = \arctan\left(\frac{\partial_{L_3}\gamma}{\partial_{L_4}\gamma}\right) \quad \text{and} \quad \Theta_\beta = \arctan\left(\frac{\partial_{L_3}\beta}{\partial_{L_4}\beta}\right) \tag{IV.58}$$

and their module, $|\nabla\gamma|$ ans $|\nabla\beta|$:

$$\begin{aligned} |\nabla\gamma| &= \sqrt{(\partial_{L_3}\gamma)^2 + (\partial_{L_4}\gamma)^2} \\ |\nabla\beta| &= \sqrt{(\partial_{L_3}\beta)^2 + (\partial_{L_4}\beta)^2} \end{aligned} \tag{IV.59}$$

The implementation of the control described in Eq. IV.55, required to estimated a driving matrix, Γ, that represent thelinearization over a wide areas in the $(\delta L_3 \times \delta L_4)$ space. However, the maps in Figure IV.11 show that the gradients are constant only if the distance between the lenses does not change, $\delta L_3 \simeq \delta L_4$.

Starting from this consideration, I decided to proceed as follow. First, I defined an arbitrary region around the best mode matching configuration and I forced the linearization inside it. After that, I numerically verified the difference between the linearized model and the effective evolution of the mismatch.

The linearization was obtained by averaging the gradient inside the dashed region in Figure IV.11. In particular, I estimated:

$$\Gamma_{\text{sim}} = \frac{1}{n_x n_y}\sum_{i,j}\Gamma(x_i, y_j) = \begin{pmatrix} -7.8 & 6.0 \\ 11.7 & -14.8 \end{pmatrix} 10^{-2}\text{mm} \tag{IV.60}$$

with $\delta L_3^{(i)} \in [-10\,\text{mm}, 10\,\text{mm}]$ and $\delta L_4^{(j)} \in [-10\,\text{mm}, 10\,\text{mm}]$, and $n_3 n_4$ are the normalisation factors. I considered the average matrix, Γ_{sim} as the linearized model of the telescope actuation.

In order to validate this linearized model, I estimated the response of the telescope based on the matrix in Eq. IV.60:

$$\begin{pmatrix} \delta\tilde{\gamma} \\ \delta\tilde{\beta} \end{pmatrix} = \Gamma_{\text{sim}} \begin{pmatrix} \delta L_3 \\ \delta L_4 \end{pmatrix}, \tag{IV.61}$$

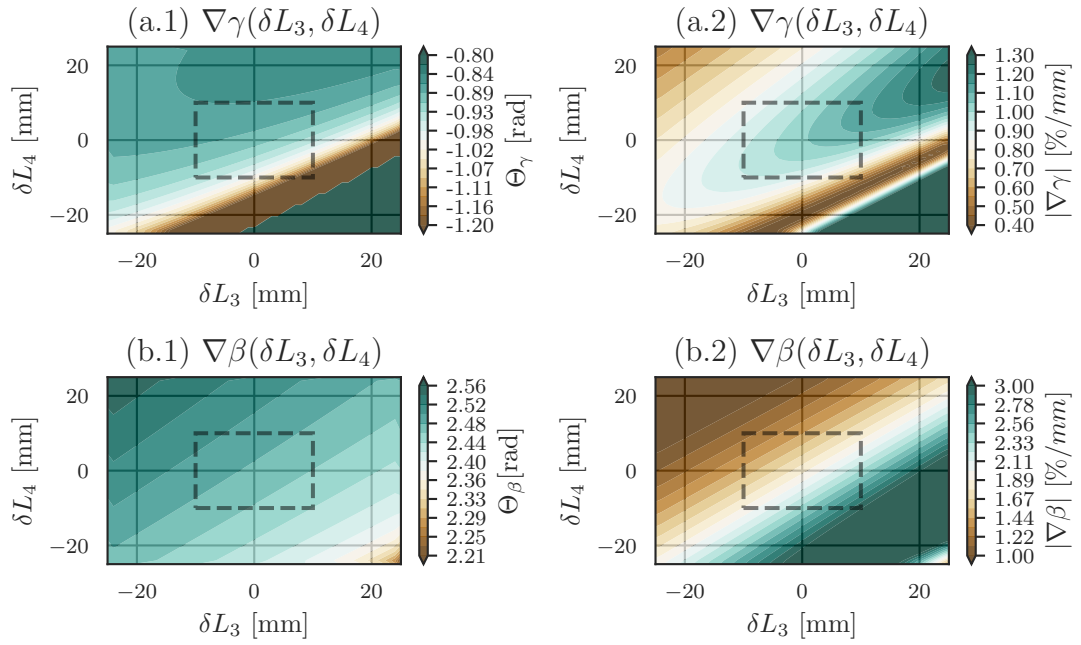

FIGURE IV.11: Representation of $\nabla\gamma$ (top plots) and $\nabla\beta$ (bottom plots) estimated from Fig. IV.10. The vectors are presented using their orientation angle with respect to the δL_3 direction ($\Theta_{\beta/\gamma}$ left plots) and their module, ($|\nabla(\beta/\gamma)|$ right plots). The region used for the estimation of Eq. IV.60 is highlighted by the dashed square.

and I estimated the normalised residuals with the response estimated by the $\mathbb{ABCD}$ model, $\gamma(\delta L_3, \delta L_4)$ and $\beta(\delta L_3, \delta L_4)$:

$$\Sigma_\gamma = 1 - \frac{1}{\gamma(\delta L_3, \delta L_4)} \left(\nabla\gamma \cdot \begin{pmatrix} \delta L_3 \\ \delta L_4 \end{pmatrix} + \gamma_0 \right) \tag{IV.62}$$

$$\Sigma_\beta = 1 - \frac{1}{\beta(\delta L_3, \delta L_4)} \left(\nabla\beta \cdot \begin{pmatrix} \delta L_3 \\ \delta L_4 \end{pmatrix} + \beta_0 \right) \tag{IV.63}$$

The absolute module of the residual represents the distance of the linearised model with respect to the effective actuation and quantifies the systematic error induced by a forced linearization. The data are represented in Fig. IV.12 where we see that the residuals are minimised in the brown area around $\delta L_3 \simeq \delta L_4$. We can assume that in this region the linearization is a good approximation of the effective response.

The next step was the estimation of the inverse of the driving matrix, Γ. This was done numerically using the numpy library[44], and it resulted in:

$$\Gamma^{-1} = \begin{pmatrix} -0.32 & -0.13 \\ -0.25 & -0.17 \end{pmatrix} 10^2 \text{mm} \tag{IV.64}$$

I tested this matrix with a second simulation in order to validate if the matrix in Eq. IV.64 is able to guide the telescope actuation. I defined two auxiliary parameters, $\tilde{\gamma}$ and $\tilde{\beta}$, which represent the desired mismatch coefficients and I used Γ^{-1} as proxy to control the telescope. In particular, I simulated the telescope action described by:

$$\begin{cases} \gamma(\delta\tilde{L}_3, \delta\tilde{L}_4) \\ \beta(\delta\tilde{L}_3, \delta\tilde{L}_4) \end{cases} \quad \text{where} \quad \begin{pmatrix} \delta\tilde{L}_3 \\ \delta\tilde{L}_4 \end{pmatrix} = \Gamma^{-1} \cdot \begin{pmatrix} \tilde{\gamma} \\ \tilde{\beta} \end{pmatrix} \tag{IV.65}$$

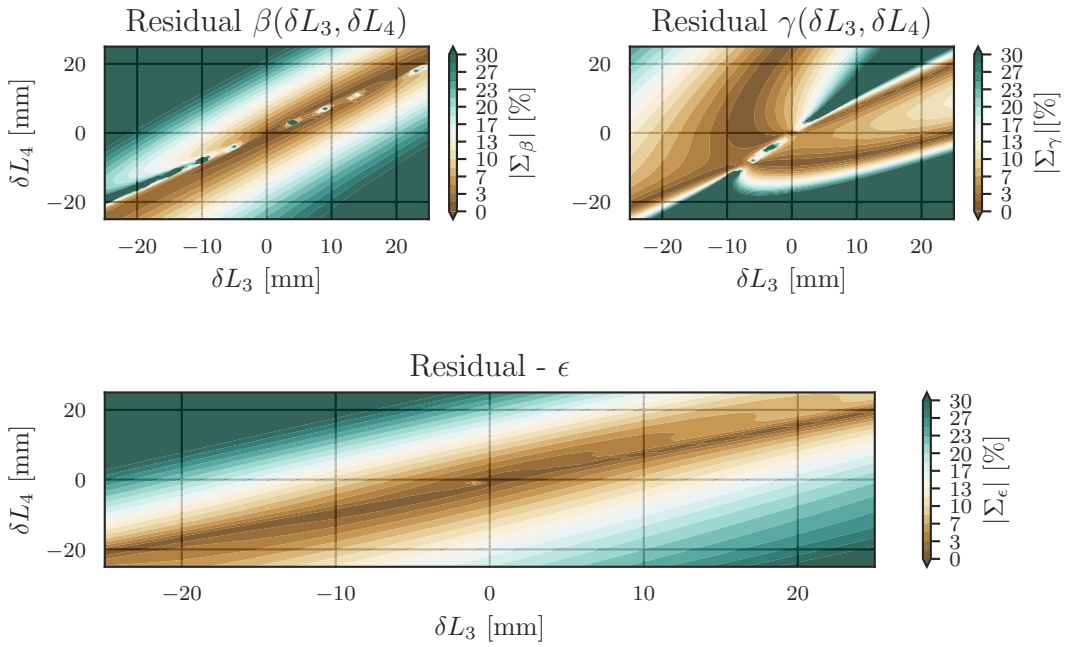

FIGURE IV.12: Normalised Residual between the ABCD model and the linearized one. Top plots describes the difference between the estimation of the mismatch parameters β(left) and γ(right). Bottom plot represent the difference between total mismatch. We can identify a region where the residual is less than 10 % around $\delta L_3 \simeq \delta L_4$.

and $\beta(\delta\tilde{L}_3, \delta\tilde{L}_4)$ and $\gamma(\delta\tilde{L}_3, \delta\tilde{L}_4)$ are the telescope response simulated using the Finesse software with the code in Appendix B.II.3.

The results of this simulation are reported in Fig. IV.13(top) where the mismatch degree of freedom are visible decoupled by the inverted driving matrix. The evolution of $\beta(\delta\tilde{L}_3, \delta\tilde{L}_4)$ is represented by horizontal level curves, whiel the evolution of γ is reprensented by vertical ones.

Moreover, I used this results to study the compatibility between the ABCD model and the linearized one. I estimated the normalised residual defined in Eq. IV.62 and Eq. IV.63 and I represented the results in Fig. IV.13(bottom), together with the not normalised residual(black lines):

$$\Delta\gamma = \gamma - \tilde{\gamma} \tag{IV.66}$$

$$\Delta\beta = \beta - \tilde{\beta} \tag{IV.67}$$

Using the inverted driving matrix, Eq.IV.64, and the Eq. IV.55, I defined two paths for the telescope lenses in order to control the two parameters separately: $(L_3, L_4)_\gamma$, in which γ changes between ± 10 %, and $(L_3, L_4)_\beta$ in which β changes between ± 10 %. These two paths are represented in Fig. IV.14, where I highlighted the possible dynamic range defined by the actuators.

Experimental Characterisation of the Telescope

The Finesse simulations and the experimental setup are not perfectly equivalent. These differences are generated by the uncertainty in the input parameters as optics positions or

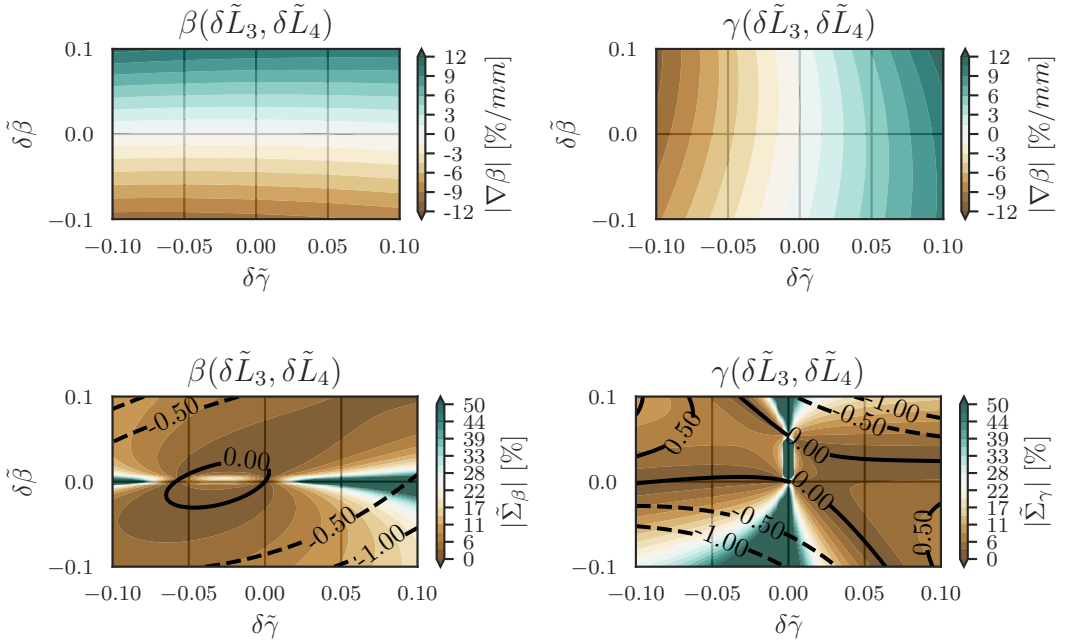

FIGURE IV.13: Validation of Driving matrix - Simulation of the Mode Matching telescope response. I used the Matrix Γ^{-1}, in Eq. IV.64, to control the telescope as a function of $\tilde{\gamma}$ and $\tilde{\beta}$ that represent the requested values of mismatch parameters γ and β. Top plots describe the telescope control on the mismatch parameters β(right) and γ(left). Bottom plots describes the difference between the estimation of the mismatch parameters β(left) and γ(right). We can identify a region where the residual is less than 10 % around $\delta L_3 \simeq \delta L_4$. The black lines represent the effective residuals, $\Delta\gamma = \gamma - \tilde{\gamma}$ and $\Delta\beta = \beta - \tilde{\beta}$ in % unit.

initial beam parameters. A perfect match between the simulations and the experiment is beyond the scope of this Thesis, inasmuch we used the simulation only as a preliminary investigation and all the results were experimentally validated and optimised.

Validation of the Telescope Simulation

The first step was the validation of the FINESSE simulation. I used the two configurations defined in Fig. IV.14 to control the telescope, and I estimated the beam profile inside the Linear Cavity. In particular, the measurement protocol was:

1. Set the telescope in the requested configuration $(L_3, L_4)_i$;
2. Alignment of the cavity, in order to reduce the amplitude of 1-st order modes $|U_1|$ to less than 3 %[13]
3. Characterise the beam shape between the Cavity mirror using the method described in Appendix A.I.1.
4. Change of the telescope configuration $(L_3, L_4)_{i+1}$;

[13] The amplitude of the mode was estimated as $|U_1| = \sqrt{\frac{P_1}{P_0}}$, where P_i is the peak height of the mode ith in the cavity spectrum.

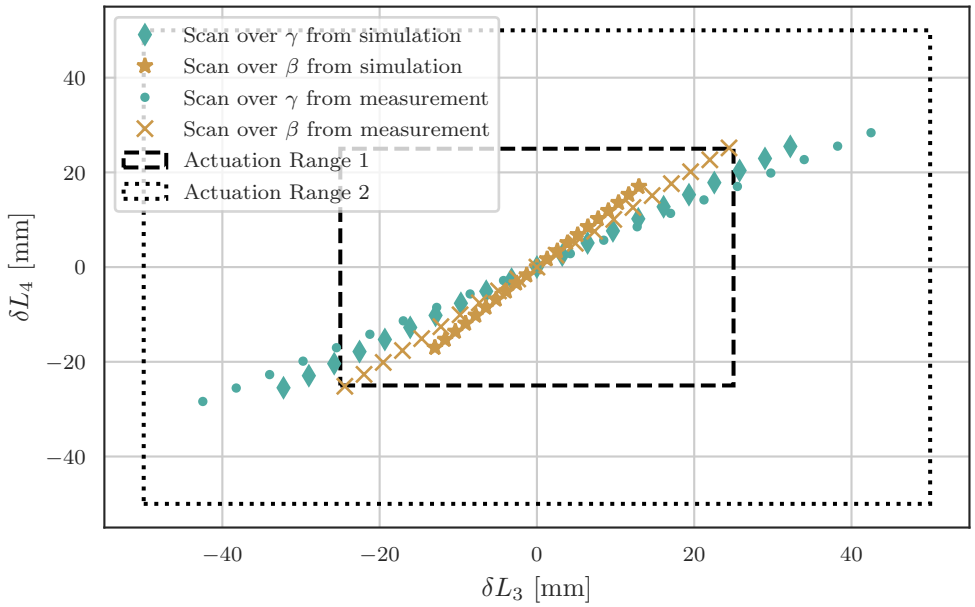

FIGURE IV.14: Telescope Paths to control β and γ, separately. Based on the Eq. IV.55, I used two driving matrices to define the telescope configurations that allow a decouple action on the mismatch parameters. The paths estimated from the simulated driving matrix, Eq. IV.73, are represented from Diamond/Green markers for the $(L_3, L_4)_\gamma$ and Star/Brown markers for the $(L_3, L_4)_\beta$. The paths estimated from the simulated driving matrix, Eq. IV.73, are represented from Dots/Green markers for the $(\tilde{L}_3, \tilde{L}_4)_\gamma$ and from Cross/Brown markers for the $(\tilde{L}_3, \tilde{L}_4)_\beta$. In both cases, I scanned γ and β between $\pm 10\,\%$. The black dashed lines represent the actuation range given by the first design of the telescope, while the dotted lines represent the actuation range of the final setup.

In this way, I was able to estimate the beam parameters inside the cavity for each telescope configuration. After that, I normalised these values using the Eq. IV.49 and Eq. IV.50, reported here for simplicity:

$$\gamma(L_3, L_4) = \frac{\langle z_0(L_3, L_4)\rangle - \hat{z}_0}{2\hat{z}_R} \tag{IV.68}$$

$$\beta(L_3, L_4) = \frac{\langle w_0(L_3, L_4)\rangle - \hat{w}_0}{2\hat{w}_0} \tag{IV.69}$$

where $\hat{w}_0$ and $\hat{z}_0$ are the theoretical values estimated in Section IV.1.3 and $\langle z_0(L_3, L_4)\rangle$ and $\langle w_0(L_3, L_4)\rangle$ are the common waist position and waist dimension of the beam that enters into the cavity measured for the (L_3, L_4) configuration of the mode matching telescope. Moreover, I used the standard approach for the error propagation [45] to estimate the variance of these parameters:

$$\sigma_\beta = \frac{1}{2\hat{w}_0}\frac{\sigma^2_{w_0^{(\tilde{x})}} + \sigma^2_{w_0^{(\tilde{y})}}}{2} \quad \text{and} \quad \sigma_\gamma = \frac{1}{4\hat{z}_R}\frac{\sigma^2_{z_0^{(\tilde{x})}} + \sigma^2_{z_0^{(\tilde{y})}}}{2} \tag{IV.70}$$

The measured mismatch were represented in the parameter space $(\gamma \times \beta)$, Fig. IV.15, where I distinguished two different data sets: $(L_3, L_4)_k$ is the data-set in which only $k =$

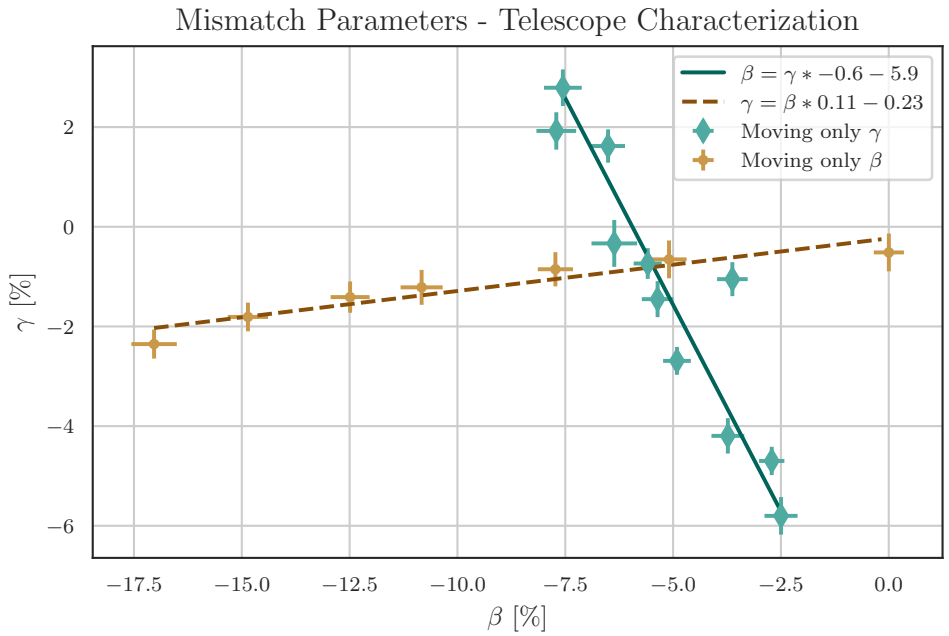

FIGURE IV.15: Validation of the Theoretical Driving Matrix. I used the matrix in Eq. IV.60 as proxy to control the telescope and I move the lenses in order to change one parameter at the time. I reported the data in the parameter space $(\gamma \times \beta)$ and I separated them in two sets: brown dots are moving only β and green diamonds are moving only γ. I fit the models described in Eq. IV.71 to quantify the decoupling on the telescope actuation: continued line for $\beta(\gamma)$ and dashed line for $\gamma(\beta)$.

β, γ should be changed. In case of a perfect separation, the data should be distributed along two lines: one parallel to the γ axis and another one parallel to the β axis. This behaviour can be quantified by interpolating the two data set with:

$$\begin{aligned} \beta &= a_{\beta,\gamma} * \gamma + \beta_0 \quad \text{for} \quad (L_3, L_4)_\gamma \\ \gamma &= a_{\gamma,\beta} * \beta + \gamma_0 \quad \text{for} \quad (L_3, L_4)_\beta \end{aligned} \tag{IV.71}$$

where the coefficients $|a_{\beta,\gamma}|$ and $|a_{\beta,\gamma}|$ can be considered as figures of merit for the decoupling. In case of perfect decoupling, these parameters should be zero and they grow proportionally to the coupling between γ and β.

$p_i(b_j)$	a_{p_i,b_j} [none]	$p_{0,i}$ [%]	R^2-value
$\beta(\gamma)$	−0.60(8)	−6.0(2)	0.87
$\gamma(\beta)$	0.11(2)	−0.2(2)	0.89

TABLE IV.6: Interpolation parameters from Fig. IV.15. The slope parameters, a_{p_i,b_j} are used as a figure of merit of the decoupling between the actuation on the two mismatch parameters, β and γ. R^2-value is defined as the proportion of the variation in the dependent variable that is predictable from the independent variables[46, p. 344].

The data reported in Figure IV.15 and the corresponding interpolation parameters reported in Table IV.6 show that the telescope dynamic range is compatible with the expected one: γ between −6 % and 2 % and β between −17.5 % and 0 %, but the telescope was not working around $\beta = 0$ and the control of γ is not perfectly decoupled from β.

Starting from these results, I improved the telescope with two minor modifications. I kept the same lenses but changed the linear stages to increase the dynamic from 45 mm to 90 mm, and I moved the lens positions in order to have the centre of the linear stage around $\beta \simeq \gamma \simeq 0$. After these upgrades, I proceed with an experimental characterisation of the telescope based on the same approach used for the simulation analysis.

Measurement and validation of the Driving Matrix

The experimental estimation of the telescope driving matrix was obtained by moving one lens at the time and estimating the mismatch parameters as described in Eq. IV.68 and Eq. IV.69. In this way, I was able to decouple the action of the lenses and consider the linear relationship:

$$\begin{aligned}
\beta(\delta L_3, 0) = \beta_3(\delta L_3) = \frac{\partial \beta}{\partial L_3} \cdot \delta L_3 + \beta_{0,3} \quad \text{and} \quad \beta(0, \delta L_4) = \beta_4(\delta L_4) = \frac{\partial \beta}{\partial L_4} \cdot \delta L_4 + \beta_{0,4} \\
\gamma(\delta L_3, 0) = \gamma_3(\delta L_3) = \frac{\partial \gamma}{\partial L_3} \cdot \delta L_3 + \gamma_{0,3} \quad \text{and} \quad \gamma(0, \delta L_4) = \gamma_4(\delta L_4) = \frac{\partial \gamma}{\partial L_4} \cdot \delta L_4 + \gamma_{0,4}
\end{aligned} \tag{IV.72}$$

where we defined β_i and γ_i as mismatch parameters as function of only lens $i = 3, 4$

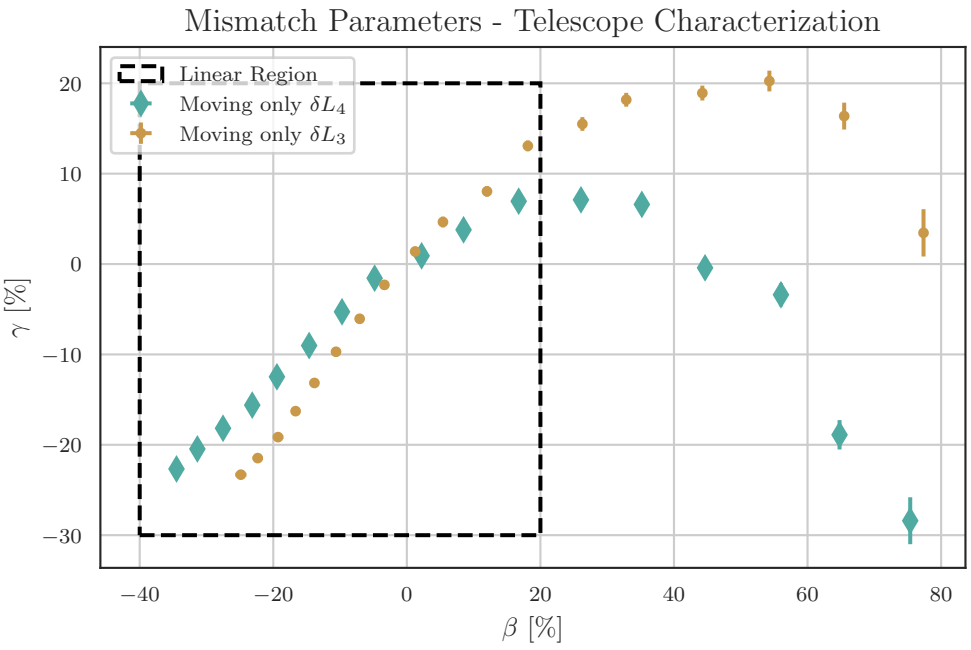

FIGURE IV.16: Experimental characterisation of the Mode Matching Telescope. I measured the telescope response by moving one lens at the time. For each point, I measured the beam shape inside the cavity and I estimated the mismatch parameters, β and γ. The data are represented in the $(\gamma \times \beta)$ parameter space: the path along δL_3 is represented by the diamond markers and the one along δL_4 by the circle markers. We assume the response inside the dashed square as linear and select this region for the experimental estimation of the Driving matrix Fig IV.17.

The data recorded in Fig. IV.16 show a not linear trend over the whole range. This behaviour was expected inasmuch I moved the telescope outside the linear region

identified in simulation analysis, $\delta L_3 \simeq \delta L_4$. I focused the analysis only in the area indicated by the dashed box in Fig. IV.16, Those points satisfy the condition $\beta < 20\,\%$ and can be considered inside the linear response region. I interpolated these data inside using the model described in Eq. IV.72. The results, collected in Table IV.7, were used to define the new inverted driving matrix:

$$\tilde{\Gamma}^{-1}_{exp} = \begin{pmatrix} 0.67(2) & 0.76(4) \\ -0.65(1) & -1.10(5) \end{pmatrix} 10^2\text{mm} \tag{IV.73}$$

that defines the new paths, $(L_3, L_4)_\gamma$ and $(L_3, L_4)_\beta$ for the telescope.

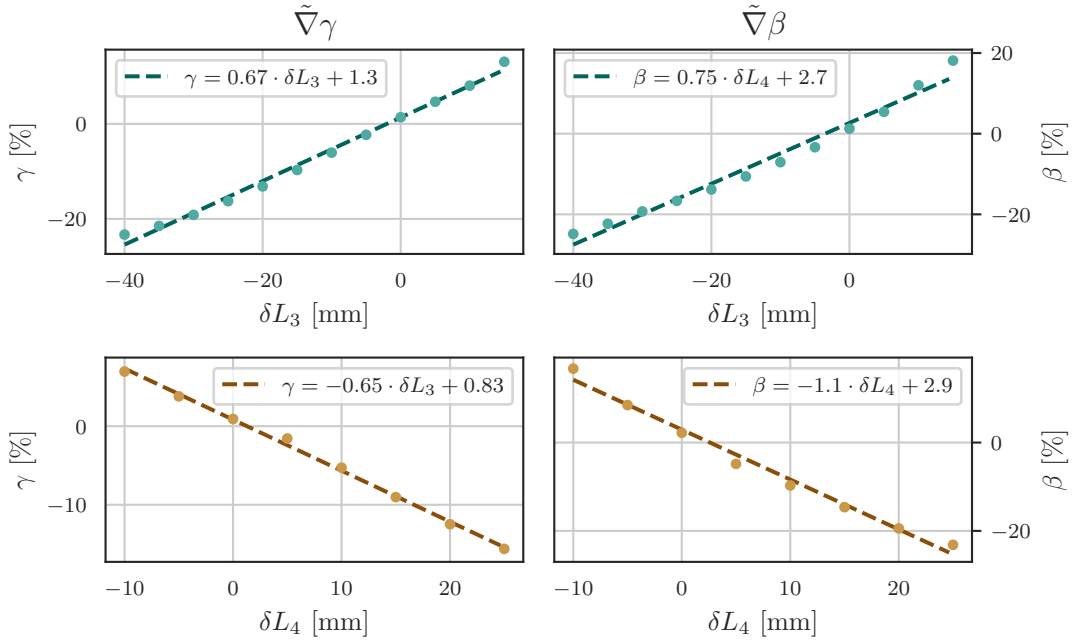

FIGURE IV.17: Experimental Driving Matrix for the Spherical Telescope. I considered the data highlighted in Fig. IV.16 and I fit the model described by Eq. IV.72. I used the linear coefficients to estimate the experimental driving matrix $\tilde{\Gamma}$.

$p_{L_j}(\delta L_i)$	$\partial_{L_i} p\ [10^{-2}\text{mm}]$	$p_{0,i}\ [\%]$	r-value
$\gamma(\delta L_3)$	0.67(2)	1.3(4)	0.99
$\gamma(\delta L_4)$	−0.65(1)	0.83(20)	1.00
$\beta(\delta L_3)$	0.76(4)	2.7(7)	0.98
$\beta(\delta L_4)$	−1.10(5)	2.9(7)	0.99

TABLE IV.7: Experimental Driving Matrix for the Spherical Telescope. Interpolation Parameter of the linear model, $p_{L_j}(\delta L_i) = \partial_{L_i} p + p_0$, where p are the measurements of the mode matching parameter $p = \gamma, \beta$, with lens L_j fixed.

The new driving matrix was validated using the same procedure describe before. The data are collected in Fig. IV.18 and the interpolation parameters in Table IV.8. As we can see from both the plot and the interpolation, the new matrix gives a better control of the telescope and it extend the actuation to the required dynamic range.

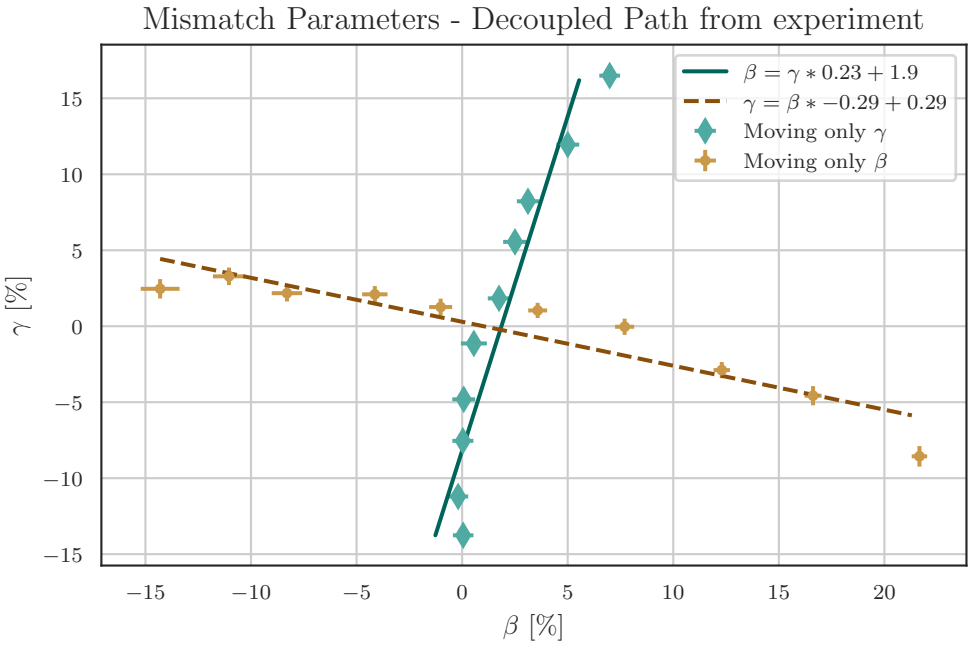

FIGURE IV.18: Validation of the Experimental Driving Matrix. I used the matrix in Eq. IV.73 as proxy to control the telescope and I moved the lenses in order to change one parameter at the time. I reported the data in the parameter space ($\gamma \times \beta$) and I separated them in two sets: brown dots are moving only β and green diamond are moving only γ. I fit the models described in Eq. IV.71 to quantify the decoupling on the telescope actuation: continued line for $\beta(\gamma)$ and dashed line for $\gamma(\beta)$.

IV.1.5. *Astigmatic Mode Matching Telescope*

The validation of the Astigmatic Mode Matching sensing requires a Matching Telescope which can control the astigmatic parameters, α, η and θ, defined in Eq. II.137. This cannot be done with the Spherical telescope described before and it requires a dedicated study.

Astigmatic Telescope Schemes

In order to control the astigmatic beam parameters, we need to break the cylindrical symmetry of the Gaussian beam and separately manipulate the beam shape along two orthogonal axes. This aberration should be induced around the spherical condition in

$p_i(b_j)$	a_{p_i,b_j} [none]	$p_{0,i}$ [%]	R^2-value[a]
$\beta(\gamma)$	0.20(3)	1.9(3)	0.88
$\gamma(\beta)$	−0.29(4)	0.3(5)	0.86

TABLE IV.8: Interpolation parameters used in Fig. IV.18. The slope parameters, a_{p_i,b_j} are used as figures of merit of the decoupling between the actuation on the two mismatch parameters, β and γ. [a] R^2 is defined as the proportion of the variation in the dependent variable that is predictable from the independent variables[46, p. 344].

such a way that the resting position of the astigmatic telescope results in a not astigmatic Gaussian beam. Similar behaviour can be obtained with the general structure of the Mode Converter Telescope, described in Section III.1.2. In this case, there are two approaches to the design of the Astigmatic Mode Matching Telescope that is discussed in Appendix A.I.2

Unfortunately, the optical table did not have enough space to implement either of those solutions, so I had to proceed with a sub-optimal implementation of an astigmatic Telescope. Instead of using a full astigmatic telescope, I induced the astigmatic aberration by installing a single cylindrical lens. The Astigmatic Telescope was composed only of three lenses, the two spherical previously used for the Spherical Mode Matching Telescope and a new cylindrical one. The telescope actuation was strongly limited: it is not possible to remove the residual astigmatism induced by the single cylindrical lens, and the four degrees of actuation[14], that is not enough to control the five degrees of freedom of the Simple Astigmatic Mismatch, Eq. II.137. In particular, only the angle θ of the astigmatic axis is decoupled from the other parameters.

The position of the cylindrical lens was optimised to induce the minimum astigmatic aberration. Following the calculation done in [47], the insertion of a lens with focal length[15] f can be represented as a perturbation of the Gaussian beam:

$$\Psi = U_0 + \frac{kw^2(z)}{4}\frac{1}{f}\mathbf{LG}_{01} = U_0 + \frac{\pi w^2(z)}{2\lambda}\frac{1}{f}\mathbf{LG}_{01}$$

where $w(z)$ is the beam radius at the lens position, z. Starting from these calculations, I assume similar results for the installation of a cylindrical lens, with the only difference that the mode excited is the corresponding Hermite Gauss, $\mathbf{HG}_{20}$:

$$\Psi = U_0 + \frac{\pi w^2(z)}{2\lambda}\frac{1}{f}\mathbf{HG}_{20}(\tilde{x},\tilde{y}) \tag{IV.74}$$

This equation indicates that the effect of the lens is proportional to the squared times the beam dimension, $w(z)$, so the aberration will be minimised by installing the lens near a beam waist.

The only available solution was the installation of the cylindrical lens inside the Mode Matching telescope, where the waist was $w_0 = 100\,\mu\text{m}$[16]. In particular, I used a cylindrical lens with effective focal lenght of 100 mm .

Characterisation of the Astigmatic Telescope

The three-lens configuration was characterised by the same approach used for the Spherical Mismatch Telescope. In particular, the action of the telescope can be represented by two $\mathbb{A}\mathbb{B}\mathbb{C}\mathbb{D}$ matrices, one for the plane orientated as the axis of the cylindrical lens, and another one for the plane orthogonal to the first one. Following the scheme in

[14] Position of the three lenses, and the angle of the cylindrical lens axis.
[15] The calculation presented in the paper uses the diopters defined as $S = \frac{1}{f}$.
[16] This value corresponds to the Spherical Telescope in the lower mismatch configuration.

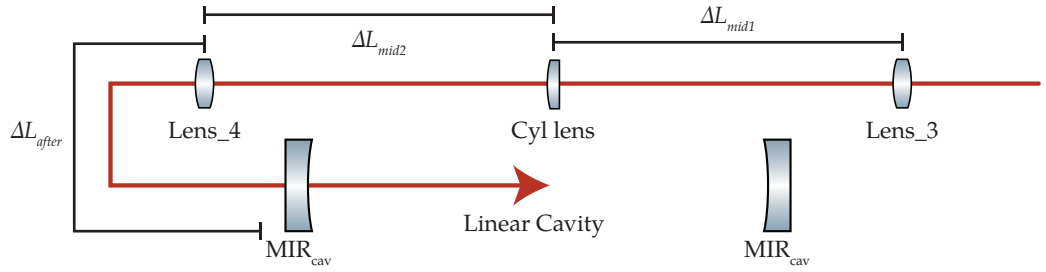

FIGURE IV.19: Astigmatic Mode Matching Telescope based on the three lens configuration. The beam is coming from the right, and it passes thought the spherical lens, Lens_3, the cylindrical lens, and the lens Lens_4. After that, it enters the linear cavity passing through the input mirror, MIR_{cav}.

Figure IV.19, we have that:

$$\mathbb{ABCD}(\text{Cyl}, L_3, L_4)_{Cyl} = \begin{pmatrix} 1 & 0 \\ -\frac{1}{f_{mir}} & 1 \end{pmatrix} \begin{pmatrix} 1 & \Delta L_{after} \\ 0 & 1 \end{pmatrix} \begin{pmatrix} 1 & 0 \\ -\frac{1}{f_4} & 1 \end{pmatrix} \begin{pmatrix} 1 & \Delta L_{mid_2} \\ 0 & 1 \end{pmatrix} \cdot \begin{pmatrix} 1 & 0 \\ -\frac{1}{f_{\text{Cyl}}} & 1 \end{pmatrix} \begin{pmatrix} 1 & \Delta L_{mid_1} \\ 0 & 1 \end{pmatrix} \begin{pmatrix} 1 & 0 \\ -\frac{1}{f_3} & 1 \end{pmatrix} \begin{pmatrix} 1 & L_3 \\ 0 & 1 \end{pmatrix} \quad \text{(IV.75)}$$

and an other one for the orthogonal axis:

$$\mathbb{ABCD}(\text{Cyl}, L_3, L_4)_0 = \begin{pmatrix} 1 & 0 \\ -\frac{1}{f_{mir}} & 1 \end{pmatrix} \begin{pmatrix} 1 & \Delta L_{after} \\ 0 & 1 \end{pmatrix} \begin{pmatrix} 1 & 0 \\ -\frac{1}{f_4} & 1 \end{pmatrix} \begin{pmatrix} 1 & \Delta L_{mid} \\ 0 & 1 \end{pmatrix} \begin{pmatrix} 1 & 0 \\ -\frac{1}{f_3} & 1 \end{pmatrix} \begin{pmatrix} 1 & L_3 \\ 0 & 1 \end{pmatrix} \quad \text{(IV.76)}$$

where f_i is the effective focal lens of the cavity mirror(f_{mir}), the spherical lens Lens_3(f_3) and Lens_4(f_4), and the cylindrical lens,Cyl, (f_{Cyl}); L_{after} is the distance between the Lens_4 and the cavity, $L_{mid_2} = L_4 - L_{Cyl}$ between Cyl and Lens_4, $L_{mid_1} = L_{Cyl} - L_3$ between Cyl and Lens_3, $L_{mid} = L_4 - L_3$ the distance between Lens_4 and Lens_3, and L_3 the position of Lens_3 with respect to the waist position before the telescope.

These two matrices define the evolution of the mismatch parameters defined as:

$$\gamma(L_{Cyl}, L_3, L_4) = \frac{\langle z_0 \rangle (L_3, L_4) - \hat{z}_0}{2\hat{z}_R} \quad \text{(IV.77)}$$

$$\beta(L_{Cyl}, L_3, L_4) = \frac{\langle w_0 \rangle (L_3, L_4) - \hat{w}_0}{\hat{w}_0} \quad \text{(IV.78)}$$

$$\eta(L_{Cyl}, L_3, L_4) = \frac{(z_0^{(\tilde{x})} - z_0^{(\tilde{y})})(L_{Cyl}, L_3, L_4)}{4\hat{z}_R} \quad \text{(IV.79)}$$

$$\alpha(L_{Cyl}, L_3, L_4) = \frac{(w_0^{(\tilde{x})} - w_0^{(\tilde{y})})(L_{Cyl}, L_3, L_4)}{\hat{w}_0} \quad \text{(IV.80)}$$

$$\epsilon = \sqrt{\beta^2 + \gamma^2 + \alpha^2 + \eta^2} \quad \text{(IV.81)}$$

where $\langle z_0 \rangle$ and $\langle w_0 \rangle$ are the spherical waist parameters defined in Eq. II.137, and $w_0^{(\tilde{x}/\tilde{y})}$ and $z_0^{(\tilde{x}/\tilde{y})}$ are the waist parameters along the internal astigmatic reference defined in Eq. II.93. This model was analysed with a simulation based on FINESSE. In particular, I considered only the movement of two lenses: (L_3, Cyl), (L_{Cyl}, L_4), and (L_3, L_4), and I simulated their action on the Mode Matching parameters. The results are reported in Fig. IV.20. The three sets of maps did not present any specific feature, so I decided to maintain the control only on (L_3, L_4).

In this case, I assume the linearity of the action (L_3, L_4) :

$$\begin{pmatrix} \gamma \\ \beta \\ \eta \\ \alpha \end{pmatrix} \simeq \begin{pmatrix} \gamma_0 \\ \beta_0 \\ \eta_0 \\ \alpha_0 \end{pmatrix} + \begin{pmatrix} \partial_{L_3}\gamma & \partial_{L_4}\gamma \\ \partial_{L_3}\beta & \partial_{L_4}\beta \\ \partial_{L_3}\eta & \partial_{L_4}\eta \\ \partial_{L_3}\alpha & \partial_{L_4}\alpha \end{pmatrix}_{(L_3^0, L_4^0)} \cdot \begin{pmatrix} \delta L_3 \\ \delta L_4 \end{pmatrix} \tag{IV.82}$$

and I estimated the driving matrix with the same approach used for the Spherical Mode Matching Telescope. I measured the telescope action by moving one lens at a time and I interpolated the data with the linear model:

$$p_{L_j}(\delta L_i) = \partial_{L_i} p + p_0 \tag{IV.83}$$

where p are the measurements of the mode matching parameters ($p = \gamma, \beta, \eta, \alpha$), with lens L_j fixed. The data are reported in Fig IV.21, while the interpolation parameters are in Table IV.9. In this way, I estimated the full driving Matrix:

$$\Gamma_{\text{astig.}} = \begin{pmatrix} 1.03 & -0.51 \\ 0.80 & -1.39 \\ 0.14 & 0.29 \\ -0.52 & -0.14 \end{pmatrix} 10^{-2}\text{mm} \tag{IV.84}$$

$p_{L_j}(\delta L_i)$	$\partial_{L_i} p$ [10^{-2}mm]	$p_{0,i}$ [%]	r-value
$\gamma(\delta L_3)$	1.03(4)	2.8(3)	1.00
$\gamma(\delta L_4)$	−0.51(4)	2.0(3)	0.98
$\beta(\delta L_3)$	0.80(3)	7.1(3)	1.00
$\beta(\delta L_4)$	−1.39(5)	7.0(4)	1.00
$\alpha(\delta L_3)$	0.14(1)	−13.2(1)	1.00
$\alpha(\delta L_4)$	0.29(1)	−13.4(1)	0.99
$\eta(\delta L_3)$	−0.52(3)	−5.9(3)	0.99
$\eta(\delta L_4)$	−0.14(5)	−5.6(4)	0.70

TABLE IV.9: Experimental estimation of the Driving Matrix for the Astigmatic Telescope. Interpolation Parameter of the linear model, $p_{L_j}(\delta L_i) = \partial_{L_i} p + p_0$, where p are the measurement of the mode matching parameter $p = \gamma, \beta, \eta, \alpha$, with lens L_j fixed.

In this case, I could not change one mismatch parameter while keeping constant the others because the driving matrix does not allow to control all the degrees of freedom together. This imposed a different approach to the characterisation of the Astigmatic Mode Matching Technique.

First, I identified the two mismatch parameters that are more sensitive to the telescope actuation, which are the spherical waist dimension, β and the astigmatic waist position,

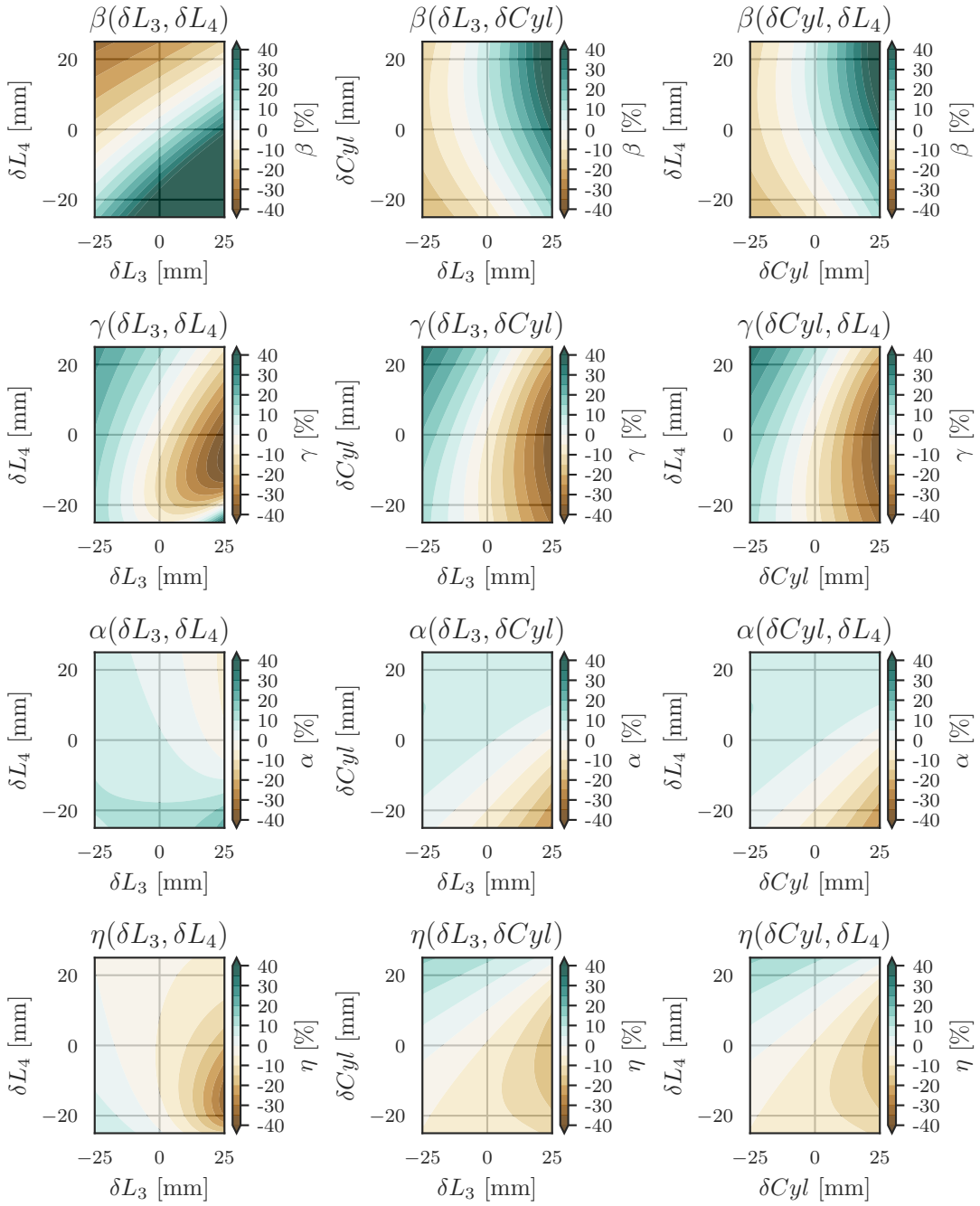

FIGURE IV.20: Simulation of the Astigmatic Mode Matching telescope. The plots describe the telescope control on the mismatch parameters(Top to bottom): β, γ, α, and η. The simulation were done by moving two lenses at the time(left to right) (L_3, L_4), (L_3, L_{Cyl}), (L_{Cyl}, L_4).

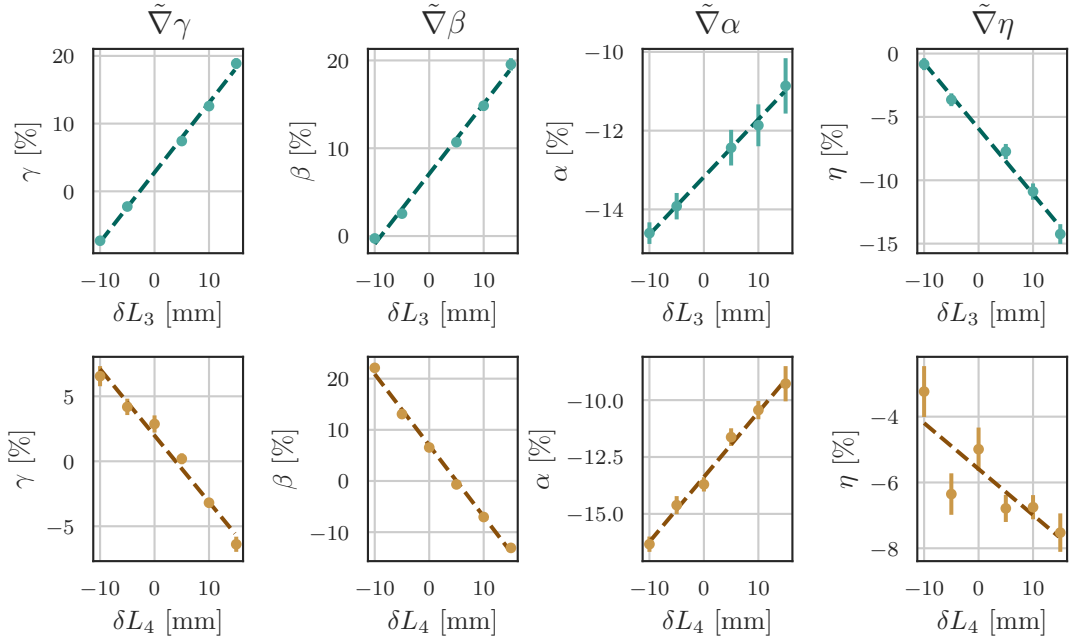

FIGURE IV.21: Experimental Driving Matrix of the Astigmatic Telescope. I measured the responses of the Astigmatic Telescope by moving δL_3 and δL_4 separately. For each point, I measured the beam shape and I estimated the mismatch parameters. I fit the model described by Eq. IV.83 and I used the linear coefficient to estimate the experimental driving matrix $\tilde{\Gamma}$, Eq. IV.84.

η. After that, I used the same approach described in Section IV.1.4 to estimate the telescope configurations for the measurement. In particular, I considered the driving matrix associated to, β and η:

$$\Gamma_{\beta,\eta}\begin{pmatrix}\partial_{L_3}\beta & \partial_{L_4}\beta\\ \partial_{L_3}\eta & \partial_{L_4}\eta\end{pmatrix}_{(L_3^0,L_4^0)} = \begin{pmatrix}0.80 & -1.39\\ -0.52 & -0.14\end{pmatrix} 10^{-2}\text{mm} \tag{IV.85}$$

and I estimated its inverse:

$$\Gamma^{-1}_{\beta,\eta} = \begin{pmatrix}16.8 & -167\\ -62.2 & -96\end{pmatrix} 10^{2}\text{mm} \tag{IV.86}$$

Using this inverted matrix, I was able to define two telescope configurations, one with β constant and one with η constant.

IV.1.6. *Wavefront Sensors*

The setup for the Astigmatic Wavefront Sensor presented in Section III can be divided into two sectors: one dedicated to the Spherical Mode Matching and based on the Mode Converter Technique, and another one dedicated to the Astigmatic mismatch and composed of four Quadrant Photodiode Sensors installed in reflection from the cavity.

Due to the contingency limitation, it was impossible to install the full setup and I had to base the validation only on two Quadrants Photodiode Sensors. In order to overcome this problem, I had to divide the validation measurement in two steps to accordingly

adapt the wavefront sensor setup. In the first phase, I installed the complete setup for the Spherical Mode Matching Sensing, composed of two Quadrant Photodiode Sensors installed after the Mode Converter Telescope and I used this setup to validate the Mode Converter Technique.

In the second Phase, I used an auxiliary optical path to detect the beam after the cavity reflection. In particular, I shuttered the path between the Mode Converter Telescope and the Quadrant Photodiode Sensor 2, and I aligned the auxiliary beam to this sensor(dashed line in Fig. IV.1). This way, I obtained a Hybrid setup to validate the Astigmatic Mismatch Wavefront Sensing.

Spherical Mode Matching Sensors

The setup for Spherical Mode Matching sensing was validated in the same condition foreseen for the installation in Advance Virgo Plus. In that case, we cannot inject an auxiliary beam from the back side of the cavities, so the installation of the *pre-converter* has to be based on the reflection of the incoming beam.

As we described in Section III.2.1, this approach leads to an imperfect tuning of the *pre-converter* telescope, which generates crosstalk between the Mode Matching signal and the Logitundal Error. This cross-talk is defined by the mismatch between the cavity and the incoming beam, and its maximum value can be estimated using Eq. III.91. In particular, I imposed a requirement on the initial Mismatch of $|\epsilon_0|^2 < 2\,\%$ that corresponds to a maximum coupling of $\kappa_{max} \simeq 16\,\%$.

This result also defines a constraint on the residual maximum residual noise on the Longitudinal control. From the Mode Matching Telescope characterization, we expected to control the mismatch parameter with the precision of $\delta\epsilon \simeq 1\,\%$. This imposes a maximum on the motion of the Longitudinal control:

$$\kappa_{max} \cdot \frac{1}{2}\frac{\delta f}{\Delta f_{FWHM}} \ll 1\,\% \rightarrow \frac{\delta f}{\Delta f_{FWHM}} \ll \frac{2}{\kappa_{max}} \simeq 0.1\,\% \tag{IV.87}$$

that will be discussed in Section IV.2.2.

Installation of the Mode Converter Telescope

The Mode converter telescope was based on two identical cylindrical lenses with focal length 100 mm, which correspond to a Mode Converter Telescope waist of 240 µm. The installation was done after optimizing the mode matching based on the amplitude of the second-order peak. Once I obtained an optical loss smaller than 2 %, I used the reflected beam as a reference and proceeded to install the Mode Converter Setup. The operations were divided into three steps:

Pre-converter Telescope I designed the Pre-converter telescope in order to match the reflected beam with the Mode Converter Mode, and I used $f_8 = 170\,\text{mm}$ and $f_9 = -70\,\text{mm}$. The beam was characterized, and the measurement of the beam profile after the telescope is reported in Fig. IV.22. From the interpolation of the data, I estimated a waist dimension of 241(3) µm.

Mode Converter Telescope The installation of the Mode Converter Telescope was done with a minor modification with respect to the standard design. In particular, I exploited the cylindrical symmetry of the linear cavity, and I rotated the cylindrical

axis of the two lenses by 45°. In this way, I could use the Quadrant Photodiode with the standard orientation +. The installation of the mode converter was divided into two main steps:

1. Installation of the first lens. The design of a symmetrical mode converter requires that the waist position of the two axes, $z_0^{(x')}$ and $z_0^{(y')}$ has to be the same. For this reason, I optimized the first Cylindrical lens by looking at the difference between these two parameters. Fig. IV.22 and Table IV.10 report the beam profile measurement after these optimizations.
2. Installation of the second lens. The second lens position can be identified using the beam shape. In particular, the cylindrical lens should be installed where the power profile is spherical. I used this position initial reference and optimized the second lens using the beam profile after the telescope to minimize the residual astigmatism.

Tuning Step	$w_0^{(x')}$ [μm]	$w_0^{(y')}$ [μm]	$z_0^{(x')}$ [cm]	$z_0^{(y')}$ [cm]	$w_0^{(c)}$ [μm]	$z_0^{(c)}$ [cm]
Pre-converter	250(2)	234(3)	41.0(2)	39.4(2)	242(2)	40.2(1)
After Cyl_1	110(1)	253(4)	40.7(2)	38.3(3)	181(2)	39.5(2)
After Cyl_2	268(6)	261(6)	37.7(3)	32.9(5)	264(4)	35.3(3)

TABLE IV.10: Tuning of the Mode Converter Telescope. Beam Parameters estimated at each step.

Gouy Phase tuning

The decoupled readout of the Mismatch parameters requires the fine-tuning of the Gouy Phase of the reflected beam on the Quadrant Photodiode Sensors. The theoretical parameters are collected in Table III.1, where we can distinguish two cases: The sensor corresponding to the waist position parameters requires a Gouy phase of $\Delta\psi = 0°$, while the one corresponding to the waist dimension requires $\Delta\psi = 45°$. These values correspond to the Gouy phase accumulated by the Fundamental mode propagated from the cavity up to the sensor. They can be tuned using a suitable telescope called Gouy Phase Telescope. In particular, we can use Eq. II.64 and define the requirement of the telescope:

$$\Delta\psi_{(\gamma,\eta)} = -\operatorname{Arg}\left[A_{(\gamma,\eta)}q_c + B_{(\gamma,\eta)}\right] = 0° \tag{IV.88}$$

$$\Delta\psi_{(\beta,\alpha)} = -\operatorname{Arg}\left[A_{(\beta,\alpha)}q_c + B_{(\beta,\alpha)}\right] = 45° \tag{IV.89}$$

where A_i and B_i are the elements of the corresponding $\mathbb{ABCD}$ matrix.

The tuning of the Gouy phase was obtained by installing a lens with $f_{10} = 282\,\mathrm{mm}$ after the Mode Converter and by using the distance between the sensors and the beam waist. I adjusted the two sensors to impose a difference between their Gouy Phase, $\Delta\Psi_2 - \Delta\Psi_1 \simeq 45°$. In particular, I installed the Quadrant Photodiode Sensor 1 in the far field area and the Quadrant Photodiode Sensor 2, near the end of the Rayleigh range. After that, I used the FINESSE simulation to estimate the effective Gouy Phases, $\Delta\Psi_i$, and I optimized the sensor position to have $2\Delta\Psi_1 = 148°$ and $2\Delta\Psi_2 = 96°$. In this way, the Quadrant Photodiode Sensor 1 will be mainly sensitive to the beam dimension:

$$\tilde{V}^{(1)}_{M.M.}(148°) =\simeq \frac{m}{\pi}\chi_1(-0.99\beta + 0.05\gamma) \tag{IV.90}$$

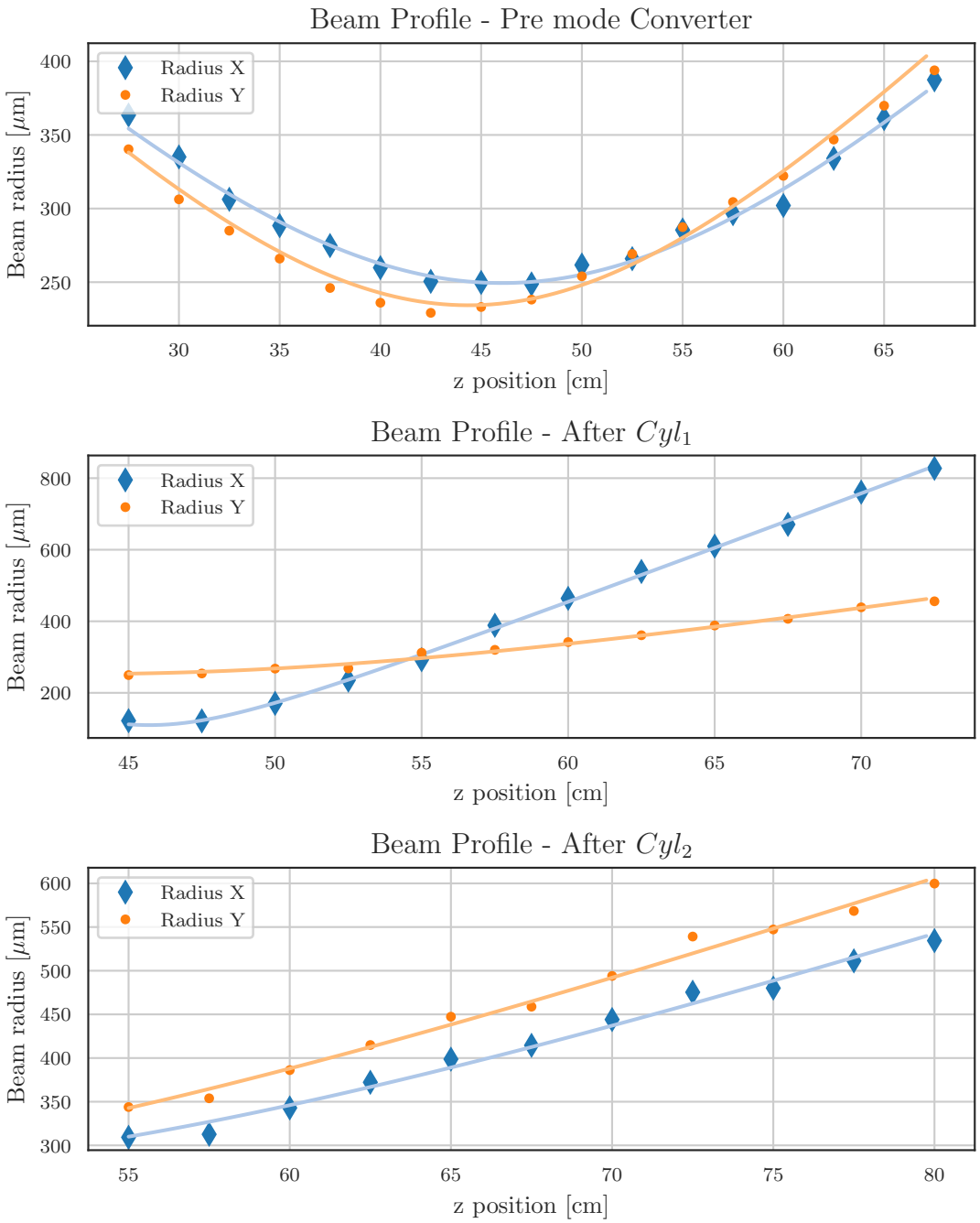

FIGURE IV.22: Tuning of the Mode Converter Telescope. Beam Profile Measurements used during the installation of the telescope. The Beam was characterized using the procedure described in Appendix A.I.1. The point represents the beam radius estimation using the Beam internal reference, while the two continuous lines represent the model used to estimate the beam parameters. Top to Bottom: Beam after the Pre-converter; Beam After the First Cylindrical Lens; Beam After the second cylindrical lens.

and the Quadrant Photodiode Sensor 2 mainly to the beam position:

$$\tilde{V}^{(2)}_{M.M.}(96°) =\simeq \frac{m}{\pi}\chi_1(-0.03\beta - 0.99\gamma) \tag{IV.91}$$

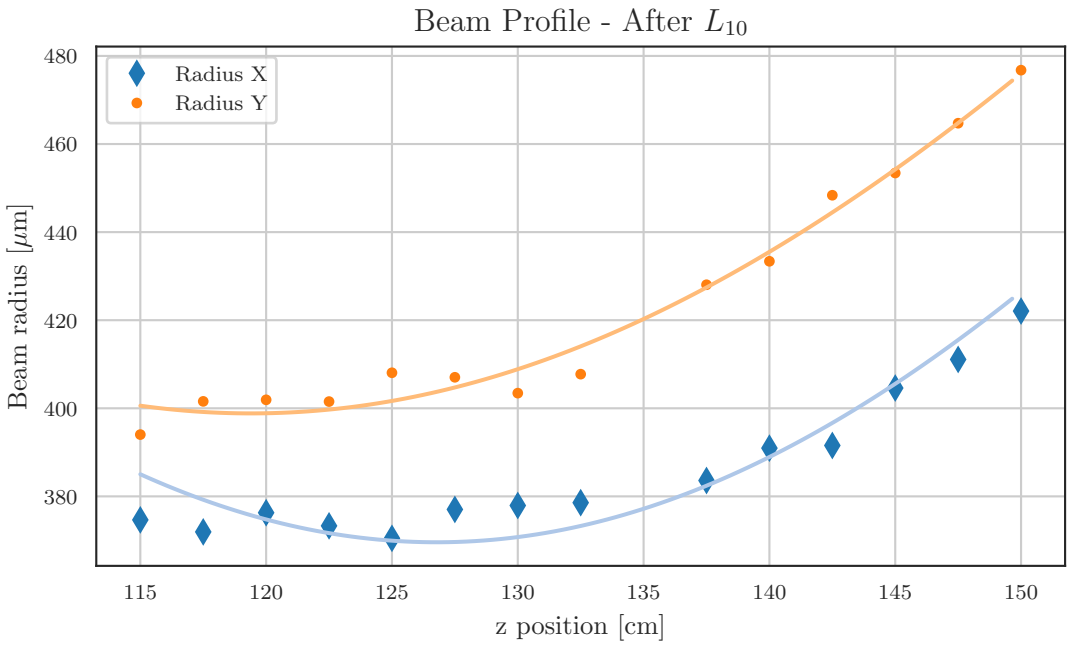

FIGURE IV.23: Spherical Mode Matching Sensor - Gouy Phase Tuning. I reported the beam profile after the Lens_10, $f_{10} = 282\,\text{mm}$, used to tune the Gouy phase of the Spherical Mismatch Sensors. The Quadrant Photodiode Sensor 1, was installed at a Gouy phase of $2\Delta\Psi_1 = 148°$. The Quadrant Photodiode Sensor 2, was installed at a Gouy phase of $2\Delta\Psi_1 = 96°$.

Astigmatic Mode Matching Sensors

The Astigmatic Wavefront sensors setup was obtained as a variation of the Spherical one. In this case, the Quadrant Photodiode Sensor 2 used a different path that started before the pre-converter and it bypassed the Mode Converter Telescope. I had to tune only the Gouy phase of the Quadrant Photodiode Sensor 2 and I designed a telescope in order to have sensitivity over both the astigmatic mismatch parameters. In particular, the Gouy phase telescope is based on two lenses, $f_{11} = 170\,\text{mm}$ and $f_{12} = -70\,\text{mm}$. The resulting beam shape was characterized by a beam profile, and I adjusted the sensor position to obtain $2\Delta\Psi_2 = 44°$.

In this configuration, the detection is composed of two sensors: Quadrant Photodiode Sensor 1 was sensitive to the beam waist parameters, β and Quadrant Photodiode Sensor 2 to:

$$\tilde{V}^{(2)}_{Asti}(44°) =\simeq \frac{m}{\pi}\chi_2^{ast}(0.71\eta\cos(2\theta) + 0.69\gamma\cos(2\theta)) \tag{IV.92}$$

where θ is the astigmatic angle.

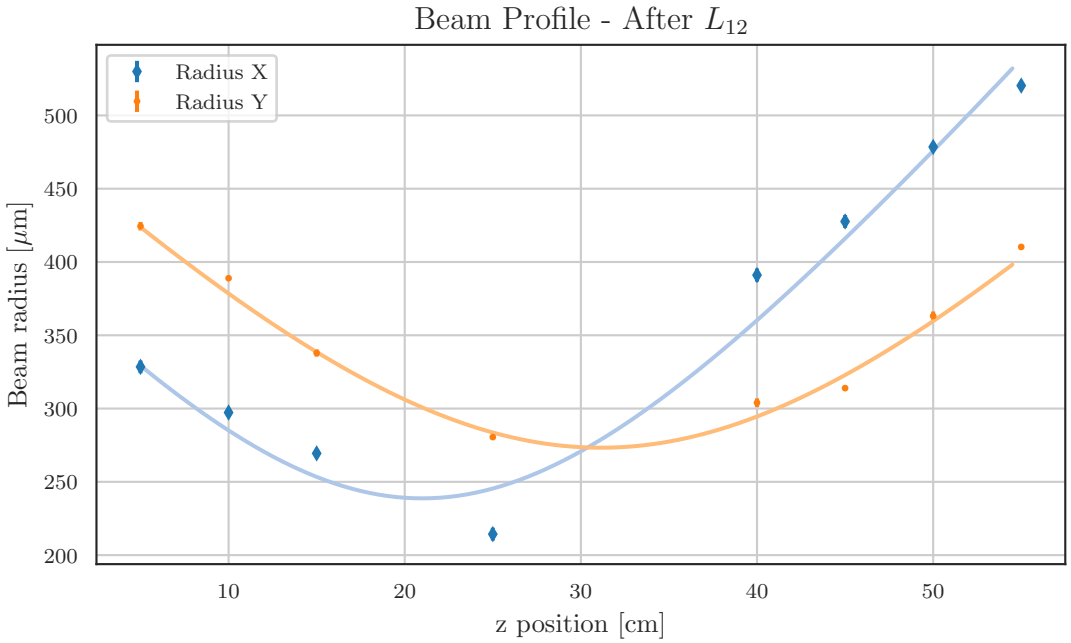

FIGURE IV.24: Astigmatic Mode Matching Sensor - Gouy Phase Tuning. I reported the beam profile after the Lens_12, $f_{12} = -70$ mm, used to tune the Gouy phase of the Spherical Mismatch Sensors.

IV.2. ELECTRONIC SETUP

The electronic setup used in the experiment is represented in Fig. IV.25, and it was composed of two parts: the Readout of the Wavefront Sensors, used for the measurement of the Mode Matching Signals, and the Longitudinal Control Loop used to maintain the Laser beam resonant with the cavity. These two parts used the same Signal Generator that produces the Local Oscillator signals in order to synchronize the phase of the different demodulation schemes. I will first present the readout system and describe its main limitations in measuring the Mode Matching signal. After that, I will introduce the Longitudinal control and discuss both the requirements and its characterization.

IV.2.1. *Wavefront Sensors Readout*

The wavefront sensors readout was used to process the signals in order to extract the Mode Matching Signal. In particular, I installed two electronic chains, one for each Quadrant Photodiode Sensor. These setups share the same structure which is composed by:

Quadrant Photodiode Sensor The Quadrant Photodiode sensors were produced by Nikhef for the Frequency Depended Squeezing Source of Virgo Advance Plus. These sensors are based on a split photodiodes, QP45-Q TO, produced by *First Sensor* and represented in Fig. IV.26. The active areas are four squares separated by a gap of 70(1) µm and with a width of 3.31(1) mm. The diodes were internally pre-amplified in order to produce two signals for each active area, one with

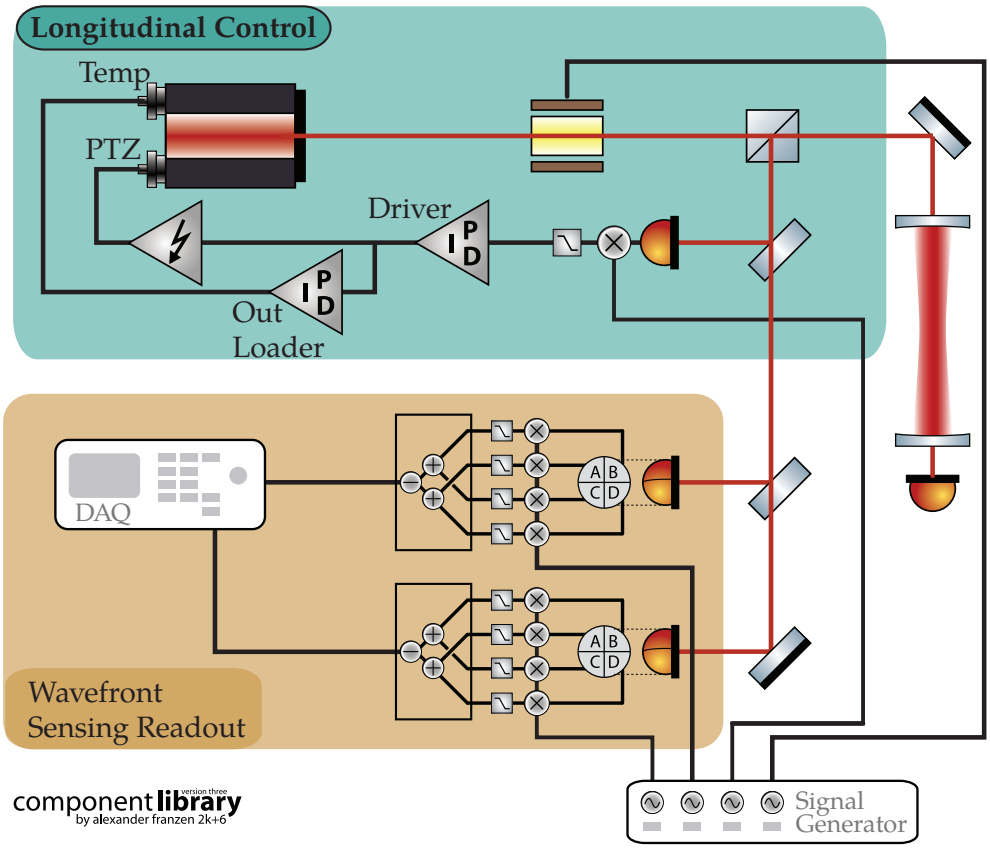

FIGURE IV.25: Electronic Scheme of the Experiment. The setup is divided into two main components: The Longitudinal Control highlighted in green and the Wavefront Sensors Readout in brown. These two systems share a Common Signal generator, that guarantees a phase synchronisation between the Electro-Optical Modulator and the different demodulation setups.

low bandwidth, DC, and one at high bandwidth[17]. The channel are named as QD[n]_ch[m]_DC/RF, where n is the identification number of the Quadrant Photodiode and m of the active area;

Demodulation Setup Each RF signal generated from the Quadrant Photodiode sensors, QD[n]_ch[m]_RF, was separately demodulated with an analogic setup described in Fig. IV.27. The scheme was based on a mixer, ADE-6, and a passive Low Pass Filter, LPF-B0R3, with a cut-off frequency of $f_{LP} = 300\,\text{kHz}$. The local oscillator signals were produced by the same Signal Generator used for the Electro-Optical Modulator. In particular, we used a single signal for each Quadrant Photodiode Sensor, which was divided in four by a power splinter ZB4PD1-500+[18];

Recombination and Readout The demodulated signals were recombined using an FPGA board produced by National Instruments. The recombined signals were Digitally Filtered with a 2-th order Low Pass Filter and cut-off frequency of $f_c = 30\,\text{Hz}$.

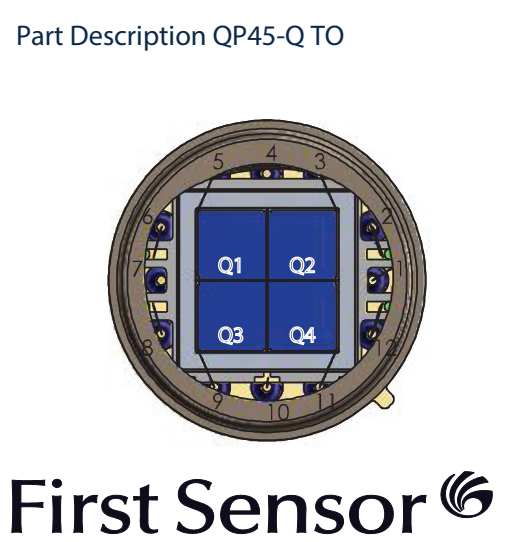

FIGURE IV.26: Quadrant Photodiode QP45-Q TO installed in the wavefront Sensors used in the experiment. The four active areas are oriented as + cross. They are 3.31 mm width and separated by a gap of 70 µm.

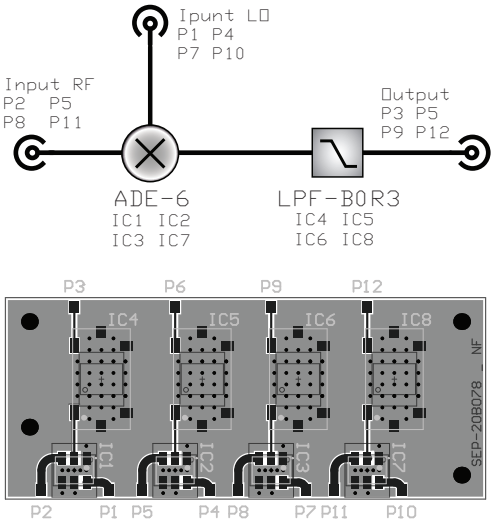

FIGURE IV.27: Demodulation Board composed by four separated demodulation setups(top scheme). The demodulator was based on a mixer, ADE-6, and a passive Low Pass Filter, LPF-B0R3, with a cutoff frequency $f_{LP} = 300\,\text{kHz}$.

This readout scheme was based on the demodulation-recombination approach in which each Active Area of the Quadrant Photodiode is individually demodulated before the recombination. This approach was imposed by the design of the Quadrant Photodiode Sensors that pre-amplify each channel separately. The signals, S_i, were first demodulated:

$$\tilde{V}_j(2\Delta\psi) = m\chi_j S_j(2\Delta\psi) \tag{IV.93}$$

[17] At the time of writing, the official characterisation was not published.
[18] All the electronic components were produced by Mini-Circuits®.

where χ_j is the dedicated conversion factor, and after they were recombined together to extract the Mismatch signal

$$\tilde{V}_{M.M.}(2\Delta\psi) = (V_1 + V_3) - (V_2 + V_4) \tag{IV.94}$$

Characterisation of the readout system

As described in Section III.2.3, the unbalance between the χ_j generates crosstalk between different signals and leads to the degradation of the Mode Matching one. In order to quantify the coupling coefficient defined in Eq. III.101, I characterized each readout chain from the Quadrant Photodiode Sensor up the signal recombination.

The measurement was based on the amplitude modulation of the beam, which was obtained by exploiting the Residual Amplitude Modulation of the Electro Optical Modulator. I rotated the Half Wave Plate (HW_3 in Figure IV.1) installed before the Electro Optical Modulater. In this way I de-tuned the polarization and created a line at $\Omega_{am} = 2\pi \times 18.75\,\text{MHz}$ and amplitude m_{am}:

$$\Psi = \Psi_0(1 + m_{am}\sin(\Omega_{am}t) \tag{IV.95}$$

After that, I added a beam dumper between the cavity mirrors to avoid extra signals, and I aligned the beam to the Quadrant Photodiode to measure the whole power profile with a single active area, A_i. In this way, the RF channel was proportional only to the modulation of the beam power:

$$S_i = \chi_i^{\text{sens}}|\Psi|^2 = \chi_i^{\text{sens}}|\Psi_0|^2(2m_{am}\sin(\Omega_{am}t + \phi_0) + \frac{m}{2}\sin(2\Omega_{am}t)) \tag{IV.96}$$

where χ_i^{sens} is the optical gain of the channel i of the Quadrant Photodiode Sensor, and I ignored the DC component.

This signal was demodulated using the analogic board in Fig. IV.27. In these measurements, I used a demodulation frequency, $\Omega_{dem} = \Omega_{am} + \Delta\Omega$, shifted of $\Delta\Omega = 2\pi \times 1\,\text{kHz}$ with respect to the modulation frequency, $\Omega_{am} = 2\pi \times 18.75\,\text{MHz}$. In this way, the signal in Eq. IV.96 was down-converted into a signal with Frequency $\Delta\Omega$:

$$\begin{aligned} V_i^{QD} &= \chi_i^{\text{demod}}\chi_i^{\text{sens}}|\Psi_0|^2 2m_{am}\cos(\phi_0 - \phi_{\text{dem}} + \Delta\Omega t) \\ &= \chi_i|\Psi_0|^2 2m_{am}\cos(\phi_0 - \phi_{\text{dem}} + \Delta\Omega t) \end{aligned} \tag{IV.97}$$

where χ_i^{demod} is the conversion factor of the demodulator, ϕ_{dem} is the demodulation phase, and, in the last step, I collected the two conversion factors into χ_i [19]. The down-converted signal was measured with lock-in amplifier[20] in order to characterize both the amplification and the phase shift of each conversion factor, χ_i. The final measurements are reported in Table IV.11, where the values of each Quadrant Sensor was normalised with respect to the first channel:

$$\tilde{\chi_j} = \frac{\chi_j}{\chi_0} = \frac{|\chi_j|}{|\chi_1|}e^{i\,\text{Arg}[\chi_j] - \text{Arg}[\chi_1]} = |\tilde{\chi_j}|e^{i\delta\tilde{\psi}_j} \tag{IV.98}$$

[19] I assumed that both χ_i^{demod} and ϕ_{dem} are not frequency dependent inside the Low Pass Filter Bandwidth, of 130 kHz.

[20] SR 830 produced by Stanford Research Systems.

Quadrant Photodiode	channel	$\delta\tilde{\psi}_j$ [deg]	$\lvert\tilde{\chi}_j\rvert$ [a.u]	DC signal [mV]
QPD 1	1	0.0	1.0	1064(3)
	2	7.3(5)	1.48(1)	1110(1)
	3	7.6(5)	1.51(1)	1118(1)
	4	4.9(3)	1.32(1)	1126(1)
QPD 2	1	0.0	1.0	1750(3)
	2	1.3(1)	0.90(1)	1783(2)
	3	2.1(1)	0.90(1)	1793(2)
	4	0.6(1)	0.83(1)	1826(2)

TABLE IV.11: Measurement of the conversion factors, χ_i of each RF chain. I reported the normalized values with respect to channel 0 of each Quadrant Photodiode sensor, Eq. IV.98, and the DC signal generated by the corresponding active area.

Quadrant Photodiode	$\left\lvert\frac{\chi_L}{\chi_{MM}}\right\rvert$ [%]	$\left\lvert\frac{\chi_H}{\chi_{MM}}\right\rvert$ [%]	$\left\lvert\frac{\chi_V}{\chi_{MM}}\right\rvert$ [%]
QPD 1	6.0(7)	14.0(7)	7.0(7)
QPD 2	4.0(2)	1.0(2)	4.0(2)

TABLE IV.12: Maximum Cross talk coefficient of the Alignment and Longitudinal Error signal in the reconstruction of the Mode Matching Signal.

With that information, I estimated the conversion factors defined in Eq. III.101, and I used them to estimate the maximum cross-talk in the reconstruction of the Mode Matching. The values, reported in Table IV.12, were used to define the cavity alignment requirement and residual motion of the Longitudinal control. The maximum misalignment was defined as the relative amplitude of the first-order mode:

$$|U_1| = \sqrt{\frac{P_1}{P_0}} \tag{IV.99}$$

where P_j is the peak height of the transmission optical power when the mode j is in resonance with the cavity. For this value, I imposed the following requirement:

$$|U_1| \leq 3\,\% \tag{IV.100}$$

The coupling of the Longitudinal control imposed by the reconstruction unbalance is lower than the one induced by the mistuning of the pre-converter, 16 % defined in Eq. IV.87. I considered only the greater value to impose the requirement on the residual noise of the Longitudinal Control loop.

IV.2.2. *Longitudinal Control Loop*

The Mode Matching Sensing technique is designed to work around the resonance condition of the cavity. This requirement has different aspects that need to be taken into consideration. On one side, the demodulated signal estimated in Section III.1.5 was based on the matching between the laser frequency f_{laser} and the resonance one, f_0, defined in Eq.II.84; On the other, Section III.III.2 describes two mechanisms that couple the difference between these two frequencies, $\delta f = f_{\text{laser}} - f_0$, into the Mode Matching signal.

The resonance condition was guaranteed with a Longitudinal Control loop based on the Pound–Drever–Hall technique[32]. This method is based on estimating the imaginary part of the cavity reflectance that shows two interesting properties. It nods at resonance and is linear with the frequency difference, δf, so that it can be used as feedback for the stabilisation loop. Moreover, this signal can be calibrated and it can be used to characterise the residual motion of the frequency difference, δf.

The Experimental implementation is based on the same scheme of the wavefront sensing technique presented in Section III. In this case, the incoming beam is phase modulated with the Electro-Optical Modulator, and the cavity reflection is measured with a Fast photodiode. The detected signal is proportional to the following:

$$S_{PDH} \propto |\Phi|^2 \left| F_0^0 e^{i\omega t} + F_0^+ \tfrac{m}{2} e^{i(\omega+\Omega t)} - F_0^- \tfrac{m}{2} e^{i(\omega-\Omega t)} \right|^2 \tag{IV.101}$$

where F_0 and $F_0^{\pm}$ are the cavity responses defined in Eq. III.6 and Eq. III.6. The Longitudinal Error Signal is obtained by the demodulation of the signal, S_{PDH} and it is proportional to[32]:

$$\epsilon_{\text{PDH}} \simeq -\frac{2}{\pi} m P_0 \frac{\delta f}{\Delta f_{\text{FHMW}}} \tag{IV.102}$$

where m the the phase modulation, P_0 the amplitude of the incoming beam carrier, Δf_{FWHM} is the cavity line-width, and δf is the difference between the laser frequency, f_{laser} in Eq.IV.30, and the resonance one, f_0, defined in Eq.II.84:

$$\delta f = f_{\text{laser}} - \underbrace{(l\Delta f_{\text{fsr}} + \Delta f_{\text{HOM}})}_{f_0} \tag{IV.103}$$

The error signal ϵ_{PDH} can also also be used to monitor the residual motion of the laser frequency, f_{laser}, with respect to the resonance one, f_0. This measurement requires a calibration of the signal which is discussed in Section IV.2.2.

This error signal stabilised the laser frequency and maintained the incoming beam resonant with the cavity. The control scheme is represented in Figure IV.25, and it is composed of two different sections:

Sensor The power of the reflected beam was measured with the fast photodiode PD_02 in Fig IV.1. These photodiodes are internally pre-amplified and provide a demodulated signal[37][21]. The local oscillator used for the demodulation was generated by the common Signal Generator.

Driver The Error signal generated by the photodiode was processed by the digital PID filter implemented with the Moku:lab board and used to control the Laser Frequency. The driver was composed of two loops:

Fast Loop This loop was based on the Error signal generated by the Pound–Drever–Hall scheme and it acted on the Piezo Electric Transducer, characterised in Section IV.1.2, to control the laser Frequency. The Filter parameters are collected in Table IV.13a.

Off-Load This loop was used to maintain the average Voltage on the Piezo Electric Transducer around 50 V. It used the actuation signal generated by the Fast

[21] The photodiode used for the demodulation scheme are the same used in the OPLL setup for Frequency Independent Squeezing source of Advanced Virgo.

Loop as input and it removed the DC offset applied to the Piezo Electric Transducer by changing the laser temperature. The Filter parameters are collected in Table IV.13b.

Fast Loop	
Proportional gain (dB)	−60.0
Integrator crossover (kHz)	125.0
Integrator saturation (dB)	32.9

(A) Fast Loop. Filter Parameters used for the actuation on the Piezo Electric Transducer. It was composed of a Saturated Integrator and a Proportional Gain.

Off-Load	
Unity gain frequency(mHz)	14.4

(B) Off-Load. Filter Parameters used for the actuation on the Crystal Temperature. It was composed by a Integrator Filter.

TABLE IV.13: Longitudinal Loop. Filter Parameter used for the laser stabilisation described in Fig. IV.25. The controller was based on two loops, with different Bandwidths.

Optimisation of the Longitudinal Control Loop

The Longitudinal control loop was optimised in two different ways. First, the Fast Loop parameters were optimised in order to reduce the residual Frequency noise, $\sigma_{\epsilon_{\mathrm{PDH}}}$, defined as:

$$\sigma^2_{\epsilon_{\mathrm{PDH}}} = \sqrt{\frac{1}{\Delta t}\left(\int_{\Delta t}(\epsilon_{\mathrm{PDH}})^2 dt - \left(\int_{\Delta t}(\epsilon_{\mathrm{PDH}} dt\right)^2\right)} \tag{IV.104}$$

Second, the Pound-Drever-Hall error signal was adjusted in order to compensate for systematic errors in the estimation of the frequency difference, δf. This optimisation was based on the injection of a dither line with frequency Ω_{dith} in the Piezo Electric Transducer in order to modulate the laser Frequency as

$$\omega = \omega_0 + \delta\omega_{slow} + \delta\omega_{fast} + m_{\mathrm{dith}}\sin(\Omega_{\mathrm{dith}}) \tag{IV.105}$$

When the laser is kept in resonance by the Longitudinal control loop, this line was visible in the power transmitted by the cavity:

$$P_t(\delta f(\Omega)) \simeq \frac{P_{max}}{1 + \left(2\frac{\delta f(\Omega)}{\Delta f_{\mathrm{FWHM}}}\right)^2} \tag{IV.106}$$

where $\delta f(\Omega)$ is the difference between the laser frequency, ω, and the resonance one, f_0. This value is kept around zero by the Fast Loop and it can be represented as:

$$\delta f(\Omega) = \delta f_0 + m_{\mathrm{dith}}\sin(\Omega_{\mathrm{dith}}) \tag{IV.107}$$

where δf_0 is the systematic error in the set point of the control loop. If we assume that $\delta f(\Omega)/\Delta f_{\mathrm{FWHM}} \ll 1$, we can approximate the transmitted power as:

$$\begin{aligned} P_t(\delta f(\Omega)) &\simeq P_{max}\left(1 - \left(2\frac{\delta f_0 + m_{\mathrm{dith}}\sin(\Omega_{\mathrm{dith}})}{\Delta f_{\mathrm{FWHM}}}\right)^2\right) = \\ &= P_{max} - \frac{4P_{max}}{\Delta f^2_{\mathrm{FWHM}}}\left(\delta f_0^2 + m^2_{\mathrm{dith}}\frac{1}{2}(1+\cos(2\Omega t)) + 2\delta f_0 m_{\mathrm{dith}} sin^2(\Omega t)\right) \end{aligned} \tag{IV.108}$$

where in the last step we expanded the frequency component. From this equation, we can see that the signal at frequency Ω is directly proportional to the systematic error δf_0, and it can be used to tune the set-point of the Longitudinal control. In particular, each time I engaged the Longitudinal Control, I injected a dither frequency $\Omega_{\text{dith}} = 270\,\text{Hz}$ and I optimised the Error signal offset by minimising the line at Ω_{dith} in the spectrum of the transmitted optical power.

Stability of the Control Loop

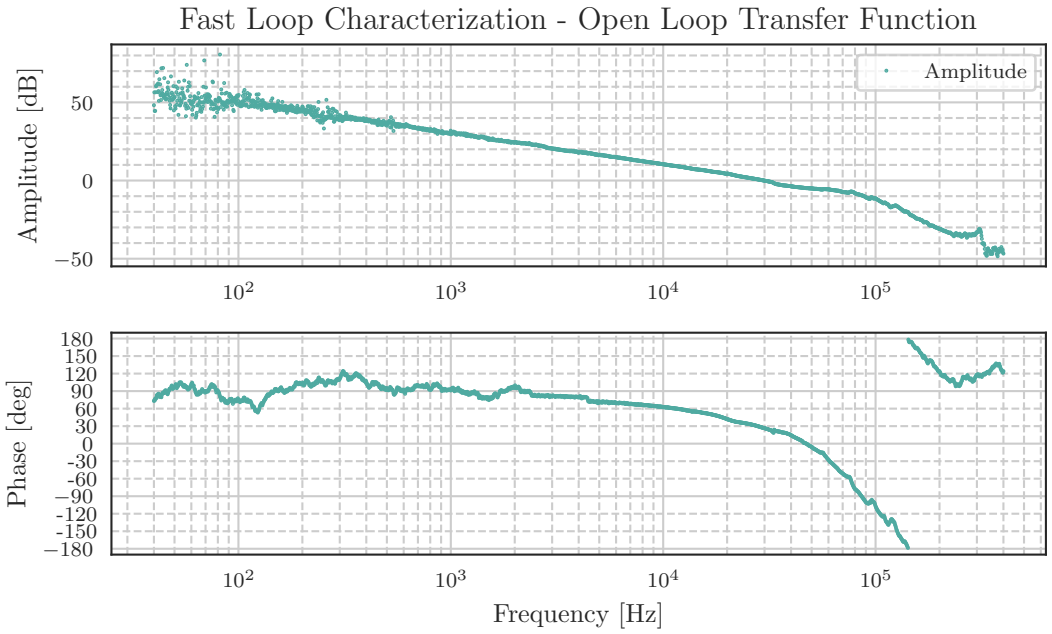

FIGURE IV.28: Longitudinal Control Loop - Open Loop Transfer Function. I estimated a Phase Margin of 26.7° and Gain Margin of 4.8 , moreover we can see that the unity gain frequency is 29.8 kHz.

In order to verify the stability of the Longitudinal control Loop, I measured the Open Loop Transfer Function of the Fast-driver and I characterised it using the Bode criterion. This method is based on the Phase Margin and Gain margin parameters. Using the frequency response function of the Moku:lab, I injected a probe line with frequency Ω_{prop} in the Piezo Electric Transducer signal and I recorded its amplitude and phase after the propagation around the full loop. I collected the electronic response at different frequencies from 400 kHz to 40 Hz, the data are represented with a Bode Plot in Figure IV.28. Using this measurement, I estimated a Phase Margin of 26.7° and a Gain Margin of 4.8 , moreover, we can see that the Unity Gain Frequency is 29.8 kHz.

Characterisation of the Longitudinal Control Loop

Once I obtained a stable resonance cavity, I verified that the residual fluctuation of the frequency difference, δf was compatible with the requirement imposed in Eq. IV.87, $\delta f / \Delta f_{FWHM} \ll 0.1\,\%$. In particular, I first calibrated the Pound–Drever–Hall error signal, and after, I studied the residual motion of δf.

Calibration Error Signal

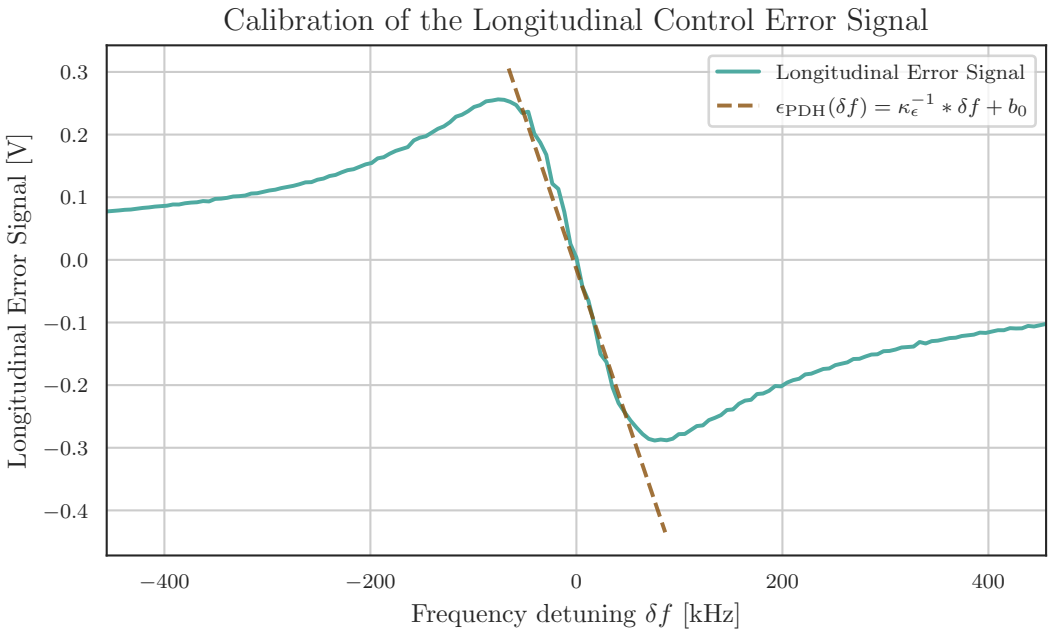

FIGURE IV.29: Calibration of the Longitudinal Error Signal. In order to estimate the calibration factor, I fitted the linear region of the Error signal and I estimated the relationship between the demodulated signal and the frequency detuning. This figure represent one of the 100 measurement of the error signal sued for the estimation of the κ_ϵ^{-1} factor.

The error signal of the Pound–Drever–Hall was calibrated using the information collected in Section IV.1.2. I measured the error signal as a function of the laser frequency and, I fitted the linear part with the model:

$$\epsilon_{\mathrm{PHD}} = \kappa_\epsilon^{-1} \delta f + b_0 \tag{IV.109}$$

In Figure IV.29, I reported one of the signal measurements with the corresponding linear model. I recorded multiple scans of the laser frequency, and estimate the calibration factor for each one. The final value was obtained by averaging them:

$$\langle \kappa_\epsilon \rangle = -202.0(50)\,\mathrm{Hz\,mV^{-1}} \tag{IV.110}$$

Residual Frequency noise

After optimising the Fast-Loop loop, I recorded the error signal of the Longitudinal Control and calibrated it using the factor, $\langle \kappa_\epsilon \rangle$. The spectrum of the residual noise, $\rho(f)$, is represented in Figure IV.30, while the total RMS is:

$$\sigma_f = 10.5\,\mathrm{kHz} \tag{IV.111}$$

The main contributions are given by a line at 60 kHz generated by environmental noise and the servo bump around 50 kHz. If we consider the f_{FWHM} estimated in Section IV.1.3, we have:

$$\frac{\sigma_f}{f_{\mathrm{FWHM}}} = 7\,\% \tag{IV.112}$$

that is outside the requirement imposed in Eq.IV.87.

In order to reduce the residual noise coupled into the Mode Matching Signal, I decided to filter the reconstructed signal, V_i^{QD}, in order to remove the contribution at High frequency. I chose a cut-off frequency of $f_c = 30\,\text{Hz}$ based on the spectrum in Fig. IV.30. The residual Frequency noise in this bandwidth can be estimated by the integration of the power spectrum, $\rho(f)$:

$$\sigma_f(50\,\text{Hz} = \int_0^{50\,\text{Hz}} \rho(f) df = 23\,\text{Hz} \tag{IV.113}$$

This value is compatible with the requirement imposed from the cross talk :

$$\frac{\sigma_f((50\,\text{Hz})}{f_{\text{FWHM}}} = \frac{23\,\text{Hz}}{152\,\text{kHz}} = 0.02\,\% \tag{IV.114}$$

inasmuch is lower than the requirement imposed Eq. IV.87.

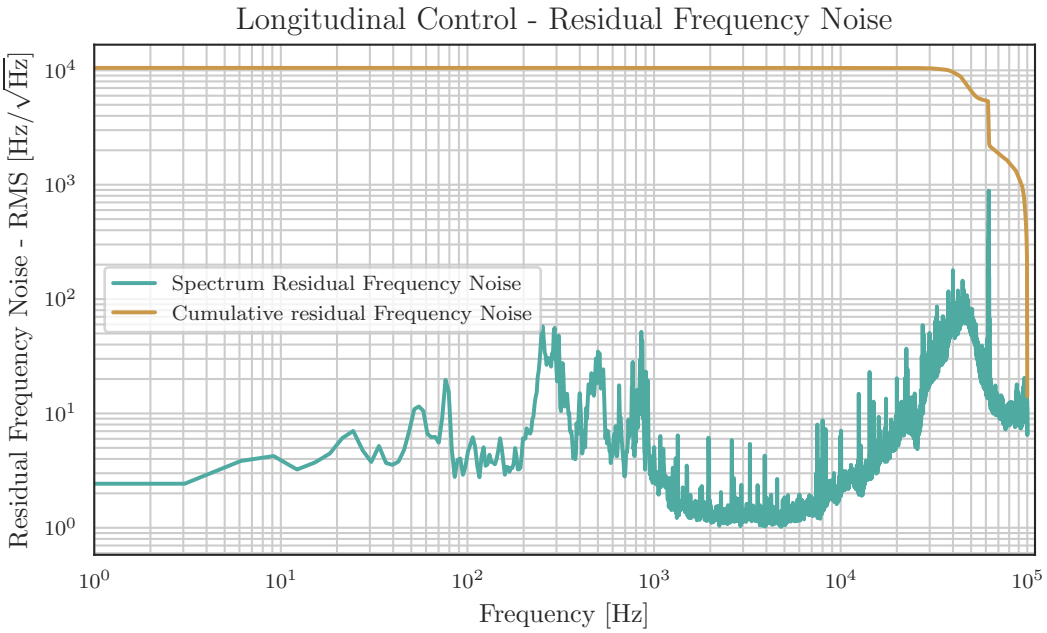

FIGURE IV.30: Longitudinal Control Loop - Residual Frequency noise. The spectrum described the different contributions to the residual Frequency noise of the Longitudinal Control Loop. We can identify: a line at 60 kHz coupled by the environment; the servo bump around 50 kHz; a group of structures around 250 Hz generated by the mechanical resonances of the Optical Breadboard and the mechanic holders. The total residual noise is $\sigma_f = 10.5\,\text{kHz}$.

V VALIDATION MEASUREMENT OF THE MODE MATCHING SENSING

V.1 Validation of the Mode Converter Technique 116
V.2 Validation of Astigmatic Mismatching Sensing 119
V.2.1 Astigmatic Ellipse Angle 119
V.2.2 Waist parameters 120

The validation study of the Mode Matching Sensing techniques was based on the absolute estimation of the mismatch parameter, which was estimated in two different ways. The total mismatch $|\epsilon|^2 = |\langle\epsilon\rangle + \delta\epsilon|^2$ was measured using the cavity spectrum. Form Eq.II.136, we have that:

$$|\epsilon|^2 = \frac{P_2}{P_0} \tag{V.1}$$

where P_2 is the integral of the resonance peak of the second order mode and P_0 of the fundamental one. The parameters β, γ, α, and η were estimated by a beam shape measurement. Using the method described in Appendix A.I.1, I characterized the beam parameters between the two cavity mirrors, and I combined these measurements with the parameters of the resonant mode estimated in Section IV.1.3.

The decoupling of the Mode Matching signal was validated by changing one beam parameter at a time. The beam shape manipulation was based on the characterization of the Mode Matching Telescopes, which is collected in the driving matrix reported in Eq. IV.72 for the Spherical Mode Matching, and in Eq. IV.84 for the Astigmatic one.

The main challenge in the linearity study was the marginalization of all the cross-talks that affected the Mode Matching Signals. The characterizations of the Mode Converter Telescope and of the electronic detection chains define two main requirements: the residual motion of the Longitudinal control should be less than 0.1 % of the cavity linewidth, Eq. IV.87, and the residual misalignment should not exceed 3 %, Eq. IV.100. Moreover, I recorded the demodulated Mode Matching signals using four different demodulation phases, $\phi_j = 0°, 90°, 180°, 270°$. These signals were combined in order to remove electronic offsets:

$$\tilde{V}_0^{QD\_i} = S_0^{QD\_i} - S_{180°}^{QD\_i} \tag{V.2}$$
$$\tilde{V}_{90}^{QD\_i} = S_{90}^{QD\_i} - S_{270°}^{QD\_i} \tag{V.3}$$

After that, the two quadratures $\tilde{V}_0^{QD\_i}$ and $\tilde{V}_{90}^{QD\_i}$ were rotated

$$\tilde{V}_I^{QD\_i} = \tilde{V}_0^{QD\_i} \sin(\Delta\phi_i) - \tilde{V}_{90}^{QD\_i} \cos(\Delta\phi_i) \tag{V.4}$$
$$\tilde{V}_Q^{QD\_i} = \tilde{V}_0^{QD\_i} \cos(\Delta\phi_i) + \tilde{V}_{90}^{QD\_i} \sin(\Delta\phi_i) \tag{V.5}$$

and the phase Δphi_i was optimised in order to minimise the variance of $\tilde{V}_Q^{QD\_i}$:

$$\Delta\bar{\psi}_i = \min_{\Delta\phi_i}\left[\sum\left(\tilde{V}_Q^{QD\_i} - \langle\tilde{V}_Q^{QD\_i}\rangle\right)^2\right] \tag{V.6}$$

All these requirements were combined in a standardised measurement protocol. The steps are:

Telescope Tuning Configuration of the telescope following the path indicated in Section IV.1.4 and Section IV.1.5

Cavity Alignment Alignment of the cavity in order to reduce the amplitude of the first order mode to less than 3 %.

Tuning Set Point of Piezo actuator Tuning of the Laser temperature in order to match the resonance frequency of the Fundamental Mode with $\langle V\rangle = 50\,\mathrm{V}$ applied to the Piezo Electric Transducer.

Longitudinal Control Engaged Engaging of the Longitudinal control and optimization of the locking point using the dither method described in Section IV.2.2

Alignment Quadrant Photodiode Sensors Alignment of the cavity reflected beam to the Quadrant Photodiode Sensors. This optimisation was obtained by looking at the Low-frequency channel of the Sensors and by equally distributing the Power over each active area.

Mode Matching Signal Recording Measurement of the Mode Matching signal, $S_{\psi_j}^{QD\_i}$ with four different demodulation phases, $\phi_j = 0°, 90°, 180°, 270°$.

Beam Profile Measurement The beam inside the cavity was characterised using the same measurement procedure used for the characterisation of the Mode Matching Telescope, Section IV.1.4

The Validation measurement was divided into two steps:

Validation of the Mode Converter Technique I used the Mode Matching Telescope characterised in Section IV.1.4 to manipulate the spherical Mismatch between the incoming beam and the cavity and recorded the Mode Matching signal using the Mode Converter Technique.

Validation of Astigmatic Mismatching Sensing I used the three-lense solution for the Astigmatic Telescope described in Section IV.1.5 and I modified the detection setup as described in Section IV.1.6. I measured the Quadrant Photodiode signal as a function of two astigmatic parameters: the ellipse angle, θ and the astigmatic waist position, η.

V.1. Validation of the Mode Converter Technique

The first validation of the Mode Converter Technique was done by Magaña-Sandoval, Vo, Vander-Hyde, *et al.*, and it was based on the comparison between the signal generated by the Quadrant Photiodes and the one generated by the Bull's eye Phodotiode[2]. That work confirmed the similarity between the two signals and confirmed the possibility of

detecting the mismatch. However, they did not investigate the linearity of the signal nor the possibility of decoupling the Mode matching degree of freedom.

The measurement presented here represents a step forward in characterising the Mode Matching technique. Thanks to the protocol defined at this chapter beginning, I was able to study the Error signal response as a function of the absolute value of the Spherical Mismatch parameter. This was made possible by three factors: first, the ability to control the beam shape based on the characterisation of the Telescope driving matrix; second, the absolute estimation of the mismatch parameters; third, the Quadrant Photodiode Gouy tuning that maximises the decoupling between the sensors' response.

The control of the beam shape and the decoupling of the sensors made it possible to simplify the relationship between the error signal and the effective mismatch. In particular, I could study it with two separate linear models: one representing the effect of the normalised variation of the waist dimension and the other one of the normalised variation of the waist position. In particular, I compared the measurement with the functions:

$$\tilde{V}_{M.M.}^{QD\_i}(\beta) = \kappa_i^{\beta}\beta + V_{0,i}^{\beta} \tag{V.7}$$

$$\tilde{V}_{M.M.}^{QD\_i}(\gamma) = \kappa_i^{\gamma}\gamma + V_{0,i}^{\gamma}. \tag{V.8}$$

where $i = 1, 2$ represents the Quadrant Photodiode number, $\tilde{V}_{M.M.}^{QD\_i}$ is the corresponding Mode Matching signal, $\kappa_i^{(\beta/\gamma)}$ represents the sensitivity to the mismatch parameter,β or γ, and $V_{0,i}^{\beta/\gamma}$ is the residual offset.

The mismatch parameters were spanned between $-15\,\%$ and $25\,\%$ for β and $-15\,\%$ and $17\,\%$ for γ, that correspond to a maximum optical loss of $2\,\%$ in power. The data are reported in Figure V.1 and the interpolation factors in Table V.1.

QD	Mismatch parameter	κ_i^b [mV %$^{-1}$]	$V_{0,i}$ [mV]	R^2
QD_1	γ	12.6(22)	−46.0(220)	0.82
	β	48.0(13)	−270.0(160)	1.00
QD_2	γ	46.9(12)	−96.0(120)	1.00
	β	−3.0(13)	−50.0(170)	0.41

TABLE V.1: Validation Measurement of the Mode Converter Technique. Fit parameters of the model described in Eq. V.7 and Eq. V.8.

The detector sensitivity verifies the decoupling of the mismatch degrees of freedom, and it matched the expectation: Quadrant Phodotiode 1 (Gouy Phase 90°) was mainly sensitive to the variation of β and Quadrant Phodotiode 2 (Gouy Phase 45°) was mainly sensitive to the variation of γ. Moreover, we can use the ratio between κ_i^{β} and κ_i^{γ} to estimate the effective Gouy phase between the cavity and the sensor $i = 1, 2$:

$$\Delta\Psi_1 = \frac{1}{2}\arctan\left(\frac{\kappa_1^{\gamma}}{\kappa_1^{\beta}}\right) = 7.4(12)^{\circ} \tag{V.9}$$

$$\Delta\Psi_2 = \frac{1}{2}\arctan\left(\frac{\kappa_1^{\gamma}}{\kappa_1^{\beta}}\right) = 43.2(8)^{\circ} \tag{V.10}$$

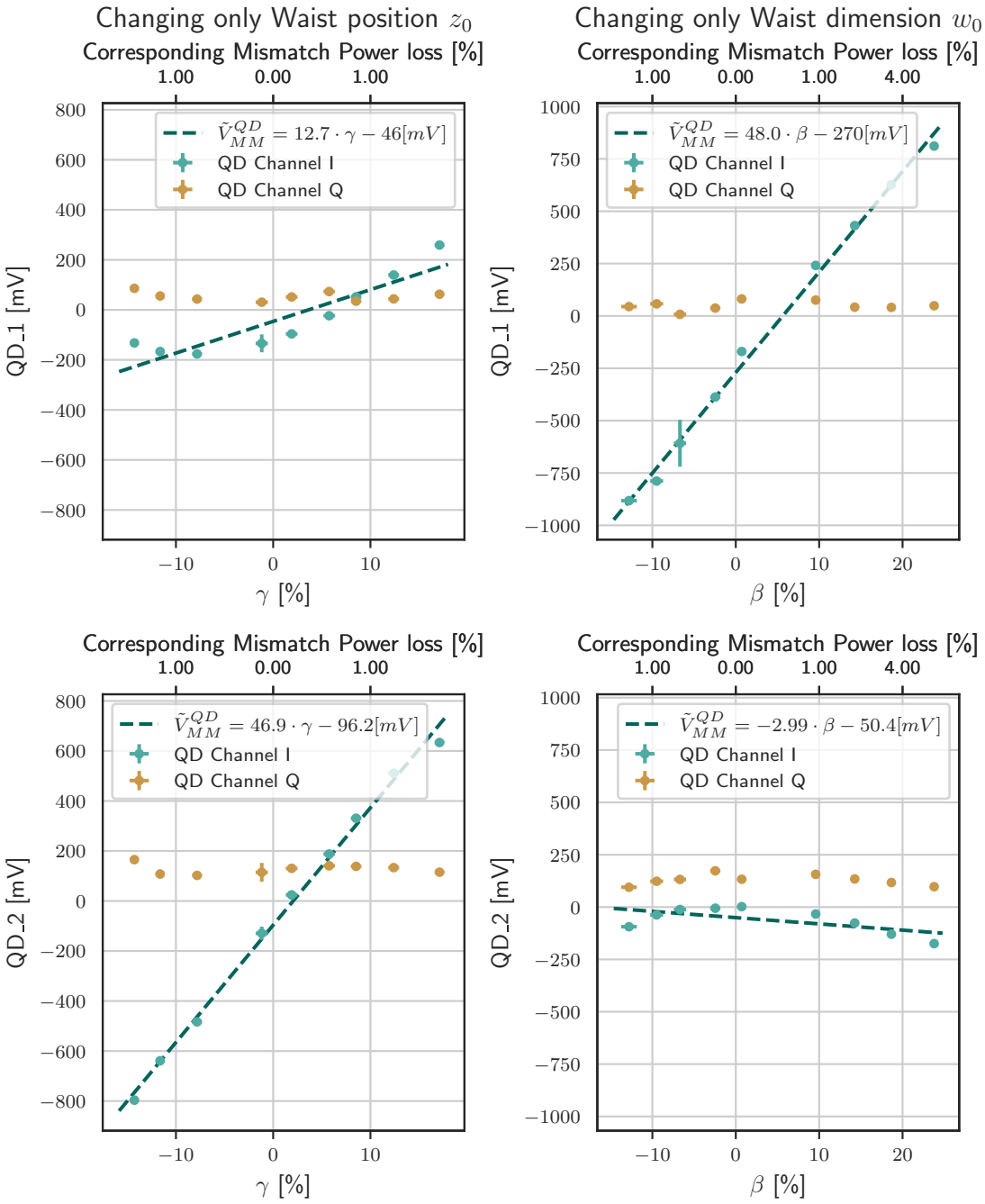

FIGURE V.1: Validation Measurement of the Mode Converter Technique. Mode Matching Signal as a function of the Spherical Mismatch parameters. The y-axis reports the signal generated by the Quadrant Phodiode after the full read-out chain. The two x-axes described the mismatch, the bottom labels report the amplitude of the mismatch parameter in %. On the opposite, the top labels report the corresponding optical loss induced by the mismatch in % of the input power. Green represents the In-phase signal proportional to the Mode Matching Error signal, while the brown dots are the constant Quadrature signal. The green line represents the linear model described in Eq. V.8 for the left plots and in Eq. V.7 for the right ones. The interpolation Parameter are reported in Table V.1.

This estimation of the sensor Gouy Phase was used to tune the position of Quadrant Photodiode 2 and to optimise the decoupling between the two parameters. I could not optimise Quadrant Photodiode 1 due to the spatial constraint of the optical table.

The linearity of the signal was verified using the coefficient of determination, R^2. This indicator can be estimated as

$$R^2 = 1 - \frac{\text{RSS}}{\text{TSS}} \tag{V.11}$$

where RSS is the Residual Square Sum

$$RSS = \sum y_i - f(x_i), \tag{V.12}$$

and TSS is the Total Square Sum:

$$TSS = \sum (y_i - \langle y_i \rangle). \tag{V.13}$$

The value of R^2 is the proportion of the variation in the dependent variable that is predictable from the independent variables[46, p. 344], and it is closer to 1 when the model, $f(x)$ fully describes the relationship between the independent variable x and dependent variable y. In particular, the model in Eq. V.7 indicates a good linearity on the relationship between Quadrant Photodiode 1 and β, and Quadrant Photodiode 2 and γ.

V.2. Validation of Astigmatic Mismatching Sensing

The validation of the Astigmatic Mode Matching Sensing technique required two small modifications of the Optical Setup. First, the Mode Matching Telescope was upgraded to the Astigmatic configuration. In this way, it was possible to control the Astigmatic mismatch parameters using the driving matrix estimated in Eq. IV.84. Second, the Wavefront Sensor setup was rearranged to monitor both the Spherical and the Astigmatic Mismatch. Quadrant Photodiode 1 was left after the Mode Converter in order to detect variation of spherical waist radius, $\beta = (w_0^{x'} + w_0^{y})/(2w_0^{cav})$, while Quadrant Photodiode 2, was moved before the Mode Converter and the Gouy phase was tuned in order to detect the astigmatic waist position, $\eta = (z_0^{x'} - z_0^{y'})/(4z_R^{cav})$.

The validation study was divided into two steps. First, I studied the relationship between the orientation of the astigmatic ellipse, θ, and the Quadrant Photodiodes. Second, I characterised the response to the variation of the Astimatic waist position, η.

V.2.1. *Astigmatic Ellipse Angle*

The relationship between the astigmatic ellipse and the Quadrant Photodiodes 1 is described in Eq.III.72. Due to the tuning of Quadrant Photodiode 2, I expected the following:

$$\tilde{V}_{M.M.}^{QD\_2}(\theta) = \frac{m}{\pi}(r_{res} - 1)\chi_i \cos(2\theta)\Re[\delta\epsilon_i] \tag{V.14}$$

and a constant signal on Quadrant Photodiode 2.

In order to test this model, I induce strong astigmatism, $\eta = 20\,\%$, to maximise the corresponding signals, and I controlled the orientation of the astigmatic ellipse by rotating the cylindrical lens of the Astigmatic Mode Matching Telescope. I recorded the

signal with both Quadrant Photodiode Sensors for each angle of the cylindrical lens. The data are reported in Fig. V.2, and they were interpolated with the linear models:

$$\tilde{V}_{M.M.}^{QD\_i}(\theta) = \kappa_i \cos(2\theta + \theta_0^i) + V_{0,i}^{\theta} \tag{V.15}$$

where θ is the orientation angle of the cylindrical lens, and κ_i collects the contribution of the mismatch parameters. The fit results are reported in Table. V.2.

$\tilde{V}_{M.M.}^{QD\_i}(\theta)$	κ_i [mV]	θ_0 [deg]	$V_{0,i}^{\theta}$ [mV]	R^2
$\tilde{V}_{M.M.}^{QD\_1}(\theta)$	$-113(5)$	$11(2)^\circ$	171(3)	0.84
$\tilde{V}_{M.M.}^{QD\_2}(\theta)$	$-261(7)$	$6(2)^\circ$	10(5)	0.89

TABLE V.2: Validation Measurement of the Astigmatic Wavefront Sensing - Ellipse Rotation. Fit parameters of the model described in Eq. V.15.

The signal recorded from the Quadrant Photodiode Sensor 2 demonstrates the cosine dependency from the ellipse angle, θ. However, we have a similar dependency on the Quadrant Photodiode 1. This behavior is not compatible with the ideal model and it can be justified with crosstalk between the astigmatic mismatch and the Spherical sensor. This hypothesis will be deepened in Section III.2.2.

V.2.2. *Waist parameters*

The second validation test was based on the same approach used for the Spherical Mismatch with one main difference. The astigmatic telescope based on the three-lens configuration cannot control all the mismatch parameters at once, so I approached the measurement differently. I used the driving matrix in Eq. IV.84 to define two paths for the astigmatic telescope: one in which the variation of β was maximised, and η kept constant and another one in which β was constant and the variation of η maximised.

The evolution of the mismatch parameters is reported in Fig. V.3, where we can see that all the parameters, except the controlled one, span between $-20\,\%$ and $20\,\%$. The moving parameters are strongly correlated, and it is possible to discriminate only when β or η are constant. For this reason, the validation of the Astigmatic Mode Matching Sensing technique is based on the following hypothesis: The Quadrant Photodiode 2 is tuned to detect only changes of η, so the corresponding error signals should change only if η changes.

The Mismatch signals are reported in Fig. V.4, and they were interpolated with the linear models:

$$\tilde{V}_{M.M.}^{QD\_i}(\beta) = \kappa_i^{\beta}\beta + V_{0,i}^{\beta} \tag{V.16}$$

$$\tilde{V}_{M.M.}^{QD\_i}(\eta) = \kappa_i^{\eta}\eta + V_{0,i}^{\eta} \tag{V.17}$$

In this case, $\kappa_i^{(\beta/\eta)}$ does not directly represent the Quadrant Photodiode sensitivity to the β/η, but they collect the effect to all the other parameters that are not controlled. In particular, $\kappa_i^{(\beta)}$ does not consider the variation of η and $\kappa_i^{(\eta)}$ the variation of β. The fit results are reported in Table. V.3

The measurements show two important results. First, the Quadrant Photodiode Sensor 1 is still sensitive to the variation of β, and the astigmatic aberration does not

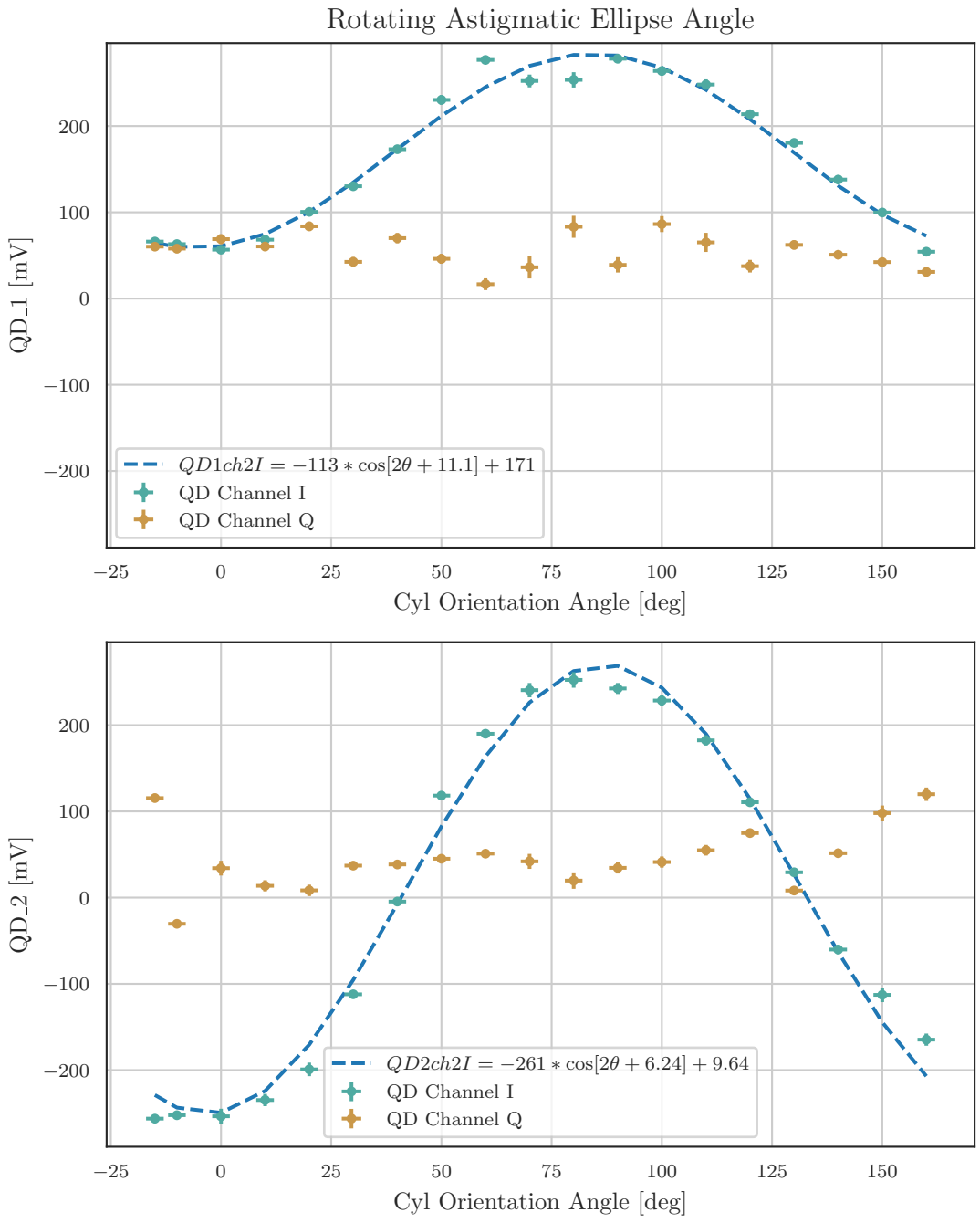

FIGURE V.2: Validation Measurement of the Astigmatic Mismatch Sensors - Ellipse Rotation. The y-axis reports the signal generated by the Quadrant Phodiode after the full read-out chain. The x-axis represents the orientation angle of the Cylindrical Lens. Green lines represent the In-phase signals extracted by the demodulation scheme and are proportional to the Mode Matching Error signal, while the brown dots are the constant Quadrature signals. The green line represents the linear model described in Eq. V.15. The interpolation Parameters are reported in Table V.2.

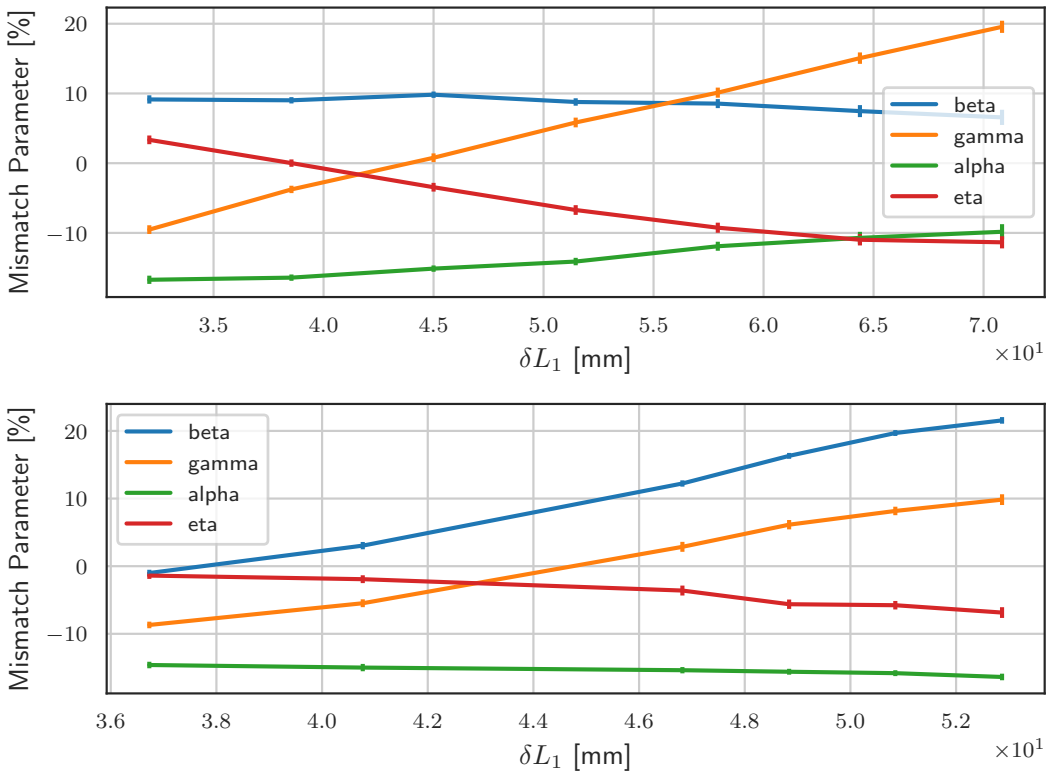

FIGURE V.3: Evolution of the Mode Matching Paratemers as a function of the Astigmatic Telescope. All the parameters, except the controlled one, span between −20 % and 20 %.

change the calibration factor. In fact, Table V.1 reported a $\kappa_1^{(\beta)} = 48.0(13)\,\mathrm{mV\,\%^{-1}}$ which is compatible with the estimation obtained here $\kappa_1^{(\beta)} = 49.0(10)\,\mathrm{mV\,\%^{-1}}$. Second, the Quadrant Photodiode 2 is sensitive only to the variation of η inasmuch $\kappa_2^{(\beta)} = 0(1)\,\mathrm{mV\,\%^{-1}}$, while $\kappa_2^{(\eta)} = 28.0(20)\,\mathrm{mV\,\%^{-1}}$.

On the other hand, the signal of Quadrant Photodiode 2 changes when β is kept constant. This behaviour is justified by the crosstalk between the astigmatic mismatch on the Spherical Mismatch Sensor. This coupling can be quantified as follows:

$$\frac{\kappa_1^{(\eta)}}{\kappa_1^{(\beta)}} = -14(2)\,\% \tag{V.18}$$

The origin of this crosstalk can be generated by an imperfect conversion of the Hermite-Guass Mode, $\mathbf{HG}_{11}^{45}$. From the analysis done in Section III.2.2, we know that in case the *pre-converter* is mistuned, the Mode Converter Telescope does not guarantee a perfect conversion of the mode $\mathbf{HG}_{11}^{45}$ and $\mathbf{LG}_{01}$. This imperfection could generate a coupling of the astigmatic parameters into the Spherical Mode Matching Signals. Using the model of Eq. III.97, we can estimate an upper bound to the Mode Converter Telescope detuning, given by

$$\delta\psi = 2\arctan\left(\frac{\kappa_1^{\eta}}{\kappa_1^{\beta}}\right) = 16(2)^\circ \tag{V.19}$$

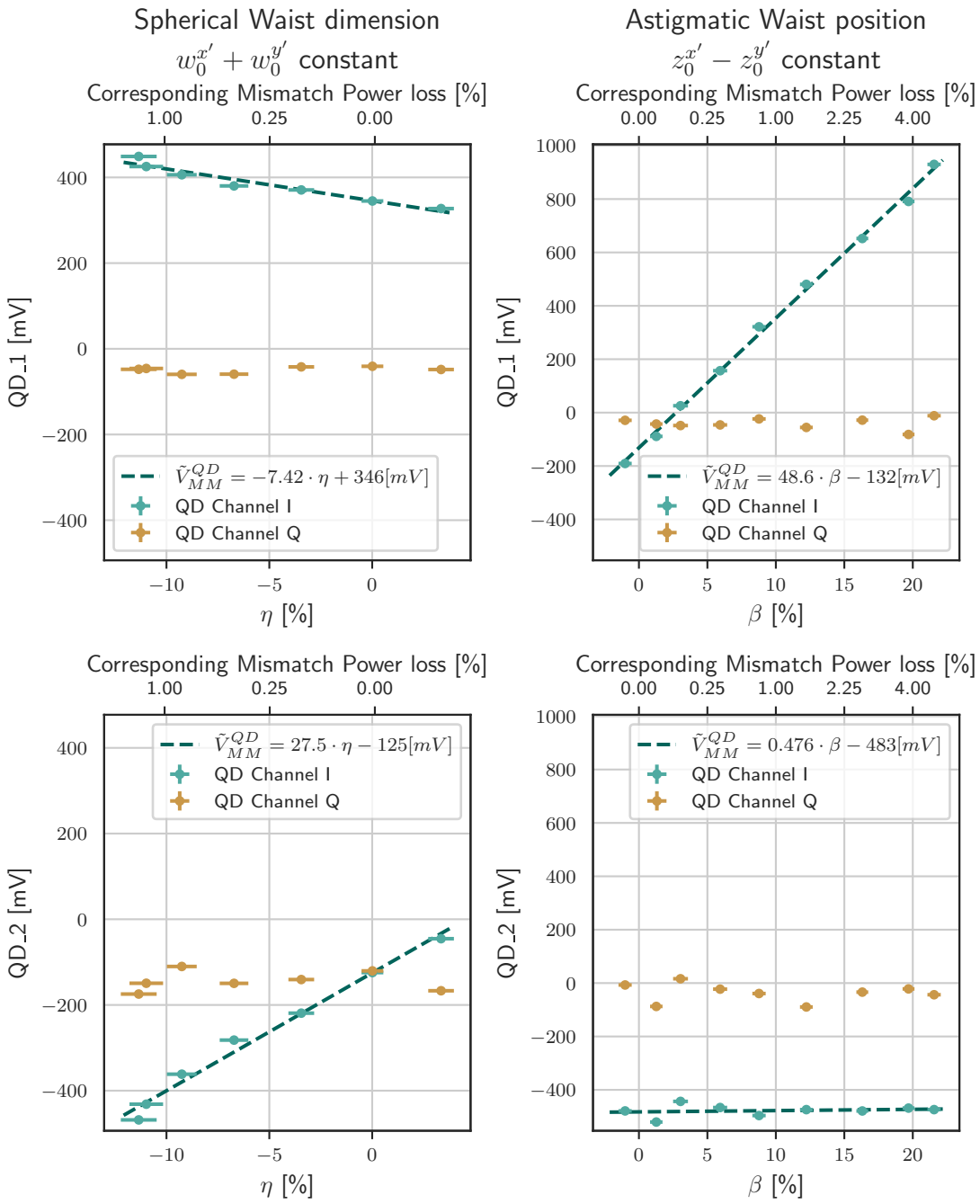

FIGURE V.4: Validation Measurement of the Astigmatic Mismatch Sensors - Waist Parameters. The y-axis reports the signal generated by the Quadrant Phodiode after the full read-out chain. The two x-axes described the mismatch, the bottom labels report the amplitude of the mismatch parameter in %. On the opposite, the top labels report the corresponding optical loss induced by the mismatch in % of the input power. Green represents the In-phase signal proportional to the Mode Matching Error signal, while the brown dots are the constant Quadrature signal. The green line represents the linear model described in Eq. V.16 for the left plots and in Eq. V.17 for the right ones. The interpolation Parameters are reported in Table V.3.

QD	Mismatch parameter	κ_i^b [mV %$^{-1}$]	$V_{0,i}$ [mV]	R^2
QD_1	η	−7(1)	346(7)	0.94
	β	49(1)	−132(11)	1.00
QD_2	η	28(2)	−125(12)	0.98
	β	0(1)	−483(12)	0.03

TABLE V.3: Validation Measurement of the Astigmatic Wavefront Sensing - Waist Parameters. Fit parameters of the model described in Eq. V.16 and Eq. V.17.

VI MODE MATCHING SENSING IN QUANTUM NOISE REDUCTION SYSTEM

The Mode Converter Technique was implemented in the Frequency Dependent Squeezing System of Advanced Virgo Plus. The Mode Matching sensor was designed to monitor the mismatch of the squeezed vacuum beam at two critical points: the beam injection to the Filter Cavity and the beam injection to the Interferometer. In this Chapter, we will briefly introduce the optical scheme of the Frequency Dependent Squeezing Source, and we will describe the implementation of the Mode Converter Technique. The installation is still ongoing at the time of writing, and the sensor signals are not calibrated.

VI.1. Frequency Dependent Squeezing

The key point of Frequency-Dependent Squeezing is manipulating the quantum noise as a function of its frequency. In particular, we want to reduce the radiation pressure at low frequencies and the shot noise at high frequencies, and this requires manipulating the phase of the squeezed vacuum beam as a function of the frequency.

From a formal point of view, the effect of the squeezing on the Quantum Noise is described by Eq. I.37:

$$S_{h_n h_n} = \frac{2\hbar}{ML^2\Omega^2}\left(K_{ITF} + \frac{1}{K_{ITF}}\right)\left(\cosh(2\xi) - \cos[2(\theta + \Theta(\Omega))]\sinh(2\xi)\right)$$

where M is the mirror mass, L the arm length, $\Theta(\Omega) = \operatorname{arccot}(K_{ITF})$ with K_{ITF} the Interferometer response, and θ is the squeezing angle. In case the squeezing angle is matched with the dispersion imposed by the Interferometer $\theta = -\Theta(\Omega)$, the Quantum noise is reduced over the whole spectrum as described by Eq. I.41:

$$S_{h_n h_n} = \frac{2\hbar}{ML^2\Omega^2}\left(K_{Mi} + \frac{1}{K_{Mi}}\right)e^{-2\xi}$$

The implementation of the Frequency Dependent Squeezing in Advanced Virgo Plus is based on a detuned resonance cavity, generally called a Filter Cavity. The idea is to use the cavity reflectance to manipulate the beam phase and impose the dispersion rule $\theta = -\Theta(\Omega)$.

The effect of the Filter Cavity can be modelled by imposing a small detuning $f - f_{res} \ll f_{\mathrm{FWMH}}$ and a high finesse $\mathcal{F} >> 1$ approximations on Eq.II.19. In this case, the cavity reflectance can be written as[48]:

$$r_{\mathrm{cav}}(\Omega) \simeq 1 - \frac{1-\epsilon}{1 + i\xi(\Omega)} \tag{VI.1}$$

where

$$\epsilon = 2\Lambda_{rt}^2\,\mathcal{F} \tag{VI.2}$$

$$\xi(\Omega) = 2\frac{\delta f}{\Delta f_{FWHM}}, \tag{VI.3}$$

and Λ_{rt} are the round trip losses of the cavity and $\mathcal{F}$ its Finesse. This expression still mixed the phase modulation with the amplitude, but they can be discriminated by rewriting the equation as

$$r_{\text{cav}}(\Omega) = |r_{\text{cav}}(\Omega)|e^{i\alpha_{cav}(\Omega)} \tag{VI.4}$$

In this way, we can distinguish between the amplitude manipulation

$$|r_{\text{cav}}(\Omega)| = \sqrt{1 - \frac{(2-\epsilon)\epsilon}{1+\xi^2(\Omega)}} \tag{VI.5}$$

from the phase manipulation

$$\alpha_{cav}(\Omega) = \arg\left[-1 + \epsilon + xi^2(\Omega) + i(2-\epsilon)\xi(\Omega)\right] \tag{VI.6}$$

To apply these equations to the squeezed vacuum, we should convert them into the two-photon pictures. The calculations can be found in [48], and they lead to the following expression of the squeezed quadrature rotation:

$$\alpha_p(\Omega) = \arctan\left(\frac{(1-\frac{\Lambda_{rt}^2}{\mathcal{F}})\Delta f_{FWHM}\delta w_{fc}}{(1-2\frac{\Lambda_{rt}^2}{\mathcal{F}})\frac{\Delta f_{FWHM}^2}{4} + \delta\omega_{fc}^2 + \Omega^2}\right) \tag{VI.7}$$

This equation depends on four different parameters of the Filter Cavity: the round trip losses, Λ_{rt}^2; the Finesse, $\mathcal{F}$; the cavity linewidth, Δf_{FWHM}^2; and the detuning w.r.t the vacuum squeezed frequency, $\delta\omega_{fc}$. During the design of Advanced Virgo Plus, these parameters were tuned to match the Interferometer response and to optimise the reduction of the Quantum Noise[35, p.342]. In particular, the design parameters are:

Parameter	
Length(m)	285
Finesse at 1064 nm	10 800
Round Trip Losses(ppm)	40

VI.2. General Design of the Frequency Dependent Squeezer

The Frequency Dependent Squeezing technique is one of the major upgrades of Advanced Virgo Plus. Its implementation is carried out by the Quantum Noise Reduction system, and it is designed as an upgrade of the Frequency Independent Squeezer source used during the last Observing Run, O3. The main goal of these upgrades is to provide a stable squeezed quadrature rotation using a detuned cavity. For these reasons, most of the system is dedicated to controlling the Filter Cavity and optimising the coupling with the squeezed vacuum beam.

The simplified scheme of the Frequency Dependent Squeezer source is described in Figure VI.1 organised into three sectors:

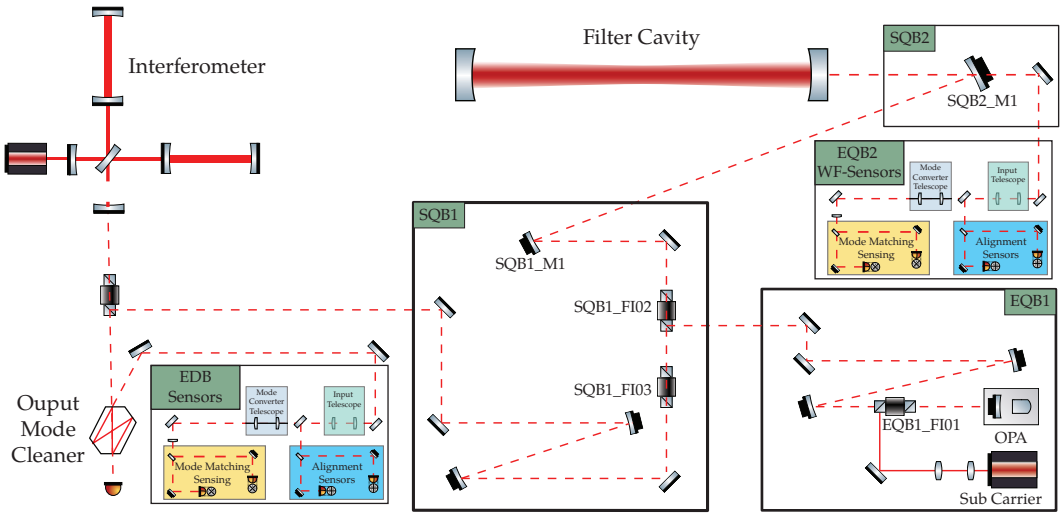

FIGURE VI.1: Simplified scheme of the Frequency Dependent Squeezer source. The optical path begins EQB1 (boom left). In this bench, we can find the Optical Parametric Amplifier, which generates the squeezed vacuum beam and the Mode Matching telescope, which fine controls the coupling with the Filter Cavity. After this preparation, the beam is sent to the suspended benches, SQB1 and SQB2, where it is expanded and injected into the Filter Cavity. Once the squeezing ellipse is rotated as a function of the frequency, the beam travels back to SQB1, where it passes through the Faraday Isolator. In the last section of this setup, the beam is manipulated by a second Mode Matching Telescope which tunes the coupling with the Interferometer.

Squeezed Vacuum Source is based on the Frequency Inpendendent Squeezing Source used during the last Observing Run, O3[22]. The squeezed vacuum is generated using an optical parametric amplifier, and it can provide up to 14 dB of squeezing[49]. Moreover, this sector is responsible for finely control the squeezed vacuum as the Mode Matching with the Filter Cavity.

Squeezed Vacuum Injection responsible for the injection of the Squeezed Vacuum to the Filter Cavity and the injection of Frequency-Dependent Squeezing to the Interferometer. These two systems are installed on two in-vacuum suspend benches: The Suspended Squeezing Bench 1(SQB1) is mainly responsible for the injection to the Interferometer, and The Suspended Squeezing Bench 2(SQB2) is responsible for the injection to the Filter Cavity;

Filter Cavity which is a Linear Cavity composed of two Suspended Mirror with Radius of Curvature of 558 m, and separated by 285 m. Moreover, the reflective coatings were selected to have a Finesse of 10 800 for $\lambda = 1064$ nm.

The optical path of the squeezed vacuum beam starts from the Optical Parametric Amplifier, which defines its original beam shape. The beam passes through a Faraday Isolator, EQB1_FI01, and is manipulated by a Telescope. This system is composed of two Curved Mirrors mounted on two translational stages, and it is responsible for the fine Mode Matching between the squeezed vacuum beam and the Filter Cavity. Once the squeezed beam is prepared, it is sent to the Suspended Benches where it is captured by Faraday Isolator, SQB1_FI02, and is expanded by another reflective telescope which

starts with SQB1_M1 and ends with SQB2_M2. After that, the squeezed vacuum beam reaches the Filter Cavity that rotates its quadrature as described by Eq. VI.7. The field reflected by the cavity is a Frequency Dependent Squeezed vacuum.

A 0.1 % peak off of the beam is extracted by SQB2_M2 and sent to the External Squeezing Bench 2(EQB2) where the Wavefront Sensors for the Filter Cavity are installed. The main component of the squeezed vacuum propagates back to SQB1, passing through both the Faraday Isolators, SQB1_FI02 and SQB1_FI03, and it is injected into the Main Interferometer by a third reflective telescope.

After travelling inside the Interferometer, the squeezed beam is sent to the OMC(OMC). This cavity filters the beam from the Interferometer and is tuned to select both the squeezed vacuum and the Interferometer signal. These beams are transmitted by the OMC and reach the Photodiodes used to detect the Gravitational Wave Signals. The beam reflected from this last cavity is sent to the External Detection Bench, which hosts the Wavefront Sensors for the OMC. We decided to use the OMC as a reference for the Mode Matching and the Alignment of the Interferometer.

Even if the squeezed vacuum beam is the main element of the Frequency Dependent Squeezing, it is not enough to control the whole system. This beam and its sidebands do not have sufficient power to produce usable error signals. For this reason, the control scheme is based on two auxiliary beams which act as bright references for the squeezed vacuum:

Green Beam is a peak-off of the Pump field used to generate the squeezed vacuum. Its wavelength is 532 nm which corresponds to half of the squeezed vacuum one.

Sub Carrier is generated by a Mephisto source. Its wavelength is 1064 nm which is equivalent to the squeezed vacuum one.

these beams are used to manage different aspects of the system. The Green beam is responsible for the first stage of the Filter Cavity Control, generating coarse error signals for Filter Cavity. The Sub Carrier acts as a bright reference of the squeezed vacuum and is responsible for the fine couple of the squeezed beam with the Filter Cavity and the Interferometer. In particular, the Mode Matching sensing of the squeezed vacuum beam is based on Sub Carrier, so we will focus the discussion only on this beam.

VI.2.1. *Sub Carrier Path*

The first part of the Sub Carrier optical path is in fiber. Here, the beam is phase modulated with a frequency of $\Omega_{SC} = 11.12\,\mathrm{MHz}$, and it is attenuated down to 10mW. After this preparation setup, the beam is propagated into free space, where it is manipulated by a two lenses telescope, and it is sent to the first Faraday Isolator of the Squeezed Beam, EQB1_FI01. The Sub Carrier polarisation is tuned to send the beam to the cavity of the Optical Parametric Amplifier. Once the beam reaches the cavity, it is reflected and starts following the same path as the Squeezed Vacuum beam. In order to guarantee the overlap with the Squeezed Vacuum, the Sub Carrier is aligned and mode matched with the cavity of the Optical Parametric Amplifier. This approach is based on the fact that the resonance mode of that cavity defines the shape of the squeezed vacuum beam, so if the Sub Carrier is perfectly matched and aligned, it has the same shape as the squeezed beam. This optimisation was obtained by changing the cavity length with a piezo actuator and locking to the resonance peak of the different Sub Carrier high order

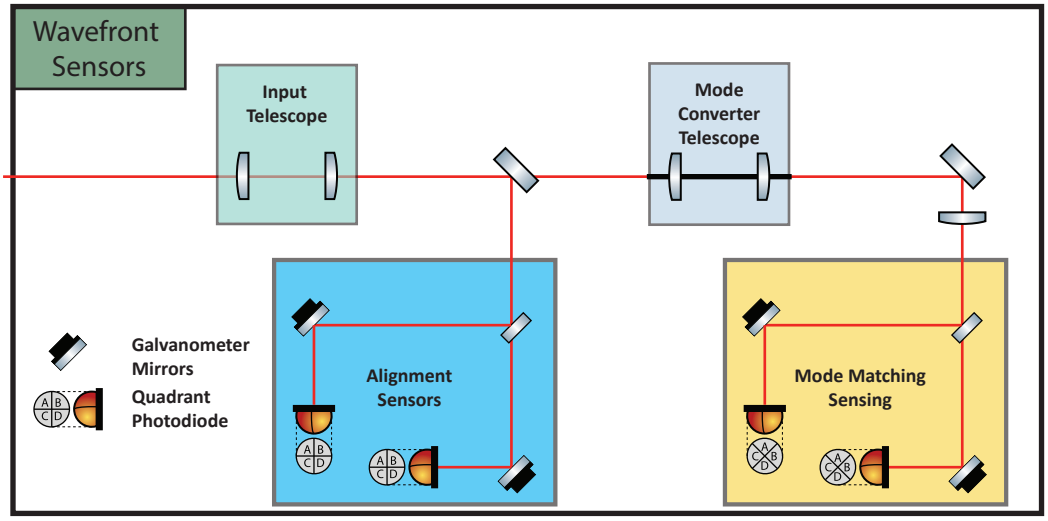

FIGURE VI.2: Wavefront Sensors. This scheme represents the general layout of the Wavefront Sensor installed in the Frequency Dependent Squeezer source. The first element is a pre-converter Telescope(green box) which is used to tune the Gouy Phase of the Alignment Sensors and to match the Mode Converter Telescope.

modes. The mode matching was improved by using the two lenses telescope installed before the EQB1_FI01.

The Sub Carrier Frequency is shifted with respect to the squeezed vacuum one. This detuning is necessary to avoid interference with the squeezed vacuum and the Interferometer main laser. Moreover, the Sub Carrier should not resonate in the cavity of the Optical Parametric Amplifier, and it should be filtered out by the OMC installed at the end of the Interferometer. On top of these constraints, we must consider the Filter Cavity detuning. In fact, the sub Carrier is responsible for the fine stabilisation of the Filer Cavity Lenght and tuning the offset between the resonance frequency and the squeezed vacuum one. In order to meet all these requirements, the Sub Carrier is phase-locked to the main laser of the squeezer source with a frequency offset of:

$$\delta\omega_{SC} = \omega_{sqz} - \omega_{SC} = 1\,262\,400\,025\,\text{Hz} \tag{VI.8}$$

VI.2.2. *Wave Front Sensing Scheme*

There are two points of the squeezing path where the Mode Matching is critical. One is the Filter Cavity, and the other one is the Interferometer. For this reason, I designed the installation of two Wavefront Sensors Setups to control the squeezed vacuum coupling with two different cavities. These setups are based on the scheme reported in Figure VI.2 and are responsible for monitoring Alignment and Mode Matching. The Alignment Sensing is based on the standard heterodyne detection presented by Anderson in [3], and it requires the installation of two Quadrant Photodiodes with a Gouy Phase difference of 90°. The Mode Matching Scheme is based on the Mode Converter technique proposed by Magaña-Sandoval, Vo, Vander-Hyde, *et al.* in [2], and it requires the installation of a Mode Converter Telescope and two Quadrant Photodiodes with a Gouy Phase difference of 45°.

The Wavefront Sensors are combined together in the same setup. In particular, the reflected beam passes through an input telescope and is split into two beams. One beam is sent to the Alignment Sensors, and the other beam is the Spherical Mode Matching One. In this way, we could use only two lenses to tune the Gouy Phase of the Quadrant Photodiode for the alignment and couple the Mode Converter Telescope. An additional third lens is required to tune the Gouy Phase of the Mode Matching Sensors. In both cases, the Mode Converter Telescope was based on the standard design presented in Section III.1.2. In particular, I used two symmetrical Cylindrical lenses with a focal length of $f = 100(2)$ mm. This choise imposes a waist of $w_0 = 246$ µm for beam under conversion.

The Electronic Quadrant Photodiode Sensors are similar to the one used in the table-top experiment described in Chapter IV. Still, in this case, the read-out scheme is fully digital. The signal generated by each sector is measured by the Virgo DAQ system, which is responsible for the digital demodulation and the recombination of the signals. Moreover, the beams are centred on the Quadrant Photodiode using a local control loop based on Galvanometer Mirrors.

This optical scheme was adapted to the two different cavities using the OptoCad simulation tool. In particular, I optimised the design of the pre-converter to the reflected beams and the alignment of the Mode Converter cylindrical axis. The final design of EQB2 is reported in Figure VI.3 while the EDB design is reported in Figure VI.4.

Filter Cavity Mode Matching Sensing

The wavefront Sensing setup for the Filter Cavity was installed on EQB2, and it uses the Sub Carrier peak-off extracted on SQB2. The installation of the optical path was based on the same procedure described in Section IV.1.6. In particular, the Mode Matching between the Sub Carrier and the Filter Cavity was optimised with the Mode Matching Telescope installed on EQB1, and the transmitted power of the Second Order Mode was reduced to less than 2 % of the Foundemtnal one[1]. The cavity reflection was extracted by the SQB2_M2, which transmitted 1 % of the power. After that, the peak-off beam passes through a Dichroic Beam splitter which reflects the Green beam and transmits the Sub Carrier. This optic induces small astigmatism on the transmitted beam. This aberration is generated by a combination of the Rayleigh Range of the Sub Carrier, $z_R = 429\,\mathrm{mm}$[2], the angle of incident 45°, the substrate thickness, $d = 19.0(1)$ mm, and the refractive index, $n_2 = 1.45$. In particular, this mirror acts as a tilted slab, and it induces a mismatch between the positions of the Sagittal waist with respect to the Transversal one[42, p.42]. Optocad Simulation indicates an offset around 200 mm which corresponds to an astigmatism $\eta = 20\,\%$. In order to compensate for this aberration, the Mode Converter Telescope was oriented parallel to the beam astigmatism. In particular, we aligned the Cylindrical lens axis orthogonal to the bench and mounted the Quadrant Photodiode with an $\times$ orientation. The Mode Converter was matched on the common beam values, $\langle w_0 \rangle = (w_0^{x'} + w_0^{y'})/2$ and $\langle z_0 \rangle = (z_0^{x'} + z_0^{y'})/2$.

Output Mode Cleaner cavity Mode Matching Sensing

The wavefront Sensing setup for the Interferometer was designed around the reflected beam coming from the OMC. The installation of this setup was based on the Single

[1] Log Entry in https://logbook.virgo-gw.eu/virgo/?r=53474.
[2] This value was estimated by the OPTOCAD simulation and assumed a perfectly matched Filter Cavity.

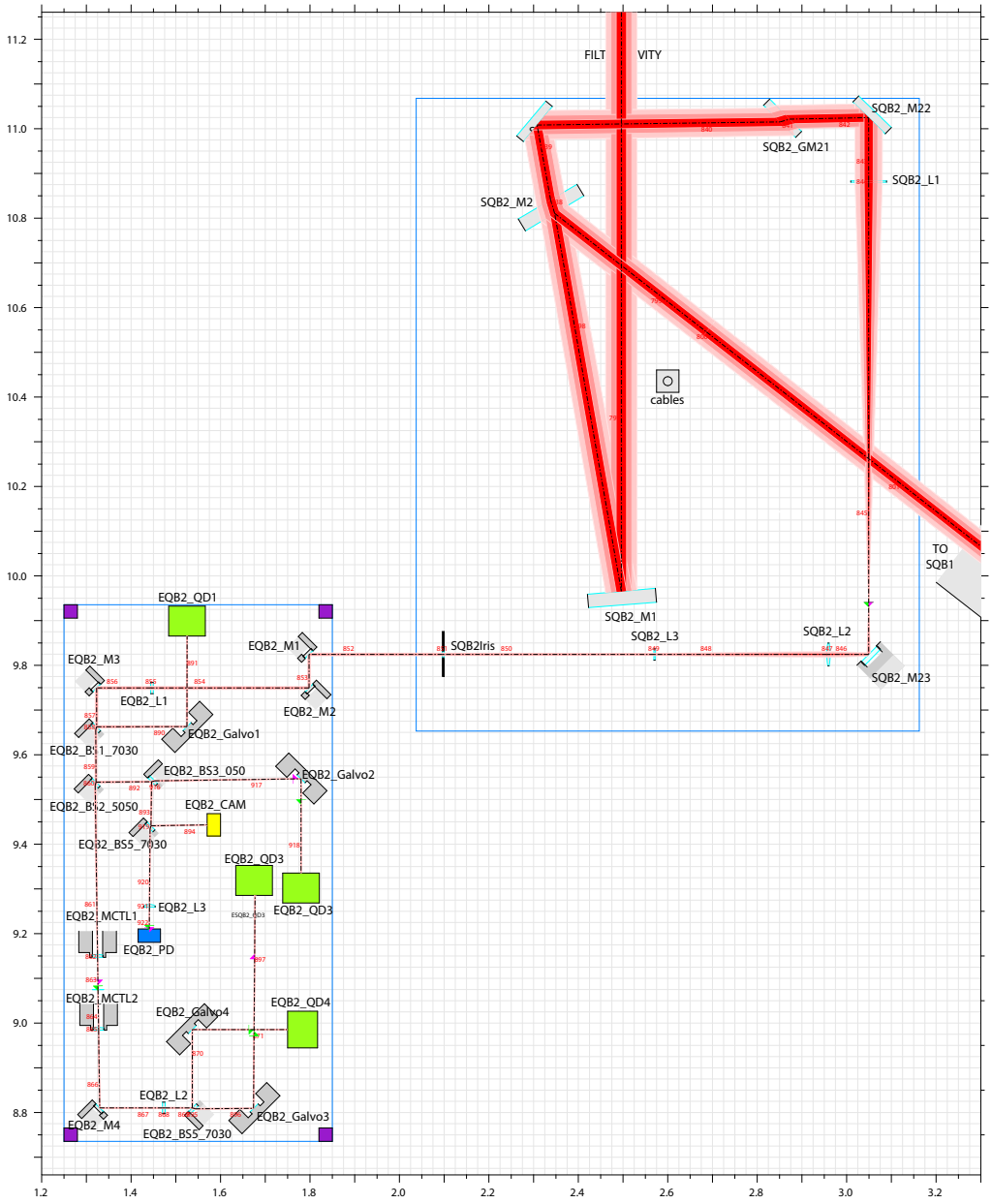

FIGURE VI.3: OPTOCAD simulation for External sQueezing Bench 2. For clarity, I focused the drawing only on the beam from the Filter Cavity. The bench on the top right is the Suspended sQueezing Bench 2, while the one on the bottom left is External sQueezing Bench 2.

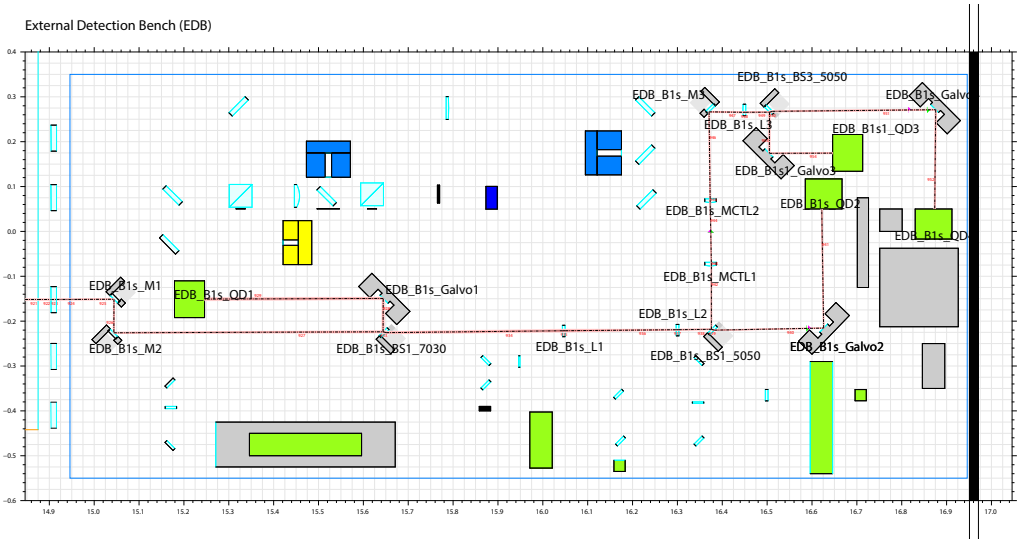

FIGURE VI.4: OPTOCAD simulation for External Detection Bench. Here, I reported only the simulation of the Output Mode Cleaner Reflection beam.

Bounce beam coming from the Main Interferometer. This beam is the simple reflection of the North Cavity Input Mirror and represents the beam shape of the Interferometer, and it was used for the off-line Mode Matching and Alignment of the OMC. After this optimisation, the transmitter power of the Second Order Mode was reduced to less than 0.64 % of the Fundamental one[3] and is mainly generated by astigmatism. In order to avoid crosstalk with the Spherical Mismatch signals, we aligned the Cylindrical lenses with an angle of 45° with respect to the bench, and we mounted the Quadrant Photodiodes in the plus cross orientation. In this way, we minimise the detector sensitivity to the $\mathbb{H}G_{11}$ mode generated by the astigmatic Mismatch. Again, the Mode Converter was matched on the common beam values, $\langle w_0 \rangle = (w_0^{x'} + w_0^{y'})/2$ and $\langle z_0 \rangle = (z_0^{x'} + z_0^{y'})/2$.

VI.2.3. *Installation of the Mode Matching Sensors*

The Commissioning of both the Mode Matching Wavefront Sensors is still under development. All the Optical components are currently installed on the Tables, but the tuning of the Mode Converter and the characterisation of the Error signal are not done.

[3] LVK presentation https://tds.virgo-gw.eu/?content=3&r=18454.

VII | SUMMARY AND OUTLOOK

VII.1. Summary

This thesis presents three main scientific contributions. The first is the independent validation of the Mode Matching Sensing technique based on the Mode Converter Telescope. This is the first method that allows characterising mismatch between a beam and the cavity kept in resonance and estimating the complex amplitude which represents this decoupling. The first validation measurement was obtained by Magaña-Sandoval, Vo, Vander-Hyde, *et al.* in [2]. The author of this work demonstrated the equivalence between the Mode Converter Technique and the Standard Heterodyne detection based on bull's eye photodiodes. The result presented in Section V.V.1 made a step forward in the validation of the technique by characterising the Mode Matching Signals as a function of the incoming beam shape. I used the Mode Matching Telescope describe in Section IV.1.4 to independently control the parameters $\beta = \delta w_0 / w_0^{cav}$, and $\gamma = \delta z_0 / (2 z_R^{cav})$, and I recorded the signal generated by two Quadrant Photodiodes installed with a differential Gouy Phase of 45°. The measurements reported in Figure V.1 demonstrate that the Mode Converter technique generates two decoupled error signals and it can characterise a Mismatch optical loss lower than 2 %. The validation study is also composed of modelling for a real Mode Converter Telescope(Section III.III.2). These tools can estimate the coupling of the Mode Matching signal with other cavity degrees of freedom and quantify the requirement for the tuning of the Mode Converter Telescope.

The second contribution is the design of an optical scheme for detecting Astigmatic Mismatch. This method was inspired by the study of a mistuned Mode Converter Telescope, and it is an extension of the technique proposed by [2]. As described in Section III.1.4, if we install four extra Quadrant Photoiodes before the Mode Converter Telescope, we can record the error signals proportional to the Astigmatic Mismatch degrees of freedom. The measurements collected in Section V.V.2 are the first step in validating the new technique: Figure V.4 reports the error signal proportional to the Astigmatic waist positions, η and Figure V.2 demonstrates the trigonometric dependency on the orientation of the astigmatic ellipse, θ. These results indicate that even the Astigmatic Mode Matching technique can characterise mismatch losses lower than 2 %.

The third contribution of this thesis is the protocol used to validate the two Techniques. The Spherical and Astigmatic Mismatch Sensing techniques were validated by studying the relationship between the mismatch degrees of freedom and the Sensors Error Signal. This approach does not make any assumption about the Sensing technique since the mismatch is estimated directly by the characterisation of the beam shape inside the cavity, and the decoupling is obtained by a calibration of the mode-matching telescope. For this reason, we could use the same protocol to validate different Mode Matching techniques and obtain a comparison between different methods.

VII.2. Outlook

The results presented in this thesis can be extended in different ways. One is the implementation of a six lenses Astigmatic telescope that will allow characterising the error signals as a function of all the mismatch parameters and studying their possible cross-talk.

From the theoretical point of view, the Mismatch model presented in Section II.II.2 is limited only to Simple Astigmatic Gaussian Beams. This study cannot be directly extended to the General Astigmatic case since we lose the definition of the beam waist. This kind of beam shape is described by[42, p. 89]:

$$U(x,y,z|\mathbb{Q}) = U_0 \exp\left[-\frac{ik}{2}\left(\frac{x^2}{q_{xx}} + \frac{2xy}{q_{xy}} + \frac{y^2}{q_{xy}}\right)\right] \tag{VII.1}$$

where the complex parameter q is replaced by a complex matrix $\mathbb{Q}$, defined by:

$$\mathbb{Q} = \begin{pmatrix} q_{xx} & q_{xy} \\ q_{yx} & q_{yy} \end{pmatrix} \tag{VII.2}$$

which is symmetric $q_{xy} = q_{yx}$. In this case, the orientation of the iso-power and iso-phase ellipses rotate within the z-propagation. This evolution destroys the beam's internal reference and makes it impossible to directly extend the calculation presented in Section II.II.2. In this case, the Taylor expansion of the General Astigmatic Gaussian beams should be based on the perturbation of the matrix, $\mathbb{Q}$, but I could not delve into this topic. My educated guess is that the General Astigmatic Mismatch can be represented by:

$$U(x,y,z) = \delta\epsilon \left[\mathbf{HG}_{11}\cos(\Theta) + \mathbf{HG}_{11}^{45}\sin(\Theta)\right] + \langle\epsilon\rangle\, \mathbf{LG}_{10} \tag{VII.3}$$

where Θ is a generic complex angle which collects information about the ellipse evolution.

Another aspect that should be delved into is the effect of a mistuned Mode Converter Telescope. The Measurements on the Astigmatic Mismatch showed a signal proportional to the Astigmatic Mismatch parameter on the Sensor dedicated to the Spherical Mode Matching. This cross-coupling is around $\kappa_1^{\eta}/\kappa_1^{\beta} \simeq 16\,\%$ and could be generated by the imperfect tuning of the Mode Converter Telescope. One possible model for this coupling can be based on a correction of Eq. III.82, which was obtained by ignoring the extra component generated by the mismatch of the second-order modes. My educated guess is that a tuning the Mode Converter based on the wrong reference should couple the astigmatic degree into the spherical mode matching signal. Moreover, it is reasonable to assume that this coupling could be comparable to the one estimated for the longitudinal control signal, which was on the order of 16 %. However, fully characterising the cross-talk between astigmatic and spherical mismatch signals requires performing the calculation in Section IV.1.6 and considering all the terms in Eq. III.81.

The natural evolution of this experiment is the implementation of an active correction of the coupling between the cavity and the beam. This control can be obtained by combing the error signal generated by the Mode Matching Sensing technique with a set of actuators that can linearly change the beam parameters.

A first approach can be based on the telescope presented in Section IV.1.4. In this case, we need to install a motorised stage to control the lens positions electronically.

However, this solution has a major flaw: as we saw in Section IV.1.4, the relationship between lens positions and beam parameters is not always linear. This problem can generate instability in the loop, and it should be avoided

To overcome this issue, we can change the actuation method by keeping the lens positions fixed and changing the focal lengths. This approach simplifies the relationship between the telescope configuration and the beam parameters as described in[47]. In this work, the authors were able to represent the small change of the lens diopters[1], $(\Delta S)^{-1}$ as an excitation of second order mode. In this way, the actuator can be interpreted as a generator of a second-order mode:

$$\Psi(\Delta S) = U_0 + i\frac{\pi}{2\lambda}w^2\Delta S\,\mathbf{LG}_{10} \tag{VII.4}$$

where w is the beam radius at the actuator position, U_0 is the fundamental mode when the actuator is at rest, $\Delta S = 0$, and $\mathbf{LG}_{10}$ is the second order mode which represents the actuation.

This study was focused on Spherical Mode Matching, but following the same generalisation done in Section II.II.2, it can be expanded to the Simple Astigmatic case. In particular, the Virgo Trento group is currently working on the technology of deformable mirrors to develop astigmatic actuators.

[1] It is more convenient to express the focal length as diopters, $S = 1/f$.

A EXPERIMENTAL TECHNIQUE

I.1. Beam Shape measurement

The beam profile measurement is done in two steps. In the first one, I measured the beam diameter, $2w_{(x'/y')}(z)$, at different positions (z_i), using the BC106N-VIS/M produced by Thorlabs. The beam profiler has different approaches for the beam diameter estimation, among which only the Ellipse fit and the 4σ method allow the study of a Simple Astigmatic Gaussian Beam.

I decided to use the Ellipse fit estimation since it is less sensitive to hot pixels and background issues. In this case, the algorithm estimates the beam diameter as the positions, (x_w, y_w) in which the power profile is a factor e^{-2} of the maximum:

$$P(x_w, y_w) =\simeq P_{\text{Max}} e^{-2}. \tag{A.1}$$

In this way, it estimates a line (x_w, y_w) and interpolates it with the ellipse function

$$\left(\frac{(x_w - x_0)\cos(\theta) + (y_w - y_0)\sin(\theta)}{2w_{x'}(z)}\right) + \left(\frac{(y_w - y_0)\cos(\theta) - (x_w - x_0)\sin(\theta)}{2w_{y'}(z)}\right) = 0. \tag{A.2}$$

In this way, the beam profile can estimate the diameter with respect to the internal reference of the beam, (x', y'). The beam shape is measured at different positions, z_i, to obtain a data set similar to the one represented in Fig. A.1. The beam parameters, $w_0^{x'/y'}$ and $z_0^{x'/y'}$, are estimated using the model:

$$w^{(x'/y')}(z) = w_0^{(x'/y')}\sqrt{1 + \left(\frac{z - z_0^{(x/y)}}{z_R^{(x'/y')}}\right)} \quad \text{with} \quad z_R^{(x'/y')} = \frac{\pi\left(w_0^{(x'/y')}\right)^2}{\lambda} \tag{A.3}$$

that is interpolated using the standard implementation of the least squares algorithm in the scipy package [50]. In this way, it is possible to characterise the two waists of the beam and estimate both the position and the dimension.

I.2. Astigmatic Mode Matching Telescope

I.2.1. *Modular Setup*

The first possible design is a modular telescope, in which a stand-alone telescope generates a simple astigmatic aberration. This setup comprises four lenses divided into two sub-telescopes, a standard spherical mode matching telescope controlling the spherical parameters and a Mode Converter that converts the spherical actuation into an astigmatic one.

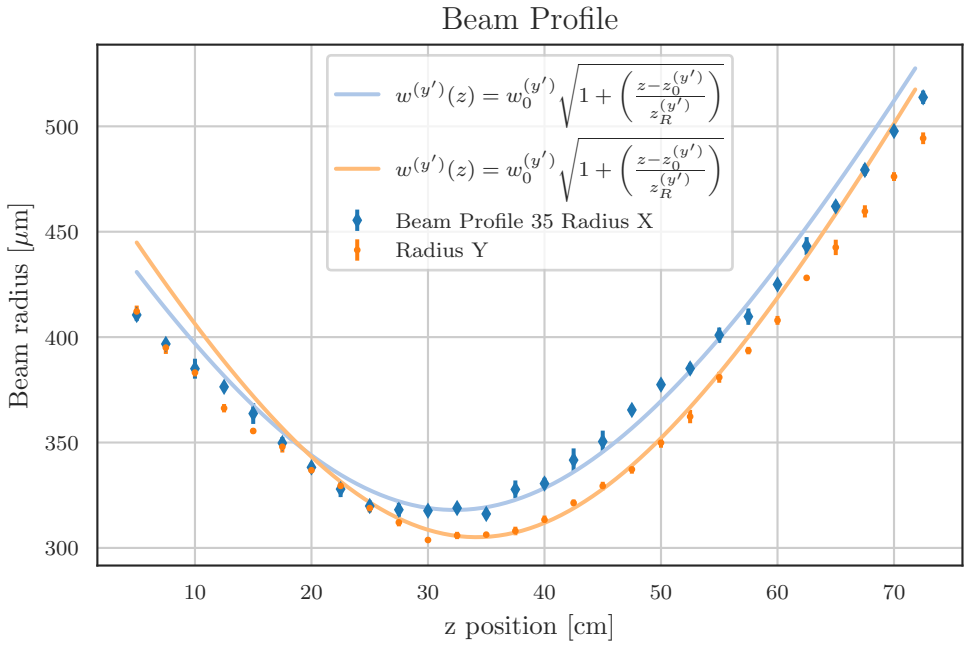

FIGURE A.1: Example of Beam Scan measurement. The Beam shape is characterised using the internal reference system of the Astigmatic Beam, (x', y'). The Beam radius is estimated using the interpolation Function of the Beam Profile.

We can briefly describe the principle behind this setup by making some simple considerations. First, we can assume that the spherical telescope can control the beam parameters around the Mode Converter Telescope mode q_{MCT}. In this case, the beam before the Mode Converter can be represented as:

$$\Psi^{pre}(q_{MCT}) = \mathbf{U}_{00}(q_{MCT}) + \epsilon_{pre}\mathbf{LG}_{01}(q_{MCT}) \tag{A.4}$$

where $\epsilon_{pre} = \beta_{pre} + i\gamma_{pre}$ are the mismatch parameters controlled by the first sub-telescope. The $\mathbf{LG}_{01}(q_{MCT})$ component will be converted by the astigmatic telescope, so the amplitude shape, after the Mode Converter becomes

$$\Psi^{pre}(q_{MCT}) = \mathbf{U}_{00}(q_{MCT}) + \epsilon_{pre}\mathbf{HG}_{11}^{45*}(q_{MCT}). \tag{A.5}$$

It is important to point out that the Hermite-Gauss mode 11 is rotated by 45° with respect to the cylindrical axis of the telescope, and it can be represented in the laboratory reference as[1]:

$$\Psi^{pre}(q_{MCT}) = \mathbf{U}_{00}(q_{MCT}) + \epsilon_{pre}\left(\mathbf{HG}_{11}^{45}(q_{MCT})\cos(2\theta) + \mathbf{HG}_{11}(q_{MCT})\sin(2\theta)\right) \tag{A.6}$$

where θ is the orientation of the cylindrical lens axis with respect to the laboratory reference. This four-lens telescope can control all the Simple astigmatic parameters: the α and η are manipulated by changing the matching between the initial beam and the Mode Converter, and the angle θ is controlled by rotating the cylindrical lenses together.

However, the modularity of this approach is not perfect. The Spherical Mode Matching Telescope is installed after the Astigmatic one, and it will rotate the phase of the

[1] See Section II.2.4.

Second Order Modes, $\mathbf{HG}_{11}$ and $\mathbf{HG}_{11}^{45}$. Assuming a generic $\mathbb{ABCD}$ matrix, the action of the third telescope can be represented using the Collins integral. In this way, we can represent the beam shape in the linear cavity as

$$\begin{aligned}\Psi^{in}(q_{in}) = \mathbf{U}_{00}(q_{in}) + \\ \epsilon_{pre}\left(\mathbf{HG}_{11}^{45}(q_{in})\cos(2\theta) + \mathbf{HG}_{11}(q_{in})\sin(2\theta)\right)\exp -i\,\mathrm{Arg}[Cq_{MCT}+D]\end{aligned} \tag{A.7}$$

where q_{in} represents the Gaussian mode after the input mirror. Following the same approach used in Section II.II.2, we can rewrite the incoming beam using the Cavity base, q_c:

$$\begin{aligned}\Psi^{in}(q_c) = \mathbf{U}_{00}(q_c) + \langle\epsilon\rangle\,\mathbf{LG}_{01}(q_{MCT}) + \\ \epsilon_{pre}e^{-i\,\mathrm{Arg}[Cq_{MCT}+D]}\left(\mathbf{HG}_{11}^{45}(q_{in})\cos(2\theta) + \mathbf{HG}_{11}(q_{in})\sin(2\theta)\right)\end{aligned} \tag{A.8}$$

where we used the same argument described in Section III.III.2 to neglect the perturbation of the high-order modes. In particular, we can see how it induces a rotation of the Astigmatic parameters:

$$\delta\epsilon = \epsilon_{pre}e^{-i\,\mathrm{Arg}[Cq_{MCT}+D]} \tag{A.9}$$

I.2.2. *Monolithic Setup*

The other possible design for the Astigmatic Mode Matching telescope is a monolithic setup composed of two cylindrical and two spherical lenses. The astigmatic actuation will be induced by moving the cylindrical and the spherical lenses. As before, we can still use the Mode Converter Theory to build a telescope that can induce the astigmatic aberration around the Spherical Gaussian beam. In particular, we can use $\mathbb{ABCD}$ matricies similar to Eq. III.17:

$$J_{x'} = \begin{pmatrix} 1-\frac{l_{mid}}{f_2} & -\frac{l_{in}l_{mid}}{f_2}+l_{in}+l_{mid} \\ -\frac{f_1+f_2-l_{mid}}{f_1f_2} & \frac{f_1(f_2-l_{in})-f_2(l_{in}+l_{mid})+l_{in}l_{mid}}{f_1f_2}\end{pmatrix} \quad \text{and} \quad J_{y'} = \begin{pmatrix} 1 & l_{mid}+l_{in} \\ 0 & 1\end{pmatrix}$$

where f_i are the effective focal length of the cylindrical lenses, l_{mid} the distance between them, and l_{in} is the position of the first lens. After that, we can impose that the rest position of the cylindrical telescope, $l_{in} = l_{in}^0$ and $l_{mid} = l_{mid}^0$, should match the beam shape long the two axes:

$$q_S(l_{in}^0, l_{mid}^0) = \frac{A_S q_0 + B_S}{C_S q_0 + D_S} = q_0 + B_T = q_T \tag{A.10}$$

in order to guarantee a telescope configuration in which the beam is not astigmatic. This requirement defines a relationship between the telescope parameters and the initial beam parameter:

$$q_0 = \left(l_{in} - \frac{l_{mid}}{2}\frac{f_2 - l_{mid}}{2(f_1+f_2-l_{mid})}\right) + \mathbf{i}\frac{\sqrt{4f_1f_2l_{mid}^2 - l_{mid}^4}}{2|f_1+f_2-l_{mid}|} \tag{A.11}$$

that corresponds to:

$$z_0 = \left(l_{in} - \frac{l_{mid}}{2} \frac{f_2 - l_{mid}}{2(f_1 + f_2 - l_{mid})} \right) \tag{A.12}$$

$$w_0 = \sqrt{\lambda \pi} \frac{\sqrt[4]{4 f_1 f_2 l_{mid}^2 - l_{mid}^4}}{\sqrt{2|f_1 + f_2 - l_{mid}|}}. \tag{A.13}$$

The Eq. A.11 cannot be analytically inverted, so the telescope parameter should be optimised numerically. The analytical model can still impose two limits on the telescope configurations. The focal lengths of the two lenses have to be with the same sign, both converging or both diverging, and the maximum distance between them is imposed by

$$l_{mid} < \sqrt{2 f_1 f_2} \quad \text{and} \quad f_1 f_2 > 0. \tag{A.14}$$

B | SIMULATION

II.1. Kat File Optical Setup

```
%%% FTblock LaserSource
################################################################################
l laser 0.0131 0 nlaser

s slasertoEOM 0 nlaser nEOMin

mod EOM 17M 0.1 1 pm nEOMin nEOMtrans
################################################################################
%%% FTend LaserSource


%%% FTblock ModeMatching
################################################################################

s s_tl1_in 0.254 nEOMtrans nl3in
lens l3 226e-3 nl3in nl3trans
s s_tl1_mid  0.6862 nl3trans nl4in
lens l4 282e-3 nl4in nl4trans
s s_tl1_out 0.3726    nl4trans npbs_in

################################################################################
%%% FTend ModeMatching


%%% FTblock Inj2Cav
################################################################################
# PBS/ cheap Faraday
dbs pbs2 npbs_in n2dump npbs_out npbs_ref

s s_4 5.0e-2 npbs_out nm6_in
bs1 m6 0 0 0 -45 nm6_in nm6_out dump dump
s s_5 10.0e-2  nm6_out nm7_in
bs1 m7 0 0 0 45 nm7_in nm7_out dump dump
s s_6 25e-2  nm7_out nIMin

# Pick off to QPD path and QPD path
s s_7 32.5e-2 npbs_ref nbs02in
```

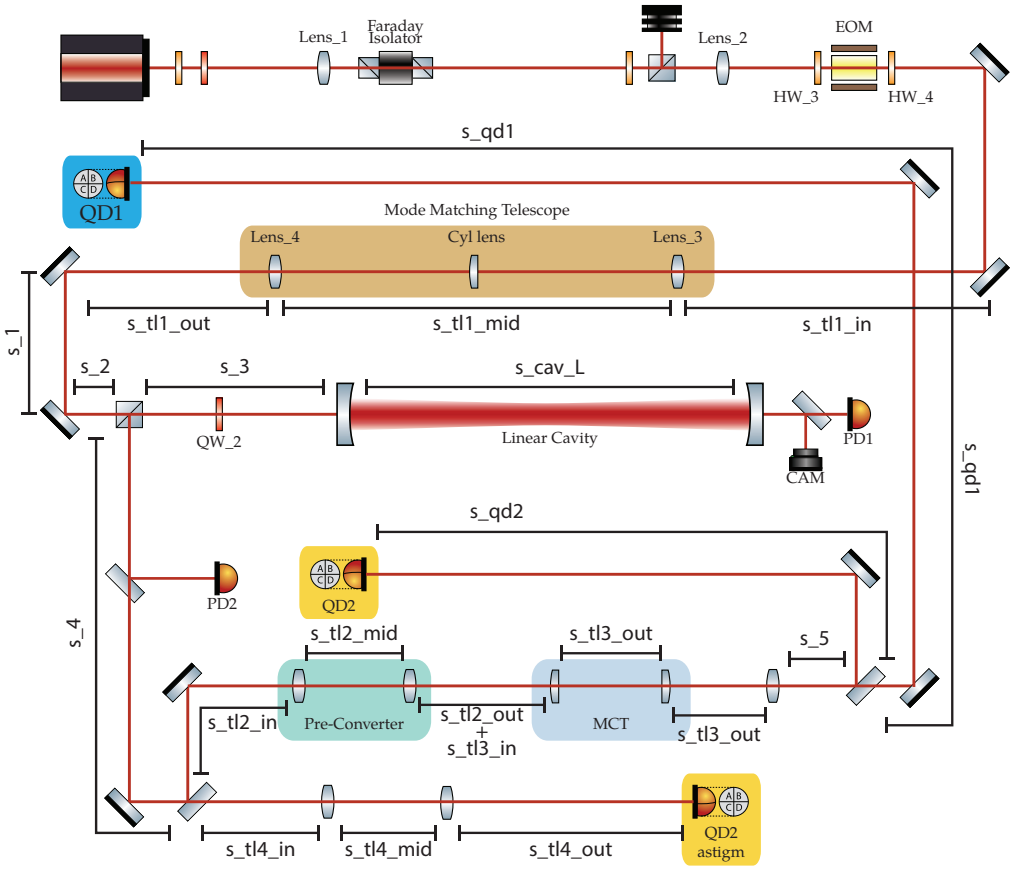

FIGURE B.1: Optical Setup for the Finesse Simulation with the name of the space and optics used in the KAT file.

```
bs bs02 0.45 0.05 45 0 nbs02in nbs02ref nbs02tran dump

###########################################################################
%%% FTend Inj2Cav


%%% FTblock Cavity
###########################################################################

m2 IMa 0 0 0 nIMin nIMbout
s s_IM 6e-3 1.4496 nIMbout nIMmid
m1 IM 0.001 0.002 0 nIMmid nIMtrans
#attr IMa Rc 1.e+16
attr IM Rc -1.
s scav 0.80 nIMtrans nEMin
m1 EM 0.001 0.002 0 nEMin nEMtrans
attr EM Rc 1.

###########################################################################
%%% FTend Cavity




%%% FTblock ModeConverter
###########################################################################

# Mode converter beam shaping telescope.
s s_tl2_in 0.09696 nbs02ref nL8in
lens L8 170e-3 nL8in nL8out
s s_tl2_mid 0.13304 nL8out nL9in
lens L9 -76e-3 nL9in nL9out
s s_tl2_out 0.09696 nL9out nfakemir_in


m1 fakemir 1 0 0 nfakemir_in nfakemir_out

# Mode converter telescope
# Mode converter lens 1
s s_tl3_in 0.0656 nfakemir_out ncyl1_in


# Mode converter lens 2
lens**  cyl1 100e-3 inf ncyl1_in ncyl1_out

# Cylindrical lens separation
# Note: focal length times square root 2
```

```
s s_tl3_mid 0.1414213562 ncyl1_out ncyl2_in

# Mode converter lens 2
lens**  cyl2 100e-3 inf ncyl2_in ncyl2_out
s s_tl3_out 0.42 ncyl2_out nLGpin

################################################################################
%%% FTend ModeConverter




%%% FTblock Gaussian
################################################################################

# With the gauss command I can optimally mode match into the cavity.
gauss inputparam EOM nEOMin 215u -44.0e-2
cav cavity IM nIMtrans EM nEMin

################################################################################
%%% FTend Gaussian


%%% FTblock LongitudinalPDs
################################################################################
### Photodiodes
## Add the typical PDH photodiode in reflection
pd1 PDH 17M -50.0226 nbs02tran
pd pdref nbs02tran
pd pdtrans nEMtrans
################################################################################
%%% FTend LongitudinalPDs

%%% FTblock RotatedQPD
################################################################################
# Spacing for proper Gouy phase at rotated QPDs. I need to fine tune
lens LGp 282.4e-3 nLGpin nLGp
s sQPD1 0.075 nLGp nQPDBSin

bs QPDBS 0.5 0.5 45 0 nQPDBSin nQPDBSrefl nQPDBStrans dump
s sQPDBStoQPD1 .405 nQPDBSrefl nQPD1
s sQPDBStoQPD2 .725 nQPDBStrans nQPD2

pd1 QPD1at0deg 17M  -79.2961 nQPD1
pdtype QPD1at0deg rotatedquadrant
pd1 QPD2at45deg 17M -85.8286 nQPD2
pdtype QPD2at45deg rotatedquadrant
```

```
pd QPD1at0deg_DC nQPD1
pdtype QPD1at0deg_DC rotatedquadrant
pd QPD2at45deg_DC nQPD2
pdtype QPD2at45deg_DC rotatedquadrant

pd1 QPD1at0deg_rf 17M 0 nQPD1
pd1 QPD2at45deg_rf 17M 0 nQPD2

########################################################################
%%% FTend RotatedQPD
```

Lens	Effective FocalLength [mm]
Lens_1	170
Lens_2	100
Lens_3	226
Lens_4	282
Lens_8	170
Lens_9	−76
Lens_10	282

TABLE B.1: Lenses used in the Optical Setup.

II.2. TWO LENS TELESCOPE CONTROL

This code allows to control a two-lens telescope by acting to the position of the two lenses, Lens_1 and Lens_2:

```
%%% FTblock ctrl_tel
########################################################################
var zL1 0
set zL1re zL1 re

var zL2 0
set zL2re zL2 re

func ds_in = $zL1re
noplot ds_in
put* {s_in} L $ds_in

func ds_mid =  $zL2re - $zL1re
noplot ds_mid
put* {s_mid} L $ds_mid

func ds_out = 0 - $zL2re
noplot ds_out
put* {s_out} L $ds_out
########################################################################
%%% FTend ctrl_tel
```

where “zL1“ and “zL2“ are the variation in position of δL_1 and δL_1 and “s_in“, “s_mid“ and “s_out“ are the space length before, in the middle and after the telescope.

II.3. Two lens telescope control with Driving Matrix

This code allows to control a two lens telescope by using a driving matrix as proxy. It uses the auxiliary parameter, $\tilde{\gamma}$ and $\tilde{\beta}$, and the driving matrix defined in Eq. IV.65

```
%%% FTblock ctrl_tel_wz
    ######################################################################
    var gamma_tel 0
    set gamma_telre gamma_tel re

    var beta_tel 0
    set beta_telre beta_tel re

    func zL1re = $gamma_telre * ({gammaL1:.6}) + $beta_telre * ({betaL1:.6})
    func zL2re = $gamma_telre * ({gammaL2:.6}) + $beta_telre * ({betaL2:.6})

    func ds_in = $zL1re
    noplot ds_in

    put* {s_in} L $ds_in

    func ds_mid =  $zL2re - $zL1re
    noplot ds_mid
    put* {s_mid} L $ds_mid

    func ds_out = 0 - $zL2re
    noplot ds_out
    put* {s_out} L $ds_out
    ######################################################################
    %%% FTend ctrl_tel_wz
```

where “gamma_tel“ and “beta_tel“ correspond to $\tilde{\gamma}$ and $\tilde{\beta}$, “gammaLi“ and “ betaLi” are the columns of Γ^{-1}, and “s_in“, “s_mid“ and “s_mid“ are the telescope length.

BIBLIOGRAPHY

[1] L. McCuller, S. E. Dwyer, A. C. Green, *et al.*, "LIGO's quantum response to squeezed states," *Physical Review D*, vol. 104, no. 6, p. 062 006, 2021, ISSN: 2470-0010. DOI: 10.1103/PhysRevD.104.062006. arXiv: 2105.12052.

[2] F. Magaña-Sandoval, T. Vo, D. Vander-Hyde, J. R. Sanders, and S. W. Ballmer, "Sensing optical cavity mismatch with a mode-converter and quadrant photodiode," *Physical Review D*, vol. 100, no. 10, p. 102 001, 2019. DOI: 10.1103/PhysRevD.100.102001.

[3] D. Z. Anderson, "Alignment of resonant optical cavities," *Applied Optics*, vol. 23, no. 17, p. 2944, 1984, ISSN: 0003-6935. DOI: 10.1364/AO.23.002944.

[4] The LIGO Scientific Collaboration, the Virgo Collaboration, R. Abbott, *et al.*, "GWTC-2.1: Deep extended catalog of compact binary coalescences observed by LIGO and virgo during the first half of the third observing run," 2021. arXiv: 2108.01045 [gr-qc].

[5] The LIGO Scientific Collaboration, the Virgo Collaboration, and the KAGRA Collaboration, "GWTC-3: Compact Binary Coalescences Observed by LIGO and Virgo During the Second Part of the Third Observing Run," pp. 1–82, 2021. arXiv: 2111.03606.

[6] R. Abbott, T. D. Abbott, S. Abraham, *et al.*, "GWTC-2: Compact Binary Coalescences Observed by LIGO and Virgo during the First Half of the Third Observing Run," *Physical Review X*, vol. 11, no. 2, p. 021 053, 2021. DOI: 10.1103/PhysRevX.11.021053.

[7] The Virgo Collaboration, "Advanced Virgo Plus Phase I - Design Report", Virgo-Technical Documentation System, Report No. VIR-0596A-19 (2019).

[8] J. Miller, L. Barsotti, S. Vitale, P. Fritschel, M. Evans, and D. Sigg, "Prospects for doubling the range of Advanced LIGO," *Physical Review D*, vol. 91, no. 6, p. 062 005, 2015, ISSN: 1550-7998. DOI: 10.1103/PhysRevD.91.062005.

[9] S. Chelkowski, H. Vahlbruch, B. Hage, *et al.*, "Experimental characterization of frequency-dependent squeezed light," *Physical Review A*, vol. 71, no. 1, p. 013 806, 2005, ISSN: 1050-2947. DOI: 10.1103/PhysRevA.71.013806.

[10] E. Oelker, T. Isogai, J. Miller, *et al.*, "Audio-Band Frequency-Dependent Squeezing for Gravitational-Wave Detectors," *Physical Review Letters*, vol. 116, no. 4, pp. 1–6, 2016, ISSN: 10797114. DOI: 10.1103/PhysRevLett.116.041102.

[11] Y. Zhao, N. Aritomi, E. Capocasa, *et al.*, "Frequency-Dependent Squeezed Vacuum Source for Broadband Quantum Noise Reduction in Advanced Gravitational-Wave Detectors," *Physical Review Letters*, vol. 124, no. 17, p. 171 101, 2020, ISSN: 10797114. DOI: 10.1103/PhysRevLett.124.171101. arXiv: 2003.10672.

[12] L. McCuller, C. Whittle, D. Ganapathy, *et al.*, "Frequency-Dependent Squeezing for Advanced LIGO," *Physical Review Letters*, vol. 124, no. 17, p. 171 102, 2020, ISSN: 0031-9007. DOI: 10.1103/PhysRevLett.124.171102.

[13] H. C. Ohanian and R. Ruffini, *Gravitation and Spacetime*. Cambridge University Press, 2013, ISBN: 9781107012943. DOI: 10.1017/CBO9781139003391.

[14] S. Hild, H. Grote, J. Degallaix, *et al.*, "DC-readout of a signal-recycled gravitational wave detector," *Classical and Quantum Gravity*, vol. 26, no. 5, p. 055 012, 2009, ISSN: 0264-9381. DOI: 10.1088/0264-9381/26/5/055012. arXiv: 0811.3242.

[15] W. B. Burton, *Advanced Interferometers and the Search for Gravitational Waves*, M. Bassan, Ed., ser. Astrophysics and Space Science Library. Cham: Springer International Publishing, 2014, vol. 404, ISBN: 978-3-319-03791-2. DOI: 10.1007/978-3-319-03792-9.

[16] F. Acernese, M. Agathos, A. Ain, *et al.*, "Virgo Detector Characterization and Data Quality during the O3 run," 2022, ISSN: 23318422. DOI: 10.48550/arXiv.2205.01555. arXiv: 2205.01555.

[17] C. M. Caves, "Quantum-Mechanical Radiation-Pressure Fluctuations in an Interferometer," *Physical Review Letters*, vol. 45, no. 2, pp. 75–79, 1980, ISSN: 0031-9007. DOI: 10.1103/PhysRevLett.45.75.

[18] ——, "Quantum-mechanical noise in an interferometer," *Physical Review D*, vol. 23, no. 8, pp. 1693–1708, 1981. DOI: 10.1103/PhysRevD.23.1693.

[19] H. Miao, *Exploring Macroscopic Quantum Mechanics in Optomechanical Devices*. Berlin, Heidelberg: Springer Berlin Heidelberg, 2012, ISBN: 978-3-642-25639-4. DOI: 10.1007/978-3-642-25640-0.

[20] ——, *Exploring Macroscopic Quantum Mechanics in Optomechanical Devices*. Berlin, Heidelberg: Springer Berlin Heidelberg, 2012, pp. 1–23, ISBN: 978-3-642-25639-4. DOI: 10.1007/978-3-642-25640-0.

[21] F. Sorrentino and J.-P. Zendri, "Squeezing and QM Techniques in GW Interferometers," in *Handbook of Gravitational Wave Astronomy*, C. Bambi, S. Katsanevas, and K. D. Kokkotas, Eds. Singapore: Springer Singapore, 2022, pp. 1–45, ISBN: 978-981-15-4702-7. DOI: 10.1007/978-981-15-4702-7_9-1.

[22] Virgo Collaboration, H. Vahlbruch, M. Mehmet, H. Lück, and K. Danzmann, "Increasing the Astrophysical Reach of the Advanced Virgo Detector via the Application of Squeezed Vacuum States of Light," *Physical Review Letters*, vol. 123, no. 23, p. 231 108, 2019, ISSN: 10797114. DOI: 10.1103/PhysRevLett.123.231108.

[23] L. McCuller, S. E. Dwyer, A. C. Green, *et al.*, "LIGO's quantum response to squeezed states," *Physical Review D*, vol. 104, no. 6, p. 062 006, 2021, ISSN: 2470-0010. DOI: 10.1103/PhysRevD.104.062006.

[24] M. Mehmet and H. Vahlbruch, "High-efficiency squeezed light generation for gravitational wave detectors," *Classical and Quantum Gravity*, vol. 36, no. 1, p. 015 014, 2019. DOI: 10.1088/1361-6382/aaf448.

[25] A. E. Siegman, *Lasers*. University Science Books, 1990, ISBN: 9781680152371.

[26] M. Born and E. Wolf, *Principles of Optics*. Cambridge University Press, 2019, ISBN: 9781108769914. DOI: 10.1017/9781108769914.

[27] S. A. Collins, "Lens-System Diffraction Integral Written in Terms of Matrix Optics," *Journal of the Optical Society of America*, vol. 60, no. 9, p. 1168, 1970, ISSN: 0030-3941. DOI: 10.1364/JOSA.60.001168.

[28] S. Peng, G. Jin, and W. Tingfeng, "Propagation equation of Hermite–Gauss beams through a complex optical system with apertures and its application to focal shift," *Journal of the Optical Society of America A*, vol. 30, no. 7, p. 1381, 2013, ISSN: 1084-7529. DOI: 10.1364/JOSAA.30.001381.

[29] M. W. Beijersbergen, L. Allen, H. van der Veen, and J. P. Woerdman, "Astigmatic laser mode converters and transfer of orbital angular momentum," *Optics Communications*, vol. 96, no. 1-3, pp. 123–132, 1993. DOI: 10.1016/0030-4018(93)90535-D.

[30] J. A. Arnaud and H. Kogelnik, "Gaussian Light Beams with General Astigmatism," *Applied Optics*, vol. 8, no. 8, p. 1687, 1969. DOI: 10.1364/AO.8.001687.

[31] G. Mueller, Q.-z. Shu, R. Adhikari, *et al.*, "Determination and optimization of mode matching into optical cavities by heterodyne detection," *Optics Letters*, vol. 25, no. 4, p. 266, 2000, ISSN: 0146-9592. DOI: 10.1364/OL.25.000266.

[32] E. D. Black, "An introduction to Pound–Drever–Hall laser frequency stabilization," *American Journal of Physics*, vol. 69, no. 1, pp. 79–87, 2001, ISSN: 0002-9505. DOI: 10.1119/1.1286663.

[33] C. Matteo, "A novel technique for laser mode-matching in gravitational wave detectors," Ph.D. dissertation, Universitá degli studi di Padova, 2020.

[34] E. Morrison, B. J. Meers, D. I. Robertson, and H. Ward, "Automatic alignment of optical interferometers," *Applied Optics*, vol. 33, no. 22, p. 5041, 1994, ISSN: 0003-6935. DOI: 10.1364/AO.33.005041.

[35] The Virgo Collaboration, "Advanced Virgo Plus Phase I - Design Report," Tech. Rep., 2019. DOI: VIR-0596A-19.

[36] B. E. A. Saleh and M. C. Teich, *Fundamentals of photonics*, ISBN: 9781439854907. DOI: 10.1002/9783527635245.ch2.

[37] M. Vardaro, "Toward a Fully Automated and Digitally Controlled Squeezed Vacuum Source for Gravitational Wave," Ph.D. dissertation, Università degli studi di Padova, 2018.

[38] P. Horowitz and W. Hill, *The Art of Electronics*. Cambridge University press, 2015, ISBN: 9780521809269.

[39] N. C. Wong and J. L. Hall, "Servo control of amplitude modulation in frequency-modulation spectroscopy: demonstration of shot-noise-limited detection," *Journal of the Optical Society of America B*, vol. 2, no. 9, p. 1527, 1985, ISSN: 0740-3224. DOI: 10.1364/JOSAB.2.001527.

[40] L. Li, F. Liu, C. Wang, and L. Chen, "Measurement and control of residual amplitude modulation in optical phase modulation," *Review of Scientific Instruments*, vol. 83, no. 4, p. 043 111, 2012, ISSN: 0034-6748. DOI: 10.1063/1.4704084.

[41] B. G. Mytsyk, A. S. Andrushchak, N. M. Demyanyshyn, *et al.*, "Piezo-optic coefficients of MgO-doped $LiNbO_3$ crystals," *Applied Optics*, vol. 48, no. 10, p. 1904, 2009, ISSN: 0003-6935. DOI: 10.1364/AO.48.001904.

[42] N. Hodgson and H. Weber, *Optical Resonators*, 15. London: Springer London, 1997, vol. 44, pp. 7870–7878, ISBN: 978-1-4471-3597-5. DOI: 10.1007/978-1-4471-3595-1.

[43] C. Bond, D. Brown, A. Freise, and K. A. Strain, *Interferometer techniques for gravitational-wave detection*, 1. Springer International Publishing, 2016, vol. 19, pp. 1–221, ISBN: 4111401600. DOI: 10.1007/s41114-016-0002-8.

[44] C. R. Harris, K. J. Millman, S. J. van der Walt, *et al.*, "Array programming with NumPy," *Nature*, vol. 585, no. 7825, pp. 357–362, 2020, ISSN: 0028-0836. DOI: 10.1038/s41586-020-2649-2.

[45] H. Ku, "Notes on the use of propagation of error formulas," *Journal of Research of the National Bureau of Standards, Section C: Engineering and Instrumentation*, vol. 70C, no. 4, p. 263, 1966, ISSN: 0022-4316. DOI: 10.6028/jres.070C.025.

[46] L. E. Ellis, A. Hughes, and D. Grawoig, *Statistics: A Foundation for Analysis*. Addison-Wesley Publishing Company, 1971, ISBN: 9780201030211.

[47] A. Perreca, A. F. Brooks, J. W. Richardson, D. Töyrä, and R. Smith, "Analysis and visualization of the output mode-matching requirements for squeezing in Advanced LIGO and future gravitational wave detectors," *Physical Review D*, vol. 101, no. 10, p. 102 005, 2020, ISSN: 2470-0010. DOI: 10.1103/PhysRevD.101.102005. arXiv: 2001.10132.

[48] P. Kwee, J. Miller, T. Isogai, L. Barsotti, and M. Evans, "Decoherence and degradation of squeezed states in quantum filter cavities," *Physical Review D*, vol. 90, no. 6, p. 062 006, 2014, ISSN: 1550-7998. DOI: 10.1103/PhysRevD.90.062006.

[49] M. Mehmet and H. Vahlbruch, "High-efficiency squeezed light generation for gravitational wave detectors," *Classical and Quantum Gravity*, vol. 36, no. 1, p. 015 014, 2019, ISSN: 0264-9381. DOI: 10.1088/1361-6382/aaf448.

[50] P. Virtanen, R. Gommers, T. E. Oliphant, *et al.*, "SciPy 1.0: fundamental algorithms for scientific computing in Python," *Nature Methods*, vol. 17, no. 3, pp. 261–272, 2020, ISSN: 1548-7091. DOI: 10.1038/s41592-019-0686-2.